PhD-FSTC-2011-04
The Faculty of Sciences, Technology and Communication

DISSERTATION

Defense held on 12/04/2011 in Luxembourg

to obtain the degree of

DOCTEUR DE L'UNIVERSITÉ DU LUXEMBOURG

EN PHYSIQUE

by

Katja M. HÖNES
Born on October 6th 1981, in Stuttgart (Germany)

PHOTOLUMINESCENCE MEASUREMENTS ON SOLAR CELL MATERIALS: CHALCOPYRITES AND KESTERITES

Dissertation defense committee

Prof. Dr. Susanne Siebentritt, dissertation supervisor
Professor, Université du Luxembourg

Prof. Dr. Uwe Rau
Forschungszentrum Jülich
Professor, Rheinisch-Westfälische Technische Hochschule Aachen

Prof. Dr. Roland Sanctuary, Chairman
Professor, Université du Luxembourg

Prof. Dr. Susan Schorr
Helmholtz Zentrum Berlin
Professor, Freie Universität Berlin

Dr. Alex Redinger
Université du Luxembourg

Contents

List of Figures

List of Tables

Chapter 1

Introduction

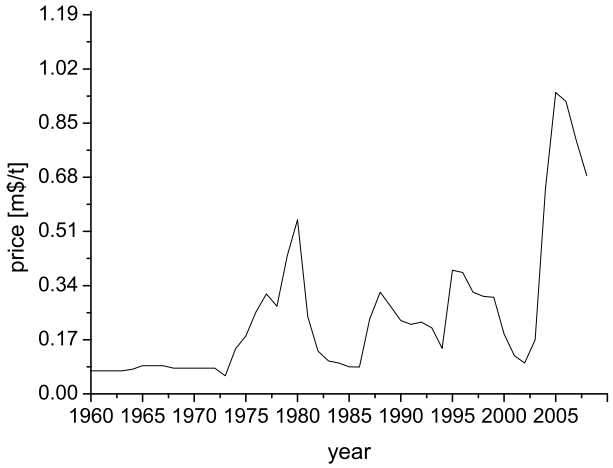

Figure 1.1: Development of the indium price in the last 50 years according to [1].

The chalcopyrite $Cu(In,Ga)Se_2$ is by now an established semiconductor for thin film solar cells. Its band gap between 1.05-1.73 eV is a good match to the maximum of the solar energy distribution available on the earth's surface [22]. Additionally it shows a high absorption coefficient, compared to other direct band gap semiconductors. The high absorption coefficient of the direct band gap, allows the use of a thin absorber layer of several μm. Several methods of absorber manufacturing (vapour deposition, electrodeposition, epitaxy or printing techniques) are available. Compared to the silicon solar cells, widely used so far, whose absorber layer are prepared by slicing a crystal grown from the melt, less energy for the manufacturing process of the absorber layer is needed. Along with the smaller thickness required, this offers the possibility of reducing costs in the production of solar cells.

Efficiencies up to 20.3 % on the laboratory scale [23] and up to 14.3 % for modules [24] are reported. 13 companies produce $Cu(In,Ga)Se_2$ modules at

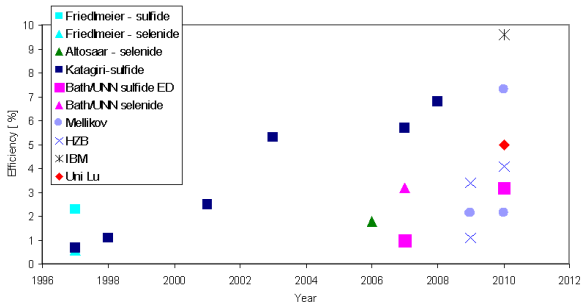

Figure 1.2: Development of the efficiency of $Cu_2ZnSnS(e)_4$ solar cells ([2]- [21])

present [25] and in 2009 172MW of thin-film modules were produced [26]. A distinctive feature of chalcopyrites is their high tolerance for deviations from stoichiometry, while still keeping the chalcopyrite structure. The low defect formation enthalpy allows compensation for deviations from stoichiometry by the formation of native defects, for example copper vacancies V_{Cu}, or antisite defects, such as a gallium atom in place of copper Ga_{Cu}. As these intrinsic defects also govern the electrical properties of the chalcopyrites, they play a crucial role for the properties of the device. However despite the good efficiencies, not much is known about the chemical nature of the defects responsible for the doping. The symmetry of the defects might be one way to determine their chemical nature and will be investigated in the following.

One major concern in fabricating thin film solar cells from the chalcopyrite $Cu(In,Ga)Se_2$ as a lower-cost alternative to silicon solar cells is the indium price. As can be seen in figure 1.1, the indium price is highly volatile. There are several reasons for this: On one hand indium is only mined as a by-product, mainly of ZnS ores. On the other hand the indium reserves are concentrated in only few countries and there exists uncertainty of the indium yield of the

known reserves. Furthermore, the demand for indium increased recently, at it is used in flat screen displays as well as in thin film photovoltaics. For the future, due to increasing demand, a further increase in the indium price is expected. One possibility to overcome this drawback is to replace the group III element indium by isoelectrical substitution by more abundant, non-toxic elements like zinc (Zn) and tin (Sn), from the second and fourth group of the periodic table. This leads from the chalcopyrite $CuInSe_2$ to the kesterite $Cu_2ZnSnSe_4$. The resulting band structure is expected to remain similar to that observed in the chalcopyrite material, leading to similar band gaps and absorption coefficients. In recent years the interest in kesterite as a solar cell material has increased as can be seen in figure 1.2 and efficiencies up to 9.6 % are reported [13].

$Cu_2ZnSnS(e)_4$ is a new material, and at present not much is known about adapted synthesis routes or material properties. One important issue is the detection of secondary phases. In $Cu_2ZnSnSe_4$ the additional phases Cu_xSe_y, $ZnSe$ or Cu_2SnSe_y are likely to occur, especially as the $Cu : Zn : Sn$ ratio region in which only kesterite forms, is reported to be small [27]. Secondary phases are detrimental to the solar cell device: highly conductive secondary phases at the grain boundaries can lead to a shunting of the solar cell, whereas a highly resistive secondary phase within the current path, will increase the series resistance. In any case the secondary phase will decrease the available volume of the absorber material. Therefore methods to identify the secondary phases are needed. In this thesis photoluminescence and X-ray diffraction measurements are investigated as possible methods for phase analysis. As kesterite, similar to the chalcopyrites, is expected to be a natively doped semiconductor, the defects will play a crucial role for the device properties. Therefore photoluminescence measurements are used to gain information about defects in kesterites.

The thesis will be organised as follows

Chapter 2 introduces the crystal structure of the materials investigated and describes the observable transitions in photoluminescence measurements.

Chapter 3 explains the different synthesis methods used to make the samples, examined in this thesis.

Chapter 4 introduces the measurement techniques.

Chapter 5 describes the possible secondary phases in the $Cu \cdot Zn \cdot Sn \cdot S$ and $Cu \cdot Zn \cdot Sn \cdot Se$ systems and demonstrates how XRD and photoluminescence measurements can be used to identify the secondary phases, which can occur during synthesis of Cu_2ZnSnS_4 and $Cu_2ZnSnSe_4$ samples.

Chapter 6 presents first results of photoluminescence measurements on polycrystalline $Cu_2ZnSnSe_4$ samples.

Chapter 7 analyses the symmetry of intrinsic defects in the chalcopyrites $CuInSe_2$ and $CuGaSe_2$. For this purpose first the basic principles of group theory are introduced, and two different models to describe defects will be presented. Subsequently polarisation-dependent photoluminescence measurements on epitaxial films and a crystal will be discussed.

Chapter 2

Chalcopyrites, Kesterites and optical transitions

2.1 Material properties

In this chapter, the two investigated material systems, the chalcopyrites $CuInSe_2$ and $CuGaSe_2$ and the kesterites $Cu_2ZnSnSe_4$ and Cu_2ZnSnS_4 shall be introduced.

2.1.1 Crystal structure

Chalcopyrites The crystal structure of chalcopyrite is shown in figure 2.1: red atoms represent copper, yellow atoms the group III element indium or gallium and dark blue atoms the chalcogen selenium. The chalcopyrites can be derived from the II-VI semiconductors, for example $ZnSe$, by isoelectric substitution of the group II element with one element from the first and one from the third group of the periodic table as depicted in figure 2.2. In doing so, the average number of valence electrons per atom remains four, maintaining the tetrahedral bonding characteristic for most semiconductors. In contrast to $ZnSe$ with one cation, the chalcopyrites have two cations to distribute over the cation sites. Therefore the face centred cubic zinc blende crystallographic unit cell of $ZnSe$ needs to be doubled, leading to the body centred tetragonal unit cell for chalcopyrite shown in figure 2.1. Thus the space group changes from $F\bar{4}3m$ for $ZnSe$ to $I\bar{4}2d$ for chalcopyrites, as will be explained in more detail in chapter 7.1.1. The tetragonal unit cell is described by the lattice constant a along the $\vec{x}$- and $\vec{y}$- direction and the lattice constant c along the $\vec{z}$-direction, as indicated in figure 2.1. The two different cation species give rise to two more structural degrees of freedom: on one hand the anion displacement u and on the other hand the tetragonal distortion η. As each selenium anion is bound to two atoms of the first group of the periodic table and two atoms from the third group, the unequal bond lengths $R_{I-VI} \neq R_{III-VI}$ lead to a displacement of the selenium atom from its ideal zinc-blende site in the plane perpendicular to the $\vec{c}$-axis. The anion displacement is defined as $u - \frac{1}{4} = (R^2_{I-VI} - R^2_{III-VI})/a^2$, where a is the lattice constant along the short edge of the tetragonal unit cell. For most of the chalcopyrites the ratio between the lattice constants in a and c direction is slightly $\frac{c}{a} \neq 2$, in contrast to what is expected for merely doubling the cubic face centred unit cell. This is called the tetragonal distortion [28].

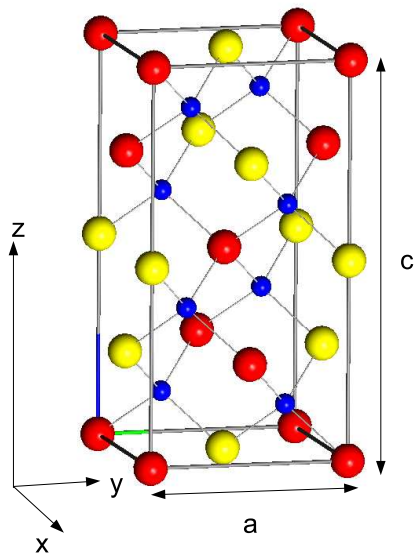

Figure 2.1: Structure of the Chalcopyrite crystal: red atoms represent Cu, yellow atoms the group III element Ga or In and blue atoms the chalcogen S or Se [29].

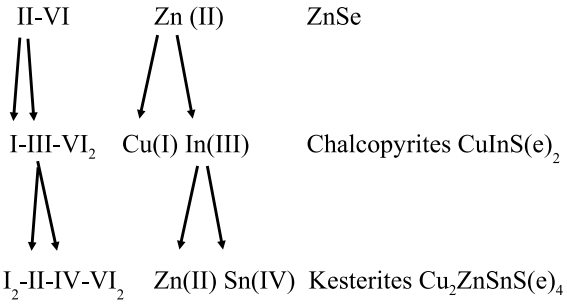

Figure 2.2: Isoelectric substitution: the average electron number of four per atom is conserved, if a group II element is substituted by elements from group I and III, and for a group III element by substituting it by elements from group II and IV.

Kesterites Repeating the isoelectric substitution for the group III element (indium or gallium), by one element from the second and one from the fourth group of the periodic system, leads from the chalcopyrites with the general formula $I\ III\ VI_2$ to the kesterites with the formula $I_2\ II\ IV\ VI_4$. Subsequently, the kesterites Cu_2ZnSnS_4 and $Cu_2ZnSnSe_4$ shall be considered. The term "kesterite" refers to both: a tetragonal compounds with the chemical formula $I_2\ II\ IV\ VI_4$ and a specific crystal structure. Kesterites crystallise in the same tetragonal body centred unit cell as chalcopyrite. However, the cations can be distributed in three different ways over the cation sites, according to whether it is the kesterite, stannite or a primitive Cu-Au-like structure. As the formation energy of the Cu-Au-like structure is higher than that of the kesterite or stannite [35], it is unlikely to be observed and will not be considered in further detail here. The kesterite and stannite structures are shown in figures 2.3 and 2.4. Copper atoms are indicated in red, zinc atoms in green, tin atoms in violet and chalcogen atoms in blue. The kesterite structure shown in figure 2.3 has $I\bar{4}$ symmetry. The cations are arranged in alternating cooper-tin and copper-zinc cation layers. The stannite structure shown in figure 2.4, on the other hand, has $I\bar{4}2m$ symmetry. Here a copper cation layer alternates with a zinc-tin cation layer. According to density functional theory calculations reported by [35],[30],[31] the formation energy of the kesterite structure is slightly smaller than that of the stannite structure, but as the energy difference is only small both structures might be observed in experiments. The kesterite and stannite structure can hardly be distinguished in X-ray diffraction experi-

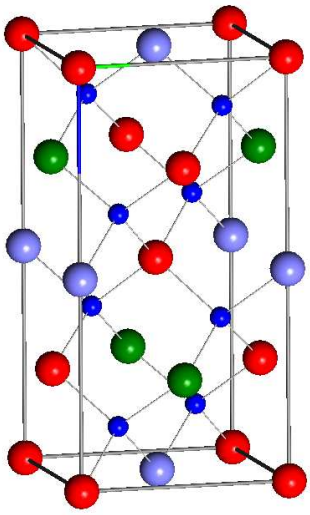

Figure 2.3: Cu_2ZnSnX_4 with $X = S, Se$ in the kesterite structure: Cu atoms are indicated in red, Zn atoms in green, Sn atoms in violet and the chalcogen atoms in blue.

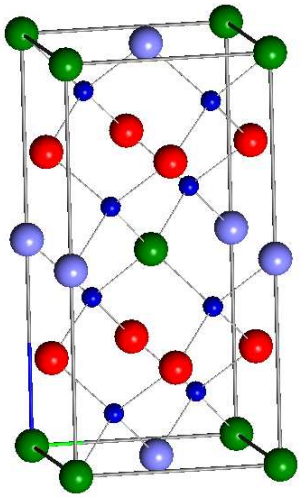

Figure 2.4: Cu_2ZnSnX_4 with $X = S, Se$ in the stannite structure: Cu atoms are indicated in red, Zn atoms in green, Sn atoms in violet and the chalcogen atoms in blue.

Cu_2ZnSnS_4

Kesterite				Stannite			
a[Å]	c[Å]	$\frac{c}{a}$		a[Å]	c[Å]	$\frac{c}{a}$	Method
5.326^a	10.663^a	2.002		5.325^a	10.629^a	1.996	calc
5.448^b	10.889^b	1.999		5.438^b	10.941^b	2.012	calc
5.428^c	10.864^c	2.001		5.436^d	10.850^d	1.996	exp

$Cu_2ZnSnSe_4$

Kesterite				Stannite			
a[Å]	c[Å]	$\frac{c}{a}$		a[Å]	c[Å]	$\frac{c}{a}$	Method
5.605^a	11.200^a	1.998		5.604^a	11.208^a	2.000	calc
5.68^e	11.36^e	2.00		5.688^f	11.338^f	1.993	exp
				5.681^d	11.338^d	1.996	exp

Table 2.1: Calculated and measured experimental lattice constants according to ^{a}[30],^{b}[31],^{c}[32],^{d}[33] and ^{e}[34].

ments, as the only difference is the zinc and copper ordering. As zinc and copper are neighbouring elements in the periodic table, they have almost the same number of valence electrons. Therefore their atomic form factor is very similar, leading to a very similar diffracted intensity for both atoms.

The calculated and measured lattice constants are given in table 2.1. For both the kesterite and the stannite structure of Cu_2ZnSnS, as well as of $Cu_2ZnSnSe_4$ a c to a ratio close to 2 was found. The degree of freedom for the anion displacement in $Cu_2ZnSnS(e)_4$ increases compared to the chalcopyrites, as the anion forms three bonds of different lengths to the three different cations in stannite and has four different bond lengths in kesterite, due to the copper atoms residing on nonequivalent lattice sites [30]. In the following, unless stated otherwise "kesterite" is used to refer to compounds with the chemical formula $Cu_2ZnSnS(e)_4$, independent of their crystal structure.

2.1.2 Defects in chalcopyrites and kesterites

Several different kinds of defects can form in semiconductors [47]: two-dimensional defects, line defects, point defects and defect clusters. A two dimensional defect, is for example, a grain boundary, whereas line defects are for example dislocations. Transmission electron microscopy (TEM) and electron beam induced current (EBIC) measurements are used in [48] to relate dislocations to regions of reduced free carrier lifetime. Line defects always degrade the electrical properties of devices and should therefore be avoided [47]. Characteristic for point defects are, that only

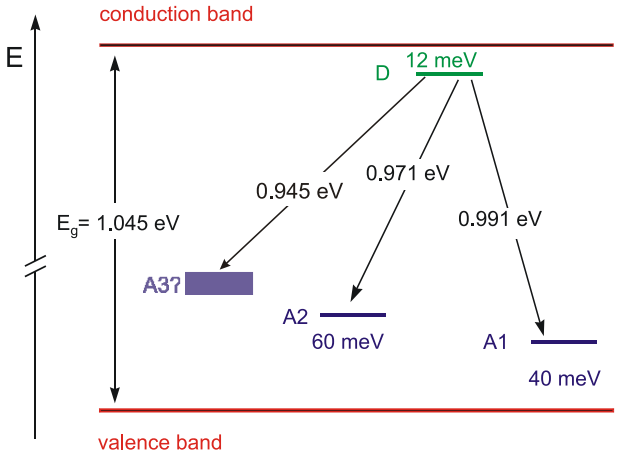

Figure 2.6: Recombination diagram for shallow defects in $CuInSe_2$ according to [43].

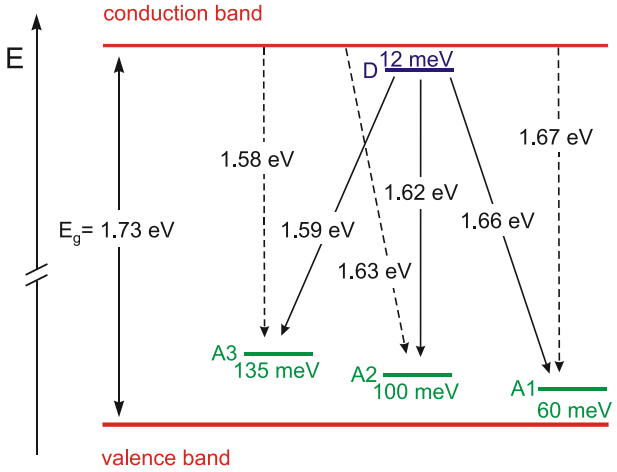

Figure 2.7: Recombination diagram for shallow defects in $CuGaSe_2$ according to [44], [45] and [46].

Point defect	Vacancies			Interstitials			Anti-site defects					
Nomenclature	V_{Cu}	V_{III}	V_{Se}	Cu_i	III_i	Se_i	Cu_{III}	III_{Cu}	Cu_{Se}	Se_{Cu}	III_{Se}	Se_{III}
electric character	A	A	D/A	D	D	A	A	DX	A	D	D	A
$\Delta H^{CuGaSe_2}[eV]$	0.66[a]	2.83[a]	2.6[b]	3.38[a]	9.9[b]	23.7[b]	1.41[a]	4.22[a]	7.4[b]	8.1[b]	3.7[b]	3.4[b]
$\Delta H^{CuInSe_2}[eV]$	0.60[a]	3.04[a]	3.00[c]	2.88[a]	9.1[e]	22.4[e]	1.54[a]	3.34[d]	5.4[d]	6.0[d]	5.0[d]	5.2[d]

Table 2.2: Formation enthalpy of the 12 possible point defects in $Cu(In,Ga)Se_2$ according to [a][36], [b][37], [c][38], [d][39] and [e][40]. The electric character is indicated by D for donor and A for acceptor state [41].

Point defect	Vacancies				Interstitials			Anti-site defects					
Nomenclature	V_{Cu}	V_{Zn}	V_{Sn}	V_S	Cu_i	Zn_i	Sn_i	Cu_{Zn}	Zn_{Cu}	Cu_{Sn}	Sn_{Cu}	Zn_{Sn}	Sn_{Zn}
electric character	A	A	A	mid gap	D	D	D	A	D	A	D	A	D
$\Delta H^{Cu_2ZnSnSe_2}[eV]$	0.77	1.12	2.82	0.99	3.13	5.92	8.11	0.01	2.42	0.87	6.54	0.69	4.11

Table 2.3: Formation enthalpy of the cation related point defects and the sulphur vacancy in Cu_2ZnSnS_4 for copper rich growth conditions according to [42]. In regards to the dependence of the formation enthalpy on the Fermi energy, the maximum value of the formation energy is given.

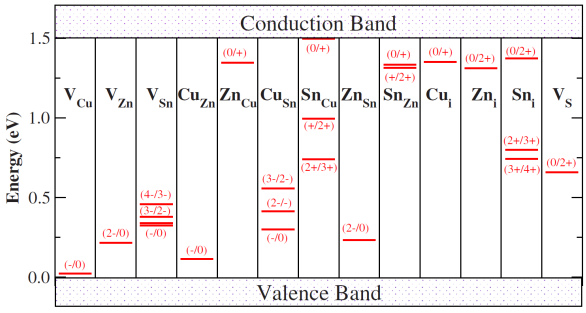

Figure 2.5: Calculated transition energy levels for Cu_2ZnSnS_4 according to [27]

one atom is involved. Point defects can be caused by either impurity atoms or native defects, for example a copper vacancy. Here, only native defects shall be considered. There are several different types of native point defects:

- Vacancies, denoted by V_A, corresponding to an unoccupied atom A lattice site
- Interstitials A_i: an atom A occupying a interstitial site
- Anti-site defects A_B indicating an atom A occupying an atom B lattice site

Point defects are of uttermost importance for chalcopyrites, as they are responsible for the doping behaviour. The same behaviour is expected for kesterites. The formation energies and the electric character for the possible point defects in the chalcopyrites $CuInSe_2$ and $CuGaSe_2$, the three vacancies, three interstitials and six anti-site defects, are given in table 2.2. The calculated formation enthalpies for the chalcopyrites show that the most likely native defects to form are vacancies, copper interstitials and Cu_{III} and III_{Cu} anti-site defects. The corresponding formation energies and the electric character of the cation related defects and the sulphur vacancies in the kesterite Cu_2ZnSnS_4 are given in table 2.3. According to the calculation the most probable defects to form are copper, zinc and sulphur vacancies and Cu_{Zn}, Cu_{Sn} and Zn_{Sn} anti-site defects. Figure 2.5 shows the calculated transition energy levels for the defects in Cu_2ZnSnS_4. Besides the sulphur vacancy V_S which results in a mid-gap state, all other defects with low formation energies give rise to acceptor states. This is in agreement with the observed p-type conductivity of kesterite samples i.e. [49], [50],[51]. The defect formation enthalpies for the chalcopyrites and Cu_2ZnSnS_4 were calculated using density functional theory, whereas a macroscopic vacancy model was used to calculate some of the vacancies in chalcopyrite.

The electric character of a defect is not always obvious. Interactions with other defects, or the change of the charge state, can introduce metastabilities: a defect can change its character from a shallow to a deep defect, or from a donor to an acceptor state [47]. For example in the chalcopyrites the copper and the selenium vacancy form a defect complex ($V_{Cu} - V_{Se}$), which changes its character from a shallow donor to a shallow acceptor, while trapping two electrons $(V_{Cu} - V_{Se})^+ + 2e^- \longleftrightarrow (V_{Cu} - V_{Se})^-$. An other example is the III_{Cu}-anti-site defect in $CuInSe_2$, which changes from a shallow into a deep state: $III^{2+}_{Cu} + 2e^- \longleftrightarrow III^0_{Cu}$. For $CuGaSe_2$ the positively charged defect is already a somewhat deep state, but becomes even deeper after electron capture. However the III_{Cu}-anti-site defect can also form neutral defect complexes with copper vacancies V_{Cu}, resulting in the passivation of the defect [52]. The low formation enthalpy of some of the defects is the reason for the tolerance of chalcopyrites to deviation from stoichiometry.

There exists several experimental methods to access the properties of defects.

One way to access the chemical nature of a defect is performing electron paramagnetic resonance (EPR) measurements. EPR measurements on copper poor $CuInSe_2$ samples after annealing in vacuum or selenium vapor, show a broad isotropic signal with a Landé-factor of $g = 2.12$. The signal disappears for samples annealed in copper vapor, therefore the EPR signal at $g = 2.12$ is assigned to a copper vacancy V_Cu according to [53]. Another narrow EPR line is observed around $g = 2.003$, close to the value of a free electron. Proposed explanations include a high local density of donors along extended defects or dislocations [54] or a V_{Cu} vacancy [53]. No agreement for the assignment between native defects and EPR signal seems to be reached. In contrast, impurity atoms, such as Ni^+ and Fe^{3+} incorporated in the chalcopyrite samples could be clearly identified by EPR measurements [53],[55], [54].

Of special importance for the device properties is the electric character of the defects, whether it is an acceptor or donor, and how deep the energy level lies in the band gap. Both $CuInSe_2$ and $CuGaSe_2$ show the same shallow defects in photoluminescence experiments: one donor and three acceptors [56]. The recombination diagrams for $CuInSe_2$ and $CuGaSe_2$ are shown in figure 2.6 and 2.7. The defect energies in $CuInSe_2$ are slightly shallower than in $CuGaSe_2$, the dominating acceptors being at a depth of 40 meV and 60 meV compared to the acceptors in $CuGaSe_2$ at 60 meV, 100 meV and 150 meV. This is in agreement with the trends predicted by an estimate of the hydrogen model, using the dielectric constant and the effective masses. For $CuGaSe_2$ this results in a 110 meV deep acceptor and a 16 meV deep donor level and for $CuInSe_2$ the acceptor is 50 meV and the donor 6 meV deep. The hydrogen model will be introduced in more

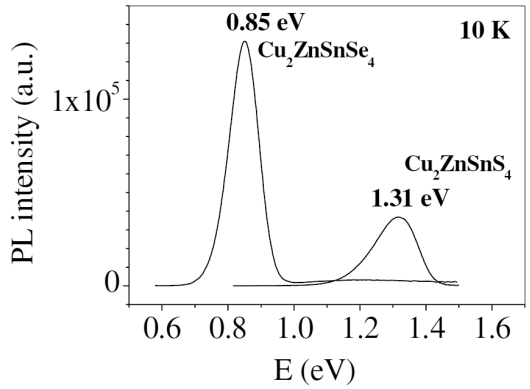

Figure 2.8: Photoluminescence spectra of $CuZnSnS_4$ and $CuZnSnSe_4$ according to [51].

detail in chapter 7.3. In addition Hall measurements allow the determination of the activation energy of a defect. In compensated samples normally only the deepest defect can be observed. Hall measurements on $CuGaSe_2$ samples confirm the activation energy found by photoluminescence measurements [56].

For kesterites, all reported photoluminescence spectra are wide and asymmetric, pointing to samples dominated by fluctuating potentials. An example of a spectrum is shown in figure 2.8. For $CuZnSnS_4$ a transition is observed around 1.31 eV [51], whereas for $Cu_2ZnSnSe_4$ transitions between 0.85 eV and 0.95 eV are reported [51], [57], [58]. It is not possible to determine the activation energy of defects from samples dominated by fluctuating potentials, as the transition energy in such samples depends on the degree of compensation. Therefore no experimental values of the defect energy levels of the kesterites are published yet.

To improve the electrical properties of the $Cu(In,Ga)Se_2$ solar cells, one challenge is to link the donor and acceptor states to the chemical nature of the defects. As seen above photoluminescence and Hall measurements can assess the activation energy of the defects and are so far the only conclusive experiments. Density functional theory calculations, on the other hand, provide reliably values for the formation energies of the defects, but have difficulties in reproducing the band gap and therefore also the energy levels of the defects correctly [59].

2.2 Photoluminescence

2.2.1 Photoluminescence transitions

A photoluminescence (PL) experiment is composed of three steps: First electrons from the valence band are excited via laser light into the conduction band. The electrons in the conduction band, as well as the holes in the valence band, thermalize, due to carrier-carrier and carrier-phonon interactions on a time scale between femto seconds and a few pico seconds. In doing so the electrons system reaches quasi thermal equilibrium [47].

In a third step the electrons and holes recombine, thereby emitting a photon [47]. This happens on a time scale between several 100 ps and a few ns. Electrons and holes can recombine directly from the bands, or with electrons or holes bound to donor or acceptor states. From the temperature and intensity dependence of the emitted photon, the type of transition can be deduced. Subsequently, the possible transitions shall be introduced [56]:

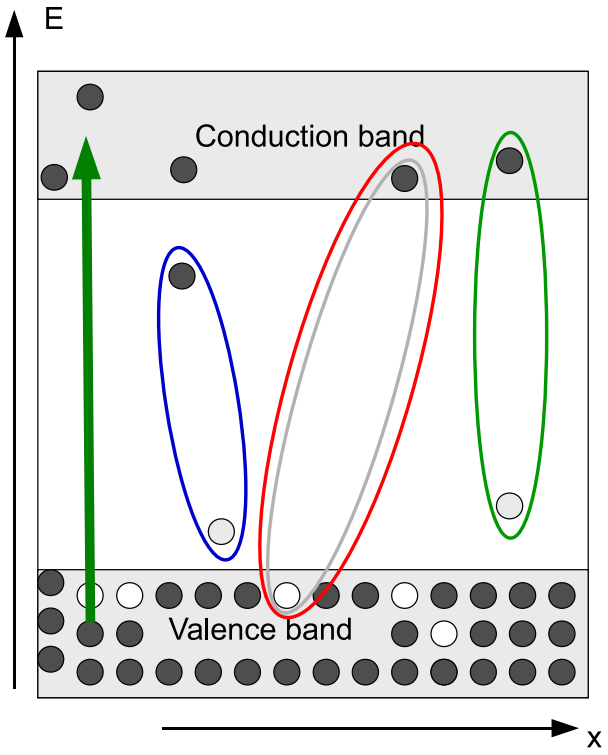

Figure 2.9: Photoluminescence transitions in a semiconductor: an excitonic transition is indicated in red, a donor-acceptor transitions in blue and a free-to-bound transition in green.

Band to band transitions

In a direct semiconductor, electrons in the conduction band recombine directly with holes in the valence band giving rise to band to band transitions. The intensity of the PL signal can be approximated by the square root like density of states in the bands and an exponential occupation factor:

$$I_{PL} \sim \begin{cases} \sqrt{\hbar\omega - E_G}\exp^{\frac{-(\hbar\omega - E_G)}{k_B T}} & for\ \hbar\omega > E_G \\ 0 & otherwise \end{cases} \tag{2.1}$$

where E_G is the band gap energy, k_B the Boltzmann constant, $\hbar\omega$ the emission energy of the luminescence light and T the temperature. With increasing temperature, the band gap of most semiconductors decrease due to the lattice thermal expansion and the increasing electron-phonon interaction. This results in a red shift of the PL band to band transition with temperature.
In some cases the electric dipole transition of an electron and a hole is forbidden by a selection rule due to the symmetry of the bands. This results in a very low oscillator strength of the corresponding matrix element and therefore band to band transitions for so called forbidden band gaps are very weak.

Excitonic transitions

At low temperatures free electrons in the conduction band and free holes in the valence band are attracted via Coulomb forces to each other and can form a bound state, a so called exciton. The energy of an excitonic transition equals

$$E_{Ex} = E_G - E_{Ex,Bin} \tag{2.2}$$

where E_G is the band gap energy of the semiconductor and $E_{Ex,Bin}$ is the binding energy of the exciton. The binding energy of an exciton can be calculated analogous to the hydrogen model:

$$E_{Ex,Bin} = \frac{m_r e^4}{2\hbar(4\pi\varepsilon_0\varepsilon_r)^2}\frac{1}{n^2} \tag{2.3}$$

$\frac{1}{m_r} = \frac{1}{m_e} + \frac{1}{m_h}$ being the reduced mass, m_e and m_h are the electron and the hole effective mass, e the unit charge, $\hbar$ Plancks constant divided by 2π, ε_0 the permittivity of vacuum, ε_r the dielectric constant at zero frequency and n the main quantum number. However normally only the first excitation level corresponding to $n = 1$ can be observed, as the intensity decreases

with $\frac{1}{n^3}$. The intensity of the PL signal on the excitation intensity can generally be described by a power law:

$$I_{PL} \sim I_{ex}^{k} \tag{2.4}$$

As the intensity of the exciton transition depends on the concentration of free electrons n, as well as free holes p, which both depend on the excitation intensity I_{ex} a k value of 2 is expected. However due to the interaction with other radiative and non-radiative processes, normally $k \leq 2$ is observed. A variation in excitation intensity has no influence on the energy position of the exciton. With increasing temperature a shift to lower energy for the excitonic transition is observed, corresponding to the decrease of the band gap energy with increasing temperature. Above a certain temperature the thermal energy exceeds the binding energy of the exciton and the exciton is quenched. The excitonic transition becomes a band-to-band transition.

Free-to-bound transition

A transition between an electron in the conduction band and a hole bound to an acceptor or between a free hole in the valence band and a donor electron is called a free-to-bound transition. The energy of the transition equals

$$E_{FB} = E_G - E_{D,A} \tag{2.5}$$

where $E_{D,A}$ is the binding energy of the involved donor or acceptor. As the PL intensity depends on the concentration of free holes p or free electrons n, a k value in equation 2.4 of $k \leq 1$ is expected. The excitation intensity does not influence the transition energy, however the peak shows a shift to lower energies with increasing temperature corresponding to the decrease of the band gap energy. As only one defect is involved in free to bound transitions, it is possible to determine the defect activation energies from its intensity dependence on temperature. The quenching activation energy E_{act} corresponds to the defect binding energy, which is characteristic for the considered defect. The intensity of the free-to-bound transition dependent on temperature can be described by the general relation for a transition with a competing thermally activated process

$$I \sim \frac{1}{1 + a \exp^{\frac{-E_{act}}{k_B T}}} \tag{2.6}$$

where a is a weakly temperature dependent proportionality constant.

Donor-acceptor transition

A donor acceptor (DA) transition starts from occupied defect states, this is a neutral donor and a neutral acceptor. The donor electron recombines with the acceptor hole, and in doing so emits a photon. This results in a positively charged donor atom and a negatively charged acceptor atom. The transition energy of a donor-acceptor transition equals

$$E_{DA} = E_G - [(E_D + E_A) + E_{Coul}] \quad with\ E_{Coul} = \frac{e^2}{4\pi\varepsilon_0\varepsilon_r r} \tag{2.7}$$

E_D and E_A being the donor and acceptor ionisation energies and E_{Coul} is the Coulomb attraction between the positively charged donor and the negatively charged acceptor. With increasing excitation intensity the density of neutral donor atoms and neutral acceptor states becomes higher, therefore the donor acceptor transitions occur closer to each other. This leads to an increase of the Coulomb term and therefore to a shift to higher energies of the DA transition. The magnitude of the shift can be described by the empiric formula

$$E_{PL}(I_{ex}) = E_{PL}(I_0) + \beta lg\frac{I_{ex}}{I_0} \tag{2.8}$$

where β equals normally several $\frac{meV}{dec}$. In samples with high defect densities the neutral donors and acceptors occur close to each other already at low excitation intensities, therefore the observed shift will be small. The PL intensity for a DA transition changes with increasing excitation intensity according to equation 2.4 with $k \leq 1$. With increasing temperature, thermal emptying of the defects becomes more important. As the radiative lifetime for close donor-acceptor pairs is shorter than that for donor-acceptor pairs with a larger distance, the probability of close pairs to recombine before the shallower defect is liberated in the band, is higher. Therefore transitions between closely neighbouring donor-acceptor pairs become more probable, leading to a small blue shift of the photoluminescence peak.

2.2.2 Potential fluctuations

Fluctuating electrostatic potentials

In a semiconductor, containing many defects, both donors and acceptors, the electrons of the donor states will recombine with the holes bound to the acceptor states, leading to positively charged donors

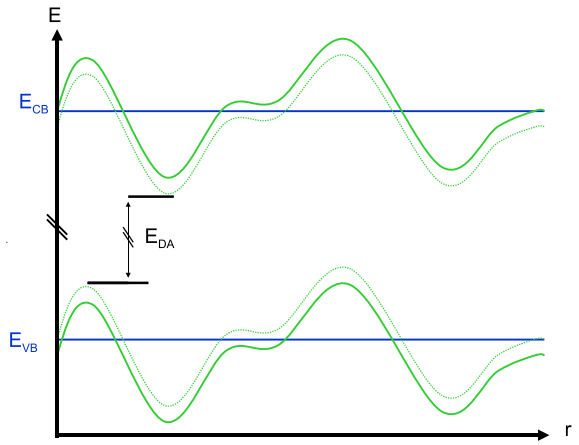

Figure 2.10: Local band gap variation in a highly compensated sample.

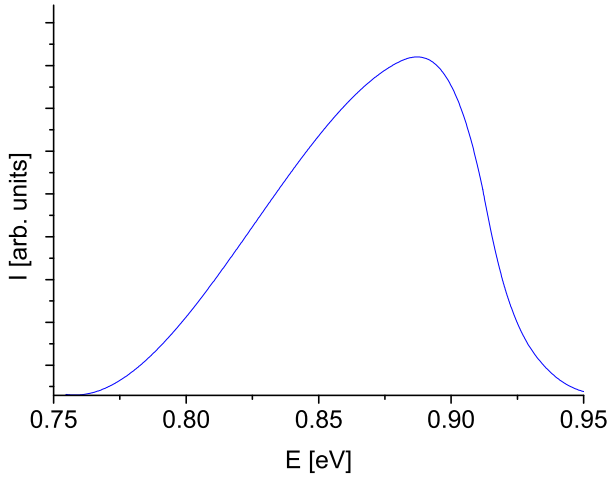

Figure 2.11: Example of a photoluminescence spectrum dominated by electrostatic potentials.

and negatively charged acceptor states. In a compensated semiconductor there is a similar amount of donors and acceptors. Therefore none, or only very few free charge carriers are created which are able to screen the charges. Subsequently, spatially distributed positively or negatively charged regions occur, which cause spatially varying electrostatic fields within the semiconductor. These electrostatic fields cause a bending of the valence and conduction band parallel to each other, as depicted in figure 2.10. In doing so, the distance between the valence and conduction band, the band gap, remains the same over the whole semiconductor. However the position of the bands compared to the uncompensated semiconductor varies. The variation of the conduction and valence band also causes a variation of the defect levels. The bending of the bands enables tunnel assisted donor-acceptor transitions between donors close to the local minima of the conduction band and acceptors close to the local maxima of the impurity band. Therefore a wide range of donor acceptor transitions with lower energy as in the uncompensated case becomes possible, resulting in a red shift of the peak and a broadening of its low energy slope. The fluctuation amplitude for a p-type semiconductor is given by

$$\gamma_0 = \frac{e^2}{4\pi\varepsilon\varepsilon_0} \frac{N_I^{\frac{2}{3}}}{p_t^{\frac{1}{3}}} \tag{2.9}$$

e representing the elementary charge, ε the static dielectric constant and ε_0 the dielectric field constant. $N_I = N_A^+ + N_D$ is the number of charged defects and $p_t = N_A - N_D$ the number of holes. Under laser excitation free charge carriers are created and the number of free charges changes to $p_t + 2\Delta p$, where $\Delta p = \Delta n$ stands for the excited charge carriers. In a highly compensated semiconductor the number of charged defects N_I is large, and thus does not change with excitation intensity. Therefore γ_0 should vary with intensity as $\gamma_0 \sim I^{\frac{-1}{3}}$. A typical feature of DA transitions in compensated semiconductors is a strong blue shift of more than 10 meV per decade with increasing excitation intensity. A higher excitation intensity leads to a higher number of free charge carriers in the semiconductor, which causes a better screening of the charged defects. Hence the electrostatic fields decrease, which leads to flatter bands. This reduces the low energy slope of the peak and shifts the maximum position to higher energies, as in the uncompensated case. The temperature dependent behaviour of defect related transitions in compensated samples is characterized by a red

shift followed by a blue shift. First the increase in temperature allows the charge carrier to reach the absolute minimum in their respective band, which results in the red shift of the peak. At higher temperatures, when the thermal equilibrium of the charge carriers is already reached, the increase of the number of free charge carriers enables a better screening of the charged defects. This results in a flattening of the bands. For $CuGaSe_2$ the change in shift direction occurs at 70K [60].

To describe the low energy slope in more detail, two different approaches are reported in literature: either the fluctuations can be treated as defects or, according to Urbach tails. For both methods it is necessary to calculated the density of states in the sample [56], [61]. Deep fluctuations can be described as defects. Thus the intensity of the PL peak I follows on the low energy side a Gaussian behaviour:

$$I \sim e^{\frac{-(E-E_0)^2}{\gamma_0^2}} \tag{2.10}$$

where E is the energy and γ_0 the fluctuation amplitude. This result is derived in [62] using screened Coulomb potentials and assuming that the local potential is only slowly varying which corresponds to the Thomas-Fermi approximation. This enables the use of a local density of states. Starting from clusters containing different numbers of atoms as the source of fluctuating potentials, the deviation from the average potential for a cluster of size w containing m atoms is calculated. From the distributions of the potentials they calculate the density of states. The same result is obtained in [63]: the authors assume randomly distributed ions as source of the fluctuations and determine the probability of finding n_i ions in a region i, containing g_i lattice sites. From the probability, they calculate the corresponding generating function as a mathematical tool to calculate the moments and so the average energy more easily. Knowing the average energy they use an inverse Laplace transform to achieve the probability density function dependent on energy which corresponds to the potential distribution function calculated in [62]. The second possibility is to treat the potential fluctuations as band tails. In [64] the potential distribution function is assumed to be Gaussian and the defects to be hydrogen like. This is in contrast to the localised defects used in both above mentioned calculations. Subsequently the probability to find z impurities with the same sign, in a region which, on average, contains m impurities is calculated. Further the density of states can be derived. As result it is found, that small fluctuations can be treated as a tail and described by an exponential function :

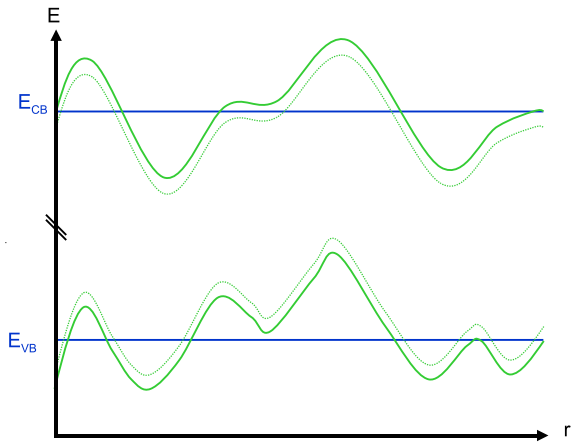

Figure 2.12: Local band gap variation in a sample with band gap fluctuations.

$$I \sim e^{\frac{-(E-E_0)}{\gamma_0}} \tag{2.11}$$

Band gap fluctuations

An other reason for a broadening of transitions peaks can be band gap fluctuations. These are caused by fluctuations in compositions or strain, in a semiconductor, which lead to locally different band gaps [65]. Thus the valence band and the conduction band fluctuate independently from each other as depicted in figure 2.12. Band gap fluctuations can be distinguished from electrostatic potential fluctuations by their intensity and temperature dependent behaviour: an increasing excitation intensity will have no influence on the peak position of a peak widened due to band gap fluctuations. However the peak position will depend on temperature: With increasing temperature the charge carrier will become able to reach the absolute minimum in the conduction band, as well as the maximum in the valence band before recombining. This results in a red shift of the peak. For a further increase of the temperature the peak position will follow the band gap, resulting in a continuing red shift with increasing temperature for most semiconductors.

Chapter 3

Synthesis techniques

This chapter briefly introduces the synthesis methods used for the deposition of the samples, which will be characterised in the following chapters. All methods used belong either to physical or chemical vapour deposition methods. Each method can be divided into several steps. In physical vapour deposition [66]

- a source material is evaporated
- the source material is transported in the vapour phase to the substrate
- the source material condenses on the substrate and forms the layer

Different deposition processes like vacuum evaporation and sputter deposition belong to the group of physical vapour deposition methods. Here the vacuum evaporation method will be discussed as a process to synthesize polycrystalline thin film $Cu_2ZnSnSe_4$ samples and its binary and ternary secondary phases.
Chemical vapour phase deposition can be divided into the following steps [67]:

- mass transport to the deposition zone
- (thermal) decomposition to produce in the precursor for the sample and by-products
- adsorption of the precursor onto the surface
- diffusion of precursor on the surface, followed by a chemical reaction leading to sample deposition
- transport of the by-products from the reaction zone

Samples from several different chemical deposition methods: $CuInSe_2$ crystals grown by the iodine vapour phase growth method, thin epitaxial $Cu(In,Ga)Se_2$ films grown by metal organic vapour phase epitaxy and polycrystalline Cu_2ZnSnS_4 thin films and samples of its competing secondary and ternary phases from electro-deposition will be characterised in the following chapters.

3.1 Physical vapour deposition methods

3.1.1 Vacuum evaporation

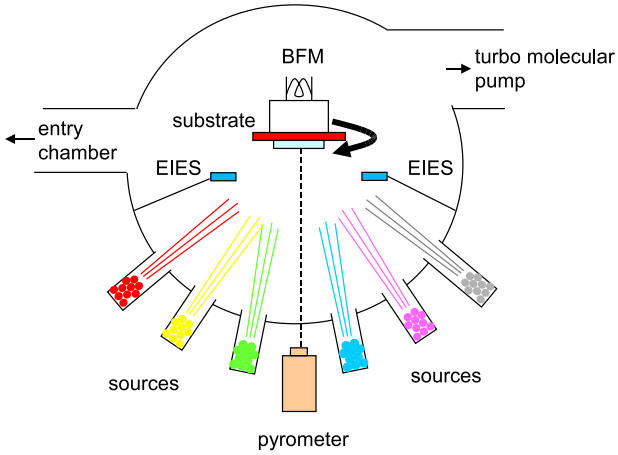

Figure 3.1: Schematic illustration of the PVD system.

In a vacuum evaporation process the source material is thermally evaporated and reaches the substrate with no or only few collisions with other gas molecules. The molecular beam epitaxy system employed to synthesize kesterite samples is shown schematically in figure 3.1. The deposition rate depends on the vapor pressure of the material and therefore on the temperature of the source. To monitor the flux of atoms to the sample surface the instrument is equipped with a beam flux monitor (BFM) and electron emission spectroscopy (EIES). From

the pyrometer signal, the sample temperature, thickness and growth rate can be determined [68], [69]. The samples are grown at substrate temperatures between 350°C and 500°C. An example of a thin film $Cu_2ZnSnSe_4$ sample grown by vacuum evaporation is shown in figure 3.2.

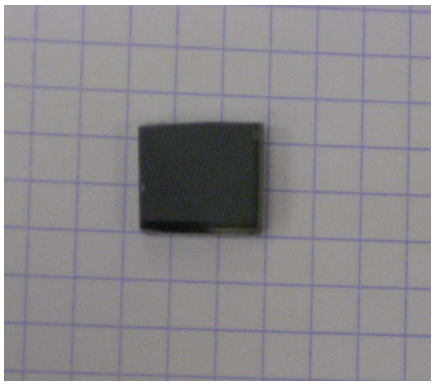

Figure 3.2: Polycrystalline thin film $CuZnSnSe_4$ sample grown by vacuum evaporation.

3.2 Chemical vapour deposition methods

3.2.1 Iodine vapour phase growth

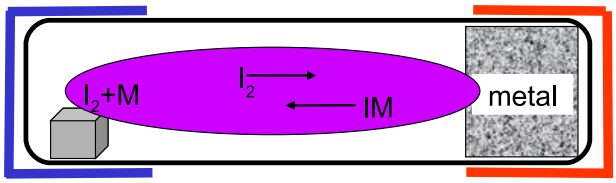

Figure 3.3: Schematic illustration of the iodine vapour growth method: At the hot end the metallic precursors react with iodine to a volatile IM compound. At the colder end the reaction is reversed: the metal atoms start forming the crystal, whereas the iodine is released.

The iodine vapour phase growth method is based on the temperature dependence of the reaction equilibrium

$$I_2 + 2Me \rightleftharpoons 2IMe \tag{3.1}$$

Stoichiometric amounts of the elements and additional iodine are filled into a quartz ampoule, which is subsequently evacuated and sealed. The ampoule is slowly heated to 600°C allowing the iodine to react with the metals. To transport all constituents to one end of the ampoule a large spatial temperature gradient is applied over 24 hours. A temperature gradient of between 880°C at the hot end and 810°C at the colder end of the ampoule is applied for 48 hours, which constitutes the crystal growing step as described for chemical vapour deposition at the beginning of this chapter: The hot end the reaction leading to IM is favourable. The gaseous IM diffuses to the cooler end, where the reaction equilibrium lies on the side of elemental metal and I_2, leading to crystal growth [70]. Figure 3.4 shows an example of a $CuInSe_2$ crystal grown by the iodine vapour phase transport method.

Figure 3.4: $CuInSe_2$ crystal grown by the iodine vapour phase growth method.

3.2.2 Metal organic vapour phase epitaxy

In metal organic vapour phase epitaxy (MOVPE) the precursor atoms to synthesize chalcopyrites (copper, indium, gallium and selenium) are bounded in organic compounds and are thus in a liquid state at room temperature. Following the steps involved in a chemical vapour deposition process as described above, hydrogen is used as the carrier gas to transport the metal organics to the deposition zone, where they decompose resulting in the precursors for the film and by-products. The precursor atoms are adsorbed onto the substrate and adopt its structure, given that the lattice constants are similar. This leads to epitaxial, this is crystalline growth. To grow the chalcopyrites $CuInSe_2$ and $CuGaSe_2$, $GaAs$ is used as a substrate, due to its small lattice mismatch [67]. Figure 3.5 shows an epitaxial $CuInSe_2$ thin film grown by metal organic vapour phase epitaxy.

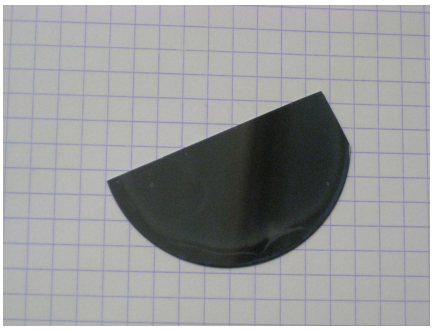

Figure 3.5: Epitaxial $CuInSe_2$ thin film grown by metal organic vapour phase epitaxy.

3.2.3 Electrodeposition

Polycrystalline Cu_2ZnSnS_4 thin films involving electrodeposition are synthesized in a two step process: first the metals are electrodeposited on molybdenum substrate. To incorporate the chalcogens sulphur or selenium, the samples are subsequently annealed in an oven in a sulphur or selenium atmosphere. In the following, first the electrodeposition process will be explained, then the annealing procedure used will be introduced.

Electrodeposition

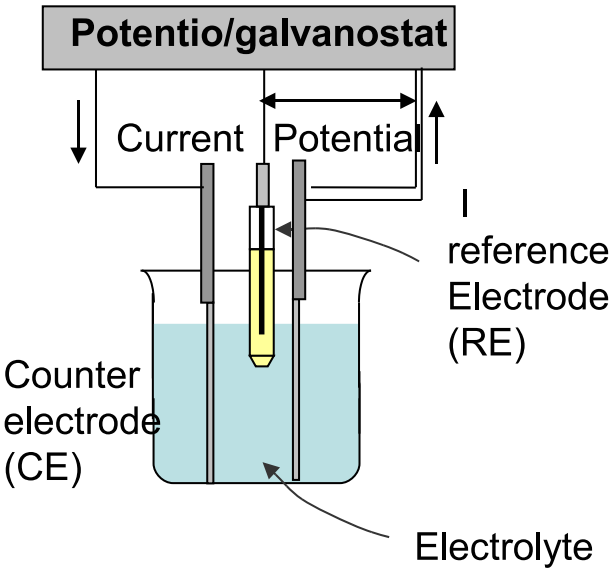

Figure 3.6: Schematic illustration of the setup used for electro deposition.

Figure 3.6 shows the setup used for electrodeposition experiments. It consists of an electrolyte containing the ions, M^{+z}, which shall be electrodeposited, a working, a reference and a counter electrode and a potentiostat.

At the electrode redox reactions according to the following equation will take place [71],[72]:

$$M^{+z} + ze \rightleftharpoons M \tag{3.2}$$

where M^{+z} are ions of charge, z, in solution, e is the number of electrons involved in the redox reaction and M is the reduced species deposited at the working electrode. An equilibrium will form between the ions, M^{+z}, and the reduced species, M. As an electron transitions is involved in the chemical reaction, a potential according to the Nernst equation will result:

$$E_e = E_e^0 + \frac{RT}{zF} ln \frac{a_{M^{+z}}}{a_M} \tag{3.3}$$

E_e^0 being the standard electrode potential, R the universal gas constant, T the temperature, F the Faraday constant and a the concentrations of M^{+z} and M, respectively. For an electrodeposition process to occur the equilibrium in equation 3.2 needs to be on the right hand side. This can be reached by changing the equilibrium potential, E_e, by applying an over potential between the reference and the working electrodes. This changes the Fermi level of the electrons in the metal electrode in relation to the lowest unoccupied molecular orbital (LUMO) of the ions dissolved in the solution. If the Fermi level of the electrons is higher than the LUMO of the ions, then a reduction reaction becomes energetically favourable and deposition takes place.
The applied voltage is measured against a reference electrode to provide a stable reference point independent of concentration variations in the electrolyte. Here, a silver chloride reference electrode is used. To improve sample homogeneity a rotating disc electrode is used, allowing control over the ion flux to the sample surface [73]. The different metals are deposited using a sequential bath deposition approach. This means the salts of the metals required for each of the precursor are dissolved in separate baths and the different species are deposited successively. Figure 3.7 shows a polycrystalline Cu_2ZnSnS_4 sample grown by electrodeposition.

Annealing procedures

To complete sample formation the metal precursors are annealed in the oven depicted in figure 3.8. The samples are loaded into a graphite box and 200 mg

Figure 3.7: Polycrystalline Cu_2ZnSnS_4 sample grown by electro-deposition.

sulphur powder is added. Next the graphite box is introduced into a glass tube which leads into the oven. To prevent sulphur loss during annealing, the box is kept under $500 \pm 10\,mbar$ N_2H_2 pressure. The samples are annealed at 570°C for a duration of 2 h.

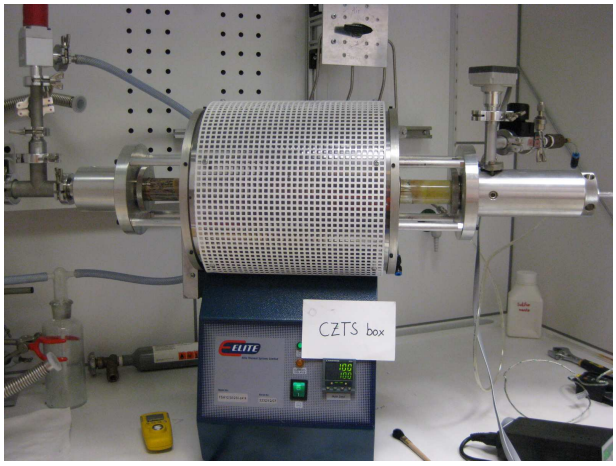

Figure 3.8: Oven used for the annealing experiment

Chapter 4

Measurement techniques

As introduced in the previous chapter, photoluminescence transitions provide information about the activation energy of defects and the degree of compensation in a semiconductor. In chapter 7 will be explained, how the symmetry of defects can be accessed by polarisation of photoluminescence transitions. Therefore the setup used to perform standard, as well as polarised photoluminescence measurements, is presented in the following. The photoluminescence measurements to identify secondary phases in $Cu_2ZnSnS(e)_4$ samples are complemented by X-ray diffraction (XRD) experiments, which is the standard method to identify phases. Hence, in the second part of this chapter, the underlying measurement principles and the setup used for XRD measurements are introduced. Apart from phase analysis, XRD measurements are used to orient a $CuInSe_2$ crystal for polarisation dependent photoluminescence measurements which determine the symmetry of its defects. This is accomplished by rocking curve and Φ-scan measurements, which will be explained in the second part of the XRD section. Besides these two, primarily used methods during my thesis, energy dispersive X-ray spectroscopy (EDX) and X-ray photoelectron spectroscopy (XPS) were used to determine the composition of the samples and secondary ion mass spectroscopy (SIMS) was used to determine the depth profile of the sample composition. A brief introduction to these three methods is given at the end of this chapter.

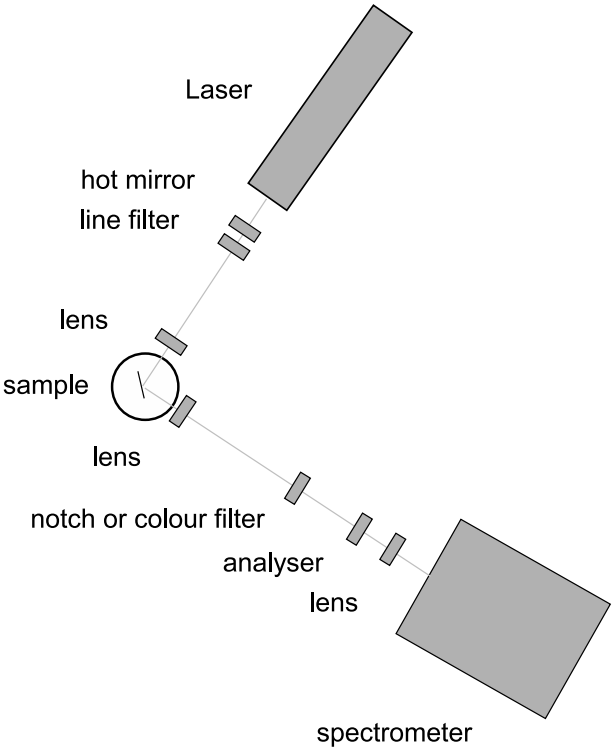

Figure 4.1: Measurement setup for photoluminescence measurements.

4.1 Photoluminescence measurements (PL)

Figure 4.1 shows the setup used for photoluminescence measurements. As introduced in chapter 2.2, photoluminescence light originates from the recombination of an electron in the conduction band and a

hole in the valence band or bound to a defect. In a photoluminescence experiment the intensity dependence on the wavelength is measured, which is usually a function of additional parameters such as the excitation power or the sample temperature.

For these experiments, the 514 nm laser line of an Argon ion laser with an excitation power between 0.2 mW and 1 W is used to excite the samples. For excitation powers below 10 mW the time stability of the laser decreases. To ensure a constant excitation power over time at low excitation powers, the excitation power of the laser is kept at 10 mW and the excitation power irradiating on the sample is adjusted by neutral density filters. To ensure that only the 514 nm laser line and no additional lines from the ion discharge plasma of the laser hit the sample a hot mirror and a line filter were used. Hot mirrors, as well as a line filters, are dielectric mirrors, which transmits only a specified wavelength range. A line filter is characterised by steep edges for the transmission close to the laser line, but reflects light only within a narrow wavelength range. The hot mirror reflects light in a wide wavelength range, yet its change from reflecting to transmitting is less steep. Therefore, combination of the two filters allows the passing light to be confined only to the laser line. The laser beam is focussed on the sample by a lens with a focal length of 5 cm. The PL signal of the sample is detected at an angle of 90° to the exciting laser beam. It is first collimated by a lens with 5 cm focal length and afterwards focussed on the spectrometer entrance by a second lens with 20 cm focal width. In the parallel part of the beam the laser line is filtered out by a Notch filter. For all measurements in the wavelength range between 950 nm (1.3 eV) and 1050 nm (1.18 eV) colour long pass filters were used instead. As the Notch filter relies on diffraction, its transmission vanishes around the second order of the laser line at 1029 nm. To avoid saturation of the cameras used to detect the luminescence light, for samples yielding high luminescence additional grey filters in the parallel part of the beam were introduced. The light passes then through a single grating spectrometer in the Czerny-Turner geometry and is detected via CCD cameras. Depending on the resolution required there are 600 $\frac{lines}{mm}$ (blazed at 500 nm and 1000 nm) and a 300 $\frac{lines}{mm}$ (blazed at 760 nm) gratings available, resulting in a nominal dispersion of 5 $\frac{nm}{mm}$ and 10 $\frac{nm}{mm}$ respectively. For wavelengths between 520 nm (2.38 eV) and 950 nm (1.31 eV) the luminescence light is detected by a Si CCD camera, for luminescence light between 950 nm (1.31 eV) and 1600 nm (0.78 eV) a InGaAs CCD camera is used. The exposure time of the camera can be varied between 0.01 ms and 1 s for the Si-camera and 0.1 s and 2 s for the InGaAs camera, depending on the strength of the photoluminescence signal of the sample. The spectra measured with the InGaAs camera, shows a wide absorption line around 1385 nm (0.9 eV), which is most probably due to water vapor contained in the air [74]. At the beginning of each measurement series a dark measurement with closed laser beam and the same settings as for the measurements on the sample was performed, to ensure that no stray light from LEDs, the computer screen or the like interferes with the measurement. To be able to do temperature dependent measurements the sample is mounted in a Helium flow cryostat, which allows the variation of the temperature between 5 K and 300 K.

4.1.1 Polarisation dependent photoluminescence measurements

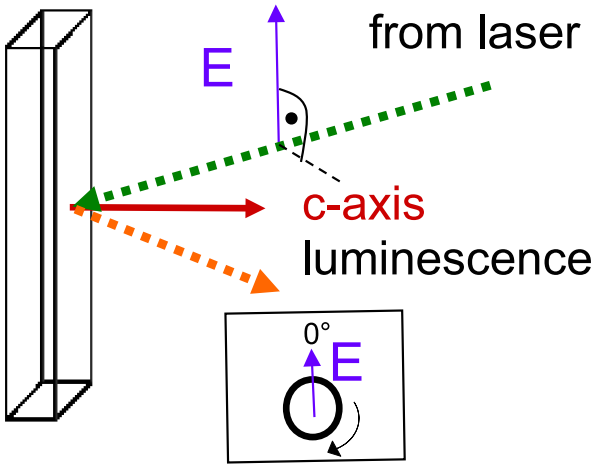

Figure 4.2: The orientation of the analyser relative to an epitaxial sample with (001) growth direction: a $\vec{E}$ field vector pointing in the direction of 12 o'clock corresponds to an analyser angle of 0°. Therefore, in this example, a measured intensity maximum at an angle of 0° corresponds in this example to a polarisation perpendicular to the $\vec{c}$-axis, whereas an measured maximum at an angle of 90° corresponds to a polarisation parallel to the $\vec{c}$-axis. Seen in the direction of the beam, the analyser turns clockwise.

For the polarisation dependent measurements, an analyser to measure the polarisation of the luminescence light is introduced additionally. Two different analysers have been used: a Glan-Thompson

prism and a film polariser. The film polariser was introduced into the parallel beam, whereas the Glan-Thompson prism, due to the small diameter was introduced in the focussed beam directly in front of the spectrometer. The analysers were mounted on a turnable stage, with the orientation such that the $\vec{E}$-field vector pointing at 12 o'clock corresponds to 0° polarisation angle, as shown in figure 4.2. The correct adjustment of the analyser was tested by measuring the polarisation of the laser beam. To account for the polarisation dependence on the transmission of the spectrometer, the response of the spectrometer, dependent to the analyser angle, of an unpolarised light source is measured. This allowed the calculation of a correction function which is applied to the measured data. As the measured polarisation relative to the sample orientation will become important for the measurements discussed in later chapters, the applied reference coordinate systems will be introduced in the following and are depicted in figure 4.3: The sample holder coordinate system is spanned by the vectors $\vec{x}_{SH}$, $\vec{y}_{SH}$ and $\vec{z}_{SH}$, whereas the coordinate system in the detection plane is indicated by $\vec{y}_D$ and $\vec{z_D}$. The sample holder coordinate system can be transformed into the detection coordinate system by a clockwise rotation of 45° about the $\vec{z}$-axis.

The second quantity of interest, besides the angle of maximum intensity, is the degree of polarisation. The degree of polarisation P is defined as:

$$P = \frac{I_{max} - I_{min}}{I_{max} + I_{min}} \tag{4.1}$$

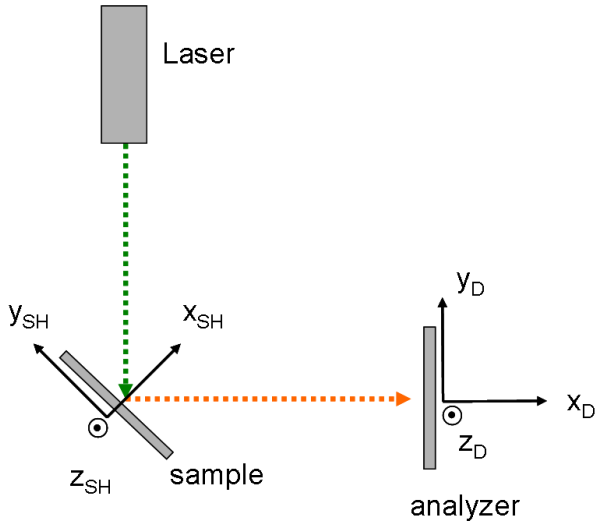

Figure 4.3: Orientation of the sample holder coordinate system relative to the detection coordinate system. The sample holder coordinate system is spanned by the vectors $\vec{x}_{SH}$, $\vec{y}_{SH}$ and $\vec{z}_{SH}$, whereas y_D, y_D and z_D represent the detection coordinate system.$\vec{z}_{SH}$ and $\vec{z}_D$ point out of the sheet.

4.2 X-ray diffraction (XRD)

In X-ray diffraction (XRD) the diffracted intensity is measured as a function of observation angle. This allows the determination of the crystal structure and orientation of a lattice and is therefore the standard method to identify phases contained in a sample. The description given here is according to [75]. As the name of the method implies, a monochromatic X-ray beam is scattered elastically by the electron cloud of an atom. If the atoms are arranged regularly, such as in a crystal, this gives rise to diffraction patterns. For constructive interference to occur, the Bragg condition, given in equation 4.2, needs to be full filled:

$$n\lambda = 2d_{hkl}\sin(\theta) \tag{4.2}$$

where λ represents the X-ray wavelength, d_{hkl} the interplanar spacing and θ the angle between the sample surface and the incoming beam $\vec{K_0}$, as well as, the scattered beam $\vec{K}$. Thus constructive interference due to scattering at two neighbouring lattice planes of distance d_{hkl} can be observed under the angle θ.

The intensity of an observed diffraction maximum is proportional to the structure factor

$$F(hkl) = \sum_n f_n \exp^{2\pi i(hx_n+ky_n+lz_n)} \tag{4.3}$$

where h,k and l are the Miller indices of the lattice plane giving rise to the reflection and the coordinates x_n, y_n and z_n are of the positions of the atom in the unit cell. f_n is the atomic form factor, which takes into account the electron density distribution in the atom. In the following, firstly the measurement setup and procedure for $\theta - 2\theta$ scans used for phase analysis will be described, secondly the measurements performed to orient a crystal will be introduced.

4.2.1 $\theta - 2\theta$-scans

θ-2θ scans are the standard procedure for phase analysis. As depicted in figure 4.4, the incoming X-ray beam hits the sample, under the angle θ, with respect to the sample surface. The intensity diffracted from the sample is detected under an angle of θ with respect to the surface, too. During measurement θ is continuously varied. The angle of the detector equals 2θ with respect to the incident X-ray beam, therefore this measurement method is called a θ-2θ scan. The scattering vector $\vec{Q}$, is the difference vector of the incident vector $\vec{K_0}$ and the scattered vector $\vec{K}$, and is always perpendicular to the plane observed in the XRD measurement. It

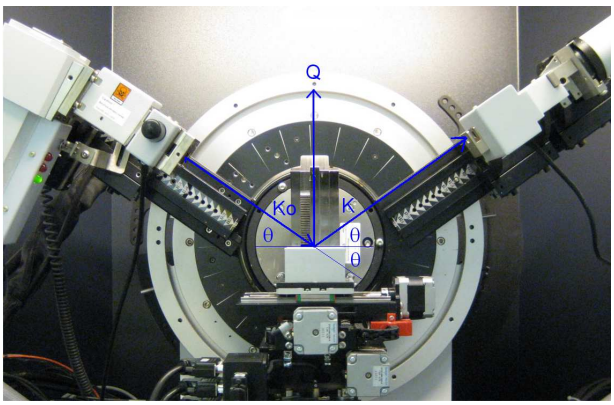

Figure 4.4: Measurement geometry for θ-2θ scans: $\vec{K_0}$ and $\vec{K}$ are the wavevectors of the incoming and the scattered beam, θ is the angle between the sample surface and the incoming, as well as the diffracted beam. The difference vector between $\vec{K_0}$ and $\vec{K}$, the scattering vector $\vec{Q}$, is always perpendicular to the observable lattice planes.

remains perpendicular to the surface during the θ-2θ scan. Therefore only lattice planes parallel to the sample surface contribute to the diffraction signal in a θ-2θ scan. When choosing measurement parameters, a compromise has to be found between using narrow slits, to be able to separate close neighbouring peaks, of particular importance in the kesterite system, and obtaining high enough diffracted intensity to be able to observe also weaker diffraction maxima in a reasonable measurement time.

A second measurement geometry used to identify phases is depicted in figure 4.5: One chooses a grazing incidence of the incoming beam, this is a small incident angle, normally below 2°. This grazing incidence has the advantage, especially for thin samples, that the path of the X-ray radiation that travels through the thin-film before penetrating into the substrate gets longer and therefore the measured intensity is increased. In grazing incidence measurements the incident angle is kept constant, whereas the angle of detection is varied by 2θ. Compared to $\theta - 2\theta$-scans, this leads to a change in the scattering vector $\vec{G}$ during the measurement. Therefore different orientated lattice planes will contribute to the diffraction signal.
For both types of measurements, the diffractometer was in the parallel beam mode, this means the X-ray beam is not focussed on the sample, but the incident

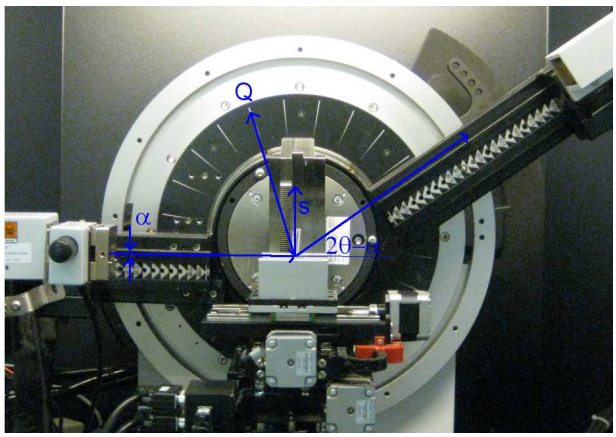

Figure 4.5: Measurement geometry for grazing incidence measurements: the source beam hits the sample with an angle α to the sample surface and the diffracted intensities are detected under an angle 2θ-α. Note that the scattering vector $\vec{Q}$ varies during the measurement and therefore does not coincidence with the surface normal $\vec{s}$.

beam is collimated. For the generation of X-rays a Cu X-ray tube is used. However it is important to keep in mind while analysing XRD diffraction patterns, that there are two $CuK\alpha$ lines: $CuK\alpha 1$ at 1.5406 Å and $CuK\alpha 2$ at 1.5444Å. The $CuK\alpha 2$ line leads to a second diffraction pattern, which is slightly shifted to the one originating from the $CuK\alpha 1$ line.

To adjust the height of the sample the diffraction maximum due to the substrate peak, molybdenum for the kesterite and gallium arsenide for the epitaxial chalcopyrite samples, was used. However especially for the molybdenum substrate, strain in the layer cannot be excluded, which would result in an error in the height adjustment. In later measurements, due to an improved sample holder, it was possible to adjust the height independently of the substrate reflections.

4.2.2 Rocking curve measurements

The crystal quality, especially if the sample is monocrystalline, can be tested by rocking curve measurements. For that purpose the Bragg angle θ_B of the main diffraction maximum determined from $\theta - 2\theta$-scans is chosen and the sample is tilted about ω as indicated in figure 4.6. Plotting the diffracted intensity dependent on omega, the full width half maximum of the resulting peak is a measure of the crystalline quality. Especially grains with slightly

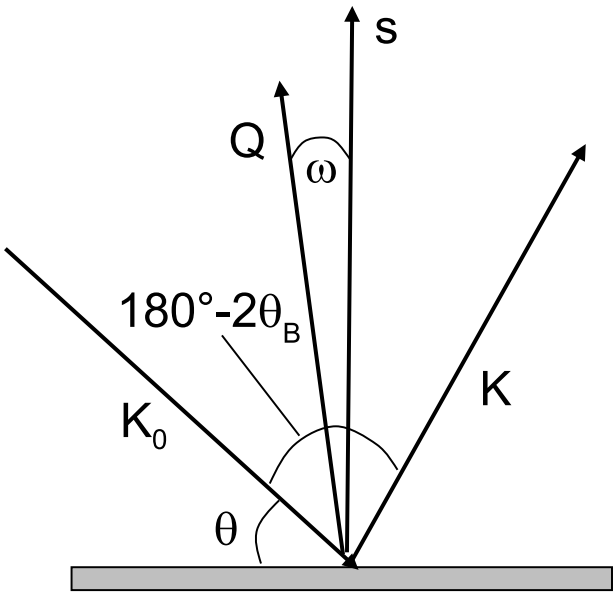

Figure 4.6: Measurement geometry for rocking curve measurements: the scattering vector Q is varied by an angle ω compared to the surface normal s, either by tilting the sample or by varying the angle θ, while keeping $180° - 2\theta_B$ constant.

differing orientation with respect to the orientation determined by $\theta - 2\theta$-scans will become visible as broadening or shoulder. Additionally rocking curve measurements reveal if the investigated lattice plane is oriented exactly parallel to the sample surface. A slight tilt will be reflected in a maximum at $\omega \neq 0$.

In practice, rocking curve measurements are performed in the following way: the angle between incoming beam $\vec{K_0}$ and scattered beam $\vec{K}$ is kept constant, according to the angle under which the diffraction maximum in the $\theta - 2\theta$-scan was observed, this is $180° - 2\theta_B$. Then the diffracted intensity depending on the θ, varying in the vicinity of θ_B, is measured. The change in θ alters the scattering vector $\vec{Q}$ with respect to the surface normal $\vec{s}$, and therefore planes with slightly different surface normals can contribute to the measured signal.

4.2.3 Φ-scans for single crystal orientation

Until now, no care was taken of the orientation of the sample in the plane parallel to the surface. This is the aim of texture analysis. To achieve this, two additional angles need to be defined (see figure 4.7) : Φ, which describes a rotation of the sample about the

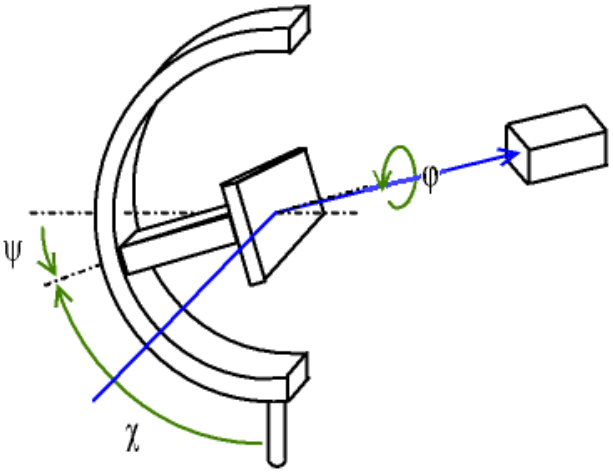

Figure 4.7: Measurement geometry used for the orientation of the crystal: the angle ϕ indicates rotations about the normal of the sample surface. The angle Ψ indicates the inclination of the surface normal with respect to the diffraction plane spanned by the vectors $\vec{K_0}$ and $\vec{K}$. [76]

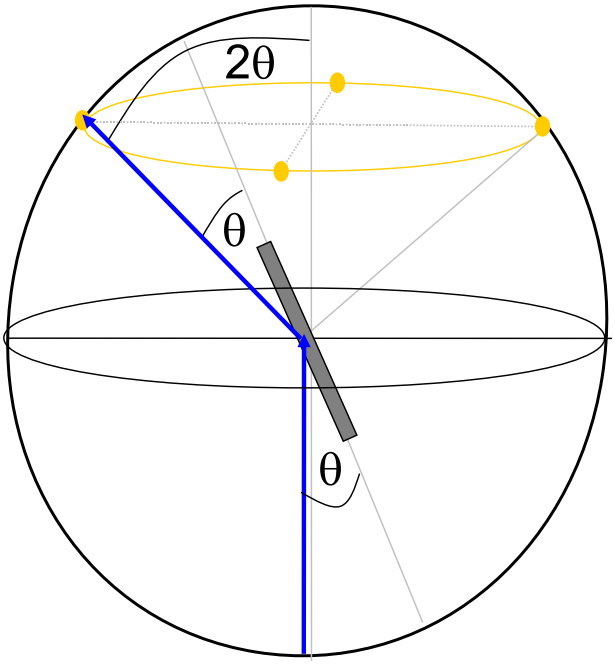

Figure 4.8: Measurement geometry for θ-2θ scans: for polycrystalline samples the diffracted intensity lies on a cone with opening angle 4θ, whereas the diffraction maximum for a crystalline sample forms a distinct point in space.

surface normal and an inclination angle, Ψ, accounting for the inclination of the surface normal with respect to the plane spanned by the vectors $\vec{K_0}$ and $\vec{K}$. In powder samples all orientations of crystallites are equally probable and the scattered intensity corresponding to a fixed scattering angle lies on a cone with opening angle 4θ, as depicted in figure 4.8. This means that the orientation of the sample with respect to Φ is insignificant. However, in single crystals a diffraction maximum corresponding to a lattice plane forms a point in space.

To determine the orientation of a crystal, the diffraction intensity of the lattice plane of interest depending on Φ, which is the rotation angle about the surface normal, need to be measured. The normal of the lattice plane of interest is not perpendicular to the surface, and therefore does not lie in the measurement plane spanned by the $\vec{K_0}$ and $\vec{K_0}$ vectors, accessible by θ-2θ scans. Thus it is necessary to incline the sample by the corresponding angle Ψ. For example, in a tetragonal lattice oriented with the (112) plane parallel to the surface, the $\vec{c}$-axis and the surface enclose an angle of $\Psi = \arctan[\frac{1}{2\sqrt{2}} \cdot \frac{c}{a}]$. So, if the $\vec{c}$-axis is to be determined, the sample needs to be tilted by $\Psi = 35.43°$. Hence the planes perpendicular to the $\vec{c}$-axis lie in the measurement plane and the direction of the $\vec{c}$-axis can be determined by choosing the angle θ_B corresponding to the (008) plane and measuring the diffracted intensity dependent on the rotation angle ϕ.

4.3 Scanning Electron Microscopy (SEM) and Energy Dispersive X-ray Spectrometry (EDX)

Scanning electron microscopy (SEM) measurements are a tool to get magnified images of the sample surface. Energy Dispersive X-ray Spectrometry (EDX) is used to determine the composition of the sample. For both methods the sample is investigated by an electron beam. The interaction of an electron beam with matter gives rise to elastic and inelastic scattering of the incident electrons. Inelastic scattering is possible via the creation of secondary electrons, continuous x-rays (bremsstrahlung), the ionisation of inner shell electrons resulting in characteristic x-ray lines or emitted Auger electrons, etc. These interactions can be used for the characterisation of materials. The difference between the electrons impinging on the

sample and the electrons emitted from the sample, via secondary electrons and back-scattered electrons, gives rise to a, so called, sample current. The sample current as well as the back-scattered electrons, or the secondary electrons, can be used to depict the surface morphology of the sample resulting in scanning electron microscopy (SEM) pictures. In energy dispersive x-ray (EDX) measurements, as well as in the related wavelength dispersive x-ray measurements (WDX), the characteristic x-ray radiation emitted from the sample is used to identify the elements, which it contains. For EDX measurements a semiconductor detector crystal is used, in which the absorbed x-ray is scattered inelastically and in doing so creates electron-hole pairs. This leads to a current pulse proportional to the energy of the incoming x-ray photon. In WDX measurements the energy resolution is achieved via diffraction of the incoming x-rays on a crystal. EDX measurements have a higher quantum efficiency than WDX measurements, whereas WDX measurements offer a better separation of the peaks [77].

4.4 X-ray Photoelectron Spectroscopy (XPS)

X-ray photoelectron spectroscopy (XPS) is a further method to determine the composition of samples, which has a lower detection limit than EDX measurements. In X-ray photoelectron spectroscopy measurements (XPS)[78], the number of escaping electrons from the sample, dependent on their energy, is measured. Excitation of electrons from the core states of the atom is achieved by X-ray radiation. The kinetic energy of the electron $E_{e,kin}$ leaving the sample equals the excitation energy of the X-rays $h\nu$ minus its binding energy E_I:

$$E_{e,kin} = h\nu - E_I \tag{4.4}$$

As the binding energy is characteristic for each element, it is possible to identify the elements contained in a sample excited by a known X-ray energy, by measuring the energy of the emitted electrons. The kinetic energy of the electrons is measured by an electron energy analyser, which consists of a spherical capacitor, where only electrons with a certain initial energy can pass without colliding with the walls. However, a second effect can be observed in the measured spectrum: the photoelectron leaves, and the vacancy in the inner shell, will be filled by an electron from an outer shell, after dissipating its energy via an Auger electron, as described in the section above. The two effects both give rise to peaks, which can be distinguished by varying the X-ray excitation wavelength. This is due to the fact that the kinetic energy of the electrons emitted due to the photoelectric effect depend on the excitation energy whereas the energy position of the peaks due to Auger electrons do not. Compared to Auger electron spectroscopy (AES), where the excitation is by an electron beam, the radiation damage in XPS is smaller.

4.5 Secondary Ion Mass Spectrometry (SIMS)

To investigate the sample homogeneity with depth, secondary ion mass spectrometry (SIMS) measurements are performed. In these measurements the number of secondary ions of a specific mass arriving at the detector depending on time is recorded. This secondary ion flux is induced by a beam of primary ions hitting the sample and giving rise to a collision cascade. The secondary ions are subsequently separated according to their mass by a mass spectrometer and detected. As SIMS measurements are here used for depth profiling, a magnetic sector SIMS in the dynamic measurement regime is used. A magnetic sector SIMS consists of an electrostatic and a magnetic section, the first sorting the secondary ions according to their energy, whereas the second separates them according to their mass. In the dynamic measurement regime a constant sputtering rate is used and the mass of the incoming secondary ions is continuously detected. As primary ions Cs^+ ions are used, a primary ion current of 15 nA is employed and the sputtered area is $250 \times 250 \mu m^2$. The sputter yield is element specific and depends strongly on the matrix in which the atom is embedded. Therefore it is only possible to obtain quantitative results for the concentration of an element in a sample from SIMS measurements, if a adequate standard is available. However qualitative changes in sample composition with depth or the detection of traces of an impurity element can be obtained without comparison to a standard [79].

Chapter 5

Phase-analysis by Photoluminescence and X-ray diffraction

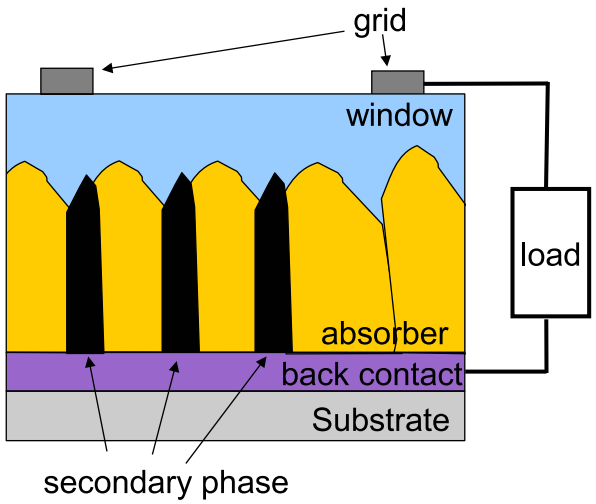

Figure 5.1: Schematic cross section of a solar cell consisting of substrate, back contact, absorber and window layer. The absorber layer contains secondary phases at the grain boundaries of the absorber grains [2].

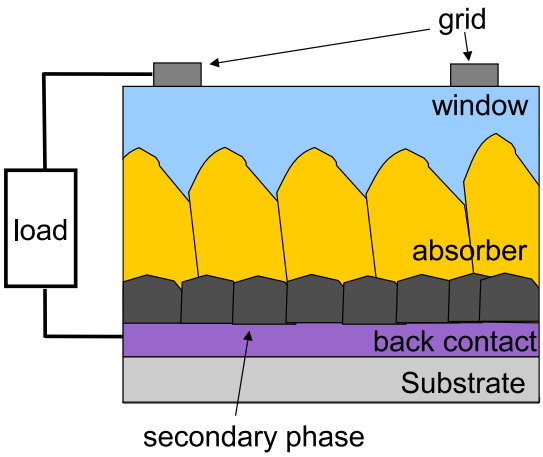

Figure 5.2: Schematic cross section of a solar cell showing a secondary phase between absorber layer and back contact [2].

In this chapter the secondary and ternary phases in the $Cu\ Zn\ Sn\ S$ and $Cu\ Zn\ Sn\ Se$ system will be discussed. When synthesising a material it is important to know in which composition range it exists and which competing phases can occur. Therefore in the first part of this chapter the phase diagrams reported in literature for the possible phases in the $CuZnSnS$ and $Cu\ Zn\ Sn\ Se$ system will be described. However phase diagrams represent the equilibrium situation, whereas sample growth occurs under non equilibrium conditions. Therefore the phases actually contained in the sample might be different from those predicted by the phase diagrams. Also phase diagrams are not necessarily available for the growth temperature. As the aim is to use $Cu_2ZnSnS(e)_4$ as a solar cell absorber material, the detection of secondary phases in the absorber is important. Secondary phases can either appear at the grain boundaries of the absorber as shown in figure 5.1 or between the absorber layer and the back or front contact as can be seen in figure 5.2. In the first case, highly conductive competing phases can enable an alternative current path to the solar cell diode and so lead to shunting of the solar cell. As a second possibility, if the band gap of the competing phase at the grain boundary is smaller than that of the absorber material, it will reduce the maximum output voltage of the solar cell, the band gap being its absolute upper limit. A secondary phase between the back contact and the absorber layer can increase the series resistance of the solar cell, if the secondary phase is highly resistive. A highly conduc-

tive phase between the back contact and the absorber on the contrary, would not harm the solar cell performance. A secondary phase on top of the absorber layer might be removed by etching before finishing the solar cell. Otherwise, depending on its properties it may degrade the band alignment of the pn-junction between the absorber and the window layer.
The standard method for the identification of phases is to make XRD measurements as described in chapter 4.2. However as the main diffraction maxima of the $ZnS(e)$, $Cu_2SnS(e)_3$ and $Cu_2ZnSnS(e)_4$ phase, have similar lattice constants and structures, they appear at very similar diffraction angles in X-ray diffraction experiments. Therefore it is very difficult to exclude that a $ZnS(e)$ or $Cu_2SnS(e)_3$ phase is contained in a sample from XRD measurements. Hence the aim of the second and third part of this chapter is to investigate if photoluminescence measurements in combination with XRD measurements can help to identify the secondary and ternary phases contained in a kesterite sample more unambiguously.

Samples containing only $Cu_yS(e)_z$, $ZnS(e)$ and $Cu_ySnS(e)_z$ are prepared under similar growth conditions as for the synthesis of kesterites to achieve the most probable secondary and ternary phases also encountered during kesterite deposition. The tin selenides and sulphides were not considered for reasons described in the next section. At the used growth and annealing temperature $SnS(e)$ loss plays already an important role, therefore no tin sulphide or selenide secondary phase is expected. In the second section sulphide kesterites prepared by annealing of electrodeposited metal precursors made by Dominik Berg will be considered. The samples are deposited and subsequently annealed as described in chapter 3.2.3 The third section deals with secondary and ternary phases in the selenide system on the basis of samples prepared by Alex Redinger by means of physical vapour deposition. More details on the preparation method can be found in chapter 3.1.1. Although the preparation methods for the sulphide and selenide kesterites are different, it is not expected that the preparation method has a significant influence on the phases present in the samples.

5.1 Literature review: competing phases in the copper tin zinc selenide and sulphide system

In the following section the possible competing phases in the system $CuZnSnS(e)$, will be presented. As in the following chapter only sulphurised or selenised samples will be considered, the $Cu\ Zn$ and $Cu\ Sn$ compounds, also known as brass and bronze, will be omitted.

5.1.1 Binary subsystems

Copper Sulphides and Selenides

Copper Sulphides Figure 5.3 shows the phase diagram of the copper sulphide system according to [80]. At room temperature depending on the copper to sulphur ratio several copper sulphide phases can be found: starting from the copper rich side monoclinic α-Chalcocite with the molecular formula Cu_2S exists, followed by orthorhombic Djurleite ($Cu_{1.96}S$), orthorhombic Anilite of stoichiometry $Cu_{1.75}S$ and a phase field containing a orthorhombic solid solution based on sulphur as well as hexagonal Covellite CuS. At 103.5°C α-chalcocite transforms into hexagonal β-chalcocite and a copper solid solution. β-chalcocite is stable up to 435°C, where it transforms into Digenite and copper. The molecular formula of Digenite is $Cu_{2-x}S$ with $x \leq 0.27$ and it crystallises into a face- centred-cubic structure. Anilite transforms at 75°C in Digenite, whereas Djurleite changes at 75°C into Digenite and Covellite. Covellite melts at 507°C. Copper rich Digenite is stable up to 1105°C, whereas copper poor Digenite melts at 813°C. The sulphur solid solution melts at 115°C. Phase transitions from a hexagonal to a cubic structure require a change of closest packing of the sulphur atoms. Such transitions have slow kinetics and lead therefore to the occurrence of metastable phases. This is the case for transitions between hexagonal chalcocite, Djurleite and covellite and cubic Digenite and Anilite phases. A complete overview of the possible metastable phases is given in [80]. Here only the tetragonal metastable phase will be mentioned as it is the only experimentally observed. The tetragonal phase is a polymorph of the Digenite phase and forms for copper to sulphur ratios of 1.85 to 1.99 and temperatures between 115°C and 145°C.

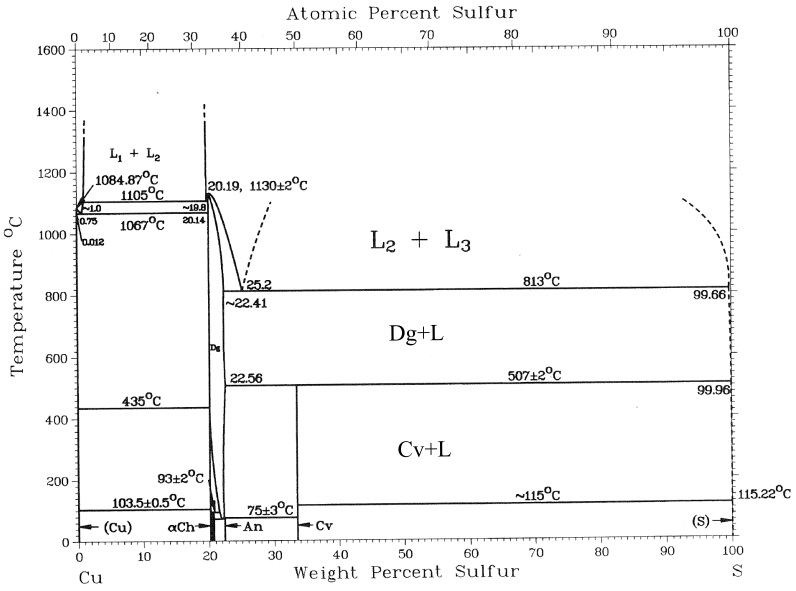

Figure 5.3: Phase diagram of the copper sulphide system according to [80]. *Ch* indicates Chalcocite, *An* Anilite, *Cv* Covellite, *Dg* Digenite and *L* the liquid phase.

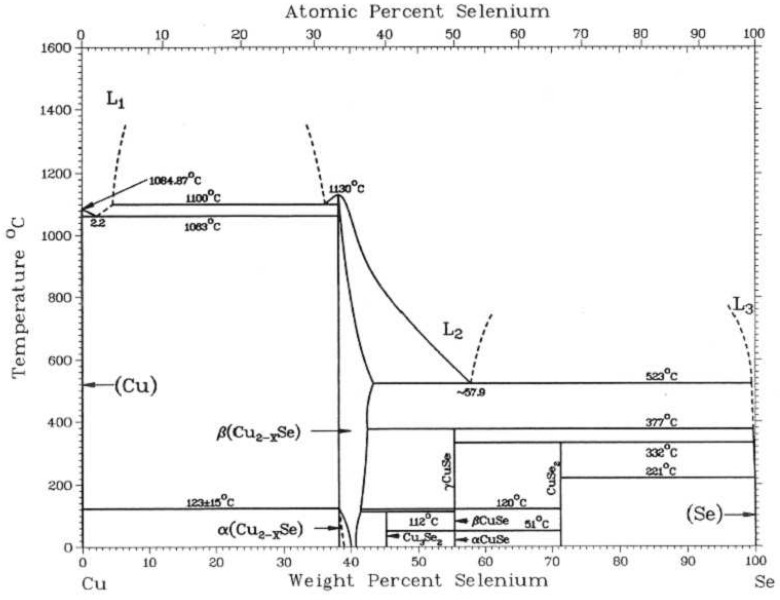

Figure 5.4: Phase diagram of the copper selenide system according to [81].

Copper Selenides In the copper selenium system four different binary phases exist: $Cu_{2-x}Se$, Cu_3Se_2, $CuSe$ and $CuSe_2$. The phase diagram of the copper selenium system is shown in figure 5.4. $Cu_{2-x}Se$ exists in a monoclinic α-phase configuration up to 123°C and transforms for higher temperatures into a cubic β-phase belonging to space group $Fm\bar{3}m$, which is stable up to 1130°C. Cu_3Se_2 has a tetragonal structure, belonging to the space group $P\bar{4}2_1m$ and decomposes at 112°C in Cu_2Se and $CuSe$. $CuSe$ exist in a hexagonal α-phase ($P6_3/mmc$) at room temperature. At 51°C it transfers into an orthorhombic β-phase, up to 120°C where a hexagonal γ- phase is formed ($P6_3/mmc$). At 377°C the $CuSe$ decomposes into $Cu_{2-x}Se$ and Se. $CuSe_2$ has an orthorhombic structure belonging to space group $Pnnm$. It decomposes into $CuSe$ and Se at 342°C.

Zinc sulphides and selenides

Zinc Sulphides Figure 5.5 shows the phase diagram of the zinc sulphide system. ZnS exists as a cubic $\alpha - ZnS$ low temperature phase ($F\bar{4}3m$) and transforms at 1020°C into a hexagonal $\beta - ZnS$ high temperature phase ($P6_3mc$).

Zinc Selenides ZnSe crystallise at room temperature in a zinc blende structure corresponding to space group $F\bar{4}3m$. Okada reports in [82] for samples consisting of equal amounts of selenium and zinc a phase transition to the wurtzite structure at $1411 \pm 2°C$. The wurtzite structure is a typical example of the hexagonal structure belonging to the $P6_3mc$ space group. According to [81] the wurtzite structure is only metastable. The melting point is at $1522 \pm 2°C$. The phase diagram is shown in figure 5.6.

Tin sulphides and selenides

Tin Sulphides Figure 5.7 shows the phase diagram of the tin sulphide system according to [81]. With increasing sulphur content, three different phases occur: SnS, Sn_2S_3 and SnS_2. SnS transforms at 602°C from the orthorhombic α low temperature phase ($Pmna$) into a cubic β-SnS high temperature phase ($F\bar{4}3m$). Four different forms of Sn_2S_3 are reported to occur between room-temperature and its decomposition at 760°C, however no structure is indicated. For SnS_2 a $\alpha - SnS_2$ low temperature phase and a $\beta - SnS_2$ high temperature phase are observed, however no consensus on the structure seemed to be reached. Due to the high vapour pressure of SnS, sublimation plays already a role at the used deposition temperatures. According to Piacente the evaporation of SnS_2 follows the following equilibria [83]

$$Sn_2S_3(s) \longrightarrow 2SnS(s) + \frac{1}{2}S_2(g) \qquad \Delta H = 54\frac{kJ}{mol} \tag{5.1}$$

$$SnS_2(s) \longrightarrow \frac{1}{2}Sn_2S_3(s) + \frac{1}{4}S_2(g) \qquad \Delta H = 112\frac{kJ}{mol} \tag{5.2}$$

$$SnS(s) \longrightarrow SnS(g) \qquad \Delta H = 220\frac{kJ}{mol} \tag{5.3}$$

Tin Selenides In the tin selenide system apart from the two elemental Sn and Se phases, two binary phases occur: orthorhombic $SnSe$, belonging to the space group $Pnma$ and hexagonal $SnSe_2$ belonging to space group $P\bar{3}m1$. The phase diagram is represented in figure 5.8. As for the tin sulphides, also for the tin selenides sublimation plays already an important role in the deposition temperature range of the PVD process : at temperatures above 400°C no SnSe sticks to the substrate [2]. The evaporation of $SnSe_2$ occurs via $SnSe$ [84]:

$$SnSe_2(s) \longrightarrow SnSe(s) + \frac{1}{x}Se_x(g) \qquad \Delta H = 105\frac{kJ}{mol} \tag{5.4}$$

$$SnSe(s) \longrightarrow SnSe(g) \qquad \Delta H = 216\frac{kJ}{mol} \tag{5.5}$$

5.1.2 Ternary subsystems

Copper Zinc Selenides and Sulphides In the phase diagram of the Cu_2S-ZnS system reported by Olekseyuk in [85] and depicted in figure 5.9, it emerges, that the solubility of Zn in Cu_2S is less than 1mol% at 397°C. Attempts by Craig to synthesize a Cu, Zn, S compound at atmospheric pressure were unsuccessful [86]. Also Birther reports in [87] $Zn_yCu_{1-y}X_2$ compounds with $X = S, Se, Te$ only for pressures at 65 kbar and higher. Therefore no ternary $Cu \cdot Zn \cdot S(e)$ phase at atmospheric pressure seems to exist.

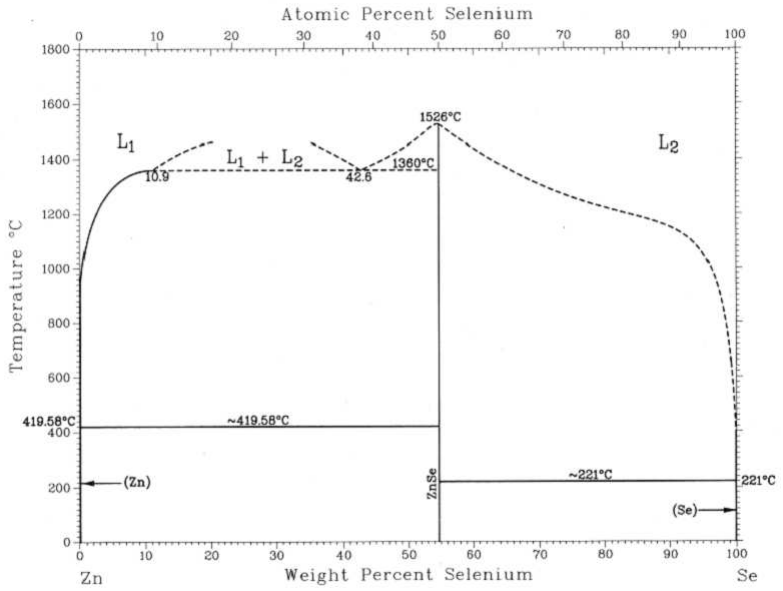

Figure 5.5: Phase diagram of the zinc sulphide system according to [81].

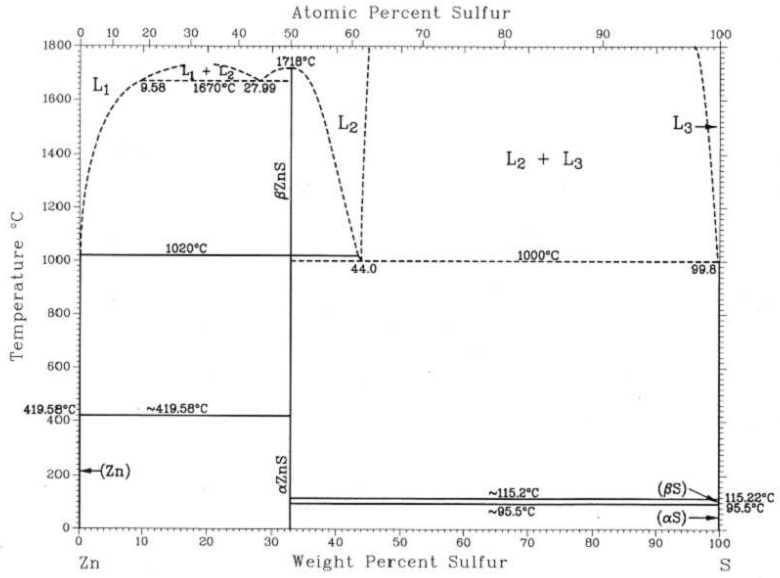

Figure 5.6: Phase diagram of the zinc selenide system according to [81].

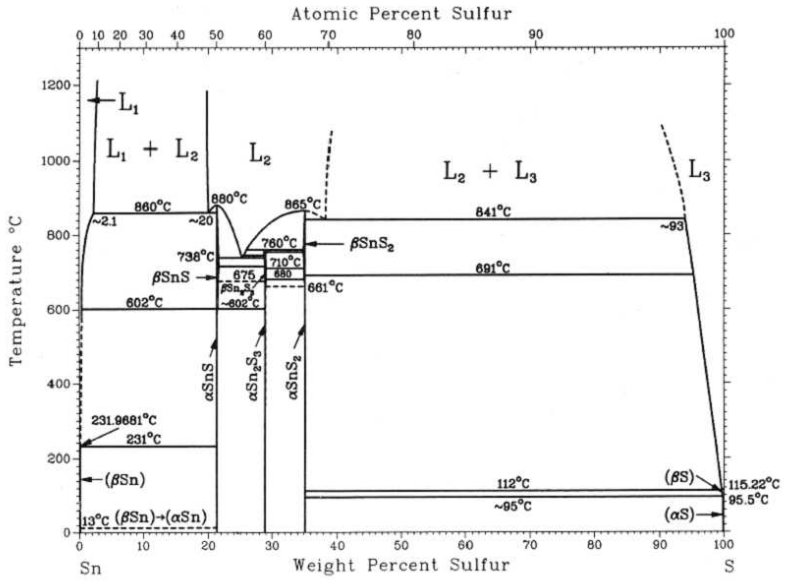

Figure 5.7: Phase diagram of the tin sulphide system according to [81].

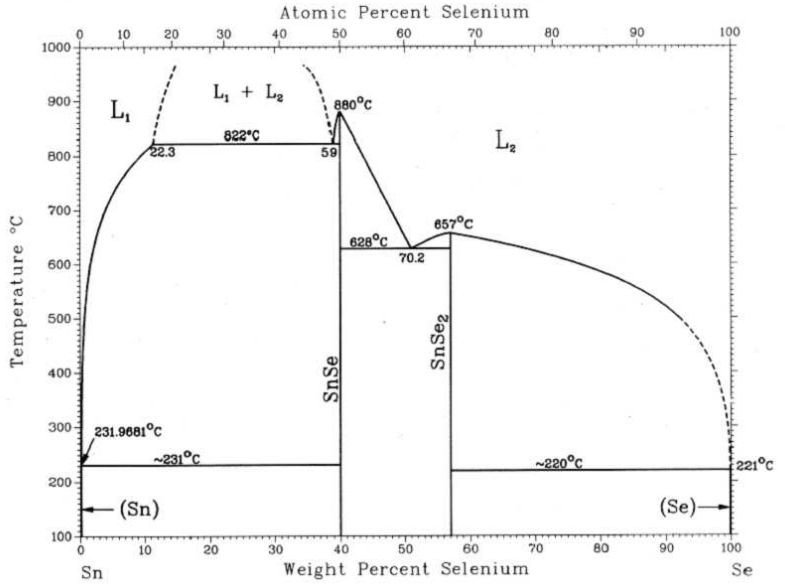

Figure 5.8: Phase diagram of the tin selenide system according to [81].

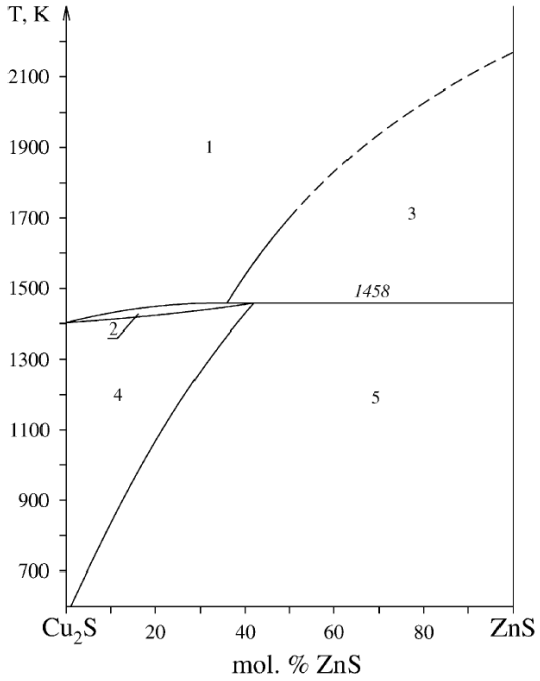

Figure 5.9: Phase diagram of the Cu_2S-ZnS system according to [85]: (1)melt, (2)melt+Cu_2S, (3) melt+ZnS, (4)Cu_2S, (5)Cu_2S+ZnS.

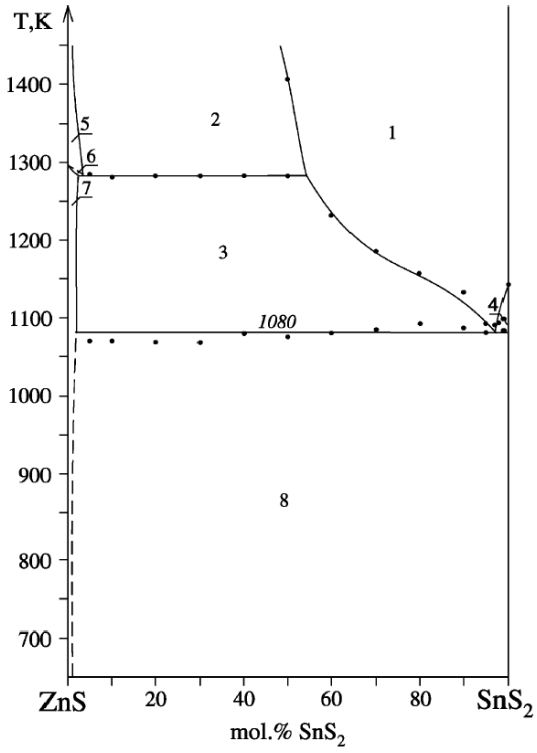

Figure 5.10: Phase diagram of the ZnS-Sn_2S system according to [85]: (1)melt, (2)melt+ZnS (wurtzite structure), (3)melt+ZnS (sphalerite structure), (4)melt+SnS_2, (5)ZnS (wurtzite structure), (6)ZnS (sphalerite structure)+ ZnS (wurtzite structure), (7) ZnS (sphalerite structure), (8) ZnS (sphalerite structure)+SnS_2.

Zinc Tin Selenides and Sulphides Also the ZnS and SnS_2 system is characterised by a very low solubility within the two components. It is not possible to dissolve more than 5mol% of SnS_2 in ZnS and less than 1mol% ZnS in SnS_2 and no ternary phase is observed [85]. Oleseyuk investigated in [88] the quasi-binary $SnSe_2$-$ZnSe$ system and no ternary compound was found.

Copper Tin Selenides and Sulphides

Copper Tin Sulphides Copper and tin are able to form with sulphur a variety of complex compounds as can be seen in figure 5.11. The tie lines between Cu_2S and SnS_2, Sn_2S_3 and SnS have been investigated by several authors. The ternary phases lie on the connection between Cu_2S and SnS_2 and on the sulphur-rich side of it. Moh observed for the isothermal section at 600°C on the Cu_2S to SnS_2 tie line an orthorhombic Cu_4SnS_4 phase, a triclinic Cu_2SnS_3 phase and a monoclinic $Cu_2Sn_3S_7$ phase [90]. The same phases were reported by Wu in [91] for an isothermal section at 500°C, however they found next to the Cu_2S - SnS_2 tie line an addi-

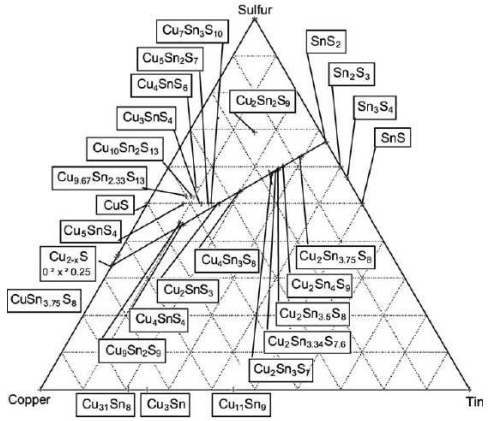

Figure 5.11: Phase triangle for the $Cu\ Sn\ S$ system according to [89]: the figure indicates all so far known $Cu\ Sn\ S$ phases.

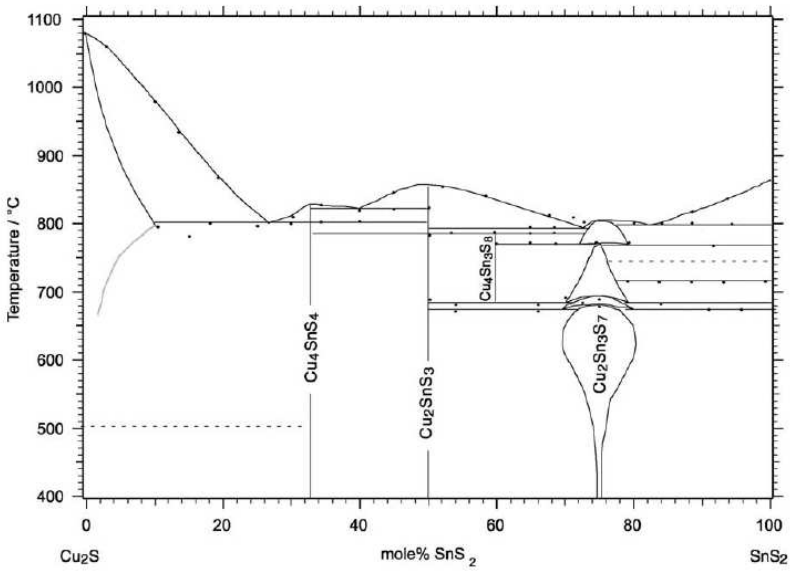

Figure 5.12: Phase diagram along the Cu_2S-SnS_2 section according to [89].

tional tetragonal $Cu_{10}Sn_2S_3$ phase and a $Cu_5Sn_2S_7$ phase, for which the symmetry could not be determined. Khanafer investigated the Cu_2S-SnS_2 tie line at 350°C in [92] and reports a Cu_4SnS_4 and a Cu_2SnS_3 phase, as the two preceding authors, but attributes a monoclinic symmetry to Cu_2SnS_3 phase. This result agrees with XRD studies on Cu_2SnS_3 crystals of Onoda [93], who also assigned a monoclinic symmetry to Cu_2SnS_3. Additionally Khanafer finds a cubic $Cu_2Sn_4S_9$ phase on the Cu_2S-SnS_2 tie line. The lattice constants and crystal systems of the phases according to the different authors are summarized in table 5.1. To summarize: on the Cu_2S-SnS_2 tie line all authors observe an orthorhombic Cu_4SnS_4 phase and a Cu_2SnS_3 phase. For Cu_2SnS_3 a monoclinic or triclinic symmetry is proposed. Moh and Wu indicate for the triclinic symmetry only one angle different from 90°, which would point to a monoclinic symmetry, but they do not discuss further, why they nonetheless assign a monoclinic unit cell.

Figure 5.12 shows exemplarily the phase diagram along the Cu_2S-SnS_2 section according to Fiechtner [89]. They observe three phases, which are stable from room temperature to above 800°C: Cu_4SnS_4, Cu_2SnS_3 and $Cu_4Sn_3S_7$. Between 685°C and 785°C an additional $Cu_4Sn_3S_8$ phase appears. They report three solid-solid phases transitions for $Cu_2Sn_3S_7$ at 675°C, 685°C and 770°C and a solid-solid phase transition for SnS_2 at 718°C.

Copper Tin Selenides For the selenide system no systematic investigation of the $Cu \cdot Sn \cdot Se$ triangle is available, however several cross sections are reported [94]: in the Cu_2Se-$SnSe$ tie line no ternary compound is formed. Figure 5.13 shows the phase diagram along the quasi binary Cu_2Se-$SnSe_2$ section: In a narrow composition range around $16at\,\%\ Sn$ only Cu_2SnSe_3 is formed. For lower tin content Cu_2Se forms as a secondary phase, whereas for higher tin contents $SnSe_2$ as additional phase is formed. Depending on the selenium content the apparent phase can be described by Cu_2SnSe_{3+x}, with $0 \leq x \leq 1$, this is Cu_2SnSe_3 and Cu_2SnSe_4 form the end points of a solid solution range. For Cu_2SnSe_3 several structures are discussed: a cubic zinc blende structure is reported [96],[97] and references therein. An orthorhombic structure up to temperatures of 450°C is proposed, which transforms at higher temperatures into a cubic zinc blende structure [95]. For copper poor and selenium rich Bridgman-Stockbarger grown samples a monoclinic structure with space group Cc is found [98]. Yet they observe a sphalerite super structure, which is due to the cation ordering reduced to the monoclinic crystal class. Gulay also finds a monoclinic structure in [99] based on XRD experiments on single crystals. Being the other end point of a solid-solution range, Cu_2SnSe_4 should assume the same symmetry as Cu_2SnSe_3. [100] reports that Cu_2SnSe_4 crystallises

Cu_2SnS_3

		a [Å]	b [Å]	c [Å]	α [°]	β [°]	γ [°]	
triclinic		6.64	11.51	19.93	90	109.45	90	[90]
monoclinic		6.25	23.1	6.25	90	109	90	[92]
triclinic		6.64	11.53	19.91	90	109.45	90	[91]
monoclinic		6.65	11.54	6.67	90	109.39	90	[93]

Cu_4SnS_4

		a [Å]	b [Å]	c [Å]	α [°]	β [°]	γ [°]	
orthorhombic		13.51	7.68	6.41	90	90	90	[90]
orthorhombic		13.7	7.75	6.45	90	90	90	[92]
orthorhombic		13.5	7.66	6.4	90	90	90	[91]

$Cu_2Sn_3S_7$

		a [Å]	b [Å]	c [Å]	α [°]	β [°]	γ [°]	
monoclinic		12.75	7.34	12.71	90	109.3	90	[90]
monoclinic		12.68	7.35	12.76	90	109.6	90	[91]

$Cu_2Sn_2S_9$

		a [Å]	b [Å]	c [Å]	α [°]	β [°]	γ [°]	
cubic		10.4	10.4	10.4	90	90	90	[92]

$Cu_{10}Sn_2S_{13}$

		a [Å]	b [Å]	c [Å]	α [°]	β [°]	γ [°]	
tetragonal		9.54	9.54	10.93	90	90	90	[91]

$Cu_5Sn_2S_7$

		a [Å]	b [Å]	c [Å]	α [°]	β [°]	γ [°]	
?		-	-	-	-	-	-	[91]

Table 5.1: Overview over the $Cu\,Sn\,S$ phases and their structure reported in literature.

Cu_2SnSe_3

		a [Å]	b [Å]	c [Å]	a [°]	b [°]	g [°]		
orthorhombic		4.03	5.7	12.08	-	-	-	up to 450°C	[95]
cubic		5.69	5.69	5.69	90	90	90	above 450°C	[95]
cubic		5.69	5.69	5.69	90	90	90		[96]
cubic		5.69	5.69	5.69	90	90	90		[97]
monoclinic		6.59	12.16	6.61	90	108.56	90		[98]
monoclinic		6.69	12.04	26.48	90	94.97	90		[99]

Cu_2SnSe_4

cubic		5.68	5.68	5.68	90	90	90		[100]

Table 5.2: Overview over the structures reported in literature for Cu_2SnSe_3 and Cu_2SnSe_4.

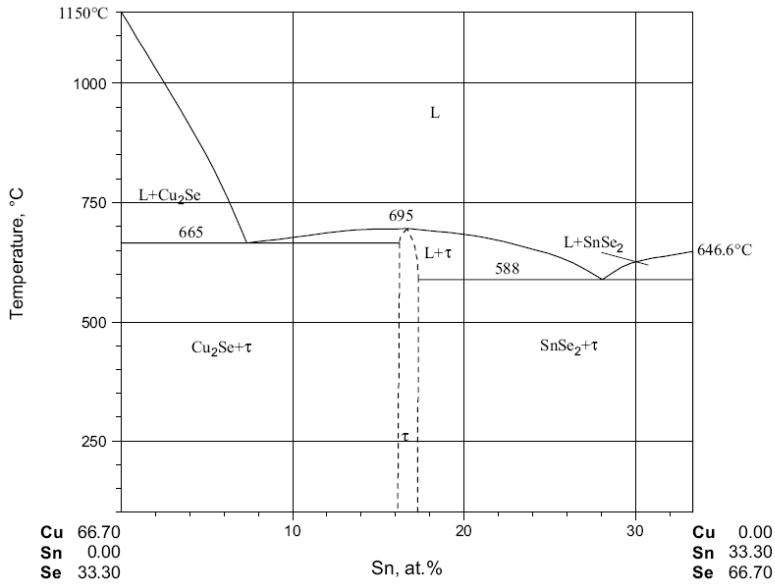

Figure 5.13: Phase diagram of the Cu_2Se-$SnSe_2$ section according to [94]. τ indicates the ternary phase Cu_2SnSe_3.

in the cubic zinc blende structure, which belongs to the space group F-43m. The propositions of the different authors are summarized in table 5.2.

5.1.3 Quaternary system

Pseudoternary phase diagrams

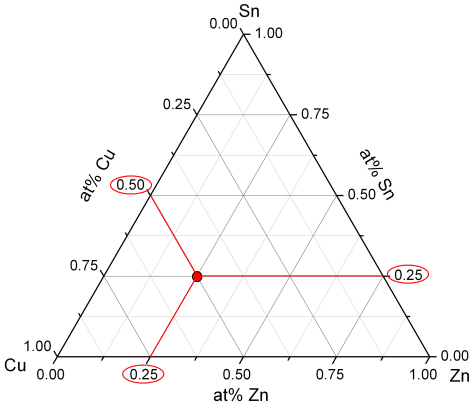

Figure 5.14: A pseudoternary phase diagram: The axes indicate the content in atomic percent of the cations Cu, Zn and Sn. Exemplarily the position of Cu_2ZnSnX_4, X being the chalcogenide is indicated.

Assuming for the quaternary system $Cu \cdot Zn \cdot Sn \cdot S(e)$, growth conditions under Chalcogen excess, its composition can be represented by only taking the cation concentrations into account. A very convenient way of doing this is to use a ternary phase diagram as depicted in figure 5.14:

The axes of the pseudo ternary phase diagram indicate the concentration of the cations Cu, Zn and Sn in atomic percent. To draw a data point into a ternary phase diagram, one chooses the appropriate composition on the axis and draws a line parallel to the axis cutting at $0\,at\%$. Taking the Zn content of kesterite $Cu_2ZnSnS(e)_4$ as example, one follows in figure 5.14 the Zn-axis to 25% and draws a line parallel to the Cu-axis. Repeating this for the Cu and the Sn content one arrives at the position of kesterite as indicated in figure 5.14.

Copper zinc tin sulphide system According to differential thermal analysis studies of [101] and [90] cubic $\alpha - Cu_2SnS_3$ and Cu_2ZnSnS_4 form a complete solid solution series for temperatures above 775°C up to the melting points of Cu_2SnS_3 and Cu_2ZnSnS_4 as depicted in figure 5.15 . Below 775°C $\alpha - Cu_2SnS_3$ starts transforming into triclinic $\beta - Cu_2SnS_3$, giving rise to a two-phase field separating the $\alpha-$ and $\beta - Cu_2SnS_3$ phases. With decreasing temperature the Cu_2ZnSnS_4 amount contained

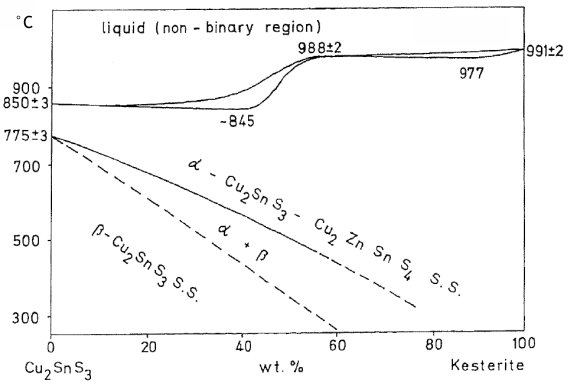

Figure 5.15: Cu_2SnS_3-Cu_2ZnSnS_4 section according to [101] and [90]: Kesterite forms a solid solution with cubic $\alpha - Cu_2SnS_3$. Below 775°C $\alpha - Cu_2SnS_3$ starts transforming into triclinic $\beta - Cu_2SnS_3$.

in the $\beta - Cu_2SnS_3$ phase increases. In the same article Moh also investigated the ZnS-Cu_2ZnSnS_4 section and found that ZnS and Cu_2ZnSnS_4 form two separated phases. Small amounts of kesterite can be dissolved in ZnS above 600°C, with a maximum of 38 at% at 972 °C.

Olekseyuk studied the $CuZnSnS$ system in [85] by differential thermal analysis and XRD measurements, resulting in the isothermal section at 400 °C represented in figure 5.16: In contrast to Moh and Roy-Choudhury, Olekseyuk does not find a solid solution between Cu_2ZnSnS_4 and Cu_2SnS_3. Instead they report a second quaternary phase: $Cu_2ZnSn_3S_4$. The composition range in which Cu_2ZnSnS_4 as the only phase forms is indicated by 1 in figure 5.16. It is surrounded by composition regions in which kesterite and additional phases form: on the copper- and zinc-rich side of kesterite, Cu_2S and ZnS will form as additional phases. Different ternary $Cu \cdot Zn \cdot Sn \cdot S$ compounds and $Cu_2ZnSn_3S_4$ form on the copper- and tin-rich side of kesterite. On the tin- and zinc-rich side of kesterite $Cu_2ZnSn_3S_4$ and ZnS is formed.

Copper zinc tin selenide system Figure 5.17 shows the isothermal section of the $Cu\ Zn\ Sn\ Se$ system according to [102] determined by thermal analysis and XRD measurements as in figure 5.16 for the sulphide system. No solid solution between $Cu_2ZnSnSe_4$ and any of the competing phases was observed. In contrast to the results for the sulphide system no second quaternary phase is

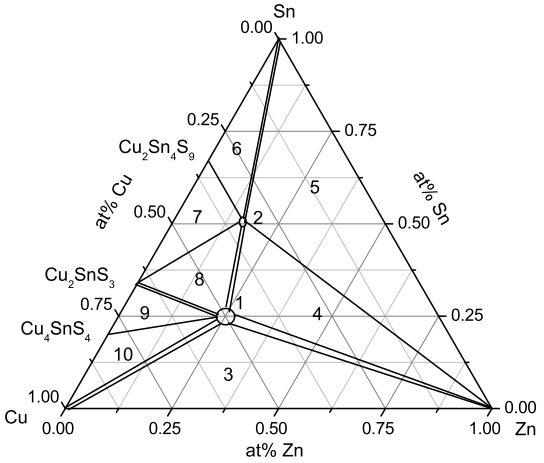

Figure 5.16: Isothermal section at 400 °C according to [85]. The numbers correspond to the following phases: (1) Cu_2ZnSnS_4, (2) $Cu_2ZnSn_3S_8$, (3) $Cu_2S + ZnS + Cu_2ZnSnS_4$, (4) $Cu_2ZnSnS_4 + Cu_2ZnSn_3S_8 + ZnS$, (5) $Cu_2ZnSn_3S_8 + ZnS + SnS_2$, (6) $Cu_2ZnSn_3S_8 + Cu_2Sn_4S_9 + SnS_2$, (7) $Cu_2ZnSn_3S_8 + Cu_2Sn_4S_9 + Cu_2SnS_3$, (8) $Cu_2ZnSnS_4 + Cu_2ZnSn_3S_8 + Cu_2SnS_3$, (9) $Cu_2ZnSnS_4 + Cu_4SnS_4 + Cu_2SnS3$, (10) $Cu_2S + ZnS + Cu_4SnS_4$, which are all limited by two phase fields.

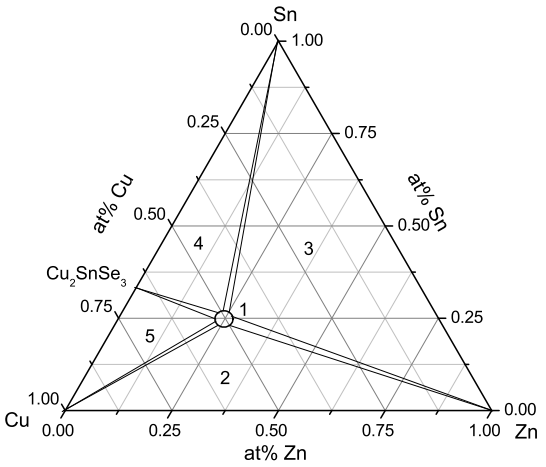

Figure 5.17: Isothermal section at 400 °C according to [102]. The numbers correspond to the following phases: (1)$Cu_2ZnSnSe_4$, (2) $Cu_2ZnSnSe_4 + Cu_2Se + ZnSe$, (3) $Cu_2ZnSnSe_4 + Sn_2Se + ZnSe$, (4) $Cu_2ZnSnSe_4 + Cu_2SnSe_3 + SnSe_2$, (5)$Cu_2ZnSnSe_4 + Cu_2SnSe_3 + Cu_2Se$, which all are limited by two phase fields.

found, but additionally a polymorphous transition for $Cu_2ZnSnSe_4$ at 580°C was observed . The region in which kesterite forms as the only phase is as narrow in the selenium system as it is in the sulphide system. However in the selenium system $Cu_2ZnSnSe_4$ is reported to form in addition to other phases in nearly all of the possible composition range.

Conclusion

Sn loss due to $SnS(e)$ evaporation plays an important role at the growth temperature, therefore no $SnS(e)$ secondary phase is expected. Cu_xS and Cu_xSe_y secondary phases are likely to occur, as they are also observed in chalcopyrite synthesis. Depending on their stoichiometry and crystal structure, their band gap and electric conductivity varies [103], so that they can decrease the band gap as well as lead to shunting of the solar cell. However, as the lattice constants of the Cu_xS and Cu_xSe_y secondary phases are different to the kesterite lattice constant, copper selenide and sulphide secondary phases should be easily detectable by XRD measurements. $Cu_2SnS(e)_3$ secondary phases are highly conductive [103], so copper tin sulphide or selenide phases at the grain boundaries can lead to a shunting of the solar cell. If $Cu_2SnS(e)_3$ forms a solid solution with kesterite as reported by some authors, it will probably be difficult to avoid $Cu_2SnS(e)_3$ secondary phases during synthesis. A further challenge is the similar lattice constant of $Cu_2SnS(e)_3$ compared to kesterite, which makes it very difficult to detect $Cu_2SnS(e)_3$ by XRD measurements. The same problem arises for $ZnS(e)$ secondary phases. $ZnS(e)$ is highly resistive. If a $ZnS(e)$ layer forms between the absorber and the back contact this leads to an increase of the series resistance of the solar cell.

5.1.4 Formation reactions for Cu_2ZnSnS_4 and $Cu_2ZnSnSe_4$

Based on the most probable solid state reactions in the copper-zinc-tin-chalcogen system, determined by epitaxially initiated solid state reactions, Hergert finds in [104] two reaction paths to form $Cu_2ZnSnS(e)_4$. Starting from the binary sulphide or selenide phases it is either possible to form $Cu_2ZnSnS(e)$ directly

$$Cu_yS(e) + ZnS(e) + SnS(e)_z \longrightarrow Cu_2ZnSnS(e)_4 \tag{5.6}$$

or via an intermediate ternary phase:

$$\begin{aligned} Cu_yS(e) + SnS(e)_z &\longrightarrow Cu_2SnS(e)_3 \\ Cu_2SnS(e)_3 + ZnX &\longrightarrow Cu_2ZnSnS(e)_4 \end{aligned} \tag{5.7}$$

with the possible valencies y and z equal to either one or two for the copper and tin sulphides. In the first reaction step in equation 5.7 also other copper tin sulphides or selenides are possible, however to achieve the correct stoichiometry in the second step $Cu_2SnS(e)_3$ is most favorable. To determine the formation temperature of $Cu_2ZnSnS(e)_4$ in-situ XRD and EDXRD annealing studies are reported. As in all attempts to analyse the secondary and ternary phases contained in $Cu_2ZnSnS(e)_4$ samples, one challenge is the very small separation of the main diffraction maxima of $Cu_2ZnSnS(e)_4$, $Cu_2SnS(e)_3$ and $ZnS(e)$. Schorr reports in [105], that the formation of Cu_2ZnSnS_4 according to reaction path 1 starts below 300°C, based on an annealing study on binary mixtures. Weber also reports a similar temperature range for the beginning of kesterite formation in an annealing study on stacked binary sulphide precursor layers [16]. Schurr, finds in an annealing study on electro-deposited precursor layers for the reaction according to reaction path 2 a somewhat higher temperature necessary to form kesterite

of 572°C [14]. The difference in formation temperature may be due to different pressures during annealing, as Schurr states that the samples are pressed together face to face, which leads to a high sulphur partial pressure. Another possible explanation could be that the two different formation paths lead to different formation temperatures.
The only experimental study on the formation temperature for $Cu_2ZnSnSe_4$ is reported by Volobujeva [9]. Annealing of precursors consisting of thin metal layers, prepared by vacuum deposition, revealed a minimum temperature of kesterite formation of 300°C.

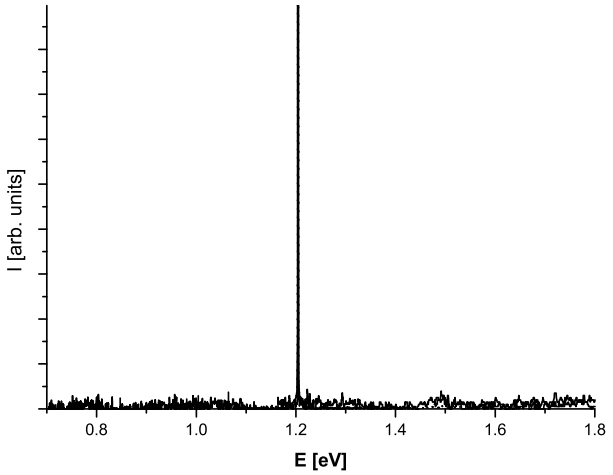

Figure 5.18: Photoluminescence spectrum of sample A measured at 550 mW excitation power at 10 K. The peak 1.2 eV corresponds to the second order of the laser line.

5.2 Phase analysis by photoluminescence and XRD measurements: Sulphides

In this section the competing phases occurring in the $Cu \cdot Sn \cdot Zn \cdot S$ system will be investigated on the basis of four samples: sample A contains only copper and sulphur, so copper sulphides are expected to form. Sample B consists mainly of zinc and sulphur. However it also contains a small copper fraction, as an intermediate copper layer is necessary to electro-deposit zinc on the molybdenum substrate, therefore copper sulphides and zinc sulphides are expected. Sample C is composed of copper, tin and sulphur, this is copper sulphides, tin sulphides and copper tin sulphides can form. Sample D consists of all four elements necessary to form kesterite: copper, zinc, tin and sulphur.

[at%]	**Cu**	**Zn**	**Sn**	**S**	**Mo**	**Cd**
A	28.3	-	-	31.4	40.3	-
A (WDX)	47.1	-	-	27.0	25.9	-
B	4.2	41.8	-	48.1	5.8	-
C	24.6	-	14.8	47.0	13.6	-
D	19.8	10.7	11.1	50.2	4.0	4.2

Table 5.3: Elemental composition of the samples used for phase analysis determined by EDX and WDX measurements at 20 keV. For the EDX accuracy see appendix A.1.

Copper sulphides Figure 5.19 shows the θ-2θ XRD scan of sample A. As the sample was thin, the most intensive diffraction maxima are due to the molybdenum substrate. The main reflections due to the sample at 46.1° and 27.7° and the smaller one at 32.1° can be attributed to the cubic $Cu_{2-x}S$ phase, which belongs to the $Fm\bar{3}m$ space group. The positions of the diffraction maxima of its reference file are given in the first line. However the cubic $Cu_{2-x}S$ phase cannot account for all reflections visible in figure 5.19: for example the maximum at 32.6° and the peak at 45.3° remain unexplained. They can be attributed to a reference which states a tetragonal phase belonging to the $P4_32_12$ space group for $Cu_{2-x}S$ ($x \leq 0.27$). The positions of its diffraction maxima are given in the second line. The composition of the sample as determined by EDX measurements yields a copper content of 28.3 $at\%$ and a sulphur content of 31.4 $at\%$, leading to a copper to sulphur ratio of 0.8-1. However in EDX measurements the peaks due to sulphur and molybdenum are very close. As the sample is very thin and therefore a high Mo signal is expected, the occurrence of both, the Mo and the S peak, may induce an error in calculating the sulphur amount. Therefore WDX measurements have been performed, which yield 47.1 $at\%$ copper and 27.0 $at\%$ sulphur corresponding to a copper to sulphur ratio of 1.7 in accordance with the stoichiometry of the Cu_{2-x} phase.

From thermodynamic considerations as described in section 5.1.1 the cubic $Fm\bar{3}m$ phase is the phase one would expect to occur, as cubic $Cu_{2-x}S$ is the only stable copper sulphide phase above 507°C. In [106] a tetragonal phase as a metastable phase of

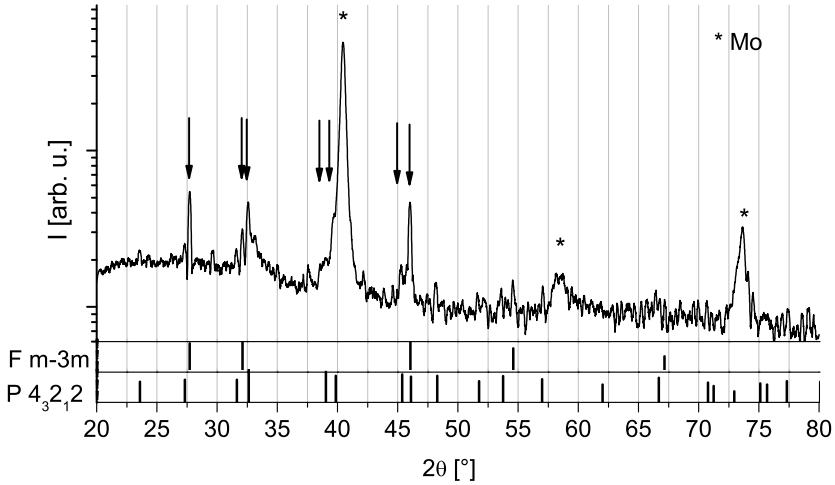

Figure 5.19: θ-2θ XRD scan of sample A: $Fm\bar{3}m$ and $P4_32_12$ indicate the positions of the diffraction maxima in the reference files for cubic and tetragonal $Cu_{2-x}S$, $P6_3/mmc$ the hexagonal CuS structure.

Cu_2S is described , which is received after annealing copper and sulphur at 140°C for 24h. Sample A was annealed at much higher temperature, however cool down was slow, so the tetragonal phase may has formed again during cool down.

Figure 5.18 shows the PL spectrum of sample A. The sharp peak at 1.2 eV is due to the second order diffraction maximum of the laser line. No PL signal due to the sample could be detected in the investigated energy range. According to [103], hexagonal $Cu_{2-x}S$ shows an indirect band gap of 1.09-1.2 eV at room temperature depending on the orientation and polarisation. The direct band gap equals 1.7 eV. The phase transition from the hexagonal to the cubic phase does not involve a change in band gap energy. However increasing x increases the free carrier absorption [103]. For the tetragonal phase a band gap of 1.24 eV at 80K is reported [103].There does not yet seem to be consensus about the type of band gap reached, as density functional theory calculations suggest a direct band gap for $Cu_{2-x}S$, pointing out the difficulty to determine the type of band gap from optical absorption measurements influenced by free charge carrier absorption [107]. A band to band transitions for an indirect band gap cannot be observed in PL measurements, however transitions between defects close to the band maxima might be visible. But this seems not to be the case. [107] remarks that Cu atoms are mobile and the copper positions in copper sulphides are not well defined, which might give rise to strong phonon scattering and electron phonon interaction. This in turn might enhance non-radiative recombination. So the lack of a PL signal cannot ultimately be explained, but as also in literature no PL for $Cu_{2-x}S$ was observed, the spectra shown in figure 5.18 matches the expectations.

Zinc sulphide The EDX values in table 5.3 indicate, that sample B consists mainly of zinc and sulphur and a small amount of copper. A thin copper layer on top of the molybdenum substrate is necessary to be able to deposit a homogeneous zinc film by electro-deposition afterwards. The diffraction pattern of this sample is shown in figure 5.20. The main diffraction maxima at 28.7°, 47.6° and 56.4° as well as the smaller reflections at 33.1°, 69.5°, 76.7° and 79.2° can be clearly attributed to ZnS in the cubic sphalerite phase. This corresponds to what one would expect, as cubic ZnS is the only stable phase up to temperatures above 1000°C as described in the previous section. The diffraction maximum at 45.9° corresponds to the position of the main diffraction maximum of $Cu_{2-x}S$, so it may indicate that there is a $Cu_{2-x}S$ phase present. From the EDX values one can roughly estimate that the $Cu_{2-x}S$ phase accounts for at most 5% to 10% of the film. This would be in agreement with the low XRD yield of this phase. As the solubility of copper atoms in a ZnS crystal is very low in this temperature range and no ternary copper zinc tin phase exists, as described in section 5.1.2, it is reasonable that also low amounts of copper lead to an copper sulphide phase and are not incorporated as impurities into the ZnS crystal .

For sample B a PL spectrum at 550 mW excitation power at 10 K was observed. Also sample B,

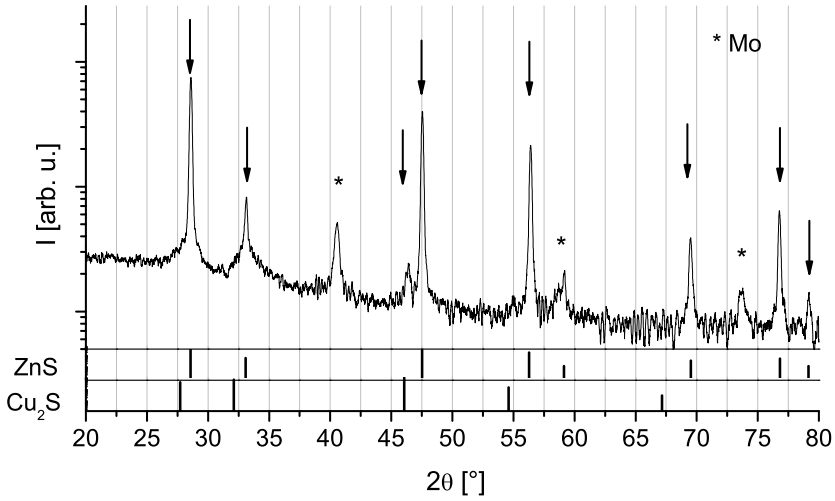

Figure 5.20: Grazing incidence XRD scan of sample B: the first line indicates the positions for ZnS belonging to the sphalerite $F\bar{4}3m$ space group. The second lines gives the positions for cubic Cu_2S.

like sample A in figure 5.18, did not show any PL signal. The room temperature band gap of ZnS is 3.7 eV [103], so one would not expect to see any band transitions in the measured energy range. Different luminescence bands related to copper impurities measured at 4 K are reported [108], [109]: a blue copper band with a maximum at 2.85 eV, a green copper band at 2.41 eV and a red copper band at 1.77 eV. Only the red copper band lies in the experimentally accessible energy range. Which luminescence band is visible in a sample depends according to [109] on the relation between the copper impurity concentration compared to a coactivator. A coactivator is in this case an element from the third group of the periodic table. In the present case, with no impurities belonging to the third group of the periodic table present in the sample, the red copper band is expected. However the samples investigated in [108], [109] are grown from an $NaCl$ melt, which is known to introduce defects. [109] suggests, that the interaction during the growth process with the Cl^- ion, leads to the formation of sulphur vacancies, which give rise to deep defects. Therefore if the transitions at 1.77 eV is due to a donor acceptor transition between a defect introduced due to a copper impurity and a deep defect induced by the growth in the $NaCl$ melt, it would not be surprising, that I do not observe this transition.

Copper tin sulphide The lower line in figure 5.21 show the θ-2θ-scan of sample C. Sample C contains copper, tin and sulphur. The main diffraction maxima at 28.4°, 33.0°, 47.29° and 56.1° as well as the smaller diffraction maxima at 20.9°, the double maxima at 31.0 and 31.4°, and the diffraction maxima at 42.5, 44.0, 58.8, 69.1, 76.3 and 78.7° match nicely with the diffraction pattern for Cu_2SnS_3 in the monoclinic $P1$ phase given in the first line. The second line gives the positions of the diffraction maxima for the tetragonal Cu_2SnS_3 phase, belonging to the $I\bar{4}2m$ space group. As the main diffraction maxima for the monoclinic, the cubic and the tetragonal phase are the same, the tetragonal Cu_2SnS_3 diffraction pattern, matches the main measured diffraction maxima, however it cannot explain the less intense ones. This is an important result, as the diffraction maxima for the tetragonal Cu_2SnS_3 phase coincides exactly with the diffraction maxima expected for Cu_2ZnSnS_4. Therefore if the chosen annealing conditions lead to monoclinic Cu_2SnS_3, it is reasonable to assume that also monoclinic Cu_2SnS_3 would be formed while synthesizing Cu_2ZnSnS_4, leading to a difference in the small diffraction maxima of the Cu_2SnS_3 and Cu_2ZnSnS_4 phases. As from the EDX values given in table 5.3 sample C is slightly tin rich, the possible occurrence of an Sn_xS_y phase was investigated. No convincing agreement with the reference data could be found. The same is true for the Cu_4SnS_4 phase.

Fernandes reports in [110] a cubic Cu_2SnS_3 phase at annealing temperatures of 400°C and a copper-richer phase due to Sn loss after annealing at 520°C. For the copper-richer phase, they assign from XRD θ-2θ scans an orthorhombic Cu_3SnS_4 phase, whereas their electron backscattered diffraction anal-

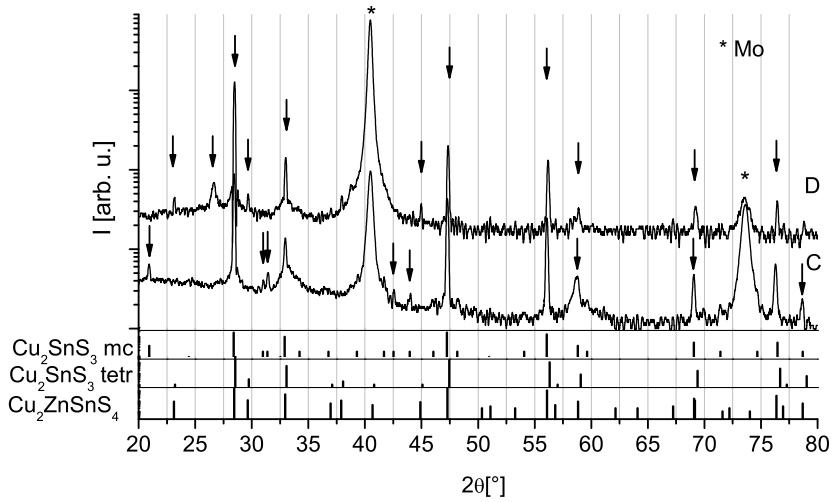

Figure 5.21: θ-2θ XRD scan of samples C (below) and D (above): the first two lines indicates the positions for Cu_2SnS_3 in the monoclinic (Cc) and triclinic (P) symmetry. The third lines gives the positions for Cu_2ZnSnS_4 phase in the tetragonal $I\bar{4}2m$ phase.

ysis (EBSD) yields orthorhombic (Pnma) Cu_4SnS_4. It is difficult to distinguish the two phases from EDX composition measurements, as already an error of $\mp 0.02\,at\%$ for the copper and tin composition value, would change the copper to tin ratio from ~ 3 to ~ 4. In the spectrum reported by Fernandes for the cubic Cu_2SnS_3 phase the diffraction maximum at 33° already shows a rather low intensity, therefore it would be difficult to observe the even weaker diffraction maxima distinguishing the cubic from the monoclinic phase. This could explain why they attribute a cubic space group, while I assign a monoclinic space group, possibly observing the same phase. Comparing the result presented in figure 5.21 to those of Fernandes implies that beside the much longer annealing duration and slightly higher temperature, the tin loss for this sample was smaller than for the one described by Fernandes. This might be explained by the different annealing procedure used: Fernandes anneals under N_2 flux, leading to a steady removal of the evaporated SnS, whereas the samples used here were annealed in a constant $N_2 + H_2$ atmosphere, in which a small SnS vapor pressure might have built up.

Figure 5.22 shows the PL spectra of sample C at 10 K and 300 mW excitation power. It shows a peak at 0.81 eV and no other peaks up to an energy of 2.2 eV were observed. The room temperature band gap reported for Cu_2SnS_3 in [103] varies between 0.59 eV determined by transport measurements and 0.91 eV from photoconductivity measurements. Fernandes reports a band gap of 0.96 eV for the

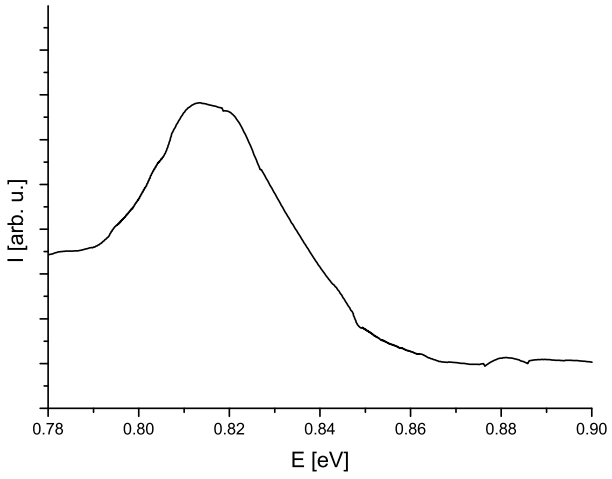

Figure 5.22: Photoluminescence spectrum of sample C measured at 300 mW excitation power at 10 K.

cubic phase, however they find considerably higher band gaps of 1.35 eV and 1.60 eV for the tetragonal and the orthorhombic phase [110]. Yet the highest transmission value is $\sim$ 30 % and the measured spectra for the tetragonal and the orthorhombic phase seem to be influenced by Urbach tails, which might add an uncertainty to the deduced values. Also a band gap of 1.065 eV from transmission measurements for Cu poor thin films is reported [111], but for the EDX values given in this article an additional SnS phase may be expected, which would also lead to a band gap at about 1.1 eV[103]. As the measurement shown in figure 5.22 is at 10 K the peak corresponds most likely to defect-related transitions, resulting in a peak energy lower than the band gap. On the other hand the band gap increases with decreasing temperature at about a rate of 0.1 meV/K, therefore the band gap will be about 30 meV larger at 10 K. Taking these two points into account, it is reasonable to assume that the peak observed in figure 5.22 belongs to a Cu_2SnS_3 related transition. That Cu_2SnS_3 related transitions can be detected in PL is an important result, as it will help to determine if a sample contains a Cu_2SnS_3 phase. Cu_2SnS_3 can be distinguished from Cu_2ZnSnS_4 by θ-2θ XRD scans only due to minor diffraction maxima, which requires long integration times. Assuming for Cu_2SnS_3 an absorption coefficient of $\alpha = 10^4 \frac{1}{cm}$ results in a penetration depth $l = \frac{1}{\alpha} = 1\mu m$. The sample C is about 900 nm thick and yields a PL signal of $I_{PL,C} = 11000\, counts$. Therefore, the maximum PL signal under these experimental conditions, if the entire penetration depth of the laser is used, would result in a PL signal of $V_{IL} = 12200\, counts$. To clearly identify the phase a PL signal of at least $I_{PL,Min} = 500\, counts$ is needed. Assuming a PL yield proportional to the number of luminescing atoms and thereby neglecting influences like non radiative recombination due to grain boundaries or bad sample quality leads to a PL signal proportional to the volume of the phase illuminated. Therefore the minimum volume fraction of Cu_2SnS_3 phase contained in the illuminated spot of a Cu_2ZnSnS_4 sample to make detection possible can be calculated. Assuming the same experimental conditions as for sample C, the minimum volume will be $V_{min} = V_{Il} * \frac{I_{PL,Min}}{I_{PL,C}} = V_{Il} * \frac{1}{24}$. Thus at least $\frac{1}{24} \sim 4\%$ of the volume penetrated by the laser beam needs to be occupied by the Cu_2SnS_3 phase, to allow its detection. If the surface of the Cu_2ZnSnS_4 sample is covered by a homogeneous Cu_2SnS_3 layer, the minimum layer thickness for Cu_2SnS_3 will be 40 nm, corresponding to about 70 monolayers of Cu_2SnS_3. However the secondary Cu_2SnS_3 phase may also occur at the grain boundaries, or as reported for the copper selenides in $CuInSe_2$ and $CuGaSe_2$ as small droplets in the grain ([112] and references therein). As long as the volume fraction of the Cu_2SnS_3 phase does not drop below 4% of the volume investigated by the beam the detection of the secondary phase will be possible.

Copper zinc tin sulphide In sample D all four elements (copper, zinc, tin and sulphur) are present. Thus not only Cu_2ZnSnS_4 can be formed, but the binary and secondary phases as well. As the EDX was measured after CdS deposition to prepare a solar cell from the sample, it shows additional Cd. The diffraction pattern of sample D is shown as the upper line in figure 5.21. It has diffraction maxima at 28.5°, 32.9°, 47.3° and 56.2°, the same as sample C. This corresponds to the very similar positions of the main diffraction maxima for Cu_2SnS_3 and Cu_2ZnSnS_4. Yet, sample D shows additional diffraction maxima at 23.1°, 29.7°, 37.9° and 45.0° which correspond to the Cu_2ZnSnS_4 phase, if one assumes that when synthesized under the same conditions as sample C, also only the monoclinic Cu_2SnS_3 phase would form. Also the smaller diffraction maxima indicating the Cu_2SnS_3 phase at 24.4°, the double peak at 31.0° and 31.4° and at 45.8 and 46.0° disappear in sample D. From this one can conclude that sample D contains the Cu_2ZnSnS_4 phase. In figure 5.23 the PL spectrum of sample D at 300 mW excitation power at 10 K is shown. The peak at 0.82eV observed in sample C is missing, instead there is a wide peak at 1.14eV. This is in agreement with the XRD results indicating that there is no ternary phase present, but Cu_2ZnSnS_4 instead. Altosaar reports a wide, broad Cu_2ZnSnS_4 PL peak measured at 10 K related to a band-tail transition at 1.31eV [51]. Compared to the measurement presented in figure 5.23 it is shifted $\sim 170\, meV$ to higher energies. Both measurements are broad and asymmetric pointing to compensated samples. In compensated samples normally a shift in energy position for the peak of $10 - 20 \frac{meV}{dec}$ with increasing excitation power is observed as stated in chapter 2.2.1. The excitation power used for the measurement is not given in [51]. Yet, a difference in excitation power of at most a factor of 500 would not be sufficient to account for the difference in maximum peak position between the two measurements, if a setup with similar focusing is used. According to den-

sity functional theory calculations by Chen [35] three different structures are possible for the Cu_2ZnSnS_4 compound: Kesterite, stannite and a primitive mixed $CuAu$ like structure, as mentioned in chapter 2.1.1. The formation energy of the three structures is very similar, so that although kesterite has the lowest formation energy, it is possible for all three structures to form in a sample. The calculated band gaps for the three structures differ by 1.5 eV to 1.35 eV for kesterite and the primitive mixed CuAu structure. So the difference in the peak position between the two sample might partially be due to different structures. However, to clarify this point further, neutron diffraction experiments would be necessary.

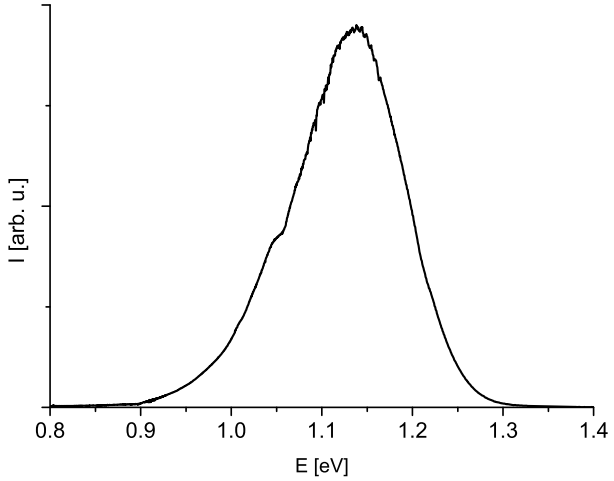

Figure 5.23: Photoluminescence spectrum of sample D measured at 300 mW excitation power at 10 K.

5.3 Phase analysis by photoluminescence and XRD measurements: Selenides

[at%]	Cu	Zn	Sn	Se	Mo
A	47.6	0.0	0.2	35.0	17.2
B	38.2	19.2	0.1	40.7	1.8
C	33.9	0.0	6.0	36.6	23.5
D	30.4	0.0	13.6	45.7	10.4
E	22.88	13.85	12.47	50.47	0.33

Table 5.4: Elemental composition of the samples used for phase analysis determined by EDX measurements at 20 keV. For the EDX accuracy see appendix A.1.

To investigate the PL signal of the binary and ternary phases in the selenide system five samples with the compositions given in table 5.4 have been grown. Sample A consists only of copper and selenium and a small trace of tin, so a copper selenide phase should be observed. Sample B contains copper, zinc and selenium so it may contain a zinc selenide phase and copper selenide phases. The samples C and D do not contain zinc, but copper, tin and selenium. So either the ternary phase Cu_2SnSe_3 or the binary phases tin selenide and copper selenide can be formed. Sample E consists of all four elements, copper, zinc tin and selenium, so kesterite can form, and the binary and ternary phases also.

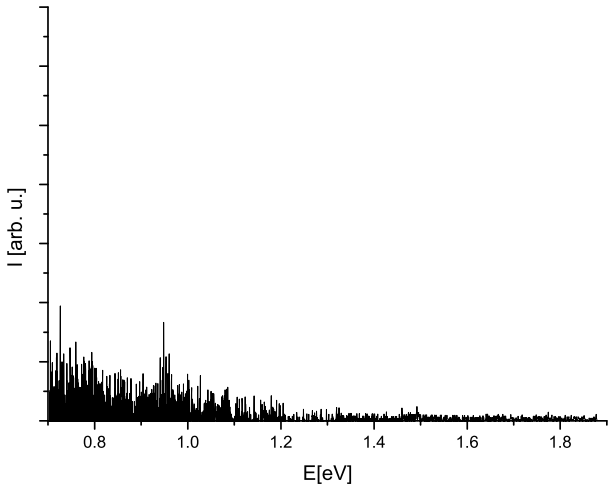

Figure 5.24: Photoluminescence spectrum of sample A measured at 10 K and 550 mW excitation power.

Copper selenide Sample A was deposited at a temperature of 515°C, but was heated to a higher temperature after deposition, what led to a deformation of the glass substrate. Due to the uneven substrate leading to a uneven height distribution over the sample and induced strain, a determination of the phase contained in the sample by XRD measurements was not possible. At a deposition temperature above 377°C as depicted in chapter 5.1.1 only the high temperature phase of $Cu_{2-x}Se$ is still stable, but during cooling a $CuSe$ phase may again form. Figure 5.24 shows the PL spectrum of sample A measured at a temperature of 10 K and 550 mW laser excitation power. It does not show any PL signal in the energy range investigated. [113] and [103] report optical absorption measurements for $Cu_{2-x}Se$ at room temperature showing a forbidden band gap of 1.2 eV. [114] finds performing tight

binding calculations using a cubic model structure for Cu_2Se an indirect band gap of $\sim 0.52\,eV$ and a direct band gap of $\sim 3.4\,eV$. They point out however, that the values of the calculated band gaps depend on the approximation used and therefore the absolute values might not be correct . Nevertheless from this calculation it seems that the direct band gap is above the experimentally accessible energy range in my setup. [115] finds in an X-ray photoelectron (XPS) and X-ray emission (XES) spectroscopy study, that the band gap in $Cu_{2-x}Se$ decreases with increasing copper content. This seems to agree with optical absorption measurements described in [116] and references therein, which observe an indirect band gap for $Cu_{2-x}Se$ with $x = 0.2$ of $E_{G,indir} = 1.4\,eV$, $E_{G,indir} = 1.2 - 1.3eV$ for $x = 0.15$ and $E_{G,indir} = 1.0 - 1.1eV$ for $x = 0$. They obtain a direct band gap of $E_{G,dir} \sim 2.2\,eV$. They observe the same value for the direct band gap of $CuSe$. To conclude: As the probability for PL transitions involving an indirect band-gap is low, they are unlikely to be observed. The direct band gap determined from the optical absorption measurements should be visible just at the edge of the measurement range of my setup. However non-radiative transitions via the indirect band gap might be more probable. I also do not observe any defect-related transitions, which is probably due to the fact that defects in $Cu_{2-x}Se$ are most likely copper vacancies due to the high mobility of copper. However as described in [114], copper vacancies can be accounted for in a defect cubic model, which leads to a narrowing of the band gap, but does not to introduce defect states in the band gap. As I do not observe any PL due to the direct band to band transition of $CuSe$, most probably no $CuSe$ formed during cooling.

Zinc selenide Figure 5.27 shows the θ-2θ scan of sample B. The first line indicate a ZnSe phase in the zinc blende structure. In the second line the positions of the diffraction maxima for the Cu_2Se phase with $Fm\bar{3}m$ symmetry are given. As long as the phase maintains the $Fm\bar{3}m$ symmetry the position of the maxima is independent of the stoichiometry which may vary for $Cu_{2-x}Se$ between $x = 0$ and $x = 0.3$. The position of the molybdenum substrate peaks is shown by black stars. Besides one peak at $2\theta = 39.49°$, which cannot be attributed to any of the phases mentioned before, the reference files fit nicely with the measured spectra. No $CuSe$ phase

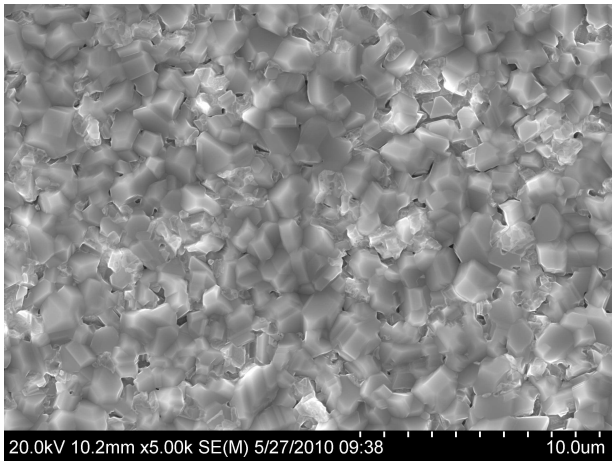

Figure 5.25: SEM picture of sample B.

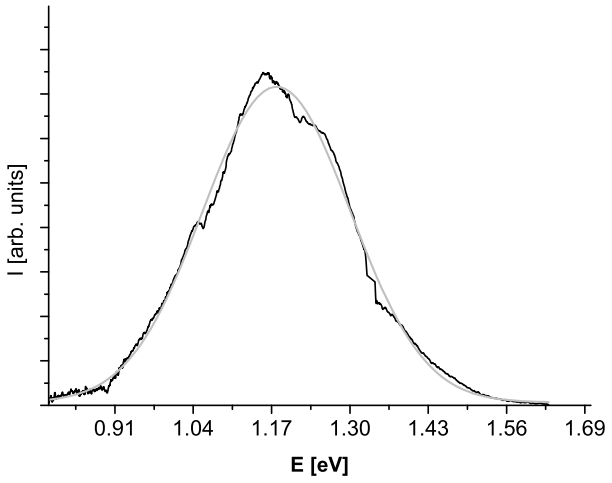

Figure 5.26: Photoluminescence spectrum of sample B at 10 K and 300 mW excitation power (black continuous line). The grey line indicates a fit with a Gaussian distribution to the measured data.

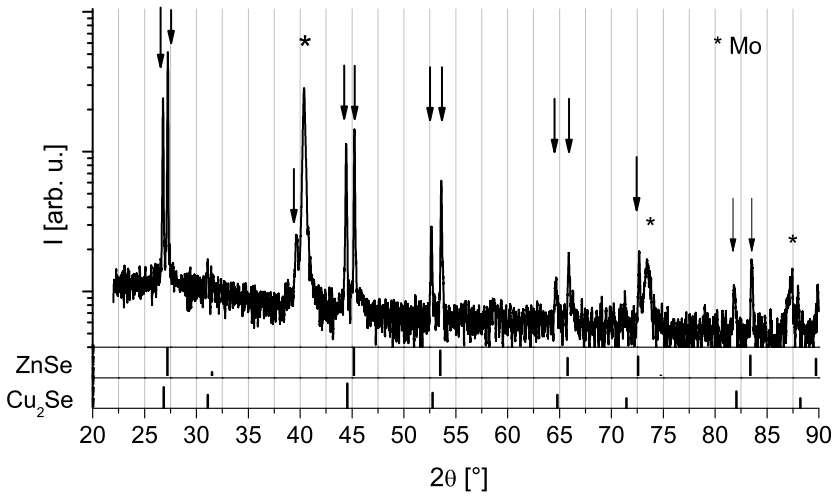

Figure 5.27: θ-2θ XRD scan of sample B: the first line indicates the position of the reference file for cubic $ZnSe$, belonging to the $F\bar{4}3m$ space group, the second line for cubic $Cu_{2-x}Se$ with $Fm\bar{3}m$ symmetry.

could be detected. The SEM image of the sample shown in figure 5.25 shows on one hand large grains with clear cut faces and on the other hand smaller grains with less clear shapes. EDX measurements on the different areas yield that the large grains are copper-rich, whereas the smaller less clearly shaped grains are zinc-rich. So SEM measurements support the two separate phases observed in the XRD measurements. Since the sample was deposited at 440°C the Cu_2Se phase, as in sample A, corresponds to what one would expect from thermodynamic considerations, too. Zinc selenide crystallizes in the whole experimentally relevant temperature range in the zinc blende structure as discussed in chapter 5.1.1.
Figure 5.26 shows the PL signal of sample B: a very wide peak, which can be described by a Gaussian distribution with a width of 290 meV and a maximum at 1.18 eV. As discussed for sample A one would not expect to observe a PL signal of the Cu_2Se band-band transition. Sample A did not show any defect related transitions either. However the additional zinc in sample B may have introduced additional defect states. According to [103]the band gap of $ZnSe$ is at 2.8 eV at 10 K. This is above the excitation energy of the laser of 2.4 eV and can therefore not be observed. However transition metals belonging to the IB group of the periodic table, such as copper, silver and gold form deep defect levels in $ZnSe$ [103],[117]. For copper a Cu^{2+} acceptor state with an ionisation energy of 0.7 eV and a 0.35 eV deep impurity center are reported [103].Yet free-to-bound transition involving those states should lead to a PL peak at higher energies. Another candidate is the zinc vacancy leading to a 1.75 eV deep donor state [103] . Free-to-bound transitions involving this defect would result in peaks in the right energy range. However, regarding the huge width of the observed peak, there are certainly more than one defect or one defect level involved in the transition. The broadening might be due to fluctuating electrostatic potentials or band gap fluctuations as introduced in chapter 2.2.2. Electrostatic potential fluctuations result normally in an asymmetric peak with a flattened low energy slope. But, the slopes of the peak in figure 5.26 follows almost perfectly a Gaussian distribution. To eliminate the possibility that the widening of the peak is due to electrostatic potential fluctuations additional temperature and intensity dependent measurements would be necessary. As shown in figure 5.25,the sample has a polycrystalline structure, which may lead to band gap fluctuations between the different grains. However no non stoichiometric $ZnSe$, nor an influence of copper inclusion on the band gap of $ZnSe$ is reported in literature. To summarise: transitions involving the zinc vacancy in the zinc selenide phase are a likely origin for the observed peak at 1.18eV. However to prove this hypothesis the spectrum of a sample containing only ZnSe need to be measured.

Copper tin selenide Figure 5.28 and 5.29 show the diffraction pattern of samples C and D. Samples C and D were grown without zinc, so the possible phases contained in the samples are either the binary copper selenide, tin selenide or one of the ternary

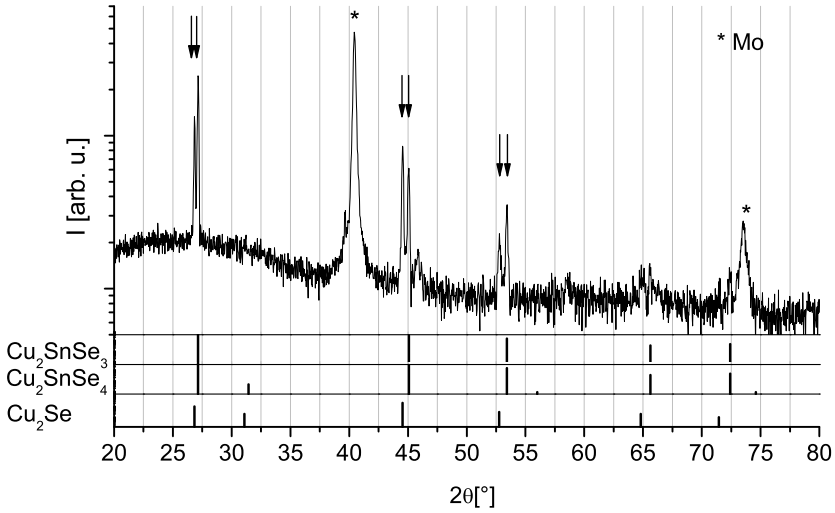

Figure 5.28: θ-2θ XRD scan of sample C

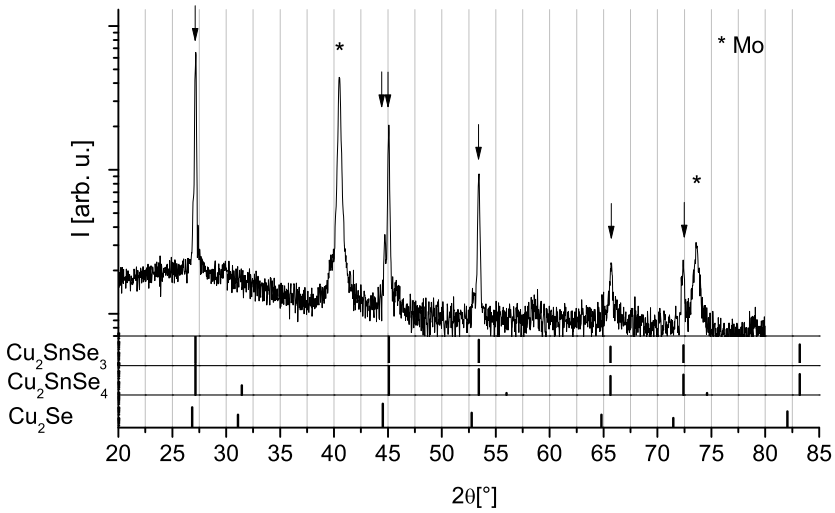

Figure 5.29: θ-2θ XRD scan of sample D.

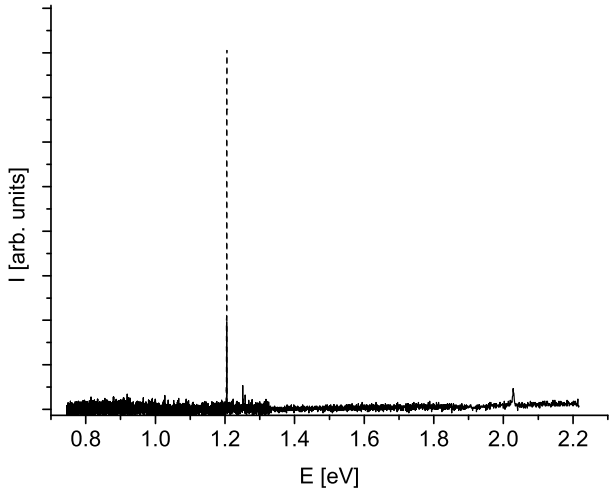

Figure 5.30: Photoluminescence spectrum of sample C measured at 500 mW excitation power at 10 K.

phases. As the sample can neither contain $ZnSe$, nor $Cu_2ZnSnSe_4$ the copper tin selenide phases can be identified by XRD measurements. Monoclinic and cubic Cu_2SnSe_3 belonging to the space groups Cc and F-43m and a cubic Cu_2SnSe_4 phase with F-43m symmetry show the same main peaks at 2θ equal to 27.2°, 45.1°, 53.3° and 65.6°. The monoclinic Cu_2SnSe_3 phase exhibits many additional diffraction maxima, which where not observed in the measurements of the two samples. The expected diffraction maxima for the cubic Cu_2SnSe_3 and Cu_2SnSe_4 phases are given in the first and second line below the diffraction pattern. As both phases belong to the same space group and have very similar lattice constants $a_{Cu_2SnSe_3} = 5.684\mathring{A}$ for Cu_2SnSe_3 and $a_{Cu_2SnSe_4} = 5.685\mathring{A}$ for Cu_2SnSe_4 it is not surprising that expect for slight variations in intensity for the diffraction maxima at 31.4° and 56.0° the diffraction pattern for both phases are almost the same. The diffraction pattern of Cu_2SnSe_4 shows an additional peak at 74.6°. These two diffraction pattern fit well to the measured spectra, which show every peak besides the small peaks at 31.4° and 56.0°. As the 31.4° diffraction maximum corresponds to the (200) plane and the 56.0° diffraction maximum to the (222) plane, the fact that these two peaks are missing cannot be explained by orientated growth. If the sample would be orientated the two missing diffraction maxima need to be members of the same family of lattice planes. Also the multiples of the two missing diffraction maxima, for instance the diffraction maxima corresponding to the (111) plane at 27.1 and the (400) plane at 65.6° can be observed in the spectrum. As the peaks at 31.4° and 56.0° are according to the reference files the two diffraction maxima with the lowest intensity. Most probably the integration time of the measurements was not long enough to be able to observe these two peaks. The measurement of sample C shown in figure 5.28 shows additional peaks at 2θ values of 26.8°, 44.56° and 52.79°. These diffraction maxima match the positions expected for the $Cu_{2-x}Se$ phase, given in the third line. For sample D the intensity of the $Cu_{2-x}Se$ diffraction maxima decreased, some of the peaks disappeared completely. This is due to the lower copper and higher tin content in comparison to sample C used for the preparation of sample D. No agreement with a tin selenide phase could be found. As described in chapter 5.1.2, literature did not yield an unambiguous picture of the phase transitions and existence regions to expect for Cu_2SnSe_3 and Cu_2SnSe_4 therefore from a thermodynamic perspective neither of the two phases can be ruled out.

Figure 5.30 shows the PL yield of sample C at 500 mW excitation power and 10 K. The sharp peak at 1.2 eV corresponds again to the second diffraction maximum of the laser line. No signal due to the sample could be detected in the investigated energy range. The same result is obtained for sample D. According to Marcano in [118] Cu_2SnSe_3 is a p-type semiconductor with a room temperature band gap of 0.84 eV. A band gap of 0.84 eV should be still observable as the low energy end of the used CCD detector is at 0.8 eV. However as the measurements were at 10K the PL signal would not be due to band to band transitions but result from defect-related transitions. Marcano observes in Hall measurements an acceptor state, which is 67 meV deep. Grossberg describes in [57] Cu_2SnSe_3 cold temperature PL transitions with a peak maximum at 0.64 eV and shoulders at 0.69 eV and 0.8 eV. Transitions to the defect state reported by Marcano, as well as the PL transitions observed by Grossberg would be outside the measurement range of our setup. The same is true for band to band transitions for the Cu_2SnSe_4 compound: according to [100] the smallest room temperature band gap is 0.35 eV and the second spin orbit split band gap is at 0.55 eV wide. Thus, both energy gaps are clearly outside the accessible measurement range.

Copper zinc tin selenide Sample E contains copper, zinc, tin and selenium, therefore $Cu_2ZnSnSe_4$, but also all competing secondary and ternary phases, can form. The θ-2θ scan of sample E is shown in figure 5.32. As $ZnSe$, Cu_2SnSe_3 and $Cu_2ZnSnSe_4$

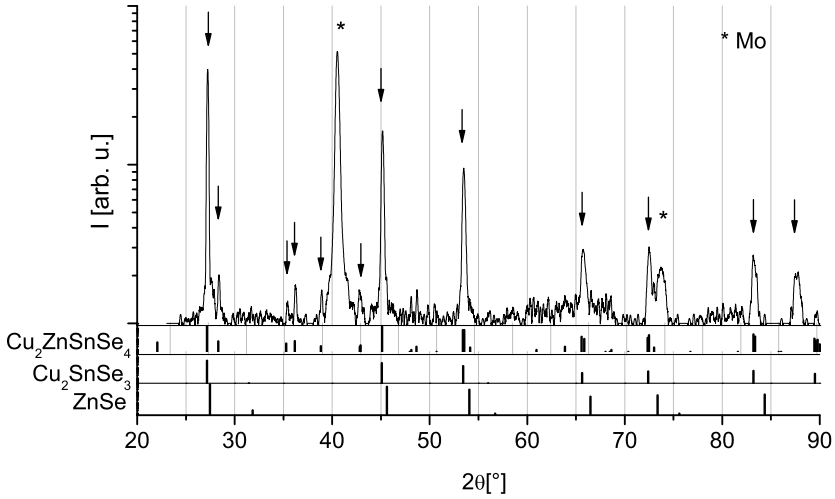

Figure 5.32: θ-2θ scan of sample E

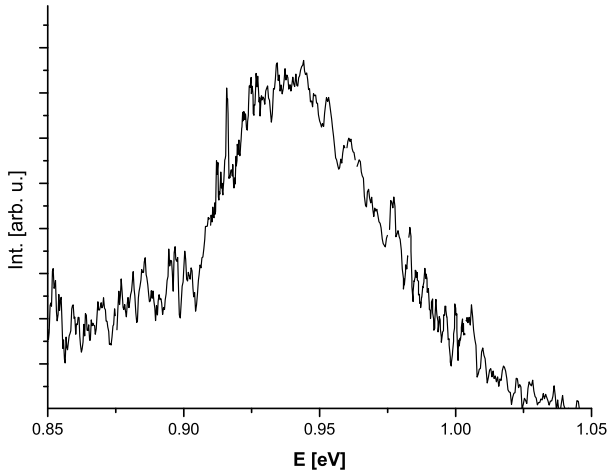

Figure 5.31: Photoluminescence spectrum of sample E measured at 500 mW excitation power at 10 K.

show its main diffraction maxima at the same 2θ positions, at 27.0°, 45.1° and 53.4°, none of the phases can be excluded from XRD measurements. However figure 5.32 shows additional reflections at 28.4°, 35.4°, 36.2°, 38.8° and 43.0°, which are unique to $Cu_2ZnSnSe_4$, as for $Cu_2ZnSnSe_4$ no tetragonal phase is reported. Hence $Cu_2ZnSnSe_4$ is, maybe amongst other phases, comprised in sample E. No reflections due to copper selenide or tin selenide are observed. Figure 5.31 shows the PL spectrum of sample E measured at 10 K and 500 mW excitation power. It shows a wide peak at 0.94 eV and no other peaks due to the sample in the measured energy range. As neither $ZnSe$, nor the copper tin selenides showed a peak at 0.94 eV this peak can be assigned to $Cu_2ZnSnSe_4$.

Conclusion and outlook

In this chapter the combination of photoluminescence and XRD measurements as a tool to detect competing phases in the $Cu \cdot Zn \cdot Sn \cdot S(e)$ system were investigated. As tin loss already plays an important role at the used growth temperatures, the $SnS(e)_z$ phases were not considered. Copper sulphide as well as copper selenide can be identified by XRD measurements. In the sulphide system ZnS can neither be identified by XRD nor by photoluminescence measurements excited with the 514 nm laser line.

Also Cu_2SnS_3 cannot be distinguished from kesterite by XRD measurements, yet shows a PL peak at 0.81eV at a well separated position from the PL peak at 1.14 eV observed for polycrystalline

	XRD	PL
Cu_2S	+	-
ZnS	-	-
Cu_2SnS_3	-	0.81 eV
Cu_2ZnSnS_4	-	1.14 eV

Cu_2Se	+	-
$ZnSe$	-	1.18 eV
Cu_2SnSe_3	-	-
$Cu_2ZnSnSe_4$	-	0.94 eV

Table 5.5: Photoluminescence peak positions and distinctness of XRD diffraction positions compared to the other secondary phases.

Cu_2ZnSnS_4. Therefore PL measurements will help to identify a Cu_2SnS_3 secondary phase present in a sample. This is crucial as Cu_2SnS_3 and Cu_2ZnSnS_4 are suspected to form a solid solution as described in chapter 5.1, therefore it is very likely that under copper rich growth conditions Cu_2SnS_3 will be formed. Due to the smaller band gap of Cu_2SnS_3 compared to Cu_2ZnSnS_4, Cu_2SnS_3 will be detrimental to the open circuit voltage of the solar cell. Copper tin selenides cannot be distinguished from kesterite by XRD measurements. There are luminescence peaks reported in literature, but they lie outside of the measurement range of the setup used. The $ZnSe$ phase shows a wide peak at 1.18 eV, which is easily distinguishable from the polycrystalline $Cu_2ZnSnSe_4$ peak at 0.94 eV. To identify the remaining phases, zinc sulphide and copper tin selenide, Raman measurements in cooperation with a group at the university of Barcelona are in progress.

Chapter 6

First results of photoluminescence measurements on kesterites

For the characteristics of the solar cell device, the doping of the absorber layer is important. For the kesterites it is expected, similar to the chalcopyrites, that the doping is governed by intrinsic defects. With photoluminescence measurements a sensitive tool to investigate the intrinsic defects is at hand. Analogues to the chalcopyrites, interesting questions for the kesterite system are: how wide is the possible $\frac{Cu}{Zn+Sn}$- and $\frac{Zn}{Sn}$-ratio range in which still kesterite forms? How does the $\frac{Cu}{Zn+Sn}$- and $\frac{Zn}{Sn}$-ratio affect the observable defect spectrum? As the interest in kesterite as a material for solar cells increased only recently, therefore also the development of adapted ways to synthesize kesterites is still at the very beginning. It turned out to be very difficult to obtain samples with sufficient crystal quality to be able to measure any photoluminescence signal at all. Due to the very limited number of luminescing samples, systematic investigations were very difficult. In the following Se kesterite samples originating from the PVD process will be investigated.

The photoluminescence signal of the as deposited Se kesterite samples turned out to be weak, rendering temperature or power dependent measurements difficult. However the strength of the photoluminescence signal can be improved by post process annealing, as will be shown in the first section. Wide asymmetric photoluminescence peaks are observed, which do not allow to draw any conclusions about defect levels. The reason for the broadening of the peaks will be investigated in the second section.

6.1 Effects of the annealing

An overview over the composition of the investigated samples is presented in table 6.1. Samples A, C and

[at%]		Cu	Zn	Sn	Se	$\mathbf{T_{dep}}$[°C]
A		22.9	13.9	12.5	50.5	390
B	A ann.	18.8	22.2	8.0	38.0	390
C		22.9	13.5	12.6	50.9	350
D	C ann.	17.4	16.2	7.5	31.8	350
E		26.6	13.3	12.0	48.2	400
F	E ann.	30.3	12.9	9.9	46.9	400

Table 6.1: Composition of the polycrystalline Se-kesterite samples discussed in this chapter determined by EDX measurements. Sample A and B are measured at 8 keV, samples C-F at 20 keV. For the EDX accuracy see appendix A.1.

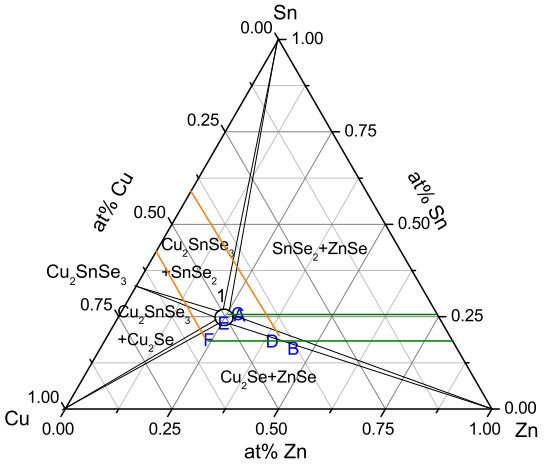

Figure 6.1: Composition of the samples A-F represented in a ternary phase diagram. In the circle indicated by (1) only $Cu_2ZnSnSe_4$, in the neighbouring fields $Cu_2ZnSnSe_4$ and the indicated secondary phases are formed.

E are as deposited samples from the PVD process.

Samples B and D represent the annealed counterparts to samples A and C, which were annealed according to procedure I in an oven, sample F is the counterpart to sample E, treated by post process annealing in the PVD according to procedure II. The different annealing procedures are explained in more detail in appendix A.3. Samples B and D contain additionally to the elements indicated in table 6.1 carbon, oxygen and about 3% sulphur, due to cross contamination during annealing. Figure 6.1 represents the metallic composition of the samples graphically: the as deposited samples were all close to stoichiometry, samples A and C slightly on the tin and zinc rich side of stoichiometric $Cu_2ZnSnSe_4$, sample E is slightly copper rich. During annealing all samples lost tin as indicated by the green line. Additionally the samples annealed according to procedure I seem to lose copper, whereas the sample annealed according to procedure II seem to lose zinc. However it needs to be considered, that the EDX values are determined assuming an homogeneous absorber. All annealed samples show in the photoluminescence measurements presented later in this chapter an additional peak due to a $ZnSe$ phase. This does not disturb the measured Zn content, if the $ZnSe$ grains are distributed uniformly over the absorber. However it will lead to an overestimation of the zinc content, if the $ZnSe$ phase occurs as a layer on top of the absorber. SIMS measurements presented later in this chapter revealed a thin $ZnSe$ layer on top of sample D, which will lead to an overestimation of the zinc content in this sample. The same effect cannot be ruled out for the other annealed samples.

Figures 6.2 and 6.3 show the photoluminescence spectra of samples A/B and E/F respectively. A common feature for both pairs is an increase in PL signal, of a factor 5 for samples A/B and 1.5 for samples E/F, and an additional wide peak appearing around 1.15 eV after annealing. However the as deposited sample E had already a factor 4 higher PL intensity than sample A. The additional peak around 1.15 eV can be ascribed to defect related transitions in ZnSe as observed in chapter 5.3. Figure 6.4 shows the spectra of samples A-E normalised to their maximum intensity. Samples A and B were measured at 500 mW excitation power, whereas the other samples were measured at 300 mW. The darker colors represent the as deposited, the brighter ones the annealed samples. Samples A/B (black/grey) show a red shift due to annealing, samples C/D (dark/light blue) a small blue shift, whereas the position of samples E/F

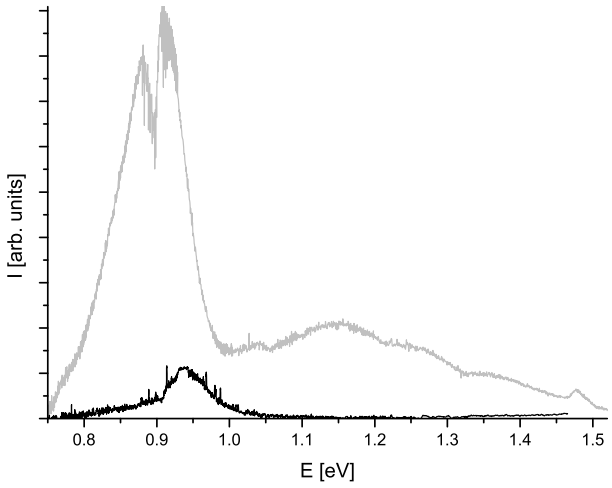

Figure 6.2: The figure shows the photoluminescence spectra of sample A (black line) and sample B (grey line) at 10 K and 500 mW excitation power.

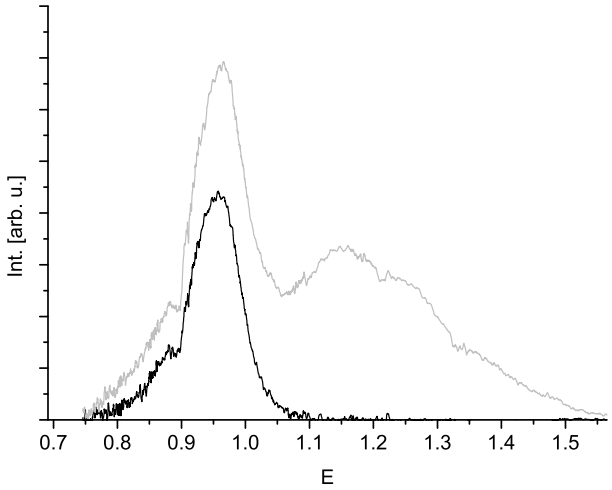

Figure 6.3: The figure shows the PL spectra of sample E (black line) and sample F (grey line) at 10 K and 300 mW excitation power.

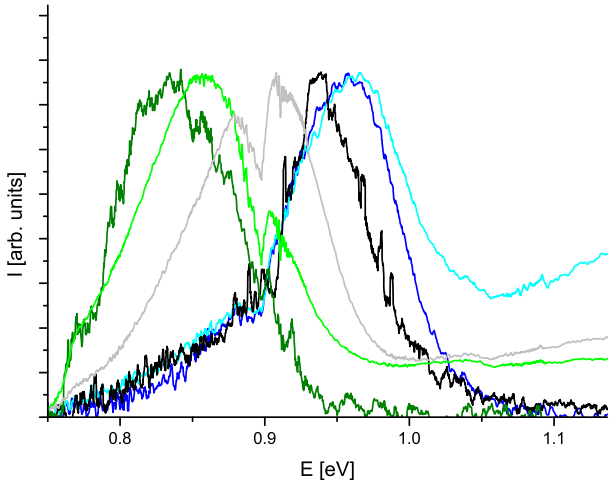

Figure 6.4: Normalised PL spectra of sample A (black), B (grey), C (green), D (light green), E (blue) and F (light blue) at 10 K.

(dark/light green) remains constant.

To analyse the effect of the annealing on the photoluminescence intensity and the peak position in more detail, subsequently XRD and SIMS measurements were performed and are reported here.

XRD measurements To determine the phases contained in the samples and their possible change during annealing $\theta - 2\theta$ scans as described in section 4.2.1 (p.20) are performed. Figure 6.5 shows the diffraction pattern of sample A (continuous black line) and sample B (dashed red line).

The most prominent difference between the two diffraction patterns is the appearance of diffraction maxima at 31.8° and 56.1° and the decrease of the diffraction maximum at 40.5° in the annealed sample B. Also the two diffraction maxima at 73.7° and 87.7° vanished in sample B. The small diffraction maximum at 40.5° and the two missing ones at 73.7° and 87.7° in the annealed sample coincidence with the positions of the diffraction maxima expected for molybdenum according to appendix A.2 indicated in the fourth row.

Apparently the metallic molybdenum phase decreases dramatically during annealing. One possible explanation is that the surplus supply of selenium during annealing leads to a selenisation of the molybdenum substrate. This would give rise to Mo_xSe_y reflections in the diffraction pattern. To test this hypothesis the diffraction maxima of Mo_3Se and $MoSe_2$ are indicated in figure 6.5 . The third possible phase Mo_3Se_4 has a rhombic crystal structure, leading to many diffraction maxima which do not coincidence with the measured diffraction pattern and has been omitted in figure 6.5. Mo_3Se shows a weak diffraction maximum at 57.2°, the shoulder of one of the additional peaks in the annealed sample. However many diffraction maxima i.e. at 24.7°, 35.2°, 39.6°, 43.5°, 50.6°, 63.2°, 68.9°, 85.2° have no counterpart in the measured diffraction pattern, so that it seems unlikely that Mo_3Se is contained in the sample. $MoSe_2$ grows in a hexagonal structure consisting of layers of molybdenum and selenium. Its diffraction maxima at 31.4°, 55.9°, 56.9° and 57.8° match well with the additional diffraction maxima in the annealed sample. The main diffraction maxima at 31.4° and 55.9° corresponding to (1 0 0) and (1 1 0) planes, suggests a preferential growth direction with the $\vec{c}$-axis parallel to the sample surface. The $\vec{c}$-axis in a layered crystal is defined perpendicular to the layers of different elements. This orientation was previously observed in studies of the annealing behaviour of molybdenum [119]. The main diffraction maxima due to the film at 27.2°, 45.2°, 53.5°, 65.7°, 72.5° and 83.1° however, do not change significantly during annealing. The diffraction pattern of the annealed sample is slightly shifted to higher angles. Comparing the reference files for $Cu_2ZnSnSe_4$, Cu_2SnSe_3 and $ZnSe$ given in the first three rows, asserts that the positions of the main diffraction maxima of this three compounds differ only slightly. Therefore it is very difficult to distinguish the three phases in XRD measurements. On the first glance none of the three above mentioned phases can be confirmed or excluded.

To investigate the phases contained in the sample in more detail figure 6.6 shows a measurement with higher resolution for the main diffraction maximum at 27°. The black solid line represents sample A, the dashed red line sample B. In the three rows below the diffraction pattern, the positions of the diffraction maxima of $Cu_2ZnSnSe_4$, Cu_2SnSe_3 and $ZnSe$ according to the reference files are given. Sample A shows a diffraction peak at 27.2°, which consists of a peak and a shoulder around 27.27°. Sample B is slightly shifted to higher diffraction angles compared to sample A and slightly wider. The diffraction maximum does not show a shoulder at 27.2° as for sample A, but shows an additional broadening at 27.4°. The shoulder at 27.27° in sample A is most probably due to the $CuK_{\alpha 2}$ radiation contained additionally in the X-ray beam. Due to the larger width of the diffraction maximum in sample B the $CuK_{\alpha 2}$ radiation does not lead to a separate peak in this case. As

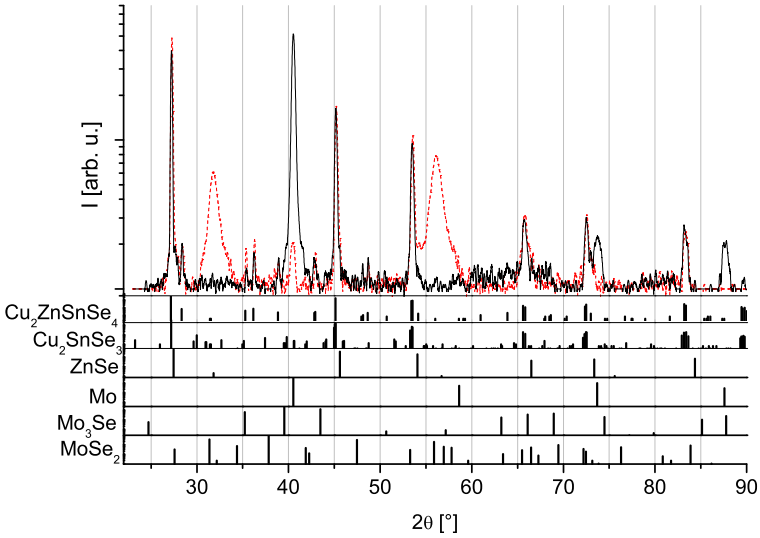

Figure 6.5: θ-2θ scan of sample A (continuous black line) and sample B (dashed red line). The rows below the diffraction pattern indicate the expected peak positions from the reference files according to appendix A.2 for $Cu_2ZnSnSe_4$, Cu_2SnSe_3, $ZnSe$, Mo, Mo_3Se and $MoSe_2$.

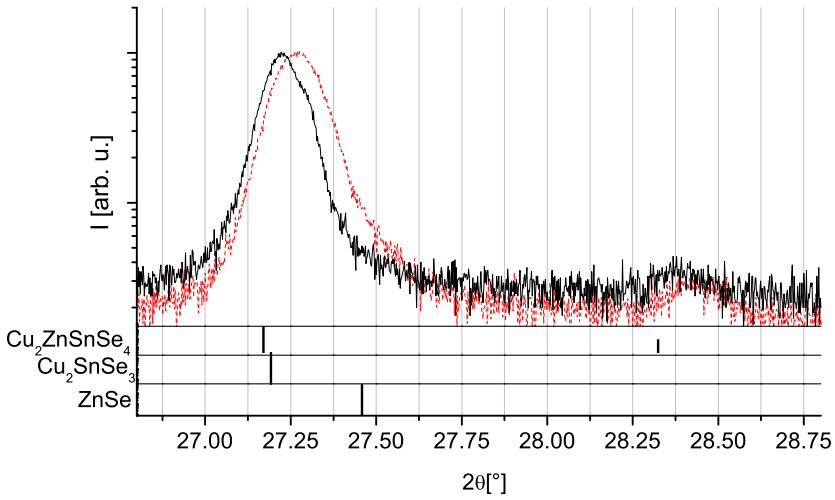

Figure 6.6: High resolution θ-2θ scan of the main diffraction maximum of sample A (continuous black line) and sample B (dashed red line).

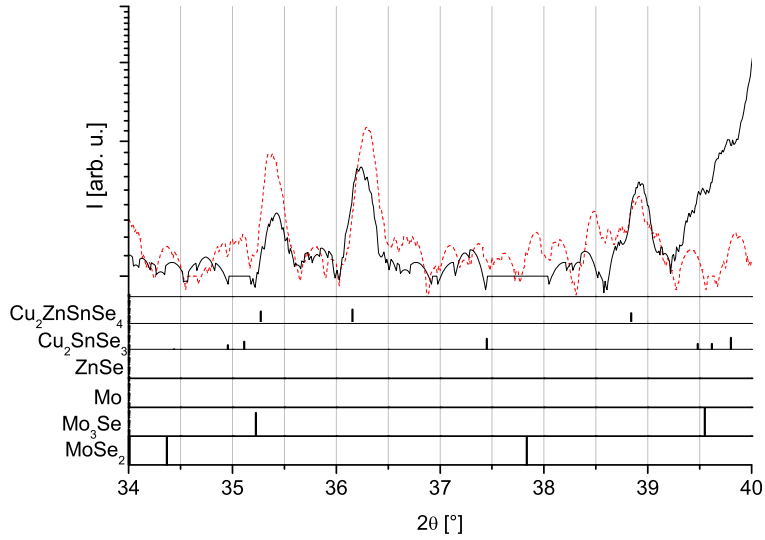

Figure 6.7: Enlarged detail of the θ-2θ scan in figure 6.5

[°]	A	B
28.4	0.15	0.16
35.4	0.24	0.21
36.2	0.23	0.22
38.9	0.18	0.23

Table 6.2: Full width half maximum of the diffraction maxima of samples A and B at 35.4 °, 36.2 ° and 38.9 °

the measurements for sample A and B are shifted for both peaks, at 27.2° and 28.4°, by the same amount, the shift is most probably due to an height alignment error. The height was adjusted on the molybdenum peak as described in chapter 4.2.1. However this leads to an error in the height of the sample, if the molybdenum layer is strained. Another reason for the shift could be the sulfur contaminations due to the annealing. Also for the measurement in figure 6.6 the resolution was not high enough to separate the three phases, therefore it is not possible to approve or exclude a phase from the peak at 27.2°. The shoulder at 27.4° may indicate a ZnSe phase in sample B, which would be in agreement with the additional observed photoluminescence peak at 1.15 eV. The small peak at 28.4° indicates a $Cu_2ZnSnSe_4$ phase. The shift between the small diffraction maxima at 28.4° and the position in the reference file might be due to sulfur cross contamination or a height error as discussed above.

Another effect of annealing might be a reduction of dislocations and other defects in the samples, thereby reducing the number of recombination centers. A reduction of the number of dislocations will be reflected in the width of the $Cu_2ZnSnSe_4$ reflections. Figure 6.7 shows a magnified detail of figure 6.5. It shows diffraction maxima at 35.4°, 36.3° and 38.9, which are unique to the $Cu_2ZnSnSe_4$ phase. At 38.9° also a diffraction maxima of the $CuSe_2$ phase can occur, however this phase is not stable above 342°C as described in chapter 5.1.1 and was not observed for the copper selenide samples investigated in chapter 5.3. Therefore it is unlikely to be observed here. Also no agreement with other copper selenides is found. The full width half maximum of the $Cu_2ZnSnSe_4$ diffraction peaks of the as deposited and annealed sample at 28.4° in figure 6.6 and 35.4°, 36.3° and 38.9° in figure 6.7 are displayed in table 6.2. No systematic change in the peak width due to annealing is visible. To conclude, both the as deposited as well as the annealed sample contain a $Cu_2ZnSnSe_4$ phase. Yet, it cannot be excluded that the samples contain also $ZnSe$ or Cu_2SnSe_3 phases. The main effect of annealing revealed by in X-ray diffraction is the selenization of the molybdenum substrate.

Secondary ion mass spectroscopy (SIMS) measurements To investigate the homogeneity of the samples through their depth secondary ion mass spectroscopy (SIMS) measurements as described in chap-

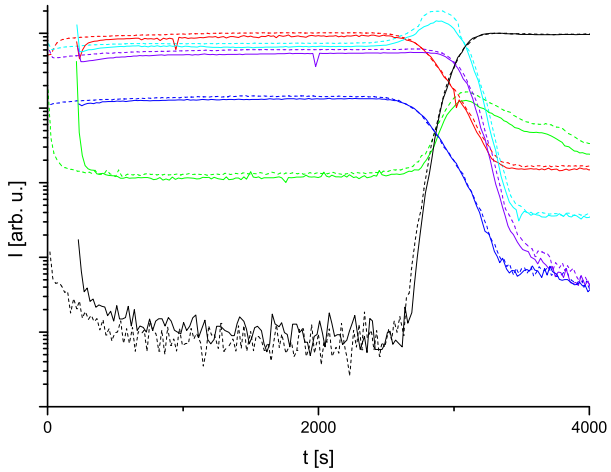

Figure 6.8: SIMS measurement results of sample A (solid line) and sample B (dashed line). The intensities of elements are indicated as follows: copper (red),zinc (light blue), tin (blue), selenium (violet), molybdenum (black) and sodium (light green).

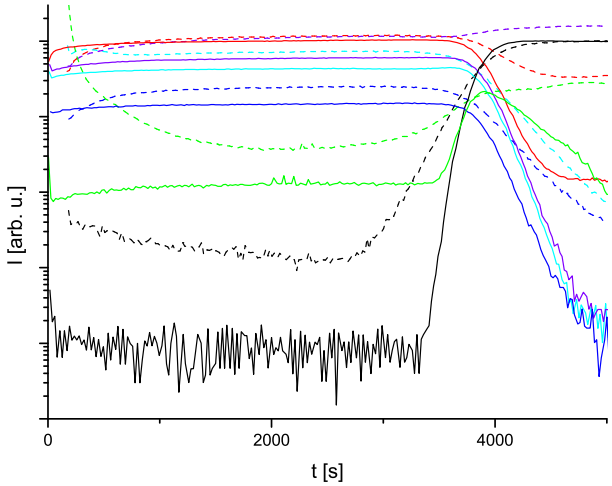

Figure 6.9: SIMS measurement results of sample C (solid line) and sample D (dashed line). The intensities of elements are indicated as follows: copper (red),zinc (light blue), tin (blue), selenium (violet), molybdenum (black) and sodium (light green).

ter 4.5 (p.23) are performed. Figure 6.8 shows the measured intensities for the different elements as a function of sputtering time for the as deposited sample A and the annealed sample B. To characterize the kesterite layer the elements copper (red), zinc (light blue), tin (blue) and selenium (violet) are measured. To determine the thickness of the sample additionally molybdenum (black) and sodium (light green) are monitored. To be able to compare the two measurements the intensities were normalised on the molybdenum signal and the time scale is shifted, so that the molybdenum back contact is reached at the same time. Therefore the signals for sample A rises about 200 s later than for sample B, which is most probably related to an increase in roughness of sample B during annealing. The overall element distribution for the two samples is very similar. Both show an homogeneous copper, tin and selenium content over the whole thickness of the kesterite layer. The zinc signal is constant over most of the layer thickness, too, but shows a peak shortly before the molybdenum signal rises. The zinc and selenium signals decrease later than the copper and the tin signal. This may point, together with the rise in the zinc signal close to the molybdenum substrate, to a ZnSe layer at the interface of the molybdenum back contact.

The very similar slope of the decreasing selenium signal for samples A and B is unexpected as from the XRD measurements described above, I would expect to see rather $MoSe_2$ than Mo for the annealed sample in the SIMS measurement.

Figure 6.9 shows SIMS measurements for sample C and D. Sample C shows a homogeneous distribution of the elements over the whole sample thickness. In comparison to sample C, sample D shows a slight increase in zinc content at the sample surface and an increase in the selenium signal at the molybdenum interface. Also the sodium distribution seems to have changed during annealing. The slight increase in zinc content at the sample surface points to a thin ZnSe layer on top of the sample, which would be in agreement, with the additional $ZnSe$ peak observed in the photoluminescence measurements. The increase in the selenium signal at the molybdenum interface is most probably due to $MoSe_2$, as one would expect for an annealed sample from the XRD measurements.

Comparing the samples A/B to the samples C/D, one difference is the zinc signal close to the molybdenum interface. It results most probably due to the different growth temperatures of the two samples: the samples A/B were grown at 390°C substrate temperature, whereas samples C/D were grown at 350°C. Redinger, as well as Ahn, report in [68] and [58] a formation of a zinc selenide layer on the molybdenum interface at growth temperatures above 350°C. Another difference for the sample pair C/D compared to the sample pair A/B discussed above, is the increase in the Se signal for the annealed sample D, when the Mo substrate is reached. As stated

above it is rather surprising, that sample B does not show an increase in the selenium signal at the molybdenum interface, as the XRD measurements showed the formation of a $MoSe_2$ phase. Additionally the Na distribution in the sample seems to change during annealing as measured for sample D, whereas it does not change according to the measurement on sample B. The behaviour of sample B according to this SIMS measurement is rather surprising and at the moment not yet understood.

Discussion SIMS measurements revealed the layered structure of samples A, B and D, this is a $ZnSe$ layer between the absorber layer and the molybdenum substrate in sample A and B and a $ZnSe$ layer on top of sample D. One now might speculate about the shifts of the photoluminescence peak position observed in figure 6.4.

EDX measurements at 20kV probe mainly the first 400 nm of the sample, but a small part of the signal results also from the area close to the molybdenum back contact. Therefore the EDX values for sample A indicate the zinc content of the absorber layer, but also include some contribution of the $ZnSe$ layer close to the molybdenum substrate. Therefore the actual zinc content in the absorber layer will be smaller than the values indicated in table 6.1 and sample A should be stoichiometric. During annealing sample B and D become more zinc rich, an effect which might be overestimated in the EDX measurements due to the formation of a $ZnSe$ phase on top of the sample, as observed in SIMS measurements for sample D. The $ZnSe$ phase might be formed by the decomposition of $Cu_2ZnSnSe_4$ and the loss of copper and tin. For sample B an additional possibility would be the diffusion of zinc from the $ZnSe$ layer at the back contact to the sample surface. Sample C is slightly zinc rich from the beginning. Sample E is stoichiometric and its annealed counterpart is zinc poor. The photoluminescence peaks of the sample pair A/B shift from higher energies to lower energies, whereas the positions of the photoluminescence peaks of the other two pairs remain approximately constant. So one may speculate if the shift of the photoluminescence peaks is related to the zinc content: for stoichiometric or zinc poor conditions the photoluminescence peak is at higher energies (samples A, E, F), whereas for zinc rich conditions the peak shifts to lower energies (samples B,C,D). The small blue shift of sample D might be explained by sulphur contamination during annealing.

Conclusion An increase of the photoluminescence signal due to annealing is observed, which points to a reduction of non radiative recombination centres. No systematic change in the width of the diffraction maxima is observed, therefore no change in the density of dislocations could be confirmed. So the annealing probably reduced the number of point defects acting as recombination centres. Also no change in the phases contained in the samples could be detected. SIMS measurements revealed a ZnSe layer between the absorber layer and the molybdenum back contact for samples A and B and a thin $ZnSe$ layer on top of sample D. Slightly different energy positions of the photoluminescence peaks observed for the different samples might be connected to different zinc and copper contents. After annealing an additional photoluminescence peak around 1.15 eV appeared, which can be assigned to defect related transitions in ZnSe. In samples B and D, the occurrence of the additional peak, might be explained by a decomposition of $Cu_2ZnSnSe_4$ at the surface of the sample, resulting in copper loss and an increase of the ZnSe phase. In sample B also zinc diffusion from the $ZnSe$ back contact might have contributed to the formation of the $ZnSe$ phase at the surface. In sample F the zinc loss or copper diffusion during annealing , might have introduced additional defect states in the $ZnSe$ phase.

6.2 Characterisation by Photoluminescence measurements

In the following section the temperature and intensity dependence of samples E/F as examples for as deposited and annealed copper rich samples and sample B as an example for a copper poor sample shall be discussed. However, as discussed in the previous sections copper rich and poor correspond to the composition of the whole sample, including additional secondary phases and thus to the growth conditions and not necessarily to the composition of the $Cu_2ZnSnSe_4$ phase. Sample D is similar to sample B and will not be discussed separately. The PL signal of the as deposited samples A and C was to low to investigate their temperature or intensity dependent behaviour.

Shape of the measured photoluminescence peaks Figures 6.10, 6.12 and 6.14 show the photoluminescence spectra of samples A, E and F mea-

sured at 300 mW excitation power and 10 K. For all three samples wide asymmetric peaks are observed. Similar results were also reported in literature [58]. To determine the position of maximum intensity of the peaks, Gaussian distributions are fitted to the measurements. Figure 6.10 shows in red the fit of one Gaussian distribution to the photoluminescence spectrum of sample B measured at 300 mW. The overall shape of the peak is Gaussian, however the low energy slope of the peak decreases slower than the Gaussian distribution and on the high energy side there seems to be an additional shoulder. Figure 6.11 shows for comparison a spectrum of sample B measured at 50 mW. Here the low energy side of the peak is well described by the Gaussian distribution indicated by the red line, whereas again on the high energy side of the peak, a second narrow peak may be observed. To include the possible second higher energy peak , fits with two Gaussian distributions are performed. The fit with two Gaussian distributions is indicated by the dark blue dashed line, the contributing single Gaussians are given by the light blue dotted lines. The peak positions and widths according to the different fits are given in table 6.3. For the measurement at 300 mW in figure 6.10 the measured peak is well described by the fit with 2 Gaussian distributions. However measurements excited with an excitation power below 125 mW turned out to be better described by a fit with one Gaussian distribution. For example in figure 6.11 the fit with two Gaussian distributions overestimates the high energy side of the peak. Subsequently the positions of the peak maximum determined by both fits will be compared.

$\mathbf{E_{max}}$	**width**	$\mathbf{E_{max}}$	**width**
B			
0.89	0.084	-	-
0.88	0.098	0.91	0.036
E			
0.95	0.070	-	-
F			
0.96	0.06	-	-

Table 6.3: Maximum position and peak width for samples B, E and F determined by fits to Gaussian distributions.

Figure 6.12 depicts the spectrum of sample E measured at 300 mW excitation power and a Gaussian distribution fitted to the data. The peak is well described by a Gaussian distribution with a maximum at 0.95 eV and a width of 70 meV, but shows an ad-

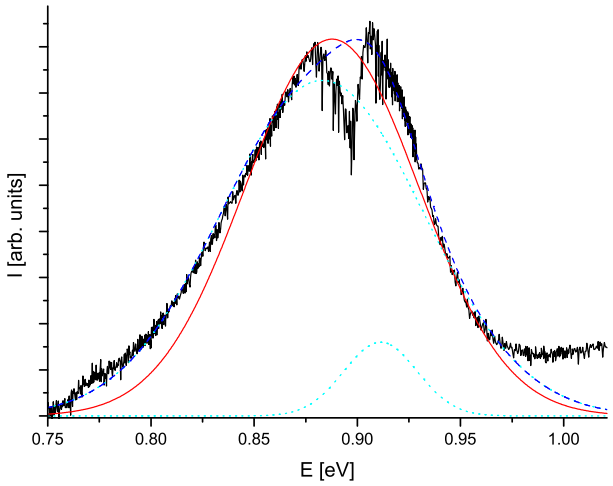

Figure 6.10: Sample B: Fit of one (continuous red line) and two (dashed dark blue line) Gaussian distribution to the photoluminescence peak measured at 300 mW excitation power. The light blue dotted lines indicate the shapes of the two single Gaussian distributions, which add up to the fit indicated by the dark blue line.

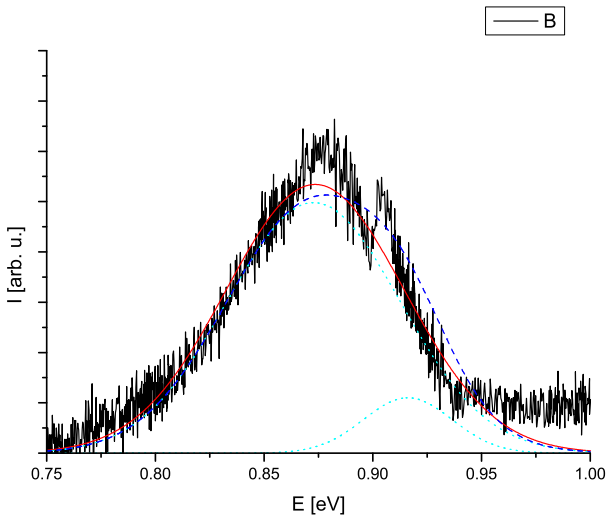

Figure 6.11: Sample B: Fit of one (continuous red line) and two (dashed dark blue line) Gaussian distributions to the photoluminescence peak measured at 50 mW excitation power. The light blue dotted lines indicate the shapes of the two single Gaussian distributions, which add up to the fit indicated by the dark blue line.

ditional tail on the low energy side of the spectrum. Attempts to fit the tail by a second Gaussian distribution are hampered by the water absorption line around 0.9 eV. Figure 6.13 depicts the spectra of sample E measured at excitation powers between 50 mW and 500 mW. Their shape remains Gaussian, as well as the maximum position appears independent of excitation power and the proportion of the tail to the peak maximum is constant. However with increasing excitation power, the photoluminescence peak becomes wider on the high energy side.

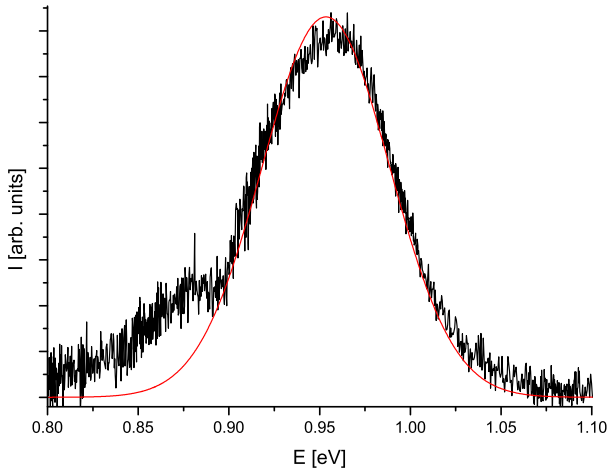

Figure 6.12: Sample E: Fit of one Gaussian distribution (continuous red line) to the photoluminescence peak measured at 300 mW excitation power.

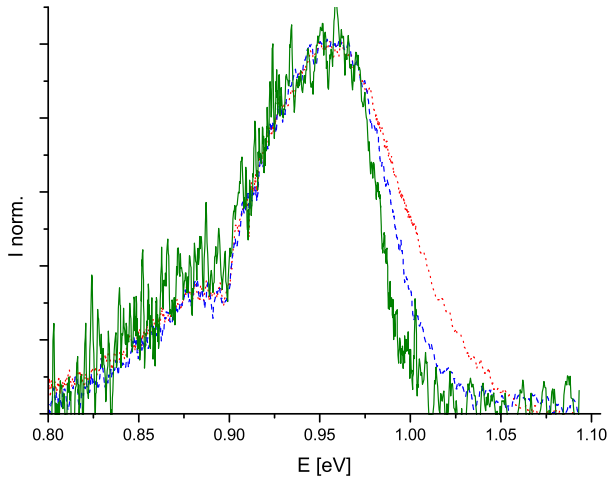

Figure 6.13: Sample E: Photoluminescence spectra at different excitation powers: 500 mW (red dotted line), 150 mW (blue dashed line) and 50 mW (green continuous line).

Also sample F can be described by one Gaussian distribution with a maximum at 0.96 eV and a width of 60 meV and a tail as can be seen in figure 6.14. However due to the second peak at 1.15 eV it turned out, that especially for the spectra measured at low excitation intensity due to the higher background compared to the signal, it was more difficult to get good fits. If a satisfactory fit was reached, was strongly depended on the chosen starting values. Spectra measured at different excitation powers are compared in figure 6.15. It shows the same trend as for sample E: the shape of the measured spectra remains Gaussian and the position and the proportion between tail and peak maximum remains constant independent of excitation power. As for sample E, the photoluminescence peak becomes wider with increasing excitation intensity. For low excitation powers, one may speculate if the main peak separates into a peak and a shoulder around 0.93 eV.

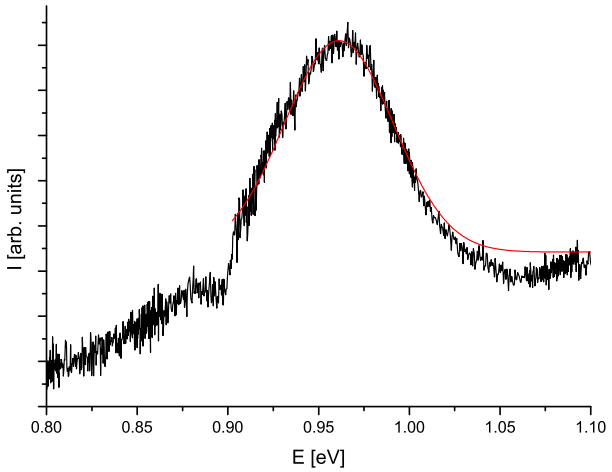

Figure 6.14: Sample F: Fit of one Gaussian distribution (continuous red line) to the photoluminescence peak measured at 300 mW excitation power.

To compare the shape of the peak for the different samples figures 6.16 and 6.17 show the spectra of samples B, E and F dependent on their distance to the respective maximum at 300 mW and 50 mW excitation power. The spectra measured at 300 mW excitation power have a similar shape for all three samples. Sample B seems to be slightly wider than samples E and F. For lower excitation power samples E and F show a more pronounced tail on the low energy slope of the peak than sample B. A stronger tail might be associated with a higher degree of compensation.

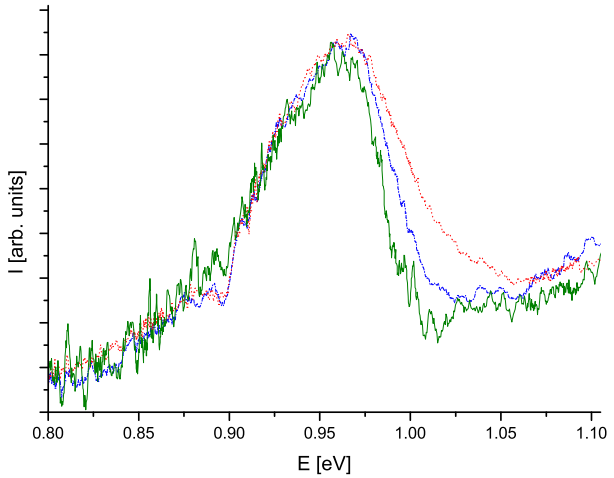

Figure 6.15: Sample F: Photoluminescence spectra at different excitation powers: 300 mW (red dotted line), 100 mW (blue dashed line) and 30 mW (green continuous line)

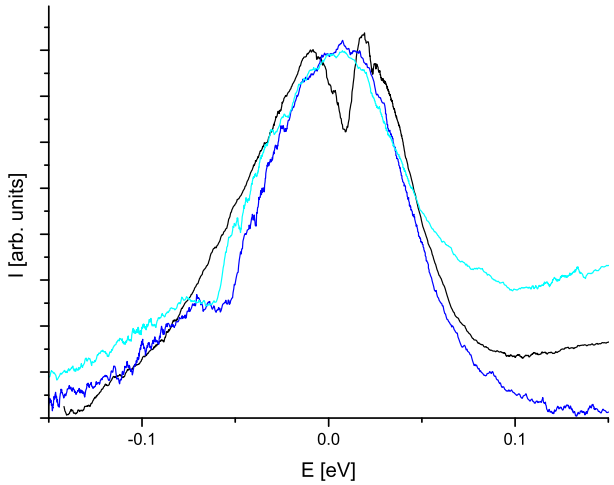

Figure 6.16: Comparison of the shape of the spectra of samples B (black), E (dark blue) and F (light blue). Plotted is the PL signal normalised to its maximum over the distance to its maximum position. The measurements are at 10 K and 300 mW excitation power.

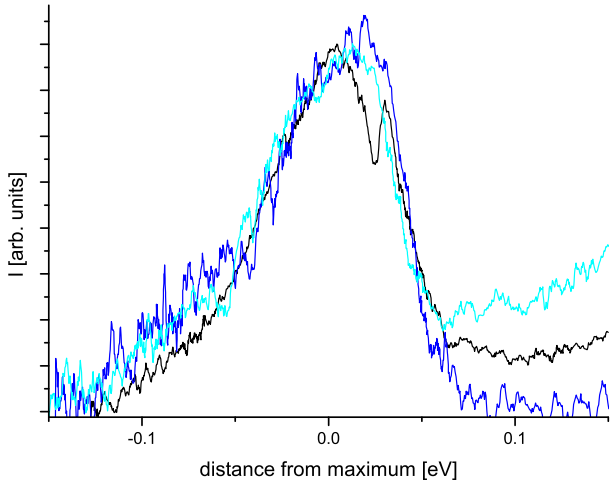

Figure 6.17: Comparison of the shape of the spectra of samples B (black), E (dark blue) and F (light blue). Plotted is the PL signal normalised to its maximum over the distance to its maximum position. The measurements are at 10 K and 50 mW excitation power.

Excitation intensity dependence To determine the kind of transition, which is the origin of the observed photoluminescence peaks, subsequently the excitation intensity dependence will be discussed.

Figures 6.18 and 6.19 show the dependence of the photoluminescence intensity on the excitation intensity. The maximum position was determined by different methods: fits with one Gaussian distribution are indicated by stars, fits by two Gaussian distributions are represented by circles and for comparison the position of maximum counts is indicated by squares. The slope of the line in the double logarithmic plots in figures 6.18 and 6.19 corresponds to the exponent of the power law $I_{PL} \sim I_{ex}^{k}$, which relates the photoluminescence intensity to the excitation intensity as introduced in section 2.2.1. The k value for sample E and F equals 0.8, whereas the k value for sample B is 0.9. So for both, the copper rich samples E and F, as well as the zinc rich sample B k is smaller than 1, which points to a defect related transition.

Figure 6.20 depicts the dependence of the maximum position of the photoluminescence peak of sample B on excitation intensity. Depending on the method used to determine the maximum position, its value varies by about 10 meV. Common to the maximum values determined by either of the three methods is a shift to higher energies with increasing excitation intensity of about $20\,\frac{meV}{dec}$. A shift to higher energies with increasing excitation intensity of more than $10\,\frac{meV}{dec}$ is a characteristic feature of

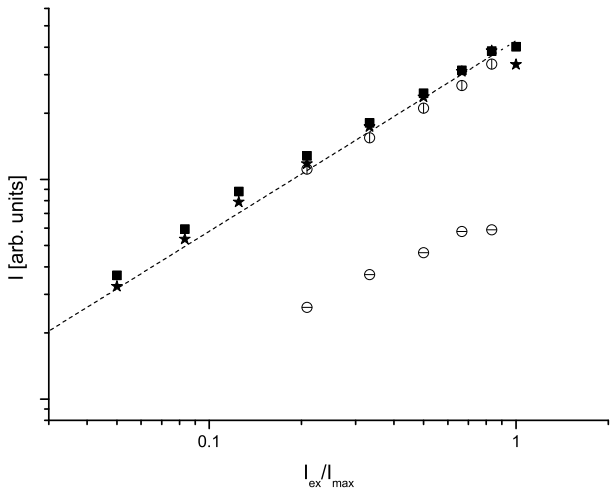

Figure 6.18: Sample B: Dependence of photoluminescence intensity on excitation intensity determined by different methods: fit with one Gaussian distributions (stars), fits with 2 Gaussian distributions (circles) and the position of maximum counts (squares).

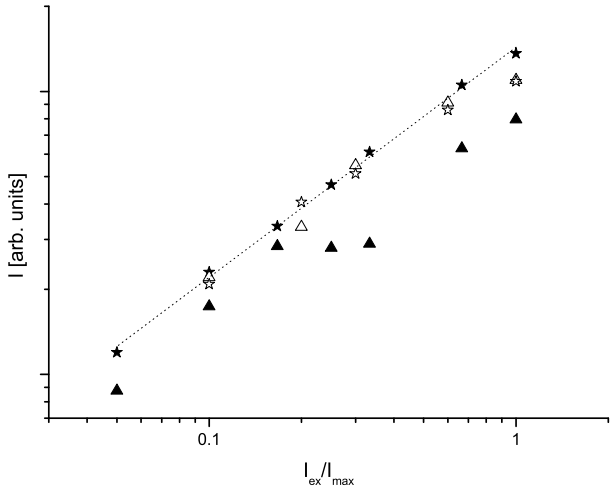

Figure 6.19: Dependence of the photoluminescence intensity on excitation intensity of sample E (empty symbols) and F (filled symbols) dependent on excitation intensity determined by different methods: fit with one Gaussian distributions (triangles) and the position of maximum counts (stars).

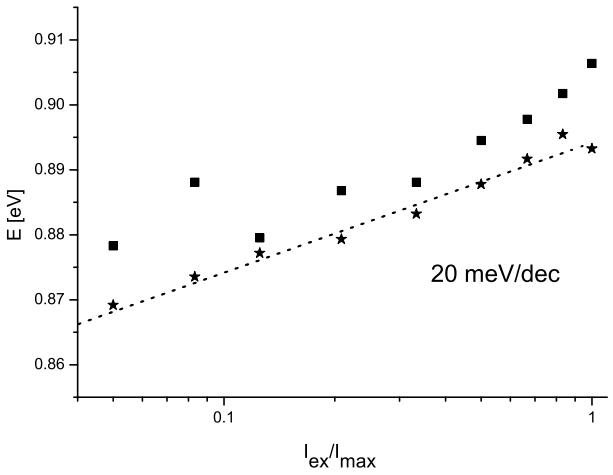

Figure 6.20: Sample B: Dependence of the peak position dependent on excitation intensity determined by different methods: fit with one Gaussian distributions (stars), fits with 2 Gaussian distributions (circles) and the position of maximum counts (squares).

fluctuating electrostatic potentials. With higher excitation intensity the number of free charge carries increases, which increases the screening of the electrostatic field and therefore reduces the bending of the bands. This results in a shift of the transition energies to higher energy values.

Figure 6.21 represents the dependence of the peak position on excitation intensity for the copper rich samples E and F. Again the maximum peak position was determined by different methods: the position of maximum counts is indicated by stars, whilst triangles show the maximum position determined by a fit to one Gaussian distribution. The open symbols represent sample E, whereas the filled symbols represent sample F. Again the different methods result in a slight difference in the energy position of 5 meV. Interestingly the position of the peak maximum seems to be independent of excitation intensity. For sample E the values scatter around 0.95 eV determined from Gaussian fits and 0.96 eV determined from the position of maximum counts. For sample F the position of maximum counts seems to shift about to $2\frac{meV}{dec}$ to higher energies taking into account the first three and the fifth point, however considering all points and the width of the peak of about $60\,meV$ the shift seems to be negligible. The peak position determined by Gaussian fits scatters around $0.96\,eV$ This matches with figures 6.13 and 6.15, where also no shift of the peak position dependent on excitation intensity was

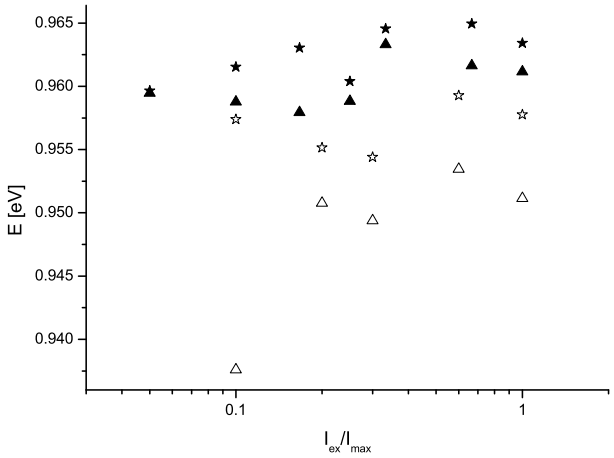

Figure 6.21: Dependence of the peak position of sample E (empty symbols) and F (filled symbols) on excitation intensity determined by different methods: fit with one Gaussian distributions (triangles) and the position of maximum counts (stars).

observed. This is an interesting result, as one would expect for wide asymmetric peaks, suspecting electrostatic potential fluctuations, a shift of tens of meV per decade as for sample B. Another explanation for the wide asymmetric shape of the peaks could be, that the width of the peak is due to band gap fluctuations. However this still does not explain the missing shift. As the measurements shown in figures 6.13 and 6.20 are at 10 K, and $k \leq 1$ the transitions are defect related. At low temperatures in a material, which contains donor as well as acceptor states, one would expect to observe donor-acceptor transitions, which on their part, would lead to a shift of the peak position of several meV per decade to higher energies with increasing excitation intensity. Yet, as the peaks are $\sim 60\,meV$ wide, a small shift of several meV might not be resolvable.

Temperature dependence Figures 6.22, 6.23 and 6.24 show the spectra of samples B, E and F measured at temperatures between 10 K and 300 K. The maximum position determined by a Gaussian fit and the position of maximum counts are indicated in figures 6.25, 6.26 and 6.27 by triangles and stars, respectively. For sample B the maximum position determined from Gauss fits shows in figure 6.25 a small shift to higher energies of about 10 meV over the measured temperature range, which corresponds to a shift of 0.06 $\frac{meV}{K}$ with increasing temperature up to 200 K followed by a slight shift to lower energies. Also, the

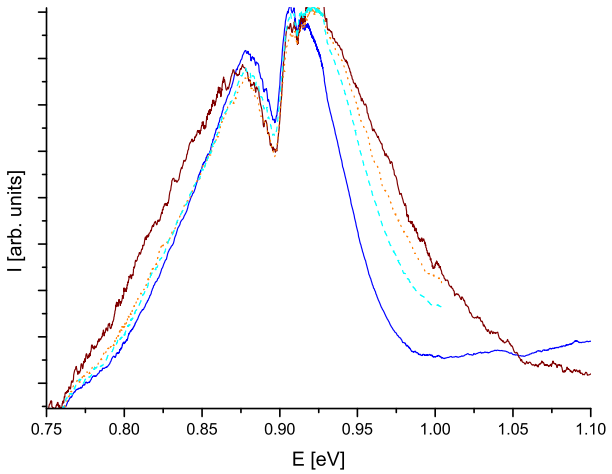

Figure 6.22: Normalised photoluminescence spectra of sample B dependent on temperature: 10 K (blue solid line), 105 K (light blue dashed line), 200 K (orange dotted line) and 300 K (dark red solid line) measured at 500 mW excitation power.

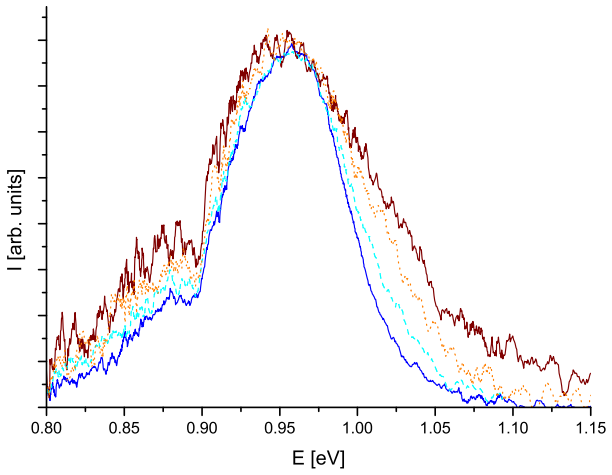

Figure 6.23: Photoluminescence spectra of sample E dependent on temperature: 10 K (blue solid line), 95 K (light blue dashed line), 200 K (orange dotted line) and 300 K (dark red solid line) measured at 300 mW excitation power.

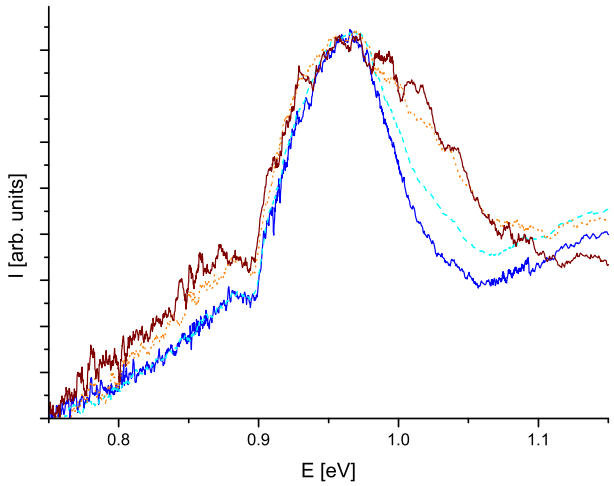

Figure 6.24: Photoluminescence spectra of sample F dependent on temperature: 10 K (blue solid line), 95 K (light blue dashed line), 250 K (orange dotted line) and 300 K (dark red solid line) measured at 300 mW excitation power.

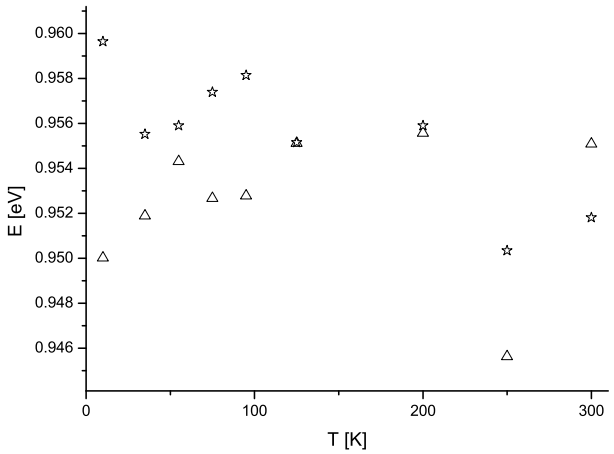

Figure 6.26: Dependence of the peak position of sample E on temperature determined by different methods: fit with one Gaussian distributions (triangles) and the position of maximum counts (stars).

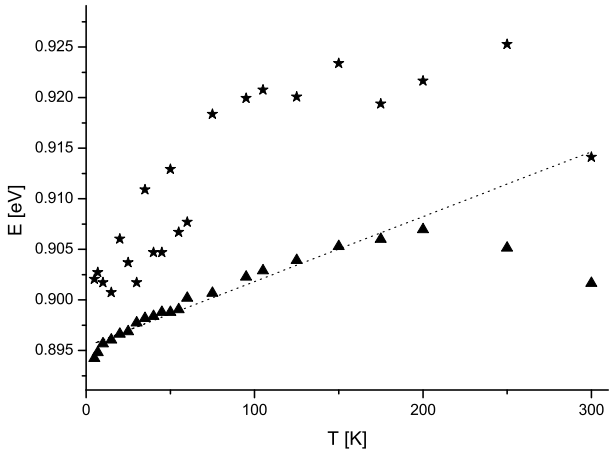

Figure 6.25: Dependence of the peak position of sample B on temperature determined by different methods: fit with one Gaussian distributions (triangles) and the position of maximum counts (stars).

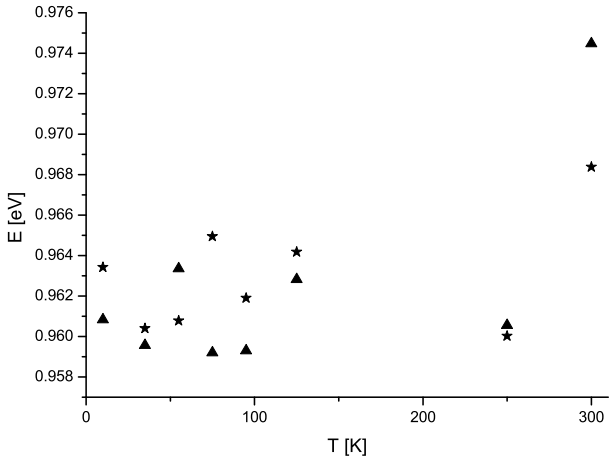

Figure 6.27: Dependence of the peak position of sample F on temperature determined by different methods: fit with one Gaussian distributions (triangles) and the position of maximum counts (stars).

position of maximum counts shows the same trend, however the values determined in this way are more scattered. This is due to the water absorption line, which is close to the maximum of the peak. Therefore, the position of maximum counts is influenced by the interpolation chosen for the water absorption line.

For defect related transitions in a compensated semiconductor, one would expect a shift to lower energies of the maximum position of the observed photoluminescence peak, as the increase in temperature allows the charge carriers to reach the global maximum of the valence and global minimum of the conduction band. This shift of the peak to lower energies is followed by a shift to higher energies, since the increasing number of charge carriers with increasing temperature causes a better screening of the electrostatic potentials as described in section 2.2.2 (p. 10). The result shown in figure 6.25 can be understood, taking into account, that the measurement is at 500 mW excitation power. Therefore already a lot of free charge carriers are created, which contribute to the partial screening of the electrostatic potentials. Thus, due to the weak bending of the bands, already at low temperatures the charge carriers are able to reach the global maximum of the valence, as well as the global minimum of the conduction band. Hence no shift of the peak maximum to lower energies is observed. A continuing increase in temperature weakens the bending of the bands further, resulting in a shift of the maximum position of the observed photoluminescence peak to higher energies. Starting from 200 K there are enough free charge carriers to screen the electrostatic potentials completely and sample B shows a shift of the maximum position of the photoluminescence peak to lower energies, as one would expect for a free-to-bound transition in a non compensated semiconductor.

Figures 6.23 and 6.24 show the position of the peak maximum dependent on temperature for samples E and F. For both samples the values for the maximum position of the peak scatter around a constant value with increasing temperature. For sample F a higher energy value for the maximum position at 300 K is determined compared to the measurements at lower temperatures. However this is an artefact, due to an additional high energy shoulder, which merges with the maximum of the main peak at 300 K as can be seen in figure 6.24. The missing of a shift of the maximum position of the photoluminescence peak with increasing temperature is surprising. As explained above, for a free-to-bound transition in an uncompensated semiconductor one expects a shift to lower energy values with augmenting temperature , parallel to the decrease of the band gap, which is observed for most of the semiconductors. For a compensated semiconductor, normally a shift of the peak to lower energies followed by a shift to higher energies is observed. Together with the results from the intensity dependent measurements, fluctuating potentials as source of the broad peaks can therefore be excluded. At this point, the behaviour of the samples E and F is not understood, but the missing shift of the maximum position with intensity and especially with temperature is an interesting observation, which deserves to be investigated in more detail. A possible source of the photoluminescence peaks observed in samples E and F might be a wide distribution of deep defects, whose energy position does not shift with the bands.

Conclusion

For all six samples wide asymmetric photoluminescence peaks are observed. The photoluminescence intensity can be increased by annealing, which may result in a reduction of defects acting as recombination centres. The energy position and its change with annealing of the observed photoluminescence peaks varies for the different investigated samples, which might be related to their different copper and zinc content. The zinc rich sample B shows a temperature and excitation intensity dependent behaviour corresponding to a semiconductor dominated by fluctuating electrostatic potentials. The copper rich samples E and F show neither a shift with increasing excitation intensity, nor with temperature. This excludes fluctuating electrostatic potentials as a source of the broadening of the peaks. A possible explanation could be a wide distribution of deep defects, whose energy position does not shift with the bands.

Chapter 7

Symmetry of Defects in Chalcopyrites

In the following chapter the symmetries of the intrinsic defects in the chalcopyrites $CuInSe_2$ and $CuGaSe_2$ shall be investigated. Defects can be described in two limiting cases: either as shallow defects, assuming the symmetry of their closest band, or as deep, localized defects, which will adopt the site symmetry of their respective lattice site. From the lattice site, being either on the metal or chalcogen sublattice, the chemical nature of the defect can be deduced. In order to probe the symmetry of the defects, polarisation dependent photoluminescence measurements are used. The allowed polarisation for defect related photoluminescence transitions can be deduced from group theoretical considerations. Therefore, in the first part of this chapter, a short introduction to group theory is given. In the second part, the symmetry of the electronic bands in the chalcopyrite will be presented. The two models to describe defects will be introduced in greater detail in the third part. Finally, in the fourth part, the results of photoluminescence measurements to determine the symmetry of the defects in $CuInSe_2$ and $CuGaSe_2$ will be given.

7.1 Group theory

7.1.1 Symmetries and groups

A symmetry transformation, for example a reflection in a mirror plane or a rotation about a symmetry axis, is defined as a transformation which does not change the appearance of the object it is applied to. To illustrate this, the chalcopyrite crystal is taken as an example. Its shape is shown in figure 7.1. Following the explanations in [47],[121] the following symmetry operations transfer it into a congruent figure:

- a rotation of 90° anticlockwise about the [001] axis followed by a reflection at the center of inversion.
- a rotation of 180° about the [001] axis.
- two fold rotations about the [100] and [010] axes indicated by the blue lines
- reflections in the (110) and (1-10) planes

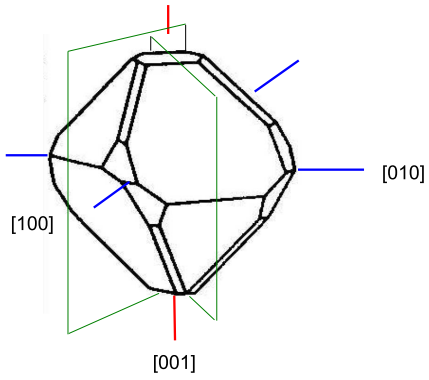

Figure 7.1: Crystal morphology of a chalcopyrite crystal [120]. The red line indicates the S_4 rotation reflection axis, the blue lines the C_2 rotation axes perpendicular to the S_4 axis and in green, the σ_d mirror planes.

Two commonly used ways of labeling symmetry operations exist: the Schönfließ notation and the international notation. In the Schönfließ notation [47], rotations are labeled C_n, n indicating a n-fold rotation. σ indicates a reflection, i, an inversion and S_n a rotation around a n-fold axis followed by a reflection on a plane perpendicular to this rotation axis. E indicates the unity operation. In the international notation [122], n indicates a n-fold rotation, with a minus sign in front or a slash above the "n" indicating a rotation-inversion operation and m points to a mirror plane. The symmetry operations of the above

example are thus C_2, σ and S_4 in the Schönfließ notation and 2, m and $\bar{4}$ in the international notation. The symmetry operations introduced form together a mathematical group. A mathematical group consists of elements which are connected by an defined operation. This relation is called a multiplication and written as $a \otimes b = c$. The operation must have the following properties [47]:

- Closure: The result, c, of the operation $a \otimes b = c$ must be a member of the group for any element a and b.
- Associativity: $(a \otimes b) \otimes c = a \otimes (b \otimes c)$ must hold for all elements of the group.
- Identity: The group must contain an identity element, e, for which holds $e \otimes a = a$ for all elements in the group.
- Inverse element: there must be an element a^{-1}, which fulfills $a^{-1} \otimes a = e$ for all members of the group.

The number of symmetry operations in a group is called the order of a group. The different symmetry operations can be represented by matrices which constitute the representation of the group. The choice of representation is not unique and the different matrices representing the same symmetry operation can be converted into each other by similarity transformations. One can distinguish between reducible and irreducible representations. The dimension of a reducible representation can still be reduced by changing it into block form, whereas in the irreducible representation the number of rows or columns already reflects the rang of the matrix. The matrices can be arranged into sets of equivalent symmetry operations, so called classes. For example, rotations about the same angle on equivalent axes belong to one class. The members of a class are commutative and have the same character, this is equal values for their traces. There exists as many irreducible representations as there are classes in the group. The order of the group g, the number of classes ν and the dimensions of the corresponding representations are related by the following formula [123]:

$$(\chi_E^1)^2 + (\chi_E^2)^2 + ... + (\chi_E^\nu)^2 = g \qquad (7.1)$$

where χ_E^ν represents the character of the unity matrix and is therefore equal to the dimension of the ν. class. The D_{2d} group, for example, has an order of 8 and consists of 5 classes. From equation 7.1 follows therefore

$$8 = 1^2 + 1^2 + 1^2 + 1^2 + 2^2. \qquad (7.2)$$

That is four classes are of dimension one and one class is of dimension two. The most important group information is compiled in character tables as shown in appendix A.4: the first line gives the symmetry elements and the first column indicates the different representations. The table displays the character for each symmetry element, in the different representations belonging to the group.

7.1.2 Symmetries of crystals

The symmetry operations introduced in the preceding section always leave at least one point fixed. This is characteristic for point groups. Point groups are used, for example, to describe the symmetry of molecules. Crystals are additionally characterised by their translational symmetry. Thus, a crystal can be thought of as a repetition of identical building blocks called crystallographic unit cells. The additional translational symmetry reduces the possible number of point groups for a crystal to 32, which are referred to as crystallographic point groups. The crystallographic point group of a crystal is reflected in its morphology, therefore the crystallographic point groups are often referred to as crystal classes [122]. Often it is more convenient to describe a crystal not by a Cartesian coordinate system, but by a coordinate system reflecting its symmetry. In doing so, one can assign the 32 crystal classes to the seven crystal systems: triclinic, monoclinic, orthorhombic, tetragonal, trigonal, hexagonal or cubic. However, choosing the coordinate axis according to the symmetry of the crystal does not necessarily lead to primitive unit cells. If the centring of the unit cell, this is whether it is primitive, body or face centred, is taken into account, results in the 14 Bravais lattices [124]. The highest symmetry for each Bravais lattice applies to the mathematical point lattice with which we have dealt so far and which is equivalent to a crystal consisting of only one kind of atoms. To pass to the more general case of a polyatomic crystal one introduces a basis. A basis can consist of several equal or different atoms and is connected to each mathematical lattice point. A lattice with a polyatomic basis often has a lower symmetry than the mathematical point lattice. Taking the chalcopyrite structure as depicted in figure 2.1 as an example, the mathematical point lattice

is tetragonal body centred and its unit cell contains two lattice points. The $CuInSe_2$ crystallographic unit cell consists of four formula units of $CuInSe_2$: four copper, four indium and eight selenium atoms. Therefore to each lattice point a basis consisting of two formula units of $CuInSe_2$ is connected.

Space groups To describe the crystal structure, not only the point groups compatible with translational symmetry, but also the translational symmetry itself, has to be taken into account. The combined operation of a rotation and a translation on a point $\vec{r}$ can be represented by $\vec{r}' = M\vec{r} + \vec{t}$, M being the matrix corresponding to the rotation and $\vec{t}$ the translation vector. Taking the translation symmetry into account generates two new symmetry elements, the screw axis and glide planes. Screw axis are axis about which a rotation followed by a translation leads to a congruent figure. In the Schönfließ notation, screw axis are referred to as C_n^k, indicating a rotation about a n-fold axis followed by a translation of k/n times the unit vector along the rotation axis. In the international notation n_m indicates a n-fold rotation, followed by a translation of $\frac{m}{n}$ times the lattice vector. Glide planes are reflections about planes followed by a translation parallel to the plane. Glide planes are indicated by σ^g in the Schönfließ notation. In the international notation a, b and c indicate a glide plane, involving a reflection followed by a translation of half a lattice vector parallel to the lattice directions a, b and c. The combination of rotations and translation gives rise to the 230 space groups.

Wyckoff positions The crystal lattice points, resulting from the connection of the basis to the mathematical lattice in a space group can be divided into sets of equal symmetry. This so called "crystallographic orbits" can be derived by applying the symmetry operations of the point group of the crystal to a point $\vec{r}$. Each crystal lattice point belonging to a specific crystallographic orbit can be reached from this starting lattice point $\vec{r}$ by the rotations and translations belonging to its site symmetry group. As there are indefinitely many possible starting points, $\vec{r_i}$, there exist an indefinite number of crystallographic orbits.

The crystallographic orbits with the same site symmetry and whose starting lattice points are related by the transformations belonging to the respective site symmetry group can be grouped into the so called Wyckoff positions [125]. Two different Wyckoff positions with the same site symmetry, but which cannot be transferred into each other by the symmetry operations of the site symmetry group belong to a Wyckoff set. The Wyckoff positions of the space group $I\bar{4}2d$ are shown in table 7.1. The space group $I\bar{4}2d$ contains five different Wyckoff positions. The Wyckoff positions a and b together form a Wyckoff set and correspond to the Cu and In atoms in chalcopyrite, respectively. Both positions have $\bar{4}../S_4$ symmetry, where $\bar{4}..$ is the oriented site symmetry symbol. The dots indicate symmetry directions which do not contribute any symmetry element to the site symmetry group. The Wyckoff c position has $2../C_2$ symmetry with respect to the $\vec{c}$-axis and is not occupied in the chalcopyrite crystal. The Wyckoff d positions correspond to Se sites in the chalcopyrite and show $.2./C_2$ symmetry. General positions with site symmetry 1 are indicated by e.

Reciprocal space and Brillouin zones

As mentioned above, a crystal can be thought of as a repetition of building blocks called the crystallographic unit cell. As many physical properties are associated with the crystal structure, for example the electron density distribution, it is sufficient to restrict the discussion of physical properties to one unit cell and apply periodic boundary conditions. This leads to the introduction of reciprocal space: Originating from X-ray crystal structure analysis as detailed in [126] one finds that analysis is simplified by representing each reflex of parallel lattice planes by a vector, which points in the direction of their surface normal vector and having the inverse length of the distance between the lattice planes. The endpoints of these vectors constitute the reciprocal lattice. The reciprocal lattice is named after the reciprocal relationship between its basis vectors and the basis vectors of the real, direct lattice:

$$\vec{a}^* = 2\pi \cdot \frac{\vec{b} \times \vec{c}}{V} \qquad \vec{b}^* = 2\pi \cdot \frac{\vec{c} \times \vec{a}}{V} \qquad \vec{c}^* = 2\pi \cdot \frac{\vec{a} \times \vec{b}}{V} \tag{7.3}$$

where $\vec{a}, \vec{b}, \vec{c}$ are the basis vectors of the direct lattice, $\vec{a}^*, \vec{b}^*, \vec{c}^*$ the basis vectors of the reciprocal lattice and V the volume of the unit cell in real space. The transition from the direct crystal lattice to the reciprocal lattice in equation 7.3 corresponds to a Fourier transform. Hence, each point in reciprocal space represents a wave vector $\vec{k}$, which is a quantity proportional to momentum.

Multiplicity	**Wyckoff letter**	**Site symmetry**	**Coordinates** $(0,0,0)+(\frac{1}{2},\frac{1}{2},\frac{1}{2})$
16	e	1	(x,y,z), $(-x,-y,z)$, $(y,-x,-z)$, $(-y,x,-z)$, $(-x+\frac{1}{2},y,-z+\frac{3}{4})$, $(x+\frac{1}{2},-y,-z+\frac{3}{4})$, $(-y+\frac{1}{2},-x,-z+\frac{3}{4})$, $(y+\frac{1}{2},x,-z+\frac{3}{4})$
8	d	.2.	$(x,\frac{1}{4},\frac{1}{8})$ $(-x,\frac{3}{4},\frac{1}{8})$, $(\frac{1}{4}),x,\frac{7}{8})$ $(\frac{3}{4},x,\frac{7}{8})$
8	c	2..	$(0,0,z)$ $(0,0,-z)$ $(\frac{1}{2},0,-z+\frac{3}{4})$ $(\frac{1}{2},0,z+\frac{3}{4})$
4	b	-4..	$(0,0,\frac{1}{2})$ $(\frac{1}{2}),0,\frac{1}{4})$
4	a	-4..	$(0,0,0)$ $(\frac{1}{2},0,\frac{3}{4})$

Table 7.1: Wyckoff positions for space group $I\bar{4}2d$ according to [121].

Equivalent to the crystallographic unit cell in direct space is the Brillouin zone in reciprocal space. Both contain all necessary information to describe the crystal. The Brillouin zone of a crystal with a tetragonal body centred unit cell is shown in figure 7.2.

The special points in the Brillouin zone, these are the points with high symmetry, are labeled with letters. Those points which are within the Brillouin zone are named with capital greek letters, whereas capital latin letters denote points at the surface of the Brillouin zone. For instance, the centre of the Brillouin zone, which is equivalent to the point of highest symmetry, is labeled Γ. The [100] direction in real space corresponds in the Brillouin zone to the $\Gamma-\Delta-X$ direction, whereas the [001] direction is equal to $\Gamma-\Lambda-M$. However, care must be taken, as the labelling of special points may vary depending on the author.

As the starting point was the crystallographic unit cell belonging to a certain Bravais lattice, it follows that crystals with the same Bravais lattice will have the same Brillouin zone.

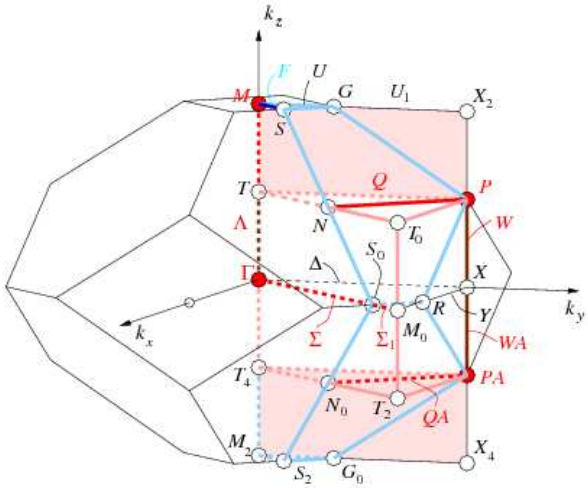

Figure 7.2: Brillouin zone of the space group $I\bar{4}2d$ according to [121].

7.1.3 Symmetry and electronic structure

The electronic structure of a crystal is described by its time independent Hamiltonian:

$$H = \frac{\hat{p}^2}{2m} + V(\vec{r}) \tag{7.4}$$

The potential $V(\vec{r})$ contains all the information about the crystal structure and its symmetry. If a system has a certain symmetry, this implies that its time independent Hamiltonian commutates with the symmetry operators. Therefore a common set of eigenvalues and eigenvectors corresponding to the Hamiltonian and the symmetry operators exists. The number of eigenvalues corresponds to the number of classes in the symmetry group. The number of eigenvectors corresponding to an eigenvalue is given by the dimension of the respective representation [47][127].

The most prominent symmetry of a crystal is its translational symmetry [47]. There is an easy way to construct wave functions which reflect the translational symmetry, this is by using so called Bloch functions. As discussed above, commutating operators have a common set of eigenfunctions, and therefore the eigenfunctions to the translation symmetry operator T can be used to construct a set of eigenfunctions for the Hamilton operator. The Bloch functions are defined as

$$\Phi_k(x) = e^{ikx} u_k(x) \tag{7.5}$$

where $u_k(x)$ is a periodic function with the periodicity of the crystal lattice. Thus a Bloch function is a plane wave, which is modulated by the periodicity of

the lattice. The eigenfunctions of the Hamilton can be expressed as a sum over Bloch functions:

$$\Phi(x) = \sum_k A_k \Phi_k(x) = \sum_k A_k e^{ikx} u_k(x) \qquad (7.6)$$

where the A_k are constants and the k are the wave vectors of the plane wave of the Bloch functions. Examples for wave functions reflecting the rotation symmetry of the Hamiltonian are given in the "basis" column in the point group tables. A plot of the energy eigenvalues over the wave vector k represents the electronic band structure of a semiconductor.

Spin-orbit interaction For heavier elements the interaction between electron spin and angular momentum cannot be neglected [47]. The spin orbit interaction is taken into account by including the term,

$$H_{SO} = \frac{\hbar}{4c^2m^2}(\nabla V \times \vec{p})\vec{\sigma} \qquad (7.7)$$

into the Hamilton operator, where the components of $\vec{\sigma}$ correspond to the Pauli spin matrices and V and $\vec{p}$ indicate the electro static potential and the electron momentum, respectively. As H_{SO} operates on the spin function of the electrons, the symmetry of the spin function needs to be taken into account. For spin functions, a rotation about 2π leads to a change of sign, hence it is no longer a unity operation. Therefore in systems that include spin, rotations about 2π are labelled as $\bar{E}$. Due to the additional symmetry operation $\bar{E}$, a group G, which without spin contains g elements , will contain additionally the elements $\bar{E}G$, when spin is considered. Due to there now being $2g$ elements belonging to G it is called a double group. However, the doubling of the symmetry elements does not necessarily lead to a doubling of the classes belonging to G, as the symmetry operations $\bar{E}C_i$ and C_i can belong to the same class. Taking the group D_{2d} as example, spin orbit interaction increases the order from 8 to 16 and leads to two additional classes, which are, according to equation 7.1

$$16 = 1^2 + 1^2 + 1^2 + 1^2 + 2^2 + 2^2 + 2^2 \qquad (7.8)$$

both of dimension two.

To determine the additional irreducible representations for the additional classes, the characters corresponding to the symmetry operations of the group in the spin state space by means of the rotation matrix S needs to be calculated:

$$S = \begin{pmatrix} cos(\frac{1}{2}\beta)e^{-\frac{1}{2}i(\alpha+\gamma)} & -sin(\frac{1}{2}\beta)e^{-\frac{1}{2}i(\alpha-\gamma)} \\ -sin(\frac{1}{2}\beta)e^{-\frac{1}{2}i(\alpha-\gamma)} & cos(\frac{1}{2}\beta)e^{-\frac{1}{2}i(\alpha+\gamma)} \end{pmatrix} \qquad (7.9)$$

where α, β and γ are the Euler angles for the rotations. The characters of the rotation matrices of the group D_{2d} in the spin state space are given in table 7.2. To calculate the characters of the additional irreducible representations belonging to the double group representation, the characters of the classes in the spin state space given in table 7.2 are multiplied with the characters of the single group representation. The result then needs to be decomposed in the irreducible representations.

Class	**E**	$\bar{\mathbf{E}}$	$\mathbf{IC_4}$	$\mathbf{I\bar{C}_4}$	$\mathbf{C_2}$	$\mathbf{C_2^{'}}$	$\sigma_\mathbf{d}$
$\mathbf{Tr\,S^{-1}}$	2	-2	$\sqrt{2}$	$-\sqrt{2}$	0	0	0

Table 7.2: Characters for the rotations belonging to the group D_{2d} in the spin state space.

Selection rules

As this thesis is concerned with the analysis of photoluminescence measurements, a special interest is in the selection rules which can be derived from group theoretical considerations. Here, the underlying principles will be discussed and the results for the different point groups will be presented in chapter 7.2. Following the description in [128] and [47] the semiclassical Hamilton operator for the interaction between an electron in a solid and an electric field is given by

$$H_{opt} = \frac{1}{2m}[\vec{p} + (\frac{e\vec{A}}{c})]^2 + V(\vec{r}) \qquad (7.10)$$

$\vec{p}$ being the momentum operator and $\vec{A}$ the vector potential in the Coulomb gauge. Here the electric field is treated classical, that is, the quantization of the electromagnetic waves into photons is neglected while the electrons in the crystal are treated quantum mechanically. Being interested only in linear optical properties, means that the quadratic term in $\vec{A}$ can be neglected, resulting in

$$H_{opt} = -\frac{e}{mc}\vec{A}\cdot\vec{p} \qquad (7.11)$$

Assuming a weak vector potential, $\vec{A}$, time dependent perturbation theory can be used to calculate the optical transition probability ω, according to Fermis golden rule:

$$\omega \sim \langle \Psi_f | H_{opt} | \Psi_i \rangle^2 \qquad (7.12)$$

The vector potential, $\vec{A}$, can be expressed in terms of the incident electric field as

$$A = -\frac{E}{2q}[e^{i(\vec{q}\vec{r}-\omega t)} + cc] \qquad (7.13)$$

where cc stands for the complex conjugate. In the following optical transitions will be concerned, this implies that the wave vector of a photon is much smaller than the wave vector of a phonon:

$$\vec{q}_{Photon} \ll \vec{q}_{Phonon}. \tag{7.14}$$

This means that the exponential function in equation 7.13 can be expanded into a Taylor series and all $\vec{q}$ dependent terms can be neglected. For a direct optical interband transition it then follows that

$$\langle \Psi_f | (-e) \vec{r} \vec{E} | \Psi_i \rangle \tag{7.15}$$

which is known as the electric dipole approximation. For a transition to be observed, the matrix element must be different from zero. In terms of group theory, this means that the reduction of the product of the representation of the vector $\vec{r}$ $\Gamma(\vec{r})$ in the dipole approximation , with the representation of the initial state $\Gamma(\Psi_i)$, needs to contain the representation of the final state $\Gamma(\Psi_i)$.

$$\Gamma(\Psi_i) \subset \Gamma(\Psi_i) \otimes \Gamma(\vec{r}) \tag{7.16}$$

As $\vec{r}$ in the dipole approximation and $\vec{p}$ in H_{opt} in equation 7.11 are both vectors, their representations, $\Gamma(\vec{r})$ and $\Gamma(\vec{p})$, will be the same. However, the irreducible representation of the vectors also depends on their orientation relative to the crystal axes. The orientation of the transition vector, $\vec{r}$ or $\vec{p}$, in the matrix element, corresponds to the polarisation of the electromagnetic wave, and hence the direction of its $\vec{E}$-vector.

7.2 The symmetries of the electronic bands in chalcopyrite

As introduced in chapter 2.1.1 the crystal structure of the chalcopyrites can be deduced from the zinc blende crystal structure. As the crystal structure and the electronic structure of a semiconductor are closely related, the symmetries of the electronic bands in chalcopyrites can be derived from those of semiconductors with zinc blende structure. At the Γ-point, a direct semiconductor with zinc blende structure, and thus $T_d/\bar{4}3m$ symmetry, has a non degenerate conduction band corresponding to a Γ_1 state. The valence band is three fold degenerate and corresponds to a Γ_{15} state as depicted in the centre of figure 7.3 [129],[130]. In passing from the cubic zinc blende lattice to the tetragonal chalcopyrite structure the symmetry of the crystal is reduced. Additionally, the deviation of the lattice constant c in the tetragonal lattice, from twice the value of the cubic lattice constant a, $(c \neq 2a)$, known as the tetragonal distortion, introduces a crystal field. This crystal field leads to a splitting of the three fold degenerate Γ_{15} band into a two fold degenerated Γ_5 and a non degenerate Γ_4 band. For $CuGaSe_2$, as for most of the other chalcopyrites, a η value of $\frac{c}{2a} < 1$ corresponds to a crystal field splitting $\Delta_{CF} < 0$. In this case the Γ_4 band is the topmost valence band. For $CuInSe_2$ however, $\eta = \frac{c}{2a} > 1$ and therefore $\Delta_{CF} > 0$, so that the twofold degenerated Γ_5 band has the higher energy. To take additionally the spin orbit interaction into account the double group notation is applied. Therefore, the characters of the irreducible representations are multiplied by the characters of the representations in the spin state space, as given in table 7.2. An example of this is shown for the Γ_5 irreducible representation in table 7.3. $Tr\,(S^{-1} \otimes \Gamma_5)$ yields a four dimensional representation. As the D_{2d} group consists only of one- and two dimensional representations, $Tr\,(S^{-1} \otimes \Gamma_5)$ must be reducible. Comparing the characters of $Tr\,(S^{-1} \otimes \Gamma_5)$ to the characters given in the character table for the D_{2d} group, $Tr\,(S^{-1} \otimes \Gamma_5)$ can be represented by a combination of the two irreducible representations $\Gamma_6 \oplus \Gamma_7$. Thus the Γ_5 band splits under the influence of spin-orbit interaction into a Γ_6 and a Γ_7 band. Performing the same calculation for the Γ_4 valence band state leads

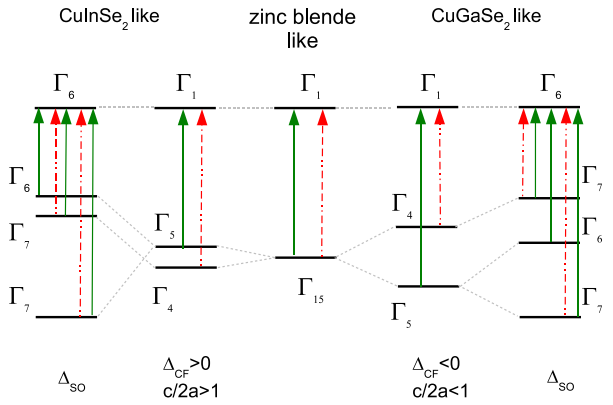

Figure 7.3: Symmetry of the conduction and valence band of $CuInSe_2$ and $CuGaSe_2$ according to [129] and [130]. Green solid arrows indicate allowed transitions for light polarised perpendicular to the $\vec{c}$-axis, whereas red dashed arrows represent transitions polarised parallel to the $\vec{c}$-axis.

to a Γ_6 state. The Γ_1 conduction band state transfers to a Γ_6 state, when spin orbit interaction is taken into account. Thus in $CuInSe_2$ the topmost valence band corresponds to a Γ_6 state, whereas in $CuGaSe2$ the topmost valence band equals a Γ_7 state.

Class	**E**	$\bar{\mathbf{E}}$	$\mathbf{IC_4}$	$\mathbf{I\bar{C}_4}$	$\mathbf{C_2}$	$\mathbf{C_2^{'}}$	$\sigma_\mathbf{d}$
$\mathbf{Tr\,S^{-1}}$	2	-2	$\sqrt{2}$	$-\sqrt{2}$	0	0	0
$\mathbf{\Gamma_5}$	2		0		-2	0	0
$\mathbf{Tr\,S^{-1}} \otimes \mathbf{\Gamma_5}$ = $\mathbf{\Gamma_6} \oplus \mathbf{\Gamma_7}$	4	-4	0	0	0	0	0

Table 7.3: Splitting of the Γ_5 band under the influence of spin-orbit interaction.

In order to calculate the polarisation of the band to band transitions, the representation of the momentum operator in the optical transition matrix element needs to be known as introduced in chapter 7.1.3. The vector parallel to the $\vec{c}$-axis corresponds to the Γ_4 representation in the chalcopyrite point group $D_{2d}/\bar{4}2m$, and the vector perpendicular to the $\vec{c}$-axis to the Γ_5 representation, as can be seen in the second column of the character table of the point group $D_{2d}/\bar{4}2m$ in the appendix A.6 on page 97. Using the group theoretical selection rules presented in chapter 7.1.3 (p.66) it is possible to calculate the polarisation of the band-to-band-transitions, an example of which is shown in table 7.4. Γ_5, the irreducible representation of the vector perpendicular to the $\vec{c}$-axis is multiplied with the irreducible representation Γ_6 of the conduction band. The result, $\Gamma_6 \otimes \Gamma_5$, is shown in the third row of the table 7.4. Reducing this result into its irreducible representations, as shown in the lower part of table 7.4, yields the irreducible representation to which transitions polarised perpendicular to the $\vec{c}$-axis are allowed. In this example $\Gamma_6 \otimes \Gamma_5 = \Gamma_6 \oplus \Gamma_7$, and thus transitions starting from a Γ_6 band to Γ_6 or Γ_7 bands, which are polarised perpendicular to the $\vec{c}$-axis are allowed. Repeating the same calculation with a vector belonging to the Γ_4 irreducible representation, corresponding to transition polarised parallel to the $\vec{c}$-axis yields: $\Gamma_6 \otimes \Gamma_4 = \Gamma_7$. Thus transitions from a Γ_6 to a Γ_6 band, corresponding to a transition between the topmost valence and the conduction band in $CuInSe_2$, are only allowed polarised perpendicular to the $\vec{c}$-axis. On the other hand transitions between the Γ_6 and the Γ_7 band, corresponding to transitions between the topmost valence band and the conduction band in $CuGaSe_2$, which are polarised parallel as well as perpendicular to the $\vec{c}$-axis, are allowed. However, when spin-orbit interaction is neglected $\Gamma(7)$ symmetry corresponds to $\Gamma(4)$ symmetry and $\Gamma(6)$ to $\Gamma(1)$ and transitions between bands with $\Gamma(1)$ and $\Gamma(4)$ symmetry are only allowed for polarisation parallel to the $\vec{c}$-axis. Therefore $CuGaSe_2$ will have a slight preference for transitions oriented parallel to the $\vec{c}$-axis. These results are summarised in table 7.5. Performing the same calculation for the zinc-blende structure results in transitions allowed independent of the polarisation of the light, as one would expect for an isotropic crystal [131].

	CIS	**CGS**
VB	Γ_6	Γ_7
CB	Γ_6	Γ_6
	$\vec{E} \perp \vec{c}$	$\vec{E} \parallel \vec{c}$, $(\vec{E} \perp \vec{c})$

Table 7.5: Symmetries of the valence and conduction band of $CuInSe_2$ and $CuGaSe_2$ according to [130], [129]. The spin-orbit and crystal field splitting is included and the polarisation of the band-band transitions indicated.

7.2.1 Crystal field splitting and the influence of strain and composition on the band ordering

As seen in the last section, the crystal field splitting influences the order of the bands. In the following section, therefore the crystal field splitting and its connection to lattice strain and composition shall be discussed in more detail. Assuming a cubic zinc-blende lattice a strain applied along the $\vec{z}$ direction leads to a splitting of the energy level as discussed in the previous section and depicted in figure 7.3. The energy position of the split off bands, dependant on the crystal field splitting, Δ_{CF}, and the spin orbit splitting, Δ_{SO}, can be calculated within the quasi cubic model according to Hoppfield [132]:

$$\begin{aligned} E_{1,3} &= E_2 - \frac{1}{2}(\Delta_{SO} + \Delta_{CF}) \\ &\pm \frac{1}{2}[(\Delta_{SO} + \Delta_{CF})^2 - \frac{8}{3}\Delta_{SO}\Delta_{CF}]^{\frac{1}{2}} \end{aligned} \tag{7.17}$$

The crystal field splitting, Δ_{CF}, is the strain related energy and is related to the tetragonal distortion in a tetragonal lattice according to [129] by

$$\Delta_{CF} = \frac{3}{2} b \left(2 - \frac{c}{a}\right) \tag{7.18}$$

where b is the deformation potential. This accounts for the change in the electron energy when the atoms

$\mathbf{D_{2d}}$	**Basis**	**E**		$\mathbf{2IC_4}$		$\mathbf{C_2}$	$\mathbf{2C_2'}$	$\mathbf{2\sigma_d}$
$\mathbf{\Gamma_6}$	$\{\alpha, \beta\}$	2	-2	$\sqrt{2}$	$-\sqrt{2}$	0	0	0
$\mathbf{\Gamma_5}$	$\{x, y\}$	2		0		-2	0	0
$\mathbf{\Gamma_6 \otimes \Gamma_5}$		4	-4	0	0	0	0	0

$\mathbf{\Gamma_6}$	$\{\alpha, \beta\}$	2	-2	$\sqrt{2}$	$-\sqrt{2}$	0	0	0
$\mathbf{\Gamma_7}$	$\{z\alpha, z\beta\}$	2	-2	$-\sqrt{2}$	$\sqrt{2}$	0	0	0
$\mathbf{\Gamma_6 \oplus \Gamma_7}$		4	-4	0	0	0	0	0

Table 7.4: Example calculations of the allowed transition polarised perpendicular to the $\vec{c}$-axis, which start from a band with Γ_6 symmetry.

are moved from their equilibrium lattice positions. Following [47], the deformation potential can be calculated by the tight binding approach:

$$b = -\frac{8}{9}(V_{pp\sigma} - V_{pp\pi}) \tag{7.19}$$

where $V_{pp\sigma}$ and $V_{pp\pi}$ are the overlap parameters. The overlap parameters are the matrix elements of the interaction Hamiltonian between two atoms forming a molecule. $V_{pp\sigma}$ and $V_{pp\pi}$ account here for the p-orbital electrons forming π and σ bonds. For a zinc-blende lattice, the deformation potential equals

$$b = -\frac{8}{9}(\frac{21\pi^2}{64} \cdot \frac{\hbar^2\pi^2}{2md^2} - \frac{-3\pi^2}{32} \cdot \frac{\hbar^2\pi^2}{2md^2}) \tag{7.20}$$

where d is the interatomic distance and m the effective electron mass. Figure 7.4 shows the crystal field splitting, Δ_{CF}, dependence on the tetragonal distortion, $\eta = 2 - \frac{c}{a}$, for different chalcopyrites. The crystal field splitting increases with increasing distortion and the values for the different chalcopyrites lie approximately on a line. This is the deformation potential is roughly equal for all chalcopyrites.
The zinc-blende structure, however is only an approximation for the chalcopyrites. In order to account for the band structure more exactly, the copper d-electrons have to be taken into account. Shirakata reported calculations of the influence of strain on the band structure of $CuAlSe_2$ [133] and $CuGaSe_2$ using a semi-empirical tight-binding method, which takes the spin-orbit interaction and the p-d hybridization into account. The results are shown in figure 7.5.

Photoreflectance measurements presented in the same article show that lattice strain only influences the crystal field splitting and has no effect on the spin orbit splitting. The common feature for both materials is the switching of the two topmost valence bands. This is due to biaxial compressive stress whereas tensile stress would enhance the band structure found

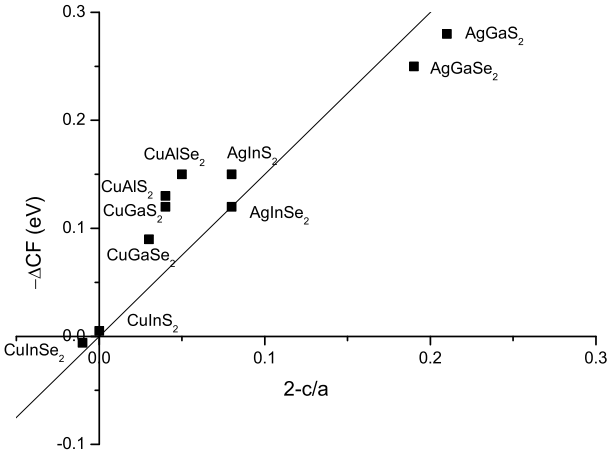

Figure 7.4: The crystal field splitting versus lattice distortion for different Chalcopyrites following [129] and [28] is shown.

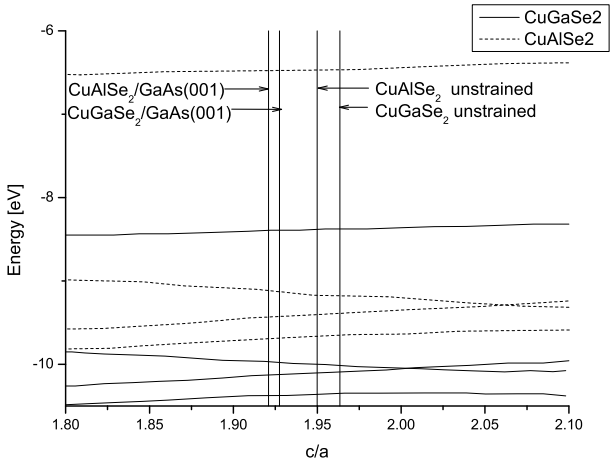

Figure 7.5: The energy of the conduction and the valence bands dependent on strain for $CuGaSe_2$ and $CuAlSe_2$ following [133] and [134]

in the unstrained compounds, namely the Γ_7 band as the topmost band. However, unlike as would be expected from equation 7.18, the $\frac{c}{a}$ ratio at which the switching of the bands occur, is material dependent. $CuGaSe_2$ shows slight deviations from $\frac{c}{a} = 2$, the point at which the crystal field, Δ_{CF}, equals zero and the lattice is undistorted, whereas quite distinct deviations are observed for $CuAlSe_2$.

However, as the expression for b given in 7.19 is calculated for a zinc-blende lattice it does not take into account the deviation of chalcopyrites from its II-VI binary counterparts, as there are the influence of the d-orbitals and the distortion of the anions from the ideal tetrahedral anion positions at $(\frac{1}{4}\,\frac{1}{4}\,\frac{1}{4})$. To clarify the shift of the band crossing from the $\frac{a}{c} = 2$ point further, table 7.6 shows the crystal field splitting, the $\frac{c}{a}$ ratio, the distortion from the ideal tetrahedral lattice site u and the estimated d-like character of the valence band maximum for different chalcopyrites reported by Shay and Wernick [129], Zunger [28] and Shirakata [133]. Figure 7.4 shows, that especially the $CuGaXI_2$ and $CuAlXI_2$ samples deviate from this line. One reason could be, as mentioned above, the deviation of the anion from the ideal tetrahedral position u. Yet, if one compares the values of u given in table 7.6 one finds no clear trend between the positions of the different samples in graph 7.4 and u. For example for the chalcopyrites $CuInS_2$ and $AgInSe_2$ which lie well to the $b = -1$ line values of u=0.21 and u=0.25 are reported, whereas $AgGaS_2$ and $AgGaSe_2$ for which u equals 0.29 and 0.28 are shifted to lower Δ_{CF} values compared to the b=-1 line. The u values of $CuAlSe_2$ and $CuGaSe_2$ lie with u=0.27 and u=0.28 between the two above mentioned examples, but their Δ_{CF} values are higher compared to the b=-1 line.
The second possible reason for the shift of the $CuGaXI_2$ and $CuAlXI_2$ relative to the b=-1 line could be the percentage of p-d hybridisation at the valence band maximum. Table 7.6 presents the calculated d-like character of the topmost valence band according to Zunger in column 4 and Shay and Wernick in column 6. The difference between the columns results from the different calculation methods used by the authors: Shay and Wernick calculated the d like character directly from the spin-orbit splitting, whereas Zunger splitted the spin-orbit splitting in a part due to the distortion of the anions from the ideal tetrahedral position ΔE_G^{Struct} and a chemical part ΔE_G^{Chem}. The chemical part $\Delta E_G^{Chem} = \Delta E_G^{d} + \Delta E_G^{EC}$ consists of a contribution due to the p-d hybridisation and a contribution due to the difference in electronegativities of the two cations. As Zunger treats the structural contribution to the change of the spin-orbit splitting and the influence of the d-orbitals separately, this values may be more accurate. Comparing the d-like character of the different chalcopyrites given in table 7.6 column 4 by Shay and Wernick one finds, that the Ag chalcopyrites have a lower contribution of d Orbitals to the top of the valence band than the Cu chalcopyrites. Comparing the d-like character of the Cu chalcopyrites in column six, shows as a trend that the $CuAlXI_2$ and $CuGaXI_2$ compounds have the higher contributions of d-orbitals to their valence band maxima as the $CuInXI_2$ compounds corresponding to a higher deviation from the b=-1 line. For $CuAlSe_2$, $CuGaSe_2$ and $CuInSe_2$ holds: the higher the d contribution to the valence band maximum, the higher the deviation of the crossing of the valence bands form the $\frac{c}{a} = 2$ point. Consequently it is reasonable to assume, that the shift of the crossing of the two topmost valence bands from the $\frac{c}{a} = 2$ point is due to the influence of the d-orbitals on the valence band maximum.

Subsequently the influence of strain on $CuInSe_2$ epitaxial samples will also be considered. The question arises, whether $CuInSe_2$ under strain behaves similarly to $CuGaSe_2$ and $CuAlSe_2$, shown in figure 7.5. The material properties are included in the semi-empirical tight-binding method calculations via the interatomic distances and, so called, Herman Skillman values, which give the energy levels for the different atomic orbitals. As Al, Ga and In are in the same main group, they have rather similar Herman Skillman values and similar lattice constants, and thus the main features of figure 7.5 should also hold for $CuInSe_2$. From figure 7.4 can be seen that $CuInSe_2$ has a positive crystal field splitting. This implies that $CuInSe_2$ lies on the right side of the switching point of the valence bands in figure 7.5. Therefore tensile strain along the $\vec{c}$-axis will lead to a more "$CuInSe_2$-like" band structure, while compressive strain will lead to an interchange of the bands and so to a "$CuGaSe_2$-like" band structure. However, as shown in figure 7.4, the crystal field splitting in $CuInSe_2$ is small, and therefore a small amount of compressive strain will be sufficient to change the ordering of the bands.

	$-\Delta_{CF}$		Estimated % d-like		Estimated % d-like		$\mu = \frac{c}{a}$	$2 - \frac{c}{a}$	u	
$CuAlS_2$	0.13	[129]	35	[129]	35.2	[28]	1.96	0.04	0.27	[28]
$CuGaS_2$	0.12	[129]	35	[129]	31.5	[28]	1.96	0.04	0.26	[28]
$CuGaSe_2$	0.09	[129]	36	[129]	25.1	[28]	1.97	0.03	0.25	[28]
$CuInS_2$	0.01	[129]	45	[129]	24	[28]	2	0	0.21	[28]
$CuInSe_2$	-0.01	[129]	34	[129]	22	[28]	2.01	-0.01	0.22	[28]
$AgGaS_2$	0.28	[129]	20	[129]	–	–	1.79	0.21	0.29	[28]
$AgGaSe_2$	0.25	[129]	16	[129]	–	–	1.81	0.19	0.28	[28]
$AgInS_2$	0.15	[129]	20	[129]	–	–	1.92	0.08	0.25	[28]
$AgInSe_2$	0.12	[129]	17	[129]	–	–	1.92	0.08	0.25	[28]
$CuAlSe_2$	0.15	[133]	-	–	27.5	[28]	1.95	0.05	0.27	[28]

Table 7.6: Tetragonal distortion μ, anion displacement u, crystal field splitting Δ_{CF} and estimated d-character of the valence band maximum of different chalcopyrite semiconductors according to Zunger [28], Shay and Wernick [129] and Shirakata [133].

Strain in epitaxially grown thin layers

The investigated samples later in this chapter are epitaxial $CuInSe_2$ and $CuGaSe_2$ thin films grown on a $GaAs$ substrate, and therefore in the following section possible sources of strain in epitaxial layers are introduced.

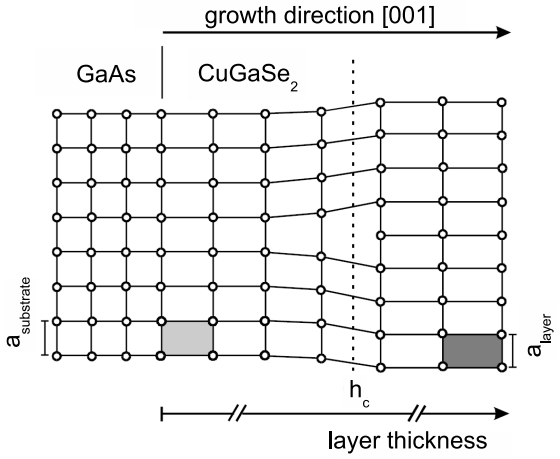

Figure 7.6: Pseudomorphic and relaxed growth in heteroepitaxy according to [134].

In epitaxially grown samples there are two possible sources of strain: firstly strain caused by the mismatch, f, between the lattice constant of the substrate and the lattice constant of the layer. This effect dominates in thin films. The layer adopts the lattice constant of the substrate and grows in the so called "pseudomorphic growth mode". The misfit, f, is given by

$$f = \frac{a_{Layer} - a_{Sub}}{a_{Sub}} \tag{7.21}$$

where a_{Layer} is the in-plane lattice constant of the film and a_{Sub} the lattice constant of the substrate. The misfit, f, gives rise to strain in the layer given by the relationship $\varepsilon_{xx} = \varepsilon_{yy} = -f$ [135]. To maintain the volume of the unit cell, the axis parallel to the direction of the growth elongates if the axis in the layer is compressed and vice versa. The strain parallel to the growth direction can be calculated according to

$$\varepsilon_{zz} = \frac{2C_{12}}{C_{11}} f \tag{7.22}$$

with C_{12} and C_{11} being the elastic constants. The pseudomorphic growth continues, until, a critical thickness, h_c, is reached when it becomes energetically favourable to create dislocations, which lead to a relaxation of the layer. The critical thickness, h_c, at which dislocation formation starts, can be calculated by two different models: firstly by an energy balance model, which equates the energy due to strain with the energy necessary to form dislocations and secondly from the balance of forces between the lattice mismatch stress, as driving force for the dislocation growth and the line tension stress in the dislocation [136],[135],[137]. Both models lead to an approximate relation between misfit f and critical thickness h_c

$$\begin{aligned} h_c &\sim \frac{1}{f} \\ h_c \cdot f &\approx 80\,nm\,\% \end{aligned} \tag{7.23}$$

The second cause of strain results from the difference in the thermal expansion coefficients of the substrate

and the layer. At the growth temperature T_G it is assumed, that the layer and the substrate adopt the same lattice constant. A larger thermal expansion coefficient, α_{layer}, of the layer, then leads to a quicker shrinking of the deposited film compared to the substrate, when the sample is cooled down to room temperature. As a result there will be tensile strain in the film. The mismatch due to different thermal expansion coefficients, α, arising in a sample cooled down to room temperature is given by:

$$f = (\alpha_{Layer} - \alpha_{Sub})(T_G - 300\,K) \tag{7.24}$$

The lattice constants and thermal expansion coefficients for $CuGaSe_2$, $CuInSe_2$ and $GaAs$ are presented in table 7.7. $CuInSe_2$ has a larger in-plane lattice constant than $GaAs$, leading to compressive strain in the pseudomorphic growth regime, whereas $CuGaSe_2$ has a smaller in-plane lattice constant, which leads to tensile strain in the pseudomorphic growth regime. $CuInSe_2$ and $CuGaSe_2$ both have a higher thermal expansion coefficient, α_a, along the $\vec{a}$-axis, than $GaAs$. This causes tensile strain in the layer after being cooled down to room temperature due to the quicker shrinkage of the film compared to the substrate. In summary, strain due to lattice mismatch in the pseudomorphic growth regime as well as strain due to the difference in thermal expansion coefficients in the relaxed layer will lead to tensile strain in the layer plane for $CuGaSe_2$. This corresponds to compressive strain along the c-axis. For $CuInSe_2$ however, strain due to the lattice mismatch will lead to compressive strain, whereas strain due to the difference in the thermal expansion coefficients results in tensile strain in the layer plane.

Influence of gallium content on the band ordering in $Cu(In,Ga)Se_2$ samples

As the valence band ordering in $CuInSe_2$ and $CuGaSe_2$ is different, the ordering of the valence bands in a $Cu(In,Ga)Se_2$ sample will depend on its gallium content. The dielectric function is determined from a series of ellipsometric spectra of $Cu(In,Ga)Se_2$ samples with different gallium content at room temperature in [130]. Using the quasi cubic Hoppfield model, as introduced in the previous section 7.2.1, the authors calculated the crystal field splitting, Δ_{CF}, and the spin orbit splitting, Δ_{SO}. The dependence of the crystal field splitting and the spin orbit splitting on the gallium content is shown in figure 7.7: the crystal field decreases almost linearly with increasing gallium content, from a slightly positive value for $CuInSe_2$ to a negative value for $CuGaSe_2$. The crystal field equals zero at $\sim 5\%$ Ga content. The spin orbit splitting, Δ_{SO}, on the other hand is nearly independent of gallium content and shows only a slight upward bowing.

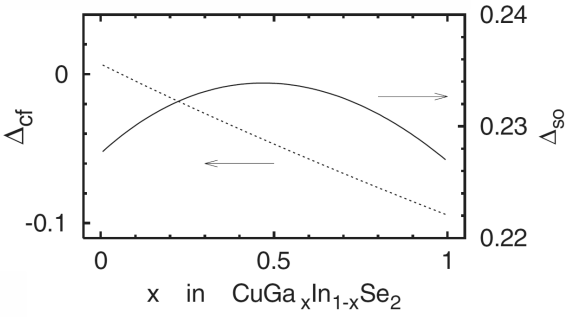

Figure 7.7: Change of crystal field Δ_{CF} and spin orbit splitting Δ_{SO} with gallium content in $CuIn_{1-x}Ga_xSe_2$ samples according to [130].

7.3 Models to describe defects

Defects can be described in two limiting cases [47]: on the one hand as shallow or hydrogen-like defects and on the other hand as deep, localised defects. To describe shallow or hydrogen-like defects, the surplus electron, in the case of a donor, or surplus hole, for an acceptor, is described in analogy to the hydrogen atom as a charge in an electrostatic potential:

$$(H_0 + U)\Psi(\vec{r}) = E\Psi(\vec{r}) \qquad with \quad U = -|e|V \tag{7.25}$$

where H_0 is the Hamiltonian of the perfect crystal and U the electrostatic potential [47]. The attractive force of the atomic core is screened by the valence electrons of the other atoms and therefore the donor electron is only weakly attracted. The screening is taken into account by the dielectric constant, ε_r, of the host crystal:

$$V = \frac{|e|}{4\pi\varepsilon_0\varepsilon_r r} \tag{7.26}$$

Equation 7.25 can be solved by using the effective mass approximation. In this method the electron mass is substituted by an effective electron mass, which takes the interaction of the electron with the

	Structure	**c [Å]**	**a [Å]**		$\alpha_{\mathbf{c}}$ **[10^{-6}K^{-1}]**	$\alpha_{\mathbf{a}}$ **[10^{-6}K^{-1}]**	
$CuInSe_2$	tetragonal	11.5910	5.7600	[138]	7.9	11.23	[139]
$CuInSe_2$					8.6	11.4	[140]
$CuGaSe_2$	tetragonal	11.02	5.6140	[29]	5.2	13.1	[141]
$GaAs$	cubic	c=a	5.6530	[142]	$\alpha_a = \alpha_c$	6.8	[142]

Table 7.7: Lattice constants and thermal expansion coefficients for $CuInSe_2$, $CuGaSe_2$ and $GaAs$.

host crystal into account. Equation 7.25 results in discrete energy levels corresponding to the binding energies of the shallow impurity and continuous energy values representing the ionised donor electron in the band. For this model to be valid the electron wave function needs to spread over several unit cells in real space. Hence, as the real space and the reciprocal space are related by a Fourier transform, it follows from the uncertainty principle $\Delta\vec{k}\Delta\vec{\omega} \approx 1$, that the extend of the Bloch functions is limited to a narrow range of $\vec{k}$ values around $k \approx 0$. Therefore, according to this model the defects will assume the symmetry of the bands at the Γ-point.

All defects whose energy level cannot be described by the hydrogen model, fall into the category "deep defects". This involves that the impurities introduce a strongly localised potential, thus violating the assumption of a slowly varying potential which is necessary for the effective mass approximation to be valid. In principal, the energy levels of deep defects can be calculated by solving the Schrödinger equation for the potential of the localised defect. However, as the potential of a defect is influenced by the relaxation processes of the defect itself as well as the relaxation of neighbouring atoms, it is often difficult to determine. As the wave function of the defect is localised, its symmetry depends on the site symmetry of the lattice site of the defect. However the division of defects into shallow and deep is not that clear-cut. For some defects the lowest energy level behaves as a deep defect, whereas higher energy levels are shallow, due to the non vanishing probability of the s symmetry wave function at the origin and therefore its higher sensitivity to the potential. A second example for the ambiguous behaviour of defects are DX centres, where a shallow donor transforms into a deep state depending on its charge state [143].

7.3.1 Group theoretical predictions for the polarisation of defect related transitions

In the following section the predictions shall be derived according to group theoretical considerations for the polarisation of the defect related photoluminescence transitions corresponding to the two models introduced above. To consider the influence on the polarisation of one defect at a time subsequent free to bound transitions are considered.

As seen above, defects described by the hydrogen model are expected to assume the symmetry of the nearest band. This results in a polarisation parallel to the $\vec{c}$-axis for free-to-bound transitions in $CuGaSe_2$ and a polarisation perpendicular to the $\vec{c}$-axis for free-to-bound transitions in $CuInSe_2$.

The symmetry of a deep defect, is determined by its site symmetry. In a descriptive model, the luminescence radiation of atoms in a crystal can be described as the oscillation of elementary electric dipoles. If a predominant axis in a crystal exists, it gives rise to an electric field parallel to this axis. The electric dipoles orient themselves in the electric field, which results in a polarisation of the photoluminescence light parallel to the predominant axis. In a cubic crystal, in which all crystal directions are equivalent, the emitted radiation will be non polarised [131]. In the $CuInSe_2$ crystal, as shown in figure 7.8, the bond length between the selenium and the copper atoms is shorter than between the selenium and the indium atoms. Therefore, the selenium atom shifts from its ideal tetrahedral position in the cubic case to an new position in the layer perpendicular to the $\vec{c}$-axis as indicated by the green arrow. At this new position, the binding forces of the selenium atom to both the copper and the indium atom are equal and therefore all electric fields cancel. Thus transitions to defects located on a selenium site, will be non-polarised in the model of localised deep defects. For the copper atoms, the shifts of the neighbouring selenium atoms in the $\vec{x}-\vec{y}$-plane approximately cancel out as depicted in figure 7.9. Therefore only a change in the distance between the

	Wyckoff position	**Symmetry**	**Donor → VB**				**CB → Acceptor**	
			$CuInSe_2$		$CuGaSe_2$		$CuInSe_2/CuGaSe_2$	
			$EIIc$	$E \perp c$	$EIIc$	$E \perp c$	$EIIc$	$E \perp c$
defect on metal site	a,b	S_4	$\Gamma_7 \oplus \Gamma_8$	-	$\Gamma_5 \oplus \Gamma_6$	-	$\Gamma_7 \oplus \Gamma_8$	-
defect on Se site	d	C_2	Γ_6, Γ_7	$2 * \Gamma_6$, $2 * \Gamma_7$	Γ_6, Γ_7	$2 * \Gamma_6$, $2 * \Gamma_7$	Γ_6, Γ_7	$2 * \Gamma_6$, $2 * \Gamma_7$

Table 7.8: Calculated allowed polarisation for the photoluminescence transitions in the site symmetry model. The table indicates the multiplication of the representation of the participating band with the transition vector $\vec{r}$, as represented in the irreducible representation of the symmetry group of the involved defect for free to bound transitions in $CuInSe_2$ and $CuInSe_2$.

copper and the selenium atoms parallel to the $\vec{c}$-axis compared to the ideal tetrahedral positions remains, which gives rise to a crystal field and corresponds to the tetragonal distortion described in chapter 2.1.1. This dominant direction parallel to the $\vec{c}$-axis, will result in a polarisation parallel to the $\vec{c}$-axis for defects on metal sites, if a s-like conduction band is assumed.

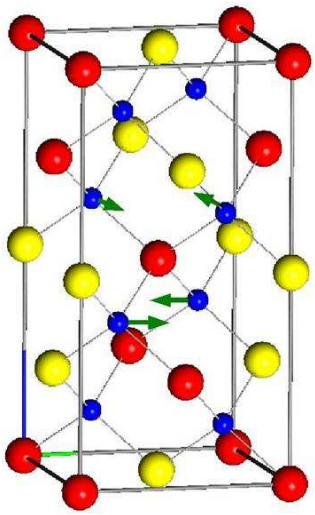

Figure 7.8: Influence of different bond lengths on the atom position in the $CuInSe_2$ crystal structure: the Se atom is shifted in the plane perpendicular to the $\vec{c}$- axis compared to its ideal tetrahedral position as indicated by the green arrow.

Similar results can be obtained from group theoretical considerations. The symmetries of different lattice sites can be described in terms of Wyckoff positions. A defect on a copper or indium metal site in

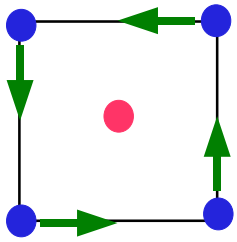

Figure 7.9: Influence of different bond lengths on a metal site: the copper atom is shown in red with the surrounding selenium atoms in blue. The shift of the selenium atoms in the x-y layer relative to the copper atom cancel each other.

the chalcopyrite structure with symmetry $D_{2d}/\bar{4}2m$ corresponds to a Wyckoff position a or b, which both have S_4 site symmetry. A defect on a chalcogen site corresponds to a Wyckoff position, d, which has C_2 site symmetry [121]. Defects localized on lattice sites can be vacancies or anti-site defects. Defects caused by interstitial atoms, as the name implies, reside not on lattice sites and can therefore not be described by Wyckoff positions. However, their site symmetry would correspond to the triclinic point group, which consists only of the identity operation. Therefore, transitions polarised parallel as well as perpendicular to the $\vec{c}$-axis are allowed.

For $CuInSe_2$ and $CuGaSe_2$ the topmost valence band has different symmetry and therefore the donor to valence band transitions has to be treated separately for each material. As the conduction band has the same symmetry for both chalcopyrites, the transitions from this band to the acceptors will have the same polarisation for both in the site symmetry model. As described in chapter 7.1.3, a transition is allowed if the reduction of the multiplication of the representation of the initial state, with the represen-

tation of the vector, $\vec{r}$, of the dipole approximation contains the representation of the final state. Table 7.8 shows the multiplication of the representation of the participating band with the transition vector, $\vec{r}$, described in the irreducible representation of the symmetry group of the involved defect. For a defect on a metal site, which gives rise to a donor as well as an acceptor state, transitions polarised parallel to the $\vec{c}$-axis can be represented by the irreducible representations of the point group of the defect. However, transitions polarised perpendicular to the $\vec{c}$-axis cannot be represented by the irreducible representations of the point group of the defect. Therefore the free-to-bound transitions are polarised parallel to the $\vec{c}$-axis. A transition to a defect on a chalcogen site, polarised parallel as well as perpendicular to the $\vec{c}$-axis, can be represented by a Γ_6 or a Γ_7 representation. The two possible representations, Γ_6 and Γ_7, result from the deduction of the representations for a subgroup from a group, which does not necessarily lead to irreducible representations. As transitions perpendicular, as well as parallel, to the $\vec{c}$-axis can be represented in the representations of the defect group, a free to bound transition to a defect on a chalcogen site is unpolarised. To summarize: in the limiting case of localised defects transitions to defects on a metal sites show a polarisation parallel to the $\vec{c}$-axis. For defects on a chalcogen site unpolarised transitions are expected.

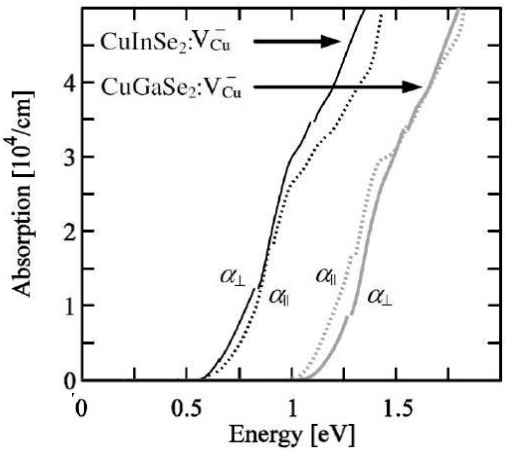

Figure 7.11: Density functional theory calculation of the absorption coefficient for transitions from the defect V_{Cu} to the conduction band of $CuInSe_2$ and $CuGaSe_2$.

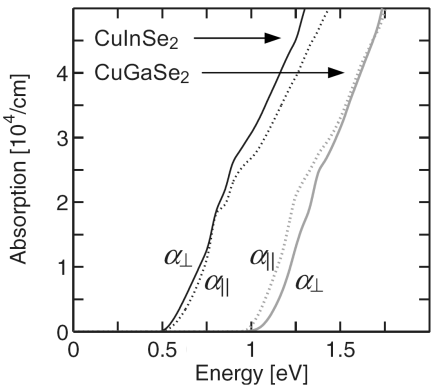

Figure 7.10: Density functional theory calculation of the absorption coefficient for band-band transitions of $CuInSe_2$ and $CuGaSe_2$

To investigate the influence of the defects on the symmetry of the bands, Clas Persson performed density functional theory calculations of the absorption coefficient for the band to band and free to bound

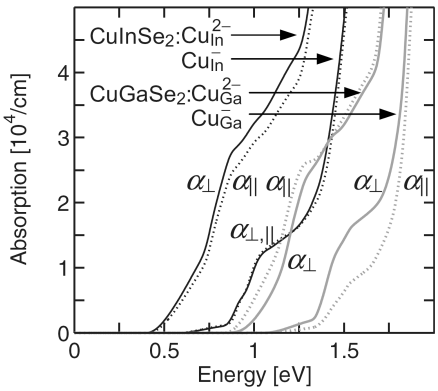

Figure 7.12: Density functional theory calculation of the absorption coefficient for transitions from the defects Cu_{III}^{-2} and Cu_{III}^{-} to the conduction band of $CuInSe_2$ and $CuGaSe_2$.

transitions [144]. As the selection rules for the absorption process as well as for photoluminescence transitions are determined by the transition matrix element, the calculated properties for the absorption process will also hold for photoluminescence transitions. Density functional theory calculations usually under-estimate the band gap of a material, but as here, only the absorption coefficient is of interest, this is of minor importance. The results for the absorption coefficient for the band to band transitions are shown in Fig.7.10: $CuInSe_2$ shows a slightly preferred polarisation perpendicular to the $\vec{c}$-axis at the onset of absorption at the band edge. This is due to the $\Gamma(6) \rightarrow \Gamma(6)$ transition, which is allowed only polarised perpendicular to the $\vec{c}$-axis, as describe above. However, there is also a contribution from the second lowest valence band, which is located only 6 meV below the valence band maximum. The second lowest valence band has $\Gamma(7)$ symmetry. As described above transitions between bands with $\Gamma(6)$ and $\Gamma(7)$ symmetry are allowed for light polarised parallel, as well as perpendicular, to the $\vec{c}$-axis. Yet $\Gamma(7)$ symmetry corresponds to $\Gamma(4)$ symmetry and $\Gamma(6)$ to $\Gamma(1)$ when spin-orbit interaction is neglected and transitions between bands with $\Gamma(1)$ and $\Gamma(4)$ symmetry are only allowed for polarisation parallel to the $\vec{c}$-axis . $CuGaSe_2$ shows a preferred polarisation parallel to the $\vec{c}$-axis, following the same arguments as for the second band of $CuInSe_2$. Figure 7.11 and Figure 7.12 show the influence of the Cu vacancy V_{Cu}, and the anti-site defect Cu_{III}^{-2}, on the absorption coefficient. As can be seen, the Cu vacancy V_{Cu} and the anti-site defect Cu_{III}^{-2} do not change the absorption coefficient much compared to the bulk band-band absorption. For comparison, the absorption due to a single charged defect Cu_{III}^{-} is shown in figure 7.12. To achieve a single charged anti-site defect, a higher degree of the valence band filling is required, and therefore lower valence bands may influence the observed symmetry of the defect. In fact, the onset of absorption, as can be seen in figure 7.12 occurs for the Cu_{III}^{-} defect in $CuInSe_2$ and $CuGaSe_2$ at higher energies compared to the bulk absorption. In this case transitions are unpolarised for $CuInSe_2$ corresponding to transitions from the third band and polarised perpendicular to the $\vec{c}$-axis for $CuGaSe_2$ corresponding to transitions from the second lowest band. To conclude: defects do not influence the symmetry of the bands, therefore the considerations in the previous sections based on the symmetry of the bands are also valid when defects are present.

Summary In this section the theoretical predictions for the polarisation of defect related transitions in the limiting cases of shallow and deep localized defects were discussed. Shallow defects, one expects to assume the symmetry of the bands, leading to transitions polarised parallel to the $\vec{c}$-axis for defect related transitions in $CuGaSe_2$ and transitions polarized perpendicular to the $\vec{c}$-axis for defect related transitions in $CuInSe_2$. For deep, localized defects, the symmetry is determined by their site symmetry, independent of the elemental composition for crystals of the same symmetry. This result in transitions polarized parallel to the $\vec{c}$-axis for defects on metal lattice sites, hence on the Wyckoff positions a and b. For defects on Wyckoff position d, this is on chalcogen lattice sites, one expects unpolarised transitions.

7.4 Determination of the symmetry of defects in chalcopyrites

As outlined in the previous section, deep, localised defects and shallow defects will have different symmetries, thus giving rise to different polarisations for the defect related photoluminescence transitions. Therefore, photoluminescence measurements will be used as a tool to determine the symmetry of the defects in $CuInSe_2$ and $CuGaSe_2$. Comparing the observed polarisations in $CuInSe_2$ and $CuGaSe_2$ samples, will thus allow the determination whether the defects behave as shallow or as deep defects. In order to determine the polarisation relative to the $\vec{c}$-axis, the orientation of the samples need to be known. Therefore measurements are performed on epitaxial grown chalcopyrite layers on GaAs substrate with the $\vec{c}$-axis perpendicular to the sample surface.

7.4.1 Symmetry of defects determined on epitaxial layers

Orientation of the measurement setup

To be able to correlate the measured polarisation to the orientation of the $\vec{c}$-axis of the sample, the measurement arrangement has to be taken into account. As introduced in chapter 4.1 (p. 17) the photoluminescence of the sample is measured at a 45° angle to the surface normal of the sample. Using the coordinate system introduced in figure 4.3 (p. 19), the $\vec{c}$-

axis points along the $\vec{x}_{SH}$ axis of the sample holder coordinate system. The polarisation of the photoluminescence transitions is measured in the plane spanned by the vectors $\vec{z}_D$ and $\vec{y}_D$ in the detection coordinate system. The sample holder coordinate system can be transferred into the detection coordinate system by a clockwise rotation of 45° about the $\vec{z}_{SH}$-axis. For light polarised perpendicular to the $\vec{c}$-axis the $\vec{E}$-field vector lies in the plane normal to $\vec{x}_{SH}$ axis of the sample holder coordinate system. It is assumed that the luminescence in all directions perpendicular to the $\vec{c}$-axis is equally strong. Therefore, the luminescence in the plane perpendicular to the $\vec{c}$-axis can be described as two parts, which are perpendicular to each other: one is chosen in the detection plane and labeled as $c_{\perp,1}$, the second part is due to the condition to be perpendicular both to the $\vec{c}$-axis and to $c_{\perp,1}$ and is called $c_{\perp,2}$. The observed intensity of the luminescence light polarised perpendicular to the $\vec{c}$-axis in the detection plane is calculated by adding the intensities of the projections of the two parts to the detection plane. As the first part, $c_{\perp,1}$, was chosen to be in the detection plane, which is parallel to the $\vec{z}_D$-axis, its entire intensity is detected, whereas for the second part, $c_{\perp,2}$, only a projection can be observed. The calculated intensity, dependent on polarisation angle, for light polarised perpendicular to the $\vec{c}$-axis, is depicted in figure 7.13 by a dotted line. The maximum intensity is observed at 0°, which corresponds to the entire intensity along the $\vec{z}_D$- axis. However, due to the second possible orientation of the $\vec{E}$- field vector in the plane perpendicular to the $\vec{c}$-axis and its projections to the detection plane, the degree of polarisation is only 50%.

Polarisation parallel to the $\vec{c}$-axis in this arrangement will be measured as a projection onto the detection plane leading to a polarisation maximum at 90°. This is indicated by a solid line in figure 7.13. As only the projection can be measured, the maximum detectable intensity is 50% of the original intensity. The degree of polarisation is 100%.
Comparing the measurements to the calculations, scattering as a source of depolarisation has to additionally be taken into account.

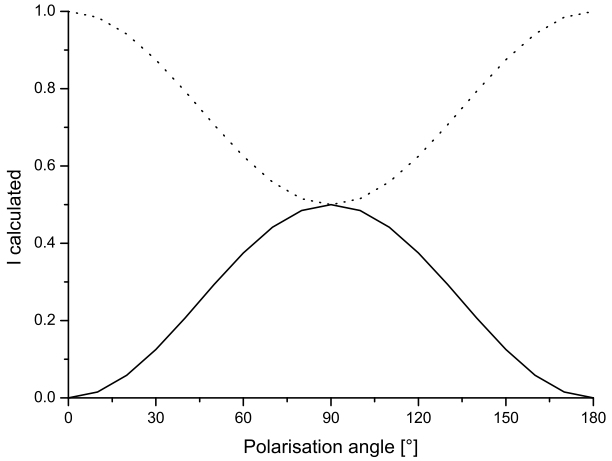

Figure 7.13: Calculated intensity, dependent on polarisation angle, for epitaxial samples grown along the (001) direction. The dotted line indicates the calculated intensity for $\vec{E} \perp \vec{c}$, the solid line for $\vec{E} \parallel \vec{c}$

Polarisation measurements on epitaxial $CuInSe_2$ and $CuGaSe_2$ samples

The calculated predictions of the preceding sections shall now be compared to the measurements. Figure 7.14 shows the measured intensity dependent on the analyser angle for the exciton (filled squares) and the free to bound transitions (open symbols) for

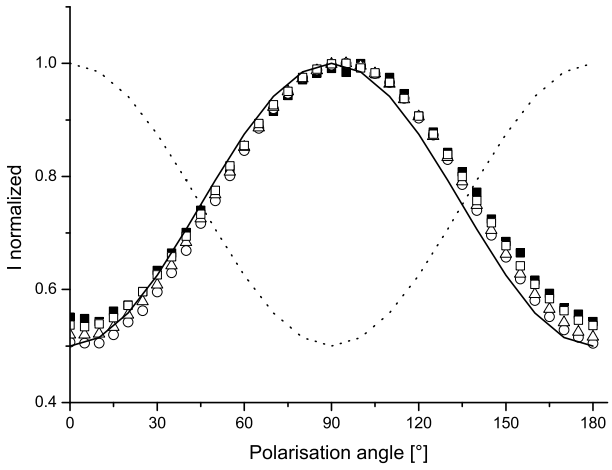

Figure 7.14: Polarisation of the excitonic transition (filled square) and the FB1 (open circle), FB2 (open triangle) and FB3 (open square) for $CuGaSe_2$. The solid black line indicates the expected polarisation angle for $\vec{E} \parallel c$ and the dotted black line for $\vec{E} \perp c$

$CuGaSe_2$ at 45 K. The change from donor-acceptor to free-to-bound transitions at 45 K, has been confirmed by temperature dependent measurements, and the exciton transition by intensity dependent measurements at 10 K. The dashed line indicates the expected polarisation for light polarised perpendicular to the $\vec{c}$-axis, the solid line for light polarised parallel to the $\vec{c}$-axis, as introduced in the previous section. The calculated intensities are scaled to the polarised fraction of the measured intensity. The measurement shows a maximum in polarisation for both the exciton and the free-to-bound transitions at 95°, corresponding to a polarisation parallel to the $\vec{c}$-axis. This is in agreement with results reported previously [145]. The degree of polarisation is 30%. The difference of 5° to the theoretical value is due to a slight misalignment of the analyser. Therefore, the symmetry of the defects could be determined either by the symmetry of the bands or by the site symmetry for a defect being on a metal site. To be able to decide which model is true, the same measurement is performed for a $CuInSe_2$ sample. This will result in the same polarisation if the symmetry of the defect is determined by the symmetry of the lattice site and the opposite polarisation if the symmetry of the defects depend on the band.

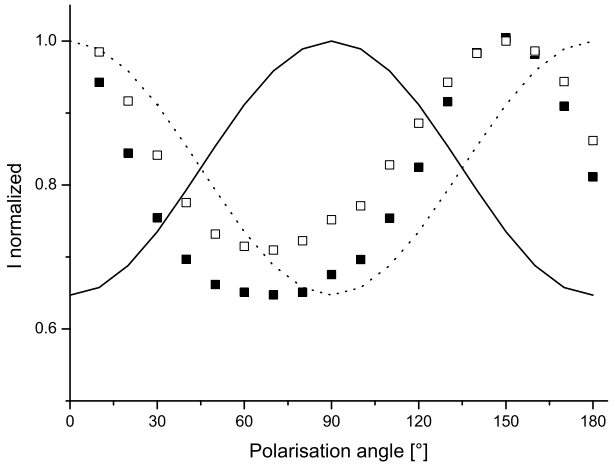

Figure 7.15: Polarisation of the excitonic transition indicated by filled squares and the FB transition indicated by open squares for a A type $CuInSe_2$ sample. The solid black line indicates the expected polarisation angle for $\vec{E} \parallel c$, the dotted black line for $\vec{E} \perp c$

The measurement result for $CuInSe_2$ at 45 K is shown in figure 7.15. The exciton and the free-to-bound transition assigned by position, both show a polarisation maximum at 150°, which is close to a polarisation perpendicular to the $\vec{c}$-axis. Thus the symmetry of the defects is determined by their closest band. The rather large shift of 30° compared to the maximum of the theoretical curve at 180° is most probably due to an alignment error of the zero position of the analyser. Unfortunately when the misalignment was discovered, the sample has been lost and the measurement could not be repeated. The degree of polarisation of the exciton is 21% and that of the free-to-bound transitions 17%.

In summary, both measurements show the same polarisation for the excitonic and the free-to-bound transitions. $CuGaSe_2$ is polarised parallel to the $\vec{c}$-axis, whereas $CuInSe_2$ is polarised perpendicular to the $\vec{c}$-axis. Hence the symmetry of the defects is governed by the symmetry of the bands and the defects do not disturb the symmetry of the bands.

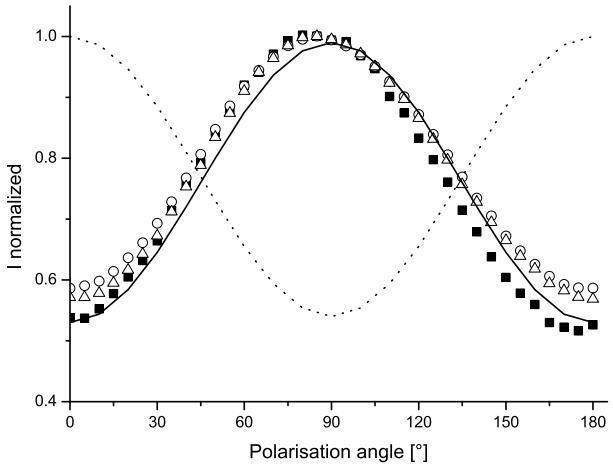

Figure 7.16: Polarisation of the excitonic transition (filled square) and the FB1 (open circle) and FB2(open triangle) for a B type $CuInSe_2$ sample. The solid black line indicates the expected polarisation angle for $\vec{E} \parallel c$ and the dotted black line for $\vec{E} \perp c$

However, as can be seen in figure 7.16, the majority of $CuInSe_2$ samples, including sometimes measurements on a different spot on the same sample, show a polarisation parallel to the $\vec{c}$-axis. Though it is important to notice that, yet as before, the polarisation of the exciton and the free-to-bound transition is the same. Given that the exciton shows the symmetry of the transition between the bands, it follows that the two topmost valence bands must have interchanged. This can happen if the crystal field splitting changes from a positive value, as normally found in $CuInSe_2$,

to a negative $CuGaSe_2$ - like value. As introduced in chapter 7.2.1, strain, as well as gallium diffusion from the GaAs substrate into the epitaxial layer, can influence the crystal field splitting and can therefore influence the band ordering in a sample. Therefore, subsequent investigations into the direction of strain dependent on sample thickness will be carried out by XRD measurements. In the following section XPS measurements are analysed to investigate if gallium diffusion from the $GaAs$ substrate into the sample takes place.

Determination of strain in the epitaxial layers

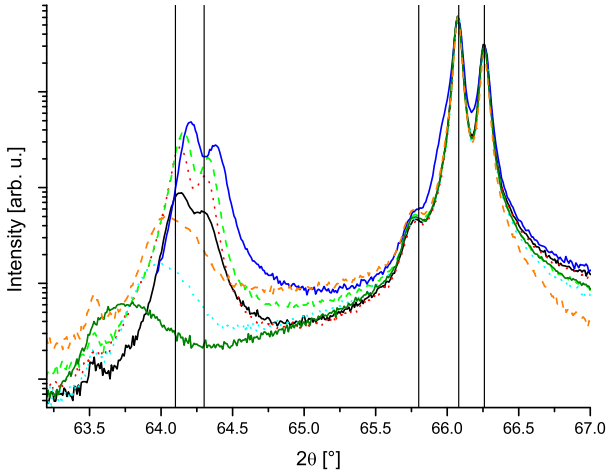

Figure 7.17: θ-2θ XRD scans of epitaxial $CuInSe_2$ samples of different thickness: 1300 nm (dark blue solid line, 800 nm (light green dashed line), 750 nm (red dotted line), 400 nm (black solid line), 300 nm (orange dashed line), 200 nm (light blue dashed line), 100 nm (dark green solid line).

As seen previously in section 7.2.1, strain can have a significant influence on the band ordering in $CuInSe_2$, as tensile stress along the $\vec{c}$-axis will enhance the $CuInSe_2$ like band structure with Γ_6 being the topmost valence band. On the other hand compressive stress parallel to the $\vec{c}$-axis can lead to a switching of the two topmost valence bands, resulting in the Γ_7 valence band on top, which corresponds to a $CuGaSe_2$ like band structure. To investigate how the lattice mismatch between the $GaAs$ substrate and the $CuInSe_2$ epitaxial layer and their different thermal expansion coefficients affect the epitaxial layer, the lattice constant of the $CuInSe_2$ films dependent on the film thickness is determined. For this purpose XRD $\theta - 2\theta$ scans of samples, with thicknesses

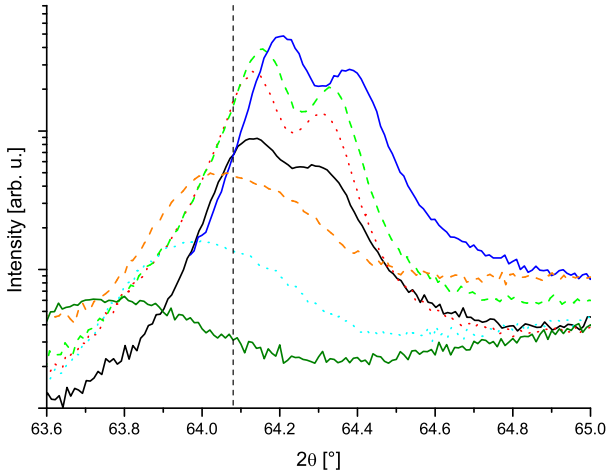

Figure 7.18: Magnified detail of the θ-2θ XRD scans of epitaxial $CuInSe_2$ samples of different thickness as shown in figure 7.17 : 1300 nm (dark blue solid line, 800 nm (light green dashed line), 750 nm (red dotted line), 400 nm (black solid line), 300 nm (orange dashed line), 200 nm (light blue dashed line), 100 nm (dark green solid line). The dashed vertical line indicates the higher diffraction angle value of the ones reported for $CuInSe_2$ in literature.

between 100 nm and 1300 nm, are performed. The result is shown in figure 7.17. The 1300 nm thick sample is indicated by a dark blue, solid line and the 100 nm thin sample by a dark green, continuous line. The samples in between are 750 nm (red dotted line), 400 nm (black solid line), 300 nm (orange dashed line), and 200 nm (light blue dashed line) thick. Figure 7.17 shows five diffraction maxima around 64.1° and 64.3°, 65.8° and at 66.08° and 66.26°. To correct for height errors of the measurement, the measurements have been shifted, so that the $GaAs$ diffraction maximum at 66.08° appears at the correct position in all measurements. The different measured intensities due to different sample sizes, have been taken into account by normalizing to the height of the GaAs diffraction maxima. From the distance between the reflections at 64.1° and 64.3°, and 66.08° and 66.26° and the ratios of the intensities of the neighbouring reflections, it can be deduced that the reflections at 64.3° and 66.26° are due to the $CuK\alpha_2$ radiation contained alongside the $CuK\alpha_1$ in the X-ray beam. The source of the small peak at 65.8° is not yet understood. However, it has occurred also in a measurement of a GaAs waver, so it is not due to the $CuInSe_2$ films. The reflections around 64.1° correspond to the $CuInSe_2$ (008) plane, for which

angles between 63.90° and 64.08° are reported in literature. As already mentioned above, the reflection at 66.08° is due to the (400) plane in GaAs. It shows a broadening of the low angle side of the 1300 nm thick sample, which might be due to strain induced by the $CuInSe_2$ layer into the GaAs substrate. For the thinner samples the width of the $CuInSe_2$ (008) reflection increases. This may either be due to a different amount of strain at different spots of the sample or due to a higher amount of dislocations due to higher strain.

Comparing the diffraction pattern of the samples with varying thickness, a characteristic is the decreasing diffraction angle, corresponding to an increasing lattice constant c with decreasing sample thickness. A change of the lattice constant depending on sample thickness points to pseudomorphic growth. Starting from the critical thickness h_c with increasing film thickness more and more dislocations are formed in the film until the film is fully relaxed.

The second possible source of strain in epitaxial films is the difference in thermal expansion coefficients of the substrate and the layer. However, strain due to different thermal expansion coefficients is discussed in literature as being independent of sample thickness for thin layers [135]. Pseudomorphic growth of a $CuInSe_2$ layer, will lead to tensile stress along the $\vec{c}$-axis. For thin samples the misfit stress will be higher, leading to a higher tensile stress. This matches the behaviour observed for the samples shown in figure 7.17, which show an increase of the lattice constant with decreasing sample thickness, corresponding to an increase of strain due to lattice mismatch. All samples shift to higher diffraction angles with increasing thickness, indicating that the unstrained lattice constant is not yet reached and therefore all samples lie in the pseudomorphic growth regime. The critical thickness, h_c, at which dislocations begin to form and relaxation of the misfit strain starts, can be calculated following the energy or force balance model, according to $h_c \cdot f \sim 80\,nm$ as introduced in chapter 7.2.1. This results for $CuInSe_2$ in a critical thickness of $h_c = 42\,nm$. Thus, it seems initially surprising to observe pseudomorphic growth up to thicknesses of more than 10 times the critical thickness. However, also for other semiconductors the energy and force balance models underestimate the critical thickness an order of magnitude [135].

The thickest sample should be the least strained due to the lattice mismatch, therefore its lattice constant should be closest to the crystal value. The diffraction angle of the 1300 nm thick sample is $2\theta = 64.2°$, as can be seen in figure 7.18, corresponding to a lattice constant of $c = 11.6\mathring{A}$. This is surprising, as the reported angles for $CuInSe_2$ crystals between $2\theta = 63.90°$ and $2\theta = 64.08°$ correspond to lattice constants between $c = 11.65\,\mathring{A}$ and $c = 11.62\,\mathring{A}$. Comparison of the measured lattice constant to the literature values suggests compressive strain instead of tensile strain, as expected for pseudomorphic growth. This might be explained by a height error, due to the adjustment of the height to the GaAs reflection. The difference of the 2θ angle between the different reference files reported for GaAs is $2\theta = 0.024°$. This cannot explain an error of $2\theta \sim 0.2°$ between the measured and the literature values. A second source of error in the height adjustment, might be strain in the GaAs substrate. However as the substrates used are GaAs wavers for epitaxy, it is reasonable to assume that they are unstrained and therefore that the GaAs peak is not shifted. The reason for the difference between the measured and the literature values is thus not due to measurement error. As explained earlier in this section, differences in the thermal expansion coefficient between the substrate and the layer can be another cause of strain in epitaxially grown layers. Since the thermal expansion coefficient $\alpha_{a,CuInSe_2}$ of $CuInSe_2$ perpendicular to the growth direction is larger than the thermal expansion coefficient $\alpha_{a,GaAs}$ of GaAs, the $CuInSe_2$ layer will shrink more during cool down than the GaAs layer. This results in tensile stress in the layer perpendicular to the growth direction. As the volume of the unit cell needs to be conserved, this corresponds to compressive stress along the $\vec{c}$-axis. Given that stress due to pseudomorphic growth and lattice mismatch are independent and can exist at the same time, this seems a reasonable explanation for the observed difference between the measured c lattice constant and the ones reported in literature. In principle, it is now possible to calculate the thickness at which the compressive strain due to the difference in thermal expansion coefficient dominates over the tensile strain due to lattice mismatch. Yet, in order to do so, the lattice constant of a unstrained layer is needed. The values reported in literature indicate, as a trend, larger lattice constants for copper rich samples compared to copper poor samples, however, there also exist reference files opposing this tendency. Due to the lack of an unambiguous value for the unstrained lattice constant, no sample thickness at which the samples change from tensile to compressive strain can be given. However, for thicker samples, compressive strain due to thermal mismatch will dom-

inate, whereas for thinner samples, tensile strain due to lattice mismatch will prevail.
A further factor which could influence the strain in the epitaxial layer is the $Cu_{2-x}Se$ secondary phase, occurring on top of copper rich $CuInSe_2$ samples, during growth. Yet $Cu_{2-x}Se$ has a cubic structure with a lattice constant of $a = 5.75\mathring{A}$ and this is between the values for $GaAs$ and $CuInSe_2$. As $Cu_{2-x}Se$ grows as islands or thin layers, compared to the $CuInSe_2$ layer, the influence of $Cu_{2-x}Se$ should be negligible.

Determination of gallium content of $Cu(In,Ga)Se_2$ samples by XPS measurements

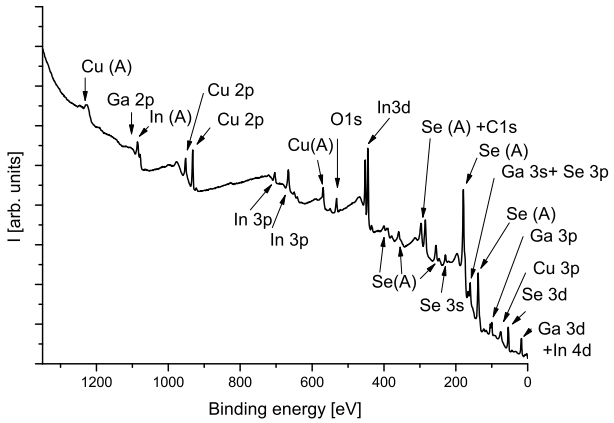

Figure 7.19: XPS spectrum measured with AlK_α radiation.

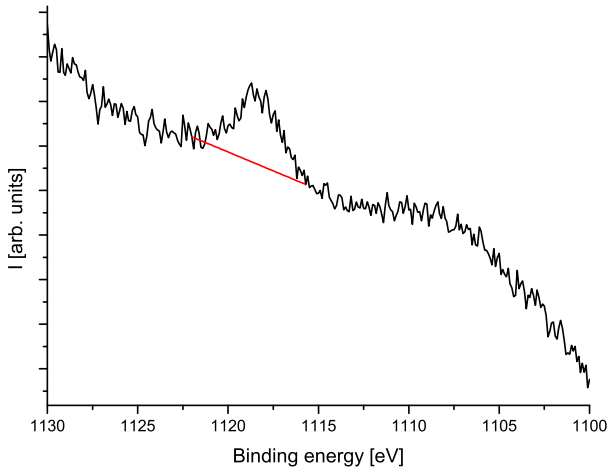

Figure 7.20: Magnified $Ga2p3$ peak of the spectrum shown in figure 7.19.

[at%]	Ga	Cu	O	In	C	Se
AlKα	0.08	4.8	12.2	10.4	55.8	16.7

Table 7.9: Elemental composition determined from XPS result shown in figure 7.19.

As discussed in section 7.2.1 the band ordering in a $Cu(In,Ga)Se_2$ sample depends on its gallium content. Since the $CuInSe_2$ epitaxial samples are grown on a GaAs substrate, gallium may diffuse from the substrate into the $CuInSe_2$ epitaxial layer forming $Cu(In_{1-x}Ga_x)Se_2$, with x being a small amount of gallium. Already small amounts of gallium can lead to a switching of the two topmost valence bands as seen in figure 7.7 (p.72). To investigate if gallium diffusions into the $CuInSe_2$ layer takes place, XPS measurements of the surface are performed. Figure 7.19 shows a XPS spectrum of a 800 nm thick epitaxial $CuInSe_2$ layer measured with AlK_α radiation. The peaks can be assigned to the different elements contained in the sample due to their binding energy. Comparing measurements with AlK_α and MgK_α radiation allows to differentiate between Auger and XPS peaks. The Auger peaks are indicated in figure 7.19 by A. The amount of an element contained in the sample is determined by the area below the corresponding XPS peak. However, to determine the area of the peak, the measured signal needs to be corrected for the background due to secondary electrons, which are created when the photoelectron is inelastically scattered on its way through the sample. As can be seen in figure 7.19, the background due to secondary electrons increases with increasing binding energy. Figure 7.20 shows an example of a magnified detail of figure 7.19 containing the $Ga2p3$ peak and its background correction. Additionally, the peak area needs to be corrected for the escaping cross section, which depends on the X-ray energy, the element and the orbital. The composition according to the spectrum shown in figure 7.19 is given in table 7.9. The most prominent feature is the high oxygen and carbon content, which is due to surface contamination. As the sample was to not be damaged, in order to be able to use it for further investigations, it was not sputtered before performing the XPS measurement, which results in a high surface contamination. As expected, the sample contains copper, indium and selenium, but also a minor gallium content can be found. It is interesting to compare the two Ga XPS peaks at 1118 eV ($2p\frac{3}{2}$) and 104 eV ($3p\frac{3}{2}$) in figure 7.19. The $Ga2p\frac{3}{2}$ peak at 1118 eV is normally the strongest peak visible in a Ga XPS spec-

trum and is about 10 times stronger than the peak due to the $Ga3p\frac{3}{2}$ level. As the peaks with higher binding energy result from within the first 1 nm of the sample, whereas approximately 10 nm of the sample contributes to the peaks with lower binding energy, the weak $Ga2p\frac{3}{2}$ peak at 1118 nm compared to the $Ga3p\frac{3}{2}$ peak at 104 nm points to a Ga gradient in the sample. A Ga gradient due to diffusion of Ga from the GaAs substrate into the $Cu(In,Ga)Se_2$ layer has also been observed previously [146]. As photoluminescence measurements have a higher penetration depth than XPS measurements, the gallium content probed by photoluminescence measurements will be higher.

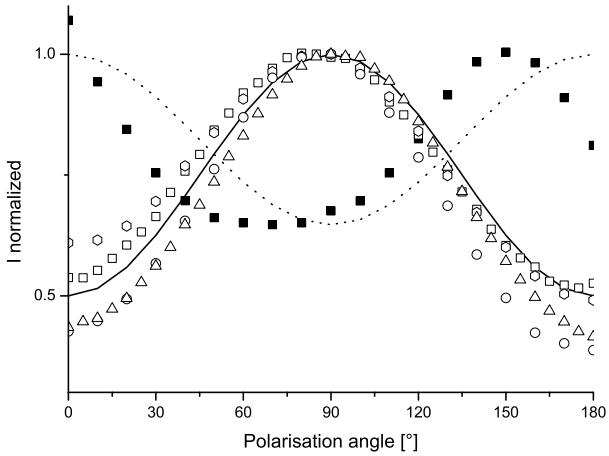

Figure 7.21: Polarisation of the excitonic transition of samples of different thickness: 1300 nm (triangle), 800 nm first spot (filled squares), 800 nm second spot (open squares), 300 nm (pentagon) and 200 nm (circle). The solid black line indicates the expected polarisation angle for $\vec{E} \parallel c$ and the dotted black line for $\vec{E} \perp c$

Discussion

Summarising the result of the XRD investigations, tensile lattice strain along the $\vec{c}$-axis in the pseudomorphic growth regime will enhance the $CuInSe_2$-like band structure in thin samples. For thicker samples, very small compressive strain due to the different thermal expansion coefficients for $CuInSe_2$ and $GaAs$ will prevail. However, the thickness at which the dominating strain changes from tensile to compressive could not be determined from XRD measurements. Therefore, figure 7.21 shows the polarisation of the exciton measured on samples with varying thickness, which reflects the band ordering and therefore the crystal field. For the thickest sample, with a layer thickness of 1300 nm, which is indicated by triangles, a polarisation parallel to the $\vec{c}$-axis is observed, as expected for a sample dominated by compressive strain. However, all other investigated samples with thicknesses as thin as 200 nm also show a polarisation parallel to the $\vec{c}$-axis. Only for the 800 nm thick sample, polarisation parallel as well as perpendicular to the $\vec{c}$-axis is detected on different spots. This is rather surprising as for the thin samples, which according to the XRD measurements lie in the pseudomorphic growth regime, tensile stress is expected to enhance the $CuInSe_2$-like band structure.

XPS measurements revealed that gallium diffusion from the GaAs substrate into the $CuInSe_2$ layer takes place. A gallium gradient over the sample depth, for close to stoichiometric samples is reported [147]. This might result in a higher gallium content in the first 100 nm of the sample probed by photoluminescence measurements for thin samples compared to thicker samples. The 800 nm thick sample seems to be thin enough to be not completely dominated by compressive strain, but on the other hand thick enough that there exist spots in which the gallium content is not sufficient to alter the band order. The gallium gradient in the samples dependent on their thickness could be determined by SIMS or depth resolved Auger measurements. However, the influence of gallium should also be reflected in a shift of the exciton to higher energies in $CuInSe_2$ samples, which are polarised parallel to the $\vec{c}$-axis, compared to spots polarised perpendicular to the $\vec{c}$-axis. Figure 7.22 compares the position of the exciton measured on two spots showing different polarisation on the 800 nm thick sample. The dotted line corresponds the spectrum of the spot showing polarisation perpendicular to the $\vec{c}$-axis, whereas the solid line represents the spectrum of the spot showing polarisation parallel to the $\vec{c}$-axis.

The exciton of the spot polarised parallel to the $\vec{c}$-axis (solid line) is shifted 14 meV to higher energies compared to the spot polarised perpendicular to the $\vec{c}$-axis (dotted line). Yet, this shift might also be due to strain variation in the sample. To investigate this in more detail figure 7.23 shows the (008) XRD diffraction maximum of this sample. Taking the full width half maximum as a measure for the strain variation over the sample, results in $\Delta\frac{c}{a} = 4.07 \cdot 10^{-3}$. Hence the change in crystal field splitting can be calculated according to equation 7.18 to $\Delta_{CF} = \frac{3}{2}b(\Delta\frac{c}{a}) = 6.1\,meV$. Thus the shift of the

exciton is at least partially due to gallium diffusion into the $CuInSe_2$ layer.

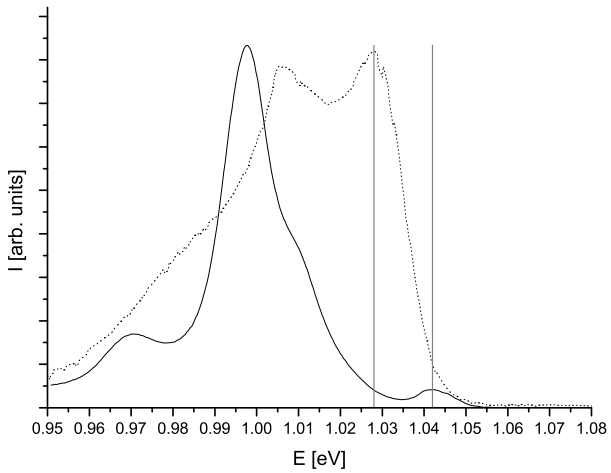

Figure 7.22: Photoluminescence spectra measured at two different spots of the 800 nm thick sample. The dotted line corresponds the spectrum of the spot showing polarisation perpendicular to the $\vec{c}$-axis, whereas the solid line represents the spectrum of the spot showing polarisation parallel to the $\vec{c}$-axis. The grey lines indicate the positions of the exciton.

Conclusion

The defect related photoluminescence transitions showed the same polarisation as the exciton in all investigated epitaxial samples indicating that the symmetry of the defects is determined by their closest band and not by the site symmetry of the defect. Yet the investigations on epitaxial $CuInSe_2$ samples also revealed that, due to strain and gallium diffusion from the GaAs substrate into the epitaxial layer, most $CuInSe_2$ samples showed a $CuGaSe_2$ like band structure. Therefore, to exclude the influence of strain and gallium diffusion, the polarisation of defects in a $CuInSe_2$ crystal will be investigated in the next section.

7.4.2 Symmetry of defects determined from measurements on a $CuInSe_2$ crystal

Orientation of the crystal

To be able to measure the polarisation relative to the $\vec{c}$-axis, the direction of the $\vec{c}$-axis relative to the sample surface needs to be known. Therefore XRD

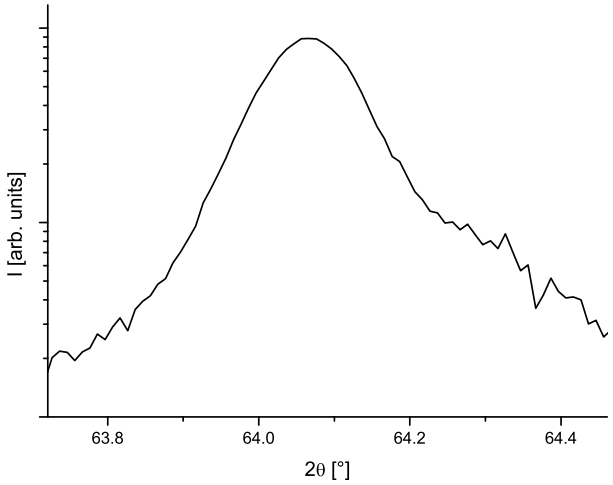

Figure 7.23: $\theta - 2\theta$ XRD scan of the 800 nm thick sample showing polarisation parallel as well as perpendicular to the $\vec{c}$-axis.

measurements are performed to determine the orientation of the $CuInSe_2$ crystal. A $\theta - 2\theta$ scan of the sample is shown in figure 7.24. Three diffraction maxima at $2\theta = 24.1°$, 26.7° and 54.9° are observed. The two main diffraction maxima at 26.8° and 54.9° correspond to the (112) and (224) lattice planes. The diffraction maximum at $2\theta = 24.1°$ is an artefact due to the $CuK\beta$ radiation. Thus the (112) lattice plane, which corresponds to the (111) plane in a cubic crystal, is parallel to the sample surface. The surface normal of the (112) plane and the $\vec{c}$-axis enclose an angle of 54.6°, therefore the $\vec{c}$-axis will lie on a cone with an opening angle of 109.1°. On this cone three reflections will be observed, corresponding to the $\vec{c}$-axis and the two possible $\vec{a}$ directions. The three axis enclose an angle of 120° to each other as depicted in figure 7.25. As an intermediate step, before continuing to determine the orientation of the $\vec{c}$-axis, it needs to be validated that the sample is single crystalline. Therefore, rocking curve measurements are performed as depicted in figure 7.26. One narrow diffraction maximum at 11.8° with a full width half maximum of 0.04° is observed. This verifies that the sample is single crystalline, as crystallites with slightly other orientations should be visible in the form of a broadening or as a shoulder. Yet, the appearance of the reflection at $\theta = 11.8°$ instead of $\theta = 13.29°$ as one would expect for a lattice plane exactly parallel to the surface, reveals that the sample was not glued completely flat to the sample holder, but is tilted by about 1°. With the knowledge, that one distinct $\vec{c}$-axis exists, its direction can be deter-

mined. In order that the cone on which the $\vec{c}$-axis will be lies in the measurement plane, the sample is tilted by $\chi = 35.43°$, as depicted in figure 7.27. It must be kept in mind that angles in XRD are measured relative to the sample surface and not as in optics to the surface normal. Subsequently the sample is rotated about ϕ to determine the orientation of the $\vec{c}$-axis. The result is shown in figure 7.28. As expected, three reflections are observed. They appear at angles of 116°, 235° and 358°. To distinguish the two $\vec{a}$ directions from the $\vec{c}$ direction, $\theta - 2\theta$ scans at $\chi = 35.26°$ and $\phi = 116°, 235°$ and $358°$ are performed as indicated by the dashed, dotted and solid line in figure 7.28. For the (008) plane, a reflection at 64.01° is expected, whereas the reflections belonging to the (400) planes correspond to an diffraction angle of 64.39°. This matches the result in figure 7.29: one reflection at smaller and two at higher angles. Thus the $\vec{c}$-axis points at 358°.

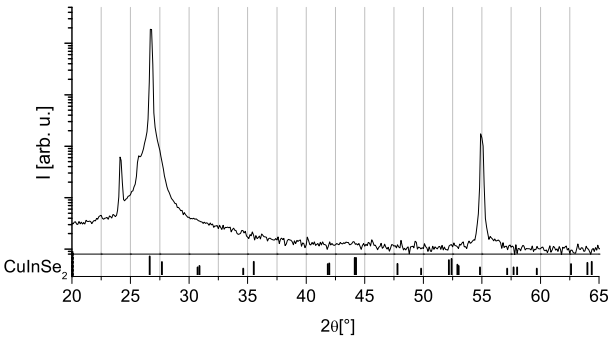

Figure 7.24: $\theta - 2\theta$ XRD scan of the $CuInSe_2$ crystal. The two main diffraction maxima at 26.8° and 54.9° correspond to the (112) and (224) plane.

Calculation of the expected polarisation angles and degrees of polarisation

Figure 7.30 shows the $CuInSe_2$ crystal sample mounted to the sample holder for photoluminescence measurements. As determined by the XRD measurements in the previous section the $\vec{c}$-axis encloses an angle of $\alpha = 2°$ with the long axis of the sample indicated by the dash dotted line and an angle of $\beta = 35°$ with the sample surface. As the $\vec{c}$-axis is not parallel to the surface normal anymore, the measured polarisation will depend on the orientation of the sample relative to the sample holder. Therefore, in addition to the **sample holder** and **detection coordinates systems** depicted in figure 4.3 (p. 19) and used to describe the epitaxial samples, a **sample coordinate system** is introduced. The sample coordinate

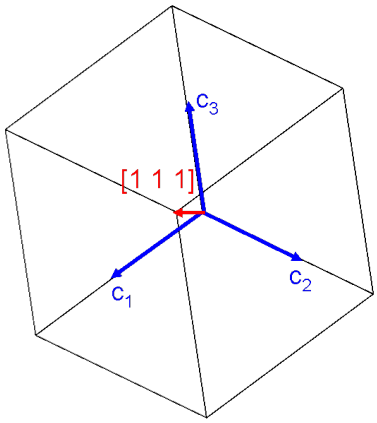

Figure 7.25: Possible orientations of the $\vec{c}$-axis in a tetragonal unit cell orientated in a way that the (112) lattice plane is parallel to the paper.

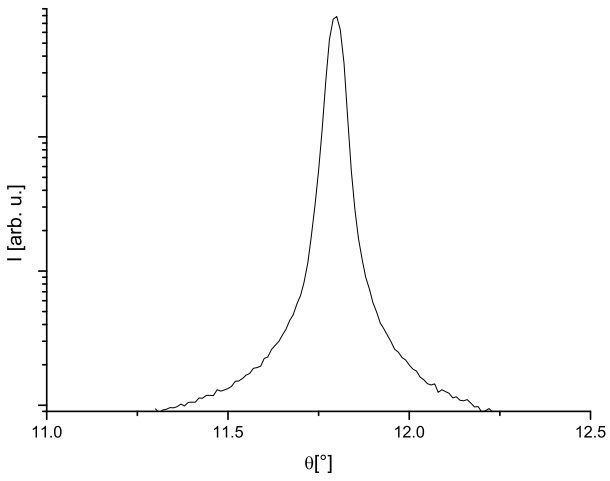

Figure 7.26: Rocking curve measurement.

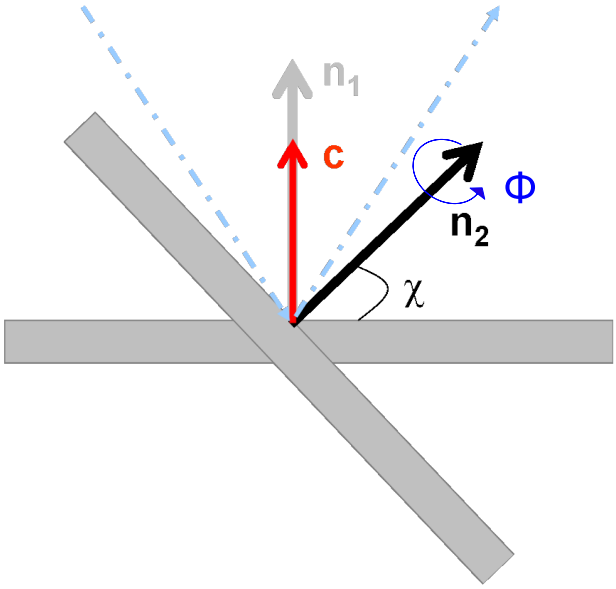

Figure 7.27: Tilt of the sample relative to the θ-2θ measurement plane for Φ-scans: for the $\vec{c}$-axis to lie in the measurement plane the sample needs to be tilted by $\chi = 35.43°$. The light blue arrows indicate the incoming and the diffracted X-ray beam, this is the measurement plane. n_1 indicates the orientation of the surface normal of the sample in the standard setup and n_2 the orientation of the surface normal of the tilted sample.

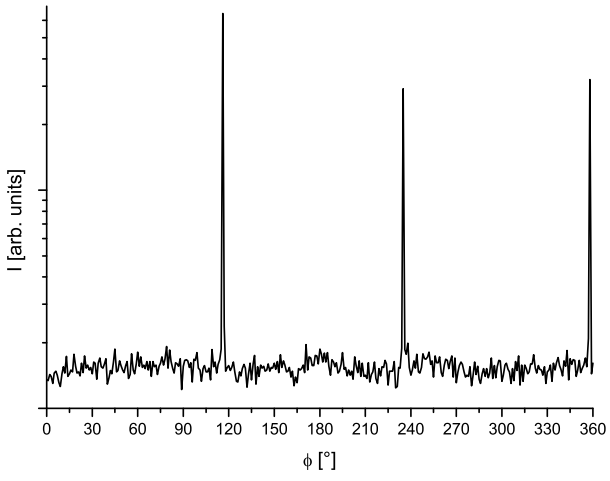

Figure 7.28: ϕ scan for the (008) reflection with $\chi = 35.43°$.

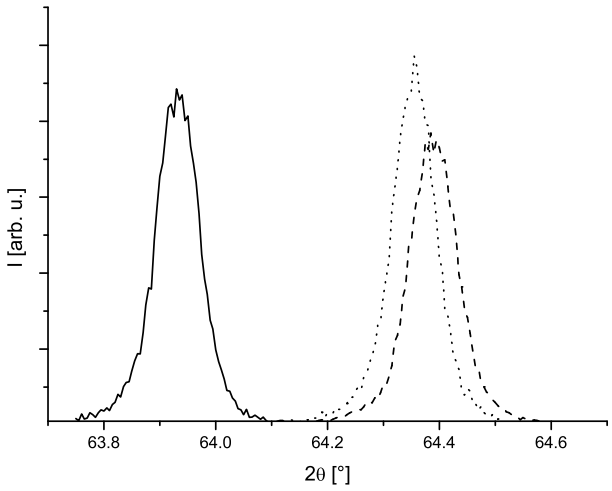

Figure 7.29: $\theta - 2\theta$ XRD scans with $\chi = 35.26°$ and $\phi = 116°$ (dashed line), $\phi = 235°$ (dotted line) and $\phi = 358°$ (solid line).

system is indicated by y_s and z_s. The angle between the $\vec{y_s}$-axis of the sample coordinate system and the $\vec{y_{sh}}$-axis of the sample holder coordinate system is given by θ. Figure 7.31 shows the orientation of the sample relative to the sample holder for $\theta = 0°$ on the left hand side and $\theta = 90°$ on the right hand side. The calculation of the expected polarisation parallel and perpendicular to the $\vec{c}$-axis in the detection plane is carried out in several steps: first the orientation of the $\vec{c}$-axis relative to the sample holder coordinate system needs to be calculated. This result is converted by a rotation of 45° into the coordinate system of the detection plane. Subsequent the fraction parallel and perpendicular to the $\vec{c}$-axis can be calculated. The script used for this calculation is given in appendix A.5. The calculated polarisation is depicted in the first row of figure 7.32 for $\theta = 0°$ and $\theta = 90°$. The black dotted line indicates the expected intensity dependent on analyser angle for photoluminescence polarised perpendicular to the $\vec{c}$-axis, the continuous black line for light parallel to the $\vec{c}$-axis. For $\theta = 0°$ light polarised perpendicular to the $\vec{c}$-axis results in a maximum at 60°, which is detectable in full intensity in this geometry. The degree of polarisation equals 74%. Light polarised parallel to the $\vec{c}$-axis gives rise to a maximum at 150°. Due to the measurement geometry only 85% of the initial intensity is detectable. The light is fully polarised. In the $\theta = 90°$ geometry, polarisation parallel to the $\vec{c}$-axis causes a maximum at 80°, however only 3% of the initial intensity can be observed in the detection plane. This can be understood, by recalling that in the $\theta = 90°$ orientation

the $\vec{c}$-axis is almost parallel to the $\vec{x_D}$-axis of the detection system. Therefore almost no light polarised parallel to the $\vec{c}$-axis lies in the detection plane. The part of the light polarised parallel to the $\vec{c}$-axis, which can be detected, is 100% polarised. Polarisation perpendicular to the $\vec{c}$-axis leads to a maximum at 170°, which lies completely in the detection plane so the entire intensity is detected. However, as the plane perpendicular to the $\vec{c}$-axis is almost parallel to the detection plane, all possible orientations perpendicular to the $\vec{c}$-axis contribute similar amounts. This results in a degree of polarisation of only 2%.

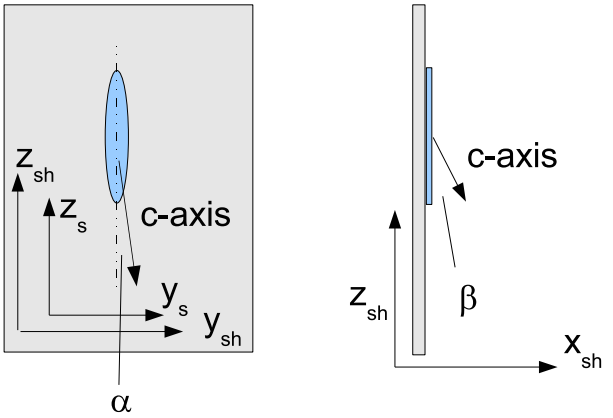

Figure 7.30: Top view and view from the side of the $CuInSe_2$ crystal sample mounted to the sample holder for PL measurements. The $\vec{c}$-axis encloses an angle of $\alpha = 2°$ with the long axis of the sample indicated by the dash dotted line and an angle of $\beta = 35°$ with the sample surface. y_s and z_s indicate the sample coordinate system, whereas x_{sh}, y_{sh} and z_{sh} represent the sample holder coordinate system.

Polarisation of the photoluminescence transitions measured on the crystal

Now the measured polarisation shall be compared to the calculated predictions in the previous section. Figure 7.33 shows the photoluminescence spectrum of the crystal at 10 K and 10 mW and 70 mW excitation power. The spectrum shows five peaks at 1.036 eV, 1.001 eV, 0.970 eV 0.941 eV and 0.898 eV. Due to the hydrogen absorption line around 0.9 eV the lowest energy peak at 0.898 eV appears to be divided into two parts. From the appearance only at high excitation powers and its high energy, the peak at 1.036 eV might be assigned to an exciton. From the positions, the remaining peaks can be assigned to being a slightly shifted DA 1 for the peak at 1.001 eV,

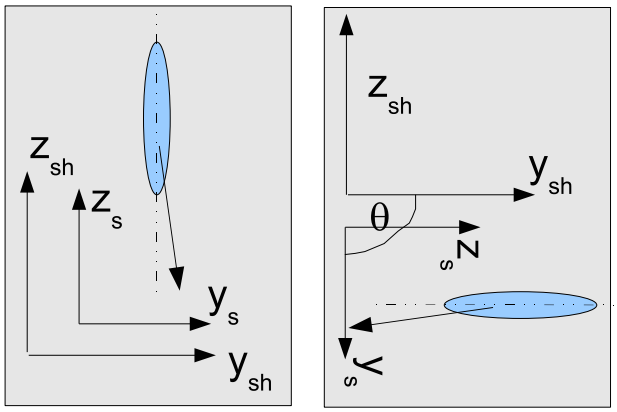

Figure 7.31: Orientation of the sample with respect to the sample holder for $\theta = 0°$ (left) and $\theta = 90°$ (right).

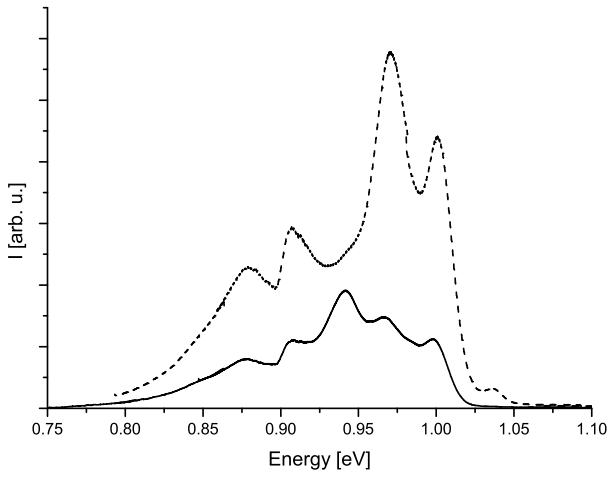

Figure 7.33: Photoluminescence spectrum of the $CuInSe_2$ crystal at 10 K measured at 10 mW (solid line) and 70 mW (dashed line) excitation power.

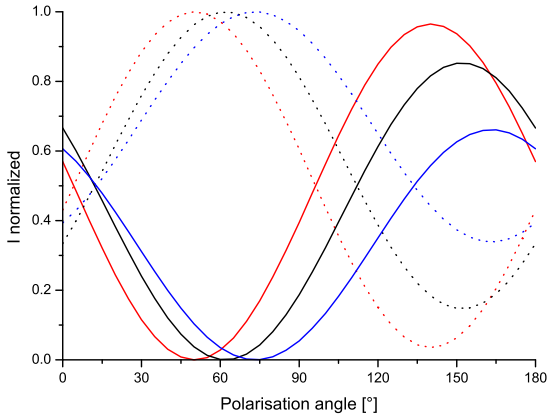

(a) *theta* = 0° calculated polarisation dependence

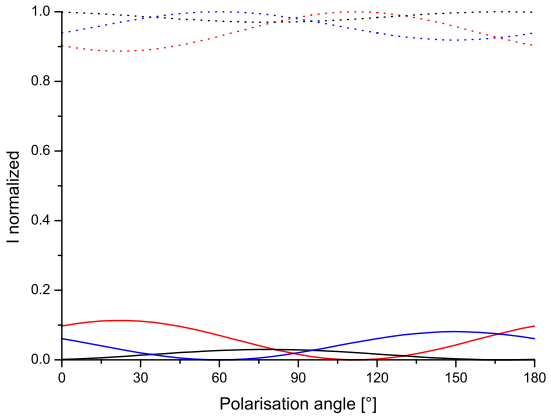

(b) *theta* = 90° calculated polarisation dependence

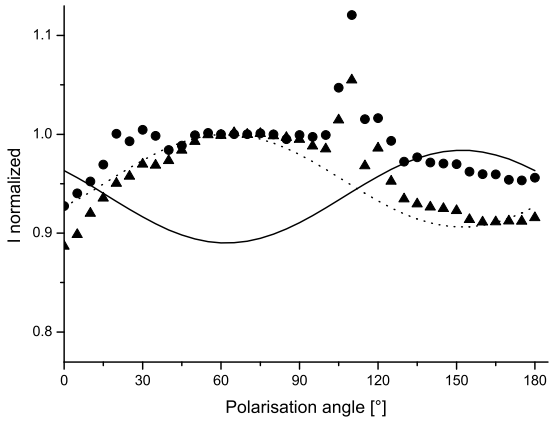

(c) *theta* = 0° measured polarisation dependence

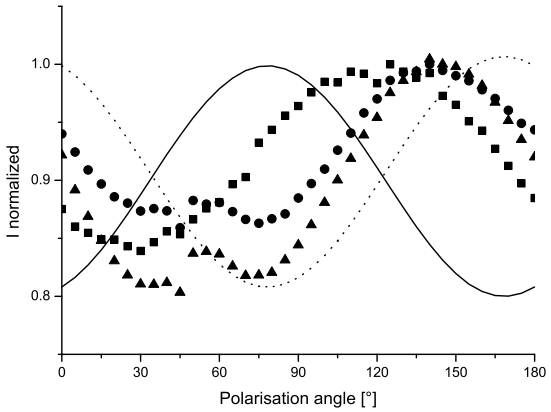

(d) *theta* = 90° measured polarisation dependence

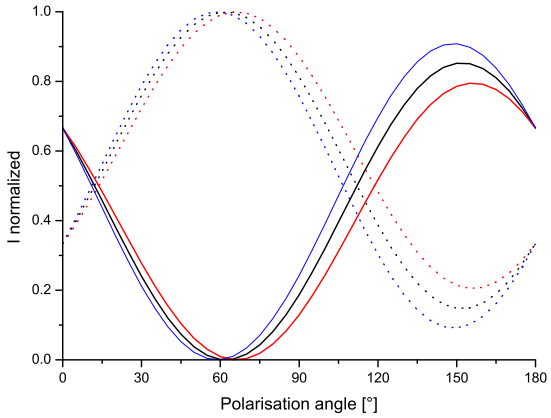

(e) *theta* = 0° calculated polarisation dependence

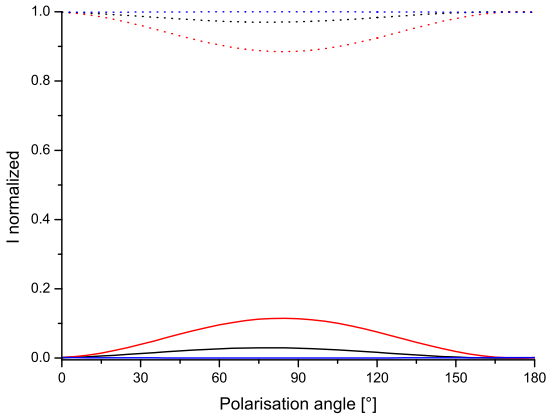

(f) *theta* = 90° calculated polarisation dependence

Figure 7.32: First row: calculated polarisation for light polarised $\perp$ to the $\vec{c}$-axis (black dotted line) and light polarised $\parallel$ to the $\vec{c}$-axis (black solid line) for the sample orientations $\theta = 0°$ and 90°. The red and blue lines indicate an error of $\Delta\theta = -20°$ and $\Delta\theta = +20°$, respectively. Second row: measured polarisations for the two different sample orientations: Squares correspond to DA1, triangles and circles to DA2 and DA3 transitions, respectively. The calculated intensities are scaled to the degree of polarisation of the measurements. Third row: influence on polarisation of an adjustment error for the angle ϕ. $\Delta\phi = -10°$ is indicated by red lines, whereas $\Delta\phi = +10°$ is represented by blue lines.

and DA 2 and DA 3 for the peaks at 0.970 eV and 0.941 eV, respectively. The fourth peak at 0.898 eV might be due to an extrinsic defect caused by iodine, as the sample was grown by iodine vapour transport. A general problem of the polarisation dependent photoluminescence measurements on the $CuInSe_2$ crystal was its low degree of polarisation. Temperature dependent measurement showed that below 100 K the angle of polarisation is independent of temperature, but the degree of polarisation increases with decreasing temperature, the presented measurements in the second row of figure 7.32 are measured at 10 K. A further difficulty arose from the change of polarisation filter. The intention was to be able to place the polarisation filter into the parallel part of the beam to minimise errors due to the incident angle of the beam on the polarisation filter. However, after some time it turned out that the new polarisation filter, in combination with the notch filter, produces artefacts. The appearance of the artefacts will be explained in more detail in appendix A.6. This implicated that sometimes the artefacts overlapped with the polarisation maximum and especially for only weakly polarised measurements it was therefore not possible to determine the polarisation maximum. This reduced the measurements in different sample orientations further.

Figure 7.32c shows the measured polarisation of the $CuInSe_2$ sample in the $theta = 0°$ orientation. The outliers around 110° and 25° are due to a too close position of the new polarisation and the Notch filter as discussed above. The measurement shows a maximum at 70° and is 6.5% polarised. The polarisation maximum is close to the polarisation maximum predicted for polarisation perpendicular to the $\vec{c}$-axis at 60° for this measurement geometry. However the degree of polarisation is much less than expected. Other measurements in this sample orientation were stronger polarised, but their maximum appeared at higher polarisation angles between 90° up to 105°. Yet, those later measurements might have a bigger error in sample orientation. The measurement at $theta = 90°$ presented in figure 7.32d, shows a maximum at 125° for the transition at 1.001 eV indicated by squares and at 145° for the transitions at 0.970 eV and 0.941 eV represented by triangles and circles. That is a rather surprising result, because for other measurements all transitions showed the same polarisation. As the polarisation peak also appears to be wider than the cos^2 function expected, one may wonder, if for this measurement some measurement artefact overlays the measurement. The degree of polarisation is around 9%, which is also stronger than expected in this measurement geometry. As described above, for a $theta = 90°$ orientation of the sample, one would expect a polarisation maxima for light polarised parallel to the $\vec{c}$-axis at 80° and for light perpendicular to the $\vec{c}$-axis at 170°. So the measurement with $\theta = 90°$ might point slightly more to a polarisation perpendicular to the $\vec{c}$-axis, however no clear assignment is possible. Also the degree of polarisation is higher than expected. A common feature of all my measurements on the $CuInSe_2$ crystal is a shift of the polarisation maximum compared to the calculated values. One possible reason could be measurements inaccuracies in the angle θ indicating the sample orientation on the sample holder or the angle ϕ, between the normal of the sample and the direction of detection x_D. Therefore the influence of an error of $\Delta\theta = \pm 20°$ was calculated and is indicated in figure 7.32a and 7.32b by blue and red lines. A rather large error of $\Delta\theta = \pm 20°$ leads to a change in the position of the polarisation maximum for the $\theta = 0°$ orientation of about 15°. For light polarised parallel to the $\vec{c}$-axis the degree of polarisation is independent of the error in θ and always 100%. For light polarised perpendicular to the $\vec{c}$-axis, the degree of polarisation varies between 50% and 95%. For the measurements in $\theta = 90°$ orientation an error of $\Delta\theta = \pm 20°$ can lead to a shift in the position of the polarisation maximum of up to 70°. The degree of polarisation for light polarised perpendicular to the $\vec{c}$-axis increases up to 6 %. Inaccuracies in the angle ϕ as represented in figure 7.32e and 7.32f only slightly influence the positions of maximum intensity for both measurement geometries. The error is found to be close to the measurement resolution of 5°. The degree of polarisation for measurements polarised perpendicular to the $\vec{c}$-axis changes for measurements in the $\theta = 0$ geometry between 65% and 85% and in the $\theta = 90$ geometry between 0% and 5%. As measurements in the $\theta = 90°$ geometry apparently are very sensitive to adjustment errors, other measurement orientations should be preferred to determine the angle of maximum polarisation. Yet, as mentioned above, due to artefacts overlaying with the measurement, measurements in other sample orientation could not be analysed. Comparing the calculated error for the measurements in $\theta = 0°$ orientation with the observed shift in the measurements, implies that an additional source of error must exist. A possible source might be compensation of the sample. This could neither be ruled out, nor validated by intensity dependent measurements. Yet, until now the source

of the shift is not understood. To conclude, the symmetry of defects observed in epitaxial samples could not be confirmed by polarisation measurements on a $CuInSe_2$ crystal. However, the polarisation measurement results from the crystal also do not contradict the findings of the measurements on the epitaxial films.

7.4.3 Conclusion

In this chapter the symmetry of intrinsic defects in the chalcopyrites $CuInSe_2$ and $CuGaSe_2$ were investigated. Measurements on epitaxial thin chalcopyrite films, showed always the same polarisation for the exciton, indicating the symmetry of the bands, and the defect related transition. Thus the symmetry of the defects is determined by its closest band and not by its site symmetry. Yet, it also emerged, that due to the small crystal field splitting in $CuInSe_2$, small amounts of gallium or compressive stress are sufficient to switch the two topmost valence bands leading to a $CuGaSe_2$ like band structure.

Chapter 8

Conclusion and outlook

The aim of this thesis was to investigate the symmetries of defects in chalcopyrites and defects in kesterites. Polarisation-dependent photoluminescence measurements on epitaxial thin $CuInSe_2$ and $CuGaSe_2$ films revealed that the intrinsic defects always show the same polarisation as the exciton, indicating that the symmetry of the defect equals the symmetry of its closest band and is independent of the site symmetry of the defect. Yet the measurements also show, that due to the small crystal field splitting in $CuInSe_2$ even small amounts of gallium diffusion from the GaAs substrate into the epitaxial $CuInSe_2$ layer or compressive strain are sufficient to invert the two topmost valence bands, leading to a $CuGaSe_2$-like band structure.

In the first part of the thesis Cu_2ZnSnX_4, with X being sulphur or selenium, was investigated as an indium free alternative to $CuInSe_2$, consisting only of non-toxic, abundant elements. One source of difficulty in synthesising $Cu_2ZnSnS(e)_4$ samples, due to its narrow formation range, is the problem of secondary phases. The standard method to identify secondary phases is XRD $\theta - 2\theta$ scans. However, as $Cu_2ZnSnSe_4$, Cu_2SnSe_3 and $ZnSe$ and their equivalents in the sulphide system have very similar lattice constants and similar structures, the diffraction maxima of all three phases occur at similar angles. Therefore it is difficult to exclude Cu_2SnSe_3 and $ZnSe$ secondary phases from XRD measurements. Hence, photoluminescence measurements were tested as an additional tool of identifying secondary phases. It turned out, that Cu_2SnS_3 and $ZnSe$ show peaks which are well separated from those of kesterite, and therefore can be identified by photoluminescence measurements. Thus, as Cu_xS, Cu_xSe, Sn_xS_y and Sn_xSe_y can be identified by XRD measurements and Cu_2SnS_3 and $ZnSe$ by photoluminescence measurements, only Cu_2SnSe_3 and ZnS remain intractable. At the moment Raman measurements in cooperation with a research group in Barcelona are in progress, to investigate if Cu_2SnSe_3 and ZnS can be distinguished from the other phases by such measurements.

As $Cu_2ZnSnS(e)_4$ is expected to be doped intrinsically, the device properties will depend on the native defects. To investigate the defects present in the samples, photoluminescence measurements were performed. Polycrystalline $Cu_2ZnSnSe_4$ samples showed wide asymmetric photoluminescence peaks around 0.9 eV. A temperature and intensity dependent behaviour corresponding to a sample dominated by fluctuating electrostatic potentials was observed for a Zn rich sample. The energy position of the photoluminescence peak of Cu rich samples was nearly independent of excitation intensity and temperature in the investigated intensity and temperature range. This is an unexpected result, which deserves to be investigated in more detail. A possible explanation might be a wide distribution of deep defects, whose energy position does not depend on the band position. It will be interesting to investigate in more detail how composition influences the observable defects, their activation energy and their behaviour as trapping or recombination center, as well as the influence of composition on the defect density.

Comparing the expected properties of defects in $Cu_2ZnSnS(e)_4$ to the known properties of defects in $Cu(In,Ga)Se_2$ several differences might arise:

- Most probably the degree of freedom for the $\frac{Zn}{Sn}$ and $\frac{Cu}{Zn+Sn}$ ratio in which kesterite and no secondary phases form is much narrower than the possible $\frac{Cu}{In}$ ratios observed for $CuInSe_2$, thus limiting the possible stoichiometry range.

- As the calculated defect formation enthalpies especially for copper related defects in kesterites

are even smaller in Cu_2ZnSnS_4 than in the chalcopyrites, the defect density will probably be higher.

- If the $Cu_2ZnSnS(e)_4$ sample assumes the crystal structure with the lowest possible formation energy might be influenced by the synthesis method used.

Up to the present, the crystal structure of Cu_2ZnSnS_4 and $Cu_2ZnSnSe_4$, this is kesterite or stannite is difficult to access and no systematic experimental investigations of its influence on the electric properties exist.

The difference between the kesterite or stannite structure, is the copper and zinc ordering. Due to the small difference in atomic form factor for zinc and copper, owing to the similar number of electrons, they cannot be distinguished in standard XRD diffraction experiments. Yet, [30] reports that the dielectric function at the band edge is strongly anisotropic in stannite compounds compared to kesterite compounds, favouring absorption perpendicular to the $\vec{c}$-axis. Therefore polarisation dependent photoluminescence measurements on epitaxial $Cu_2ZnSnS(e)_4$ samples, can serve as a tool to distinguish the kesterite from the stannite structure. This would make it possible to investigate whether or not, the two different structures have an influence on the electrical properties of the material.

Acknowledgements

A lot of persons contributed to this work, whom I would like to thank:

Zuallererst möchte ich ganz herzlich Susanne Siebentritt danken, für viel Enthusiasmus, geduldiges Diskutieren von Ergebnissen, dafür dass sie immer ein offenes Ohr hat, das Ermöglichen vieler toller Sommerkurse und Konferenzen und ihren großen Einsatz für unsere Gruppe.

Uwe Rau and Roland Sanctuary for being part of my CET committee.

Susan Schorr and Alex Redinger for being part of the jury.

Alex Redinger, Dominik Berg, Guillaume Zoppi, Jes Larsen, Jon Major, Jonathan Scragg, Levent Gütay, Mare Altosaar, Susan Schorr and Yvonne Tomm for the samples.

Danielle Schoder für die unzähligen organisatorischen Kleinigkeiten, um die sie sich kümmert und die nur auffallen, wenn sie nicht da ist und sie dann nicht klappen

Thomas Schuler für das Reparieren und Programmieren jeglicher Geräte und tolle Konzerte und Feten in Losheim

Michel Eickenberg, Elisabeth Zscherpel and Karin Burger for some of the PL measurements

Jürgen Bläsing for help and instruction for the determination of the $\vec{c}$-axis.

Jes Larsen and Levent Gütay for some of the XRD measurements of the $CuInSe_2$ films, Johannes Fischer for the $\theta - 2\theta$ scan of the crystal, and Dominik Berg and Alex Redinger for some of the kesterite XRD measurements.

Alex Redinger, Dominik Berg and Thomas Schuler for the EDX measurements and SEM pictures.

Jérome Guillot for the XPS measurements

Nathalie Valle for the SIMS measurements

Helen Meadows, Colin Buckland and Phil Dale for proofreading in terms of English grammar and spelling

Yasuhiro Aida and Masato Kurihara for the drawings of the equipment

Michel Kremer for the ordering of over 100 long distance loan books and articles

the "Dommeldangers" Carola, Sharoni, Yael, Sascha, Julie, Martin, Phil, Florencia and Sofia for the good time in Luxembourg.

Martin for the 1,5 nice years living together in Merl.

und meiner Familie für ihre vielfältig Unterstützung.

Appendix A

Appendix

A.1 EDX-accuracy

In performing EDX measurements there are several effects, which can influence the accuracy of the determined composition values:

The reproducibility of the measurement To verify the reproducibility the composition measurement was repeated 10 times on the same spot. The result are given in table A.1. The standard deviation is for all elements $\leq 0.7\,at\%$.

$at\%$	**Cu**	**Zn**	**Sn**	**S**	**Se**	**Mo**
Mean	38.02	20.33	20.51	12.50	39.43	21.44
Std. deviation	0.05	0.07	0.03	0.05	0.04	0.05

Table A.1: Reproducibility of the composition measurement for the elements copper, zinc, tin, sulphur, selenium and molybdenum.

Matrix effects In principal the fraction of an element contained in a sample is proportional to its measured intensity compared to a known standard [148], [149].

$$\frac{C_i}{C_{i,St}} = \frac{I_i}{C_{i,St}} \tag{A.1}$$

C_i and I_i being the concentration and the intensity of the element i, and $C_{i,St}$ and $I_{i,St}$ of the known standard. However to obtain the correct composition matrix effects have to be accounted for:

$$\frac{C_i}{C_{i,St}} = [ZAF]_i \frac{I_i}{C_{i,St}} \tag{A.2}$$

The matrix effect is composed of the atomic number effect, the absorption effect and the fluorescence effect.

- The atomic number effect summarises influences connected to the atomic number of the considered element: this is backscattering and energy loss. Backscattering describes the loss of beam electrons due to elastic scattering before being able to excite characteristic X-rays. The back scattering coefficient depends strongly on the atomic number of the atom. Also the energy loss due to inelastic scattering depends on the atomic number.
- The absorption effect describes the reabsorption of created X-rays by the sample according to

$$\frac{I}{I_0} = exp[-\frac{\mu}{\rho}(\rho\, t)] \tag{A.3}$$

I being the measured intensity, I_0 the generated intensity, μ the mass absorption coefficient,ρ the density and t the path length of of the generated intensity through the sample. The ratio $\frac{\mu}{\rho}$ depends on the excitation wavelength used and on the investigated element. The absorption effect is the most significant of the three contributions to the matrix effect for quantitative analysis.

- The generated characteristic X-ray from element A can be reabsorbed from element B and excite an inner electron from element B, leading to a characteristic X-ray of element B.

The matrix effects are accounted for by the INCA software, which is used to analyse the measured EDX spectra. The software indicates the standard deviation for the calculated composition values. The values are given in table A.2. However the correction function used by the software involves several assumptions:

- geometrical effects like roughness, thickness or shape have no influence on the measured intensity
- the sample is homogeneous over the whole thickness
- the sample is stable under electron beam irradiation.

which are not necessarily true for the here investigated samples.

at%	**Cu**	**Zn**	**Sn**	**S**	**Se**	**Mo**
Std. deviation ZAF	0.13	0.12	0.06	0.24	0.15	0.18

Table A.2: Uncertainty in the composition determination induced by matrix effects.

A.2 XRD reference files

In the following the XRD reference files according to the ICDD data base used to analyse the XRD pattern are presented:

Sulphides	ICDD Reference File	Space Group	Crystal System
Cu_2ZnSnS_4	01-075-4122		tetragonal
Cu_3SnS_3	04-010-5719	Cc	monoclinic
Cu_3SnS_3	00-027-0198	$P1$	triclinic
Cu_3SnS_3	01-089-4714	$I\bar{4}2m$	tetragonal
$Cu_{2-x}S$	00-024-0061	$Fm\bar{3}m$	cubic
$Cu_{2-x}S$	01-072-1071	$P4_32_12$	tetragonal
ZnS	00-005-0566	$F\bar{4}3m$	cubic
Mo	00-042-1120	$Im\bar{3}m$	cubic

Table A.3: ICDD XRD reference pattern used for the analysis of sulphide system.

Selenides	ICDD Reference File	Space Group	Crystal System
$Cu_2ZnSnSe_4$	04-010-6295	$I\bar{4}2m$	tetragonal
Cu_3SnSe_3	01-072-8034	Cc	monoclinic
$CuSe_2$	04-004-2178	$Pnnm$	orthorhombic
$Cu_{2-x}Se$	01-073-2712	$Fm\bar{3}m$	cubic
$ZnSe$	04-001-6858	$F\bar{4}3m$	cubic
Mo	00-042-1120	$Im\bar{3}m$	cubic
Mo_3Se	04-007-3415	$Pm\bar{3}n$	cubic
$MoSe_2$	04-004-8782	$P6_3/mmx$	hexagonal
$MoSe_2$	04-003-6623	$R3m$	rhombohedral
Mo_3Se	04-007-3415	$Pm\bar{3}n$	cubic
Mo_3Se_4	04-007-1388	$R\bar{3}$	rhombohedral

Table A.4: ICDD XRD reference pattern used for the analysis of selenide system.

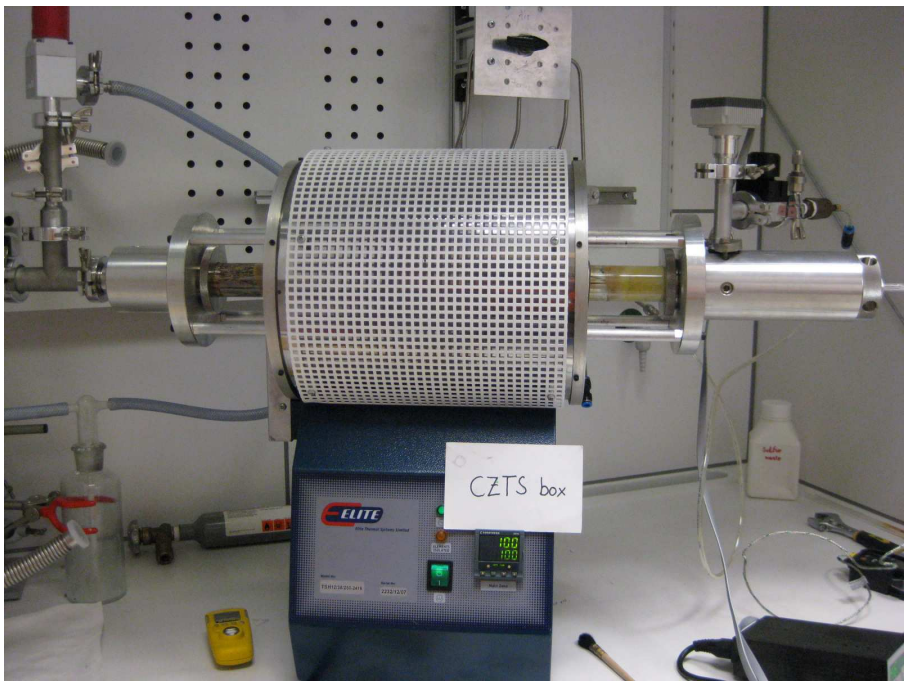

Figure A.1: Oven used for the annealing experiment

A.3 Post process annealing procedures

For the post process annealing of the polycrystalline Se-kesterite samples 2 different annealing procedures have been used:

Annealing in the oven

The setup used is depicted in figure A.1. First the samples are loaded into a graphite box and 200 mg selenium powder is added. Next the graphite box is introduced into a glass tube which leads into the oven. To prevent selenium loss during annealing, the box is kept under argon pressure of around 800 mbar. The temperature is raised during 15 minutes to 540°C and is than kept constant until the first Se condensate becomes visible on the glass tube. This was the case after 7 min and subsequently the oven was switched off and cooled down over night. As the temperature is measured in the oven on the outside of the glass tube the temperature in the box is most probably 10- 20°C lower than indicated on the thermocouple. After cool down only a weak ring of Se condensate was visible on the glass tube, indicating that most of the selenium remained inside the box. According to most reports in the literature summarized in chapter 5.1.4 kesterite formation starts around 300°C. An upper limit to the possible annealing temperature represents the melting point of the soda lime glass used as substrate at 600°C. Therefore as a compromise an annealing temperature of 540°C was chosen. Also other groups reported successful annealing results at this temperature [13],[15].

Post-process annealing in the PVD

As a second annealing method post process annealing in the PVD was considered. After the deposition the sample was kept at 500°C for 120 min at a Se pressure of 10^{-8} mbar.

A.4 Character tables of the used point groups

In the following the character tables of the point groups discussed in the previous chapters are presented according to [128]. The first column indicates the irreducible representation, the second column the basis functions and the first row the classes of the group. The double-valued representations are given below the dashed line. α and β indicate the spin up and spin down states of the electron spin.

T_d

T_d	Basis	E		$6IC_4$		$3C_2$	$6\sigma_d$	$8C_3$	
Γ_1	$x^2+y^2+z^2$	1		1		1	1	1	
Γ_2	$x^4(y^2-z^2)+y^4(z^2-x^2)+z^4(x^2-y^2)$	1		-1		1	-1	1	
Γ_3	$(2z^2-x^2-y^2, \sqrt{3}(x^2-y^2))$	2		0		2	0	-1	
Γ_4	$yz(y^2-z^2)$, $zx(z^2-x^2)$, $xy(x^2-y^2)$	3		1		-1	-1	0	
Γ_5	yz, zx, xy	3		-1		-1	1	0	
Γ_6	α, β	2	-2	$\sqrt{2}$	$-\sqrt{2}$	0	0	1	-1
Γ_7	$xy\alpha+(yz+izx)\beta$, $-xy\beta+(yz-izx)\alpha$	2	-2	$-\sqrt{2}$	$\sqrt{2}$	0	0	1	-1
Γ_8	$\sqrt{3}(x^2-y^2)\beta$, $-(2z^2-y^2-x^2)\alpha$, $-(2z^2-y^2-x^2)\beta$, $\sqrt{3}(x^2-y^2)\beta$	4	-4	0	0	0	0	-1	1

Table A.5: Character table of the T_d point group.

D_{2d}

D_{2d}	**Basis**	E		$2IC_4$		C_2	$2C_2'$	$2\sigma_d$
Γ_1	z^2, xyz	1		1		1	1	1
Γ_2	$z(x^2-y^2)$	1		1		1	-1	-1
Γ_3	x^2-y^2	1		-1		1	1	-1
Γ_4	z, xy	1		-1		1	-1	1
Γ_5	$\{x, x\}$	2		0		-2	0	0
Γ_6	$\{\alpha, \beta\}$	2	-2	$\sqrt{2}$	$-\sqrt{2}$	0	0	0
Γ_7	$\{z\alpha, z\beta\}$	2	-2	$-\sqrt{2}$	$\sqrt{2}$	0	0	0

Table A.6: Character table of the D_{2d} point group.

S_4

S_4	**Basis**	E		IC_4		C_2		IC_4^3	
Γ_1	xyz	1		1		1		1	
Γ_2	z	1		-1		1		-1	
Γ_3	$x-iy$	1		-i		-1		i	
Γ_4	$x+iy$	1		i		-1		-i	
Γ_5	α	1	-1	ρ	$-\rho$	-i	i	$-\rho*$	$\rho*$
Γ_6	β	1	-1	$\rho*$	$-\rho*$	i	-i	$-\rho$	$-\rho$
Γ_7	$(x+iy)\beta$	1	-1	$-\rho$	ρ	-i	i	$\rho*$	$-\rho*$
Γ_8	$(x-iy)\alpha$	1	-1	$-\rho*$	$\rho*$	i	-i	ρ	ρ

Table A.7: Character table of the S_4 point group.

C_2

C_2	Basis	E		C_2	
Γ_1	z	1		1	
Γ_2	x	1		-1	
Γ_3	α	1	-1	-i	i
Γ_4	β	1	-1	i	-i

Table A.8: Character table of the C_2 point group.

A.5 Script to calculated the expected polarisation in the detection plane

```
function[Mess2]=plot_Pol_senk_parallel_4c(Mess2)
%plottet Kurve für E II c und E senkr c für K1
%Version 15.2.11
clear('c_Probe','c_Probehalter','c_Probehalter_norm','c_Detekt','c_Detekt_yz','c_det_Parall',...
'c_det_Winkel_Normale','c_det_Winkel_yzEbene','c_det_Winkel_yzEbene','c_det_Proj_parall_yzEbene',...
'cos_Fkt_parall','c_senkr_1','c_det_Winkel_c_senkr1','cos_Fkt_senkr_1a','c_senkr_2','c_senkr_2_yz',...
'c_det_Winkel_c_senkr2','c_det_senkr_2','c_det_Proj_senkr_2','cos_Fkt_senkr_1b')

Mess_m=1;
k=1; %Daten(k) fÜr Polarisationswinkel für plots


%Drehwinkel der Probe auf Probehalter
%0°= lange Achse des Kristalls ist parallel zu langer Achse des
%Probehalters
%Drehmatrix dreht im Uhrzeigersinn
theta=90

%Vektor parallel zur c-Achse der Probe

c_Probe=1/(sqrt((sind(35.26))^2+(sind(2))^2+(-cosd(35.26))^2))*[sind(35.26);sind(2); -cosd(35.26)];
%c_Probe=[1;0; 0];

%Drehung der Probe auf dem Probehalter
c_Probehalter= [1 0 0;0 cosd(theta) sind(theta); 0 -sind(theta) cosd(theta); ]*c_Probe;

%Normierung der c-Achse
c_Probehalter_norm=c_Probehalter/
....sqrt(c_Probehalter(1,1)^2+c_Probehalter(2,1)^2+c_Probehalter(3,1)^2)

%c-Achse im Detektionssystem, dazu wird das Koordinatensystem um phi=45° im
%Uhrzeigersinn gedreht
phi=55
c_Detekt=[cosd(phi) -sind(phi) 0; sind(phi) cosd(phi) 0; 0 0 1]*c_Probehalter_norm;

%Winkel zwischen z-Achse(=0°)und c_Detekt:
c_Detekt_yz=c_Detekt(2:3,1);
z_Detekt=[0;1];
%dot(c_Detekt_yz,z_Detekt)/(sqrt(c_Detekt(2,1)^2+c_Detekt(3,1)^2)*1)
c_det_Parall_gegUz=acosd(dot(c_Detekt_yz,z_Detekt)/...
(sqrt(c_Detekt_yz(1,1)^2+c_Detekt_yz(2,1)^2)*1))


%Matlab rechnet Winkel gegen Uhrzeigersinn, ich messe Winkel aber im
%Uhrzeigersinn und acos kann Winkel nur zwischen 0-180° eindeutig zuordnen
%wegen cos(180-alpha)=cos(180+alpha). Deswegen Fallunterscheidung: wenn c
%im 1. oder 2. Quadranten gegen den Uhrzeigersinn liegt, liefert acos
%Winkel gegen UZ. Wenn c im 3. oder 4. Quadranten liegt liefert acosd
```

```
%Winkel im Uz Sinn.
if c_Detekt_yz(1,1)<=0
    c_det_Parall=180-c_det_Parall_gegUz;
else
    c_det_Parall=c_det_Parall_gegUz;
end


        % %Winkel zwischen c_Detekt und xd (Normale zur yd-zd-Ebene) um Projektion
        % der c-Achse auf y-z,d.h. Detektionsebene zu bestimmen.
         x_Detekt=[1;0;0];

%Projektion der c-Achse auf Detektionseben: Betrag des y und z Anteil des Vektors in der
%Projektionsebene.
        c_det_Proj_parall_yzEbene=sqrt(c_Detekt_yz(1,1)^2+c_Detekt_yz(2,1)^2)
        cos_Fkt_parall=c_det_Proj_parall_yzEbene*cosd(Mess2{1,Mess_m}.Daten(k).Pol-c_det_Parall);


%Ebene senkr. zu c

    %in Ebene senkrecht  zu c sind zwei zueinander senkrechte
    %Achsen/Vektoren
    %möglich
    %1. Vektor/Achse (in Detektionsebene)



            c_senkr_1=cross(x_Detekt,c_Detekt);
            c_senkr_1_norm=c_senkr_1/(sqrt(c_senkr_1(1,1)^2+c_senkr_1(2,1)^2+c_senkr_1(3,1)^2));
            %Matlab rechnet Winkel gegen Uhrzeigersinn, ich messe Winkel aber im
            %Uhrzeigersinn und acos kann Winkel nur zwischen 0-180° eindeutig zuordnen
            %wegen cos(180-alpha)=cos(180+alpha). Deswegen Fallunterscheidung: wenn c
            %im 1. oder 2. Quadranten gegen den Uhrzeigersinn liegt, liefert acos
            %Winkel gegen UZ. Wenn c im 3. oder 4. Quadranten liegt liefert acosd
            %Winkel im Uz Sinn.
            c_det_Winkel_c_senkr1_gegUz=acosd(dot( c_senkr_1_norm,[0;0;1]));

            if c_senkr_1_norm(2,1)<=0
                c_det_Winkel_c_senkr1=180-c_det_Winkel_c_senkr1_gegUz;
            else
                c_det_Winkel_c_senkr1=c_det_Winkel_c_senkr1_gegUz;
            end


            cos_Fkt_senkr_1a=cosd(Mess2{1,Mess_m}.Daten(k).Pol-(c_det_Winkel_c_senkr1));


    %2.Vektor/Achse senkr. zu c
    %senkrecht auf c_senkr_1 und auf c
```

```
        c_senkr_2=cross(c_Detekt,c_senkr_1);
        c_senkr_2_norm=c_senkr_2/(sqrt(c_senkr_2(1,1)^2+c_senkr_2(2,1)^2+c_senkr_2(3,1)^2));

        %Brechenung des winkel zur z-Achse(=0°), verwende dazu y-und
        %z-Koordinate als Projektion auf y-z Ebene
        c_senkr_2_yz=c_senkr_2_norm(2:3,1);
         %Matlab rechnet Winkel gegen Uhrzeigersinn, ich messe aber mit
        %Uhrzeigersinn
        c_det_Winkel_c_senkr2_gegUz=acosd(dot( c_senkr_2_yz,[0;1])/(sqrt(c_senkr_2_yz(1,1)^2...
         +c_senkr_2_yz(2,1)^2)*1));

         if c_senkr_2_yz(1,1)<=0
             c_det_Winkel_c_senkr2=180-c_det_Winkel_c_senkr2_gegUz;
        else
            c_det_Winkel_c_senkr2=c_det_Winkel_c_senkr2_gegUz;
        end

        %Projektion

        c_det_Proj_senkr_2=sqrt(c_senkr_2_norm(2,1)^2+c_senkr_2_norm(3,1)^2);
        cos_Fkt_senkr_1b=c_det_Proj_senkr_2*...
        cosd(Mess2{1,Mess_m}.Daten(k).Pol-(c_det_Winkel_c_senkr2));



%Beide Anteile senkrecht zueinander addiert. Addiere Intensitäten
%nicht Vektoren
%figure
    hold on
    grid on
    axes_handle_1=gca;
    set(axes_handle_1,'FontSize',14);
    axis([0 180 0 1]);

%senkrencht zu c-Achse
    %Berechnete Kurven müssen auf 1 normiert werden, um sie mit
    %Messkurven zu vergleichen

    %Polarisationsgrad der Messung
    Norm=1;

  cos2_Fkt_senkr_zus=Norm*(cos_Fkt_senkr_1a.^2+cos_Fkt_senkr_1b.^2);

  h2a_1=plot(Mess2{1,Mess_m}.Daten(k).Pol,cos2_Fkt_senkr_zus,'k:');
 % plot(Mess2{1,Mess_m}.Daten(k).Pol,cos_Fkt_senkr_1a.^2,'b:');
 % plot(Mess2{1,Mess_m}.Daten(k).Pol,cos_Fkt_senkr_1b.^2,'r:');


%II zur c-Achse
 cos2_Fkt_parall=Norm*cos_Fkt_parall.^2;
h2b_1=plot(Mess2{1,Mess_m}.Daten(k).Pol,cos2_Fkt_parall,'k--');
```

```
   Mess2{1,Mess_m}.Daten(k).I_Pol_berechnet.senkr=cos2_Fkt_senkr_zus;
   Mess2{1,Mess_m}.Daten(k).I_Pol_berechnet.parall=cos2_Fkt_parall;


      V_handle=[h2a_1,h2b_1];
    %legend(V_handle,'E senkr c','E II c ')
%
end
%
end
```

A.6 Experimental pitfalls

In doing measurements, effects from diverse, sometimes unexpected sources may occur. Special care must be taken, when doing photoluminescence measurements on kesterite and other hardly luminescing samples:

- to not introduce strong luminescing sample into the cryostat at the same time.
- to background signal due to small bits of GaAs, originating from the substrate of the epitaxial $Cu(In,Ga)Se_2$ samples, which are measured in the same cryostat. This is especially important, as GaAs has almost the same band gap as Cu_2ZnSnS_4, leading therefore to photoluminescence peaks in the same wavelength range. The measured spectrum for Zn doped and undoped GaAs is shown in figure A.2.

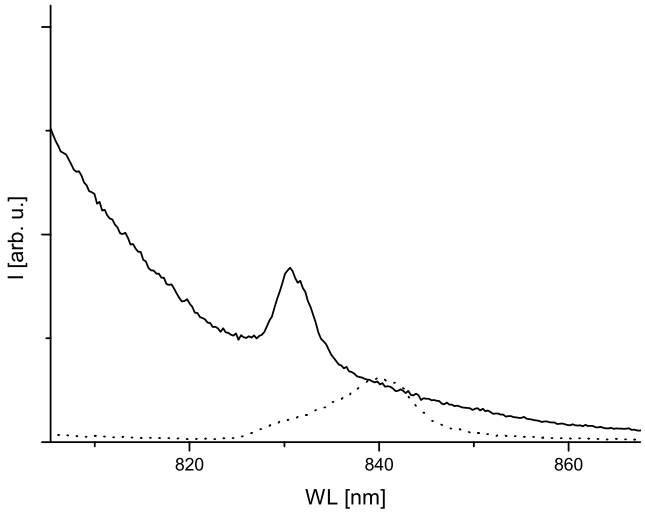

Figure A.2: Photoluminescence signal due to Zn doped (continuous line) and undoped GaAs.

For polarisation dependent measurements needs to be considered, that

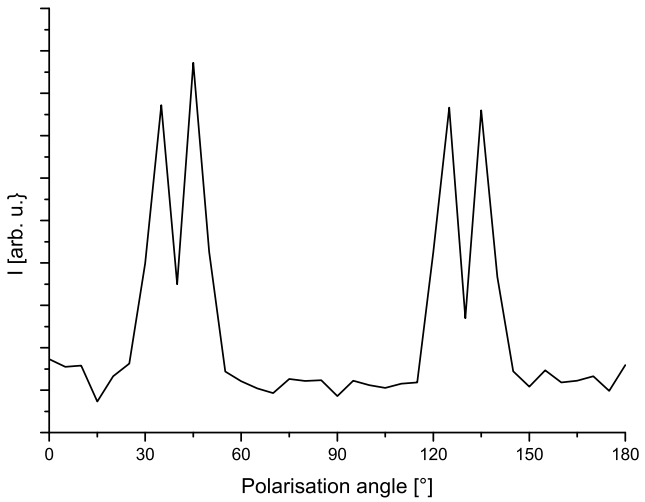

Figure A.3: Artefacts arising for a too close position of the polymer polarisation filter and the Notch filter.

- the mounting of the Glan-Thompson prism to the turnable stage is fixed. However the Glan-Thompson prism is able to turn with respect to the mounting.

- the Notch filter directly in front of the polymer polarisation filter, gives rise to artefacts as shown in figure A.3. Eventually due to reflection of the refracted beam from the Glan-Thompson prism.

Bibliography

[1] U.S. Geological survey. Indium statistics. 2009.

[2] T. A. M. Friedlmeier. *Multinary Compounds and Alloys for Thin-Film Solar Cells: Cu_2ZnSnS_4 and $Cu_(In, Ga)(S, Se)_2$*. PhD thesis, Universität Stuttgart, 2001.

[3] H. Katagiri, N. Sasaguchi, S. Hando, S. Hoshino, J. Ohashi, and T. Yokota. Preparation and evaluation of Cu_2ZnSnS_4 thin films by sulfurization of E-B evaporated precursors. *Solar energy materials and solar cells*, 49(1-4):407–414, 1997.

[4] H. Katagiri, M. Nishimura, T. Onozawa, S. Maruyama, M. Fujita, T. Sega, and T. Watanabe. Rare-metal free thin film solar cell, BookTI -Proceedings of the power conversion conference - Nagaoka 1997, Vols I and II. pages 1003–1006, 1997.

[5] H. Katagiri, K. Saitoh, T. Washio, H. Shinohara, , T. Kurumadani, and S. Miyajima. Development of thin film solar cell based on Cu_2ZnSnS_4 thin films. *Solar energy materials and solar cells*, 65(1-4):141–148, 2001.

[6] H. Katagiri, K. Jimbo, K. Moriya, and K. Tsuchida. Solar cell without environmental pollution by using CZTS thin film,. In K. Kurokawa, L. L. Kazmerski, B. McNelis, M. Yamaguchi, C. Wronski, and W. C. Sinke, editors, *BookTI - Proceedings of 3rd world conference on photovoltaic energy conversion*, number A-C, pages 2874–2879, 2003.

[7] K. Jimbo, R. Kimura, T. Kamimura, S. Yamada, W. S. Maw, H. Araki, K. Oishi, and H. Katagiri. Cu_2ZnSnS_4-type thin film solar cells using abundant materials. *Thin solid films*, 515(15):5997–5999, 2007.

[8] H. Katagiri, K. Jimbo, S. Yamada, T. Kamimura, W. S. Maw, T. Fukano, T. Ito, and T. Motohiro. Enhanced conversion efficiencies of Cu_2ZnSnS_4-based thin film solar cells by using preferential etching technique. *Applied physics express*, 1(4), 2008.

[9] O. Volobujeva, J. Raudoja, E. Mellikov, M. Grossberg, S. Bereznev, and R. Traksmaa. $Cu_2ZnSnSe_4$ films by selenization of Sn-Zn-Cu sequential films. *Journal of Physics and Chemistry of Solids*, 70(3-4):567 – 570, 2009.

[10] K. Timmo, M. Altosaar, J. Raudoja, K. Muska, M. Pilvet, M. Kauk, T. Varema, M. Danilson, O. Volobujeva, and E. Mellikov. Sulfur-containing $Cu_2ZnSnSe_4$ monograin powders for solar cells. *Solar energy materials and solar cells*, 94(11, Sp. Iss. SI):1889–1892, 2010.

[11] K. Wang, O. Gunawan, T. Todorov, B. Shin, S. J. Chey, N. A. Bojarczuk, D. Mitzi, and S. Guha. Thermally evaporated Cu_2ZnSnS_4 solar cells. *Applied physics letters*, 97(14), 2010.

[12] B.-A. Schubert, B. Marsen, S. Cinque, T. Unold, R. Klenk, S. Schorr, and H.-W. Schock. Cu_2ZnSnS_4 thin film solar cells by fast coevaporation. *Progress in Photovoltaics: Research and Applications*, 19(1):93–96, 2011.

[13] T. K. Todorov, K. B. Reuter, and D. B. Mitzi. High-Efficiency Solar Cell with Earth-Abundant Liquid-Processed Absorber. *Advanced Materials*, 22(20):E156–E159, 2010.

[14] R. Schurr, A. Hölzing, S. Jost, R. Hock, T. Voss, J. Schulze, A. Kirbs, A. Ennaoui, M. Lux-Steiner, A. Weber, I. Kötschau, and H.-W. Schock. The crystallisation of Cu_2ZnSnS_4 thin film solar cell absorbers from co-electroplated Cu-Zn-Sn precursors. *Thin Solid Films*, 517(7):2465 – 2468, 2009.

[15] A. Ennaoui, M. Lux-Steiner, A. Weber, D. Abou-Ras, I. Koetschau, H.-W. Schock, R. Schurr, A. Hoelzing, S. Jost, R. Hock, T. Voss, J. Schulze, and A. Kirbs. Cu_2ZnSnS_4 thin film solar cells from electroplated precursors: Novel low-cost perspective. *Thin solid films*, 517(7):2511–2514, 2009.

[16] A. Weber, R. Mainz, T. Unold, S. Schorr, and H.-W. Schock. In-situ XRD on formation reactions of Cu_2ZnSnS_4 thin films. *physica status solidi (c)*, 6(5):1245, 2009.

[17] M. Altosaar, J. Raudoja, K. Timmo, M. Danilson, M. Grossberg, M. Krunks, T. Varema, and E. Mellikov. $Cu_2ZnSnSe_4$ monograin powders for solar cell application, BookTI - Conference Record of the 2006 IEEE 4th World Conference on Photovoltaic Energy Conversion, Vols 1 and 2. pages 468–470, 2006.

[18] H. Araki, Y. Kubo, K. Jimbo, W. S. Maw, H. Katagiri, M. Yamazaki, K. Oishi, and A. Takeuchi. Preparationof Cu_2ZnSnS_4 thin films by sulfurization of co-electroplated Cu-Zn-Sn precursors. In S. Sadewasser, D. AbouRas, B. Lake, and H. W. Schock, editors, *Physica Status Solidi C Current Topics in Solid State Physics*, volume 6, pages 1266–1268, 2009.

[19] A. Redinger, D. M. Berg, P. J. Dale, and S. Siebentritt. The Consequences of Kesterite Equilibria for Efficient Solar Cells. *Journal of the American Chemical Society*, 133(10):3320, 2011.

[20] G. Zoppi, I. Forbes, R. W. Miles, P. J. Dale, J. J. Scragg, and L. M. Peter. $Cu_2ZnSnSe_4$ in Film Solar Cells Produced by Selenisation of Magnetron Sputtered Precursors. *Progress in photovoltaics*, 17(5):315–319, 2009.

[21] J.J. Scragg. *Studies of Cu_2ZnSnS_4 films prepared by sulurisation of electrodeposited precursors.* PhD thesis, University of Bath, 2010.

[22] S. J. Fonash. *Solar cell devices.* Academic Press, 1981.

[23] ZSW. *press release.* 23.8.2010.

[24] Miasolé. 2.9.2010.

[25] *Photon international*, February 2011.

[26] *Photon International*, March 2010.

[27] S. Chen, X. G. Gong, A. Walsh, and S.-H. Wei. Defect physics of the kesterite thin-film solar cell absorber Cu_2ZnSnS_4. *Applied Physics Letters*, 96(2):021902, 2010.

[28] J. E. Jaffe and A. Zunger. Theory of the band-gap anomaly in ABC_2 chalcopyrite semiconductors. *Physical Review B*, 29(4):1882, 1984.

[29] L. Mandel, R. D. Tomlinson, and M. J. Hampshire. *Journal of Applied Crystallographie*, 10(130), 1977.

[30] C. Persson. Electronic and optical properties of Cu_2ZnSnS_4 and $Cu_2ZnSnSe_4$. *Journal of Applied Physics*, 107(5):053710, 2010.

[31] J. Paier, R. Asahi, A. Nagoya, and G. Kresse. Cu_2ZnSnS_4 as a potential photovoltaic material: A hybrid Hartree-Fock density functional theory study. *Phys. Rev. B*, 79(11):115126, 2009.

[32] S. Schorr, H.-J. Hoebler, and M. Tovar. A neutron diffraction study of the stannite-kesterite solid solution series. *European Journal of Mineralogy*, 19:65–73(9), 2007 2007.

[33] S.R. Hall, S.A. Kissin, and JM Stewart. Stannite and kesterite -Distinct minerals or components of a solid-solution. *Acta crystallographica section A*, 31(Suppl. S):S67, 1975.

[34] G. S. Babu, Y. B. Kishore Kumar, P. U. Bhaskar, and V. S. Raja. Effect of post-deposition annealing on the growth of $Cu_2ZnSnSe_4$ thin films for a solar cell absorber layer. *Semiconductor Science and Technology*, 23(8):085023, 2008.

[35] S. Chen, X. G. Gong, A. Walsh, and S.-H. Wei. Crystal and electronic band structure of Cu_2ZnSnX_4 (X = S and Se) photovoltaic absorbers: First-principles insights. *Applied Physics Letters*, 94(4):041903, 2009.

[36] S.-H. Wei, S. B. Zhang, and A. Zunger. Effects of Ga addition to $CuInSe_2$ on its electronic, structural, and defect properties. *Applied Physics Letters*, 72(24):3199–3201, 1998.

[37] H. Neumann. Vacancy formation enthalpies in $A^I B^{III} C_2^{VI}$ chalcopyrite semiconductors. *Crystal Research and Technology*, 18(7):901, 1983.

[38] S.-H. Wei, S. B. Zhang, and A. Zunger. Effects of Na on the electrical and structural properties of $CuInSe_2$. *Journal of Applied Physics*, 85(10):7214–7218, 1999.

[39] H. J. Möller. Structure and defect chemistry of grain boundaries in $CuInSe_2$. *Solar Cells*, 31(1):77 – 100, 1991.

[40] C. Rincón, C. Bellabarba, J. González, and G. Sánchez Pérez. Optical properties and characterization of $CuInSe_2$. *Solar Cells*, 16:335 – 349, 1986.

[41] S. M. Wasim. Transport properties of $cuinse_2$. *Solar Cells*, 16:289–316.

[42] S. Chen, J.-H. Yang, X. G. Gong, A. Walsh, and S.-H. Wei. Intrinsic point defects and complexes in the quaternary kesterite semiconductor Cu_2ZnSnS_4. *Physical Review B*, 81(24):245204, 2010.

[43] S. Siebentritt, N. Rega, A. Zajogin, and M. Ch. Lux-Steiner. Do we really need another PL study of $CuInSe_2$? *physica status solidi (c)*, 1(9):2304, 2004.

[44] A. Bauknecht, S. Siebentritt, J. Albert, and M. Ch Lux-Steiner. Radiative recombination via intrinsic defects in $Cu_xGa_ySe_2$. *Journal of Applied Physics*, (89):4391, 2001.

[45] S. Schuler, S. Siebentritt, S. Nishiwaki, N. Rega, J. Beckmann, S. Brehme, and M. C. Lux-Steiner. Self-compensation of intrinsic defects in the ternary semiconductor $CuGaSe_2$. *Physical review B*, (69):045210, 2004.

[46] S. Siebentritt, I. Beckers, T. Riemann, J. Christen, A. Hoffmann, and M. Dworzak. Reconciliation of luminescence and Hall measurements on the ternary semiconductor $CuGaSe_2$. *Applied Physics letters*, (86):091909, 2005.

[47] P.Y. Yu and M. Cardona. *Fundamentals of Semiconcutors - Physics and Materials Properties*. Springer, 3 edition, 2005.

[48] R. G Waters. Diode Laser degradation meachnisms: a review. *Progress in Quantum Electronics*, 15:153–174, 1991.

[49] N. Nakayama and K. Ito. Sprayed films of stannite Cu_2ZnSnS_4. *Applied Surface Science*, 92:171 – 175, 1996.

[50] J. J. Scragg, P. J. Dale, L. M. Peter, G. Zoppi, and I. Forbes. New routes to sustainable photovoltaics: evaluation of Cu_2ZnSnS_4 as an alternative absorber material. *physica status solidi (b)*, 245(9):1772, 2008.

[51] M. Altosaar, J. Raudoja, K. Timmo, M. Danilson, M. Grossberg, J. Krustok, and E. Mellikov. $Cu_2Zn_{1-x}Cd_xSn(Se_{1-y}S_y)_4$ solid solutions as absorber materials for solar cells. *physica status solidi (a)*, 205(1):167, 2008.

[52] S. Siebentritt, M. Igalson, C. Persson, and S. Lany. The electronic structure of chalcopyrites - bands, point defects and grain boundaries. *Progress in Photovoltaics: Research and Applications*, 18(6):390, 2010.

[53] K. Sato. EPR studies of point defects in $Cu-III-VI_2$ chalcopyrite semiconductors. *Materials Science in Semiconductor Processing*, 6(5-6):335 – 338, 2003.

[54] J. M. Tchapkui-Niat, A. Goltzene, and C. Schwab. Paramagnetic defects in as-grown and iron doped $CuInSe_2$. *Journal of Physics C: Solid State Physics*, 15(22):4671, 1982.

[55] M. Birkholz, P. Kanschat, T. Weiss, M. Czerwensky, and K. Lips. Low-temperature electron-paramagnetic-resonance study of extrinsic and intrinsic defects in $CuGaSe_2$. *Phys. Rev. B*, 59(19):12268–12271, 1999.

[56] S. Siebentritt. Shallow defects in the Wide Gap Chalcopyrite $CuGaSe_2$. In S. Siebentritt and U. Rau, editors, *Wide-Gap chalcopyrites*, Matierials Science. Springer, 2006.

[57] M. Grossberg, J. Krustok, K. Timmo, and M. Altosaar. Radiative recombination in $Cu_2ZnSnSe_4$ monograins studied by photoluminescence spectroscopy. *Thin Solid Films*, 517(7):2489 – 2492, 2009.

[58] S. Ahn, S. Jung, J. Gwak, A. Cho, K. Shin, K. Yoon, D. Park, H. Cheong, and J. H. Yun. Determination of band gap energy E_g of $Cu_2ZnSnSe_4$ thin films: On the discrepancies of reported band gap values. *Applied Physics Letters*, 97(2):021905, 2010.

[59] S. Estreicher. Theory of Defects in Semiconductors - Recent Developments and Challenges. *The electrochemical society: Interface*, 14(1):28, 2005.

[60] J. K. Larsen, K Burger, L Gütay, and S. Siebentritt. Temperature dependence of potential fluctuations in chalcopyrites. *submitted*, 2011.

[61] S. Siebentritt, N. Papathanasiou, and M. Ch. Lux-Steiner. Potential fluctuations in compensated chalcopyrites. *Physica B: Condensed Matter*, 376-377:831 – 833, 2006.

[62] E. O. Kane. Thomas-Fermi Approach to Impure Semiconductor Band Structure. *Physical Review*, 131(1):79, 1963.

[63] T. N. Morgan. Broadening of Impurity Bands in Heavily Doped Semiconductors. *Physical Review*, 139(1A):A343, 1965.

[64] A. P. Levanyuk and V. V. Osipov. Edge luminescence of direct-gap semiconductors. *Uspekhi fizicheskikh nauk (Sov.Phys. Usp.)*, 24(3):187–215, 1981.

[65] J. H. Werner, J. Mattheis, and U. Rau. Efficiency limitations of polycrystalline thin film solar cells: case of $Cu(In,Ga)Se_2$. *Thin Solid Films*, 480-481:399 – 409, 2005.

[66] D.M. Mattox. *Handbook of physical vapor deposition (PVD) processing*. Noyes Publications.

[67] C. A. Jones and P. O'Brien. *CVD of compound semiconductors*. Wiley-VCH, 1997.

[68] A. Redinger and S. Siebentritt. Coevaporation of $Cu_2ZnSnSe_4$ thin films. *Applied Physics Letters*, 86(20):092111, 2010.

[69] Y. Aida. Optimization of the 3-stage process for CIGS solar cells. 2009.

[70] M.A Herman, W Richter, and H Sitter. *Epitaxy - Physical Principles and Technical Implementation*. Springer, 2004.

[71] A. C Fisher. *Electrode Dynamics*. Oxford University Press, 1996.

[72] R.K Pandey, S.N. Sahu, and S. Chandra. *Handbook of semiconductor electrodeposition*. Marcel Dekker, 1996.

[73] D. Berg. A baseline process of the formation of kesterites using electo-deposition. Bath, 2009.

[74] G.M Haleand and M.R Querry. Optical constants of water in the $200nm$ to $200\mu m$ wavelength region. *Applied Optics*, 12:555–563, 1973.

[75] M Birkholz. *Thin film analysis by X-ray scattering*. Wiley-VCH, 2009.

[76] Ch. Dang Ngoc Chan. *Graph Euler cradle*. 2010.

[77] J. I. Goldstein, D.E. Newburry, P. Echlin, D.C. Joy, A.D. Roming, C.E. Lyman, C. Fiori, and E. Lifshin. *Scanning Electron Microscopy and X-Ray Microanalysis*. Plenum Press, New York, 1992.

[78] D Briggs and M.P. Seah. *Practical surface analysis - by Auger and X-ray Photoelectron Spectroscopy*. John Wiley and Sons, 1987.

[79] CRP Lippmann Département Sciences et Analyse des Matériaux (SAM). *Nanobeams - European PhD School Week 2*. 2007.

[80] D. Chakrabarti and D. Laughlin. The Cu-S (Copper-Sulfur) system. *Journal of Phase Equilibria*, 4(3):254 – 271, 1983.

[81] T. B. Massalski. *Binary alloy phase diagrams*. ASM, Materials Park, Ohio, 2. ed edition, 1990.

[82] H. Okada, T. Kawanaka, and S. Ohmoto. Study on the ZnSe phase diagram by differential thermal analysis. *Journal of Crystal Growth*, 165(1-2):31 – 36, 1996.

[83] V. Piacente, S. Foglia, and P. Scardala. Sublimation study of the tin sulfides SnS_2, Sn_2S_3 and SnS. *Journal of alloys and compounds*, 177(1):17–30, DEC 5 1991.

[84] H. Wiedemeier and G. Pultz. Equilibrium sublimation and thermodynamic properties of $SnSe$ and $SnSe_2$. *Zeitschrift für anorganische und allgemeine Chemie*, 499(4):130, 1983.

[85] I. D. Olekseyuk, I. V. Dudchak, and L. V. Piskach. Phase equilibria in the $Cu_2S - ZnS - SnS_2$ system. *Journal of alloys and compounds*, 368(1-2):135–143, 2004.

[86] J. R. Craig and G. Kullerud. The Cu-Zn-S system. *Mineralium Deposita*, 8(1):81 – 91, 1973.

[87] T.A. Bither, P.C. Donohue, W.C. Cloud, P.E. Bierstedt, and H.S. Young. Mixed-Cation Transition Metal Pyrite Dichaldogenides-High Pressure Synthesis and Properties. *Journal of Solid State Chemistry*, (1):526–533, 1970.

[88] O. V. Parasyuk, I. D. Olekseyuk, I. I. Mazurets, and L. V. Piskach. Phase equilibria in the quasi-ternary ZnSe-Ga_2Se_3-$SnSe_2$ system. *Journal of Alloys and Compounds*, 379(1-2):143 – 147, 2004.

[89] S. Fiechter, M. Martinez, G. Schmidt, W. Henrion, and Y. Tomm. Phase relations and optical properties of semiconducting ternary sulfides in the system Cu-Sn-S. *Journal of Physics and Chemistry of Solids*, 64(9-10):1859 – 1862, 2003.

[90] G. Moh. Tin-Containing Mineral Systems - Part II: Phase relations and mineral assemblages in the Cu-Fe-Zn-Sn-S system. *Chemie der Erde*, 34:1–61, 1975.

[91] D. Wu, C.R. Knowles, and L.L. Chang. Copper-tin sulphides in the system Cu-Sn-S. *Mineralogical Magazine*, 50:323–325, 1986.

[92] M. Khanafer, J. Rivet, and J. Flahaut. Études du ternaire Cu-Sn-S. *Bulletin de la société chimique de France*, 12:2670–2676, 1974.

[93] M. Onoda, X. Chen, A. Sato, and H. Wada. Crystal structure and twinning of monoclinic Cu_2SnS_3. *Materials Research Bulletin*, 35(9):1563 – 1570, 2000.

[94] Rössler U. Schulz M. Madelung, O. *New Series IV/11C1*, volume III/41C of *The Landolt-Börnstein Database*. Springer Materials.

[95] J. Rivet. Contribution a l'Etude de quelques Combinaisons ternaires sulfurees, seleniees ou tellurees du Cuivre avec les Elements du Groupe IV b . *J. Ann. Chim. (Paris)*, 10:243, 1965.

[96] B. B. Sharma, R. Ayyar, and H. Singh. Stability of the Tetrahedral Phase in the $A_2^I B^{IV} C_3^{VI}$ Group of Compounds. *physica status solidi (a)*, 40(2):691, 1977.

[97] L. D. C. Bok and J. H. de Wit. Zur Kenntnis einiger ternärer Sulfide und Selenide. *Zeitschrift für anorganische und allgemeine Chemie*, 324(3-4):162–167, 1963.

[98] G. Marcano, L. M. de Chalbaud, C. Rincón, and G. Pérez. Crystal growth and structure of the semiconductor Cu_2SnSe_3. *Materials Letters*, 53(3):151 – 154, 2002.

[99] L.D. Gulay, M. Daszkiewicz, T.A. Ostapyuk, O.S. Klymovych, and O.F Zmiy. Monoclinic Cu_2Se_3Sn. *Acta Crystallographica C*, C66:i58–i60, 2010.

[100] G. Marcano, C. Rincon, G. Marin, R. Tovar, and G. Delgado. Crystal growth and characterization of the cubic semiconductor Cu_2SnSe_4. *Journal of Applied Physics*, 92(4):1811, 2002.

[101] K. Roy-Choudhury. Experimental investigations of the solid solution series between Cu_2SnS_3 and Cu_2ZnSnS_4 (kesterite). *Neues Jahrbuch für Mineralogie, Monatshefte*, 9:432–434, 1974.

[102] I. V. Dudchak and L. V. Piskach. Phase equilibria in the $Cu_2SnSe_3 - SnSe_2 - ZnSe$ system. *Journal of Alloys and Compounds*, 351(1-2):145 – 150, 2003.

[103] O. Madelung, U. Rössler, and M. Schulz. , volume III/41C of *The Landolt-Börnstein Database*. Springer Materials.

[104] F. Hergert and R. Hock. Predicted formation reactions for the solid-state syntheses of the semiconductor materials Cu_2SnX_3 and Cu_2ZnSnX_4 (X = S, Se) starting from binary chalcogenides. *Thin Solid Films*, 515(15):5953 – 5956, 2007.

[105] S. Schorr, A. Weber, V. Honkimäki, and H.-W. Schock. In-situ investigation of the kesterite formation from binary and ternary sulphides. *Thin Solid Films*, 517(7):2461 – 2464, 2009.

[106] A. Janosi. La structure du sulfure cuivreux quadratique. 17(3):311–312, 1964.

[107] P. Lukashev, W. R. L. Lambrecht, T. Kotani, and M. van Schilfgaarde. Electronic and crystal structure of $Cu_{2-x}S$: Full-potential electronic structure calculations. *Physical Review B*, 76(19):195202, 2007.

[108] O. Madelung, U. Rössler, and M. Schulz. *Zinc sulfide (ZnS) visible luminescence of ZnS*, volume III/41C of *The Landolt-Börnstein Database*. Springer Materials.

[109] Sh. Shinoya. Luminescence of Lattices of the ZnS type. In P. Goldberg, editor, *Luminescence of Inorganic solids*. Academic Press, 1966.

[110] P. A. Fernandes, P.M.P. Salome, and A.F. da Cunha. *A study of ternary Cu_2SnS_3 and Cu_3SnS_4 thin films perpared by sulfurizing stacked metal precursors*, volume 43. 2010.

[111] T. A. Kuku and O. A. Fakolujo. Photovoltaic characteristics of thin films of Cu_2SnS_3. *Solar Energy Materials*, 16(1-3):199 – 204, 1987.

[112] V. Nadenau, D. Hariskos, H.-W. Schock, M. Krejci, F.-J. Haug, A. N. Tiwari, H. Zogg, and G. Kostorz. *Microstructural study of the $CuGaSe_2$ interfacial region in $CuGaSe_2$ thin films*, volume 85. 1999.

[113] G. K. Padam. The properties of chemically deposited Cu_{2-x} deposited thin films. *Thin solid films*, 150:L89, 1987.

[114] E. J. D. Garba and R. L. Jacobs. The electronic structure of $Cu_{2-x}Se$. *Physica B+C*, 138(3):253 – 260, 1986.

[115] E. P. Domashevskaya, V. V. Gorbachev, V. A. Terekhov, V. M. Kashkarov, E. V. Panfilova, and A. V. Shchukarev. XPS and XES emission investigations of d-p resonance in some copper chalcogenides. *Journal of Electron Spectroscopy and Related Phenomena*, 114-116:901 – 908, 2001.

[116] V. M. García, P. K. Nair, and M. T. S. Nair. Copper selenide thin films by chemical bath deposition. *Journal of Crystal Growth*, 203(1-2):113 – 124, 1999.

[117] H. Chacham, J. L. A. Alves, and M. L. De Siqueira. Microscopic models for Cu, Ag and Au cationic substitutional impurities and the metal vacancy in ZnSe. *Solid State Communications*, 60(5):411 – 414, 1986.

[118] G. Marcano, C. Rincon, L. M. de Chalbaud, D. B. Bracho, and G. Sanchez Perez. Crystal growth and structure, electrical, and optical characterization of the semiconductor Cu_2SnSe_3. *Journal of Applied Physics*, 90(4):1847, 2001/08/15/.

[119] D. Abou-Ras, G. Kostorz, D. Bremaud, M. Kälin, F. V. Kurdesau, A. N. Tiwari, and M. Döbeli. Formation and characterisation of $MoSe_2$ for $Cu(In, Ga)Se_2$ based solar cells. *Thin Solid Films*, 480-481:433 – 438, 2005.

[120] C Röhr. *Skript zur Vorlesung: Methoden der Anorganischen Chemie.*

[121] M.I. Aroyo, J. M. Perez-Mato, C. Capillas, E. Kroumova, S. Ivantchev, G. Madariaga, A. Kirov, and H. Wondratschek. Bilbao Crystollographic Server: 1. Databases and crystallographic computing programs. *Zeitschrift für Kristallografie*, 221(1):15–27, 2006.

[122] G. Kloess. *Vorlesungsskript Kristallographie 1.* 2007.

[123] H. Jones. *The theory of Brillouin zones and electronic states in crystals.* North-Holland Publishing Company, Amsterdam, 1960.

[124] Th. Hahn. *International tables of crystallography.* Springer, Dordrecht, 5., rev. ed., repr. with corr edition, 2005.

[125] R.A. Evarestov. *Quantum chemistry of solids - The LCAO First Principles Treatment of Crystals.* Springer Series in Solid-State Sciences. Springer, Berlin.

[126] W. Massa. *Kristallstrukturbestimmung.* Vieweg+Teubner, 5 edition, 2007.

[127] E. Wigner. Über die elastischen Eigenschwingungen symmetrischer Systeme. *Gesellschaft der wissenschaftlichen Nachrichten, Math.-Phys.*, (2), 1930.

[128] T. Inui, Y. Tanabe, and Y. Onodera. *Group theory and its applications in physics.* Springer Series in Solid-State Sciences 78. 1996.

[129] J. L. Shay and J. H. Wernick. *Ternary chalcopyrite semiconductors, growth, electronic properties, and applications.* Pergamon Pr, Oxford [u.a.], 1975.

[130] M. I. Alonso, M. Garriga, C. A. Durante Rincón, E. Hernández, and M. León. Optical functions of chalcopyrite $CuGa_xIn_{1-x}Se_2$ alloys. *Applied Physics A: Materials Science und Processing*, 74(5):659 – 664, 2002.

[131] Feofilov. *The physical basis of polarized emission.* Consultants Bureau, New York, 1961.

[132] Fine structure in the optical absorption edge of anisotropic crystals. *Journal of Physics and Chemistry of Solids*, 15:97–107, 1960.

[133] S. Shirakata, S. Isomura, and S. Chichibu. Photoreflectance Characterization of Lattice Strain in Wide-Gap $Cu-III-VI_2$ Epitaxial Layers. *Transactions of the Material Research Society of Japan*, 20:782–785, 1996.

[134] A. Bauknecht. *$CuGaSe_2$ für die Anwendung in der Photovoltaik - Metallorganische Gasphasenepitaxie und optische Charakterisierung $CuGaSe_2$ for Photovoltaic Applications.* PhD thesis, FU Berlin, 2000.

[135] S. C. Jain, M. Willander, and H. Maes. Stresses and strains in epilayers, stripes and quantum structures of III - V compound semiconductors. *Semiconductor Science and Technology*, 11(5):641, 1996.

[136] R Hull and E.A Stach. Equilibrium and metastable strained layer semiconductor heterostructures. *Electronic materials*, 1:21–28, 1996.

[137] D. Dunstan. Strain and strain relaxation in semiconductors. *Journal of Materials Science: Materials in Electronics*, 8(6):337 – 375, 1997.

[138] M. Kh. Rabadanov and I. A. Verin. X-ray diffraction study of $CuInSe_2$ single crystals. *Neorganicheskie Materialy*, 34(20), 1998.

[139] I.V. Bondar and N.S. Orlova. . *Inorganic Materials*, (21):967, 1985.

[140] H. Haupt and K. Hess. . *Inst. Phys.Conf. Ser.*, 35:5, 1977.

[141] H.J. von Bardeleben and R. D. Tomlinson. *Journal of Physics C: Solid State Physics*, (13):L1097, 1980.

[142] D. E. Pierron, L. D. Parker, and B. J. McNeely. Coefficient of expansion of gallium arsenide from -62 to 200°C. 21(2):290, 1966.

[143] S. Lany and A. Zunger. Intrinsic DX Centers in Ternary Chalcopyrite Semiconductors. *Phys. Rev. Lett.*, 100(1):016401, 2008.

[144] K. Hönes, M. Eickenberg, S. Siebentritt, and C. Persson. Polarization of defect related optical transitions in chalcopyrites. *Applied physics letters*, 93(092102), 2008.

[145] S. Siebentritt, S. Augustin, N. Papathanasiou, D. Hebert, A. Rockett, J. Bläsing, and M.-Ch. Lux-Steiner. Polarized Luminescence of Defects in $CuGaSe_2$. *MRS Proceedings*, Y13(1012), 2007.

[146] C. H. Lei, A. A. Rockett, I. M. Robertson, N. Papathanasiou, and S. Siebentritt. Interface reactions and Kirkendall voids in metal organic vapor-phase epitaxy grown $Cu(In, Ga)Se_2$ thin films on GaAs. *Journal of Applied Physics*, 100(11, 114915):8, 2006.

[147] D. J. Schroeder, G. D. Berry, and A. A. Rockett. Gallium diffusion and diffusivity in $CuInSe_2$ epitaxial layers. *Applied Physics Letters*, 69(26):4068–4070, 1996.

[148] A. Redinger. *EDX.* Le Tholy, 2010.

[149] J. I. Goldstein. *Scanning electron microscopy and X-ray microanalysis.* Kluwer Academic/Plenum Publ, New York [u.a.], 3. ed edition, 2003.